Université de Strasbourg

UNIVERSITÉ DE STRASBOURG







ÉCOLE DOCTORALE des Sciences de la Vie et de la Santé

THÈSE présentée par :

Simon LO VECCHIO

Soutenue le : 30 septembre 2020

Pour obtenir le grade de : **Docteur de l'Université de Strasbourg**Discipline/Spécialité : **Physique Cellulaire**

Brisures de symétrie et directionnalité dans les systèmes vivants

THÈSE dirigée par :

Daniel RIVELINE Directeur de Recherche, Université de Strasbourg, IGBMC

RAPPORTEURS:

Pascal SILBERZAN Directeur de Recherche, Université de Paris, Institut Curie

Thomas LECUIT Directeur de Recherche, Collège de France, Université de Marseille,

IBDM

AUTRES MEMBRES DU JURY:

Kinneret KEREN Professor, Technion, Israel Institute of Technology

Anna KICHEVA Professor, IST Austria

Carine MEIGNIN Professeur, Université de Strasbourg, IBMC

Université de Strasbourg

UNIVERSITÉ DE STRASBOURG







ÉCOLE DOCTORALE des Sciences de la Vie et de la Santé

THESIS presented by:

Simon LO VECCHIO

Defended on: 30th september 2020

To obtain the degree: **Docteur de l'Université de Strasbourg**

Discipline: Cell Physics

Symmetry breaking and directionality in living systems.

THESIS directed by:

Daniel RIVELINE Directeur de Recherche, Université de Strasbourg, IGBMC

REFEREES:

Pascal SILBERZAN Directeur de Recherche, Université de Paris, Institut Curie

Thomas LECUIT Directeur de Recherche, Collège de France, Université de Marseille,

IBDM

OTHER JURY MEMBERS:

Kinneret KEREN Professor, Technion, Israel Institute of Technology

Anna KICHEVA Professor, IST Austria

Carine MEIGNIN Professeur, Université de Strasbourg, IBMC

REMERCIEMENTS

Ce manuscrit de thèse est le fruit d'un travail collaboratif.

Je souhaite remercier mon Directeur de thèse, Daniel Riveline, sans qui ce projet n'aurait pas été possible. Il m'a soutenu depuis le début de mon stage en Master II jusqu'à aujourd'hui. Les échanges répétés que nous avons eus ont participé à aiguiser mon esprit critique. Il m'a poussé à défendre mes idées en toute circonstance. Ces débats scientifiques — et parfois non scientifiques — ont été importants pour ma construction personnelle et professionnelle. Je sais que nous aurons encore l'opportunité d'échanger autour de nouveaux projets.

Ensuite, j'aimerais remercier Valérie Lamour. Son investissement dans le double cursus Médecine-Sciences et son soutien indéfectible ont permis de mener à bien ce projet de thèse. Sans elle et sans sa volonté de créer un nouveau cursus de recherche pour les médecins, je ne serais probablement pas en train de rédiger ces pages. Merci Valérie.

I would like to thank all the members of the Jury who kindly accepted to review my work: Thomas Lecuit, Pascal Silberzan, Kinneret Keren, Anna Kicheva, and Carine Meignin. It's a pleasure for me to have such a great expertise on my work.

Je souhaite ensuite remercier tous mes collaborateurs. Ils ont apporté leur expertise et leur regard critique mais ils ont également contribué, grâce aux interactions répétées que j'ai pu avoir avec eux, à m'apprendre beaucoup. Merci à Raphaël Voituriez, à Laurent Navoret et Marcela Szopos, à Pascal Didier, à Michaël Ryckelynck ainsi qu'à Olivier Pertz. Merci aussi à Stéphanie Baudrey qui a pris beaucoup de son temps à m'aider en microfluidique.

I would like to thank also all the lab members, past and present. Alka Bhat, Linjie Lu, Tristan Guyomar, Rémi Berthoz, Michèle Lieb. A special thanks to Raghavan Thiagarajan, who taught me a lot.

Merci également à David Gonzalez-Rodriguez et Carine Meignin. Lors de nos échanges, ils ont participé à formuler des questions profondes qui ont fait mûrir certaines idées de ce travail.

Je souhaite remercier Erwan Grandgirard, Elvire Guiot, Bertrand Vernay, Didier Hentsch, Yves Lutz et Marcel Boeglin. Ils ont su m'aider et me conseiller pendant ces quatre années sur la plateforme d'imagerie.

Merci également à ma famille et à mes amis les plus proches – ils se reconnaîtront tous – qui ont su rendre les quelques moments difficiles agréables. Ils savent combien je tiens à eux.

Merci enfin à ma compagne, qui a réussi à me supporter pendant ces quatre années et qui a participé aux meilleurs moments comme aux pires. Sans le savoir, elle a elle aussi participé à mener à bien ce projet et à l'écriture de ces pages. Merci à elle.

RÉSUMÉ DES TRAVAUX DE THÈSE

Lors du développement, ou lors de certains processus physiologiques ou pathologiques, les cellules peuvent migrer de manière directionnelle, sur des distances qui représentent plusieurs fois leur taille cellulaire. Pour ce faire, elles doivent briser leur symétrie et garder en mémoire la polarité acquise. Ce processus actif est gouverné par les petites GTPases Rho qui réarrangent le cytosquelette d'acto-myosine et génèrent localement la création de structures cellulaires comme les adhésions focales, les lamellipodes ou les filopodes.

Si la migration des cellules adhérentes sur une surface homogène est maintenant bien caractérisée, la compréhension des mécanismes qui mènent une cellule individuelle à migrer de manière directionnelle n'est pas complète. Ces phénomènes, observés *in vivo*, sont souvent attribués à la présence de gradients chimiques dans le micro-environnement cellulaire, bien que leur quantification et leur caractérisation soient souvent manquantes.

Ces mouvements directionnels émergent également à l'échelle multicellulaire. Dans certains contextes développementaux, des groupes de dizaines de cellules brisent spontanément leur symétrie et sont soumis à de larges mouvements cohérents. Si ces migrations peuvent partager des similarités avec les mouvements individuels, l'extrapolation d'un système à l'autre n'est pas toujours correcte : cette propriété émergente d'un ensemble multicellulaire doit être étudiée à part, en prenant en compte ses particularités, afin d'extraire des règles simples d'interaction et de migration.

Ce travail de thèse, interdisciplinaire à l'interface entre la Biologie et la Physique, aura consisté à dégager des règles simples qui gouvernent les évènements de brisures de symétrie spontanées et les migrations dirigées, à l'échelle individuelle ou à l'échelle multicellulaire.

LA DYNAMIQUE COLLECTIVE DES ADHÉSIONS FOCALES GOUVERNE LA DIRECTION DES MIGRATIONS CELLULAIRES

Simon Lo Vecchio, Raghavan Thiagarajan, David Caballero, Vincent Vigon, Laurent Navoret, Raphaël Voituriez, Daniel Riveline

Les migrations cellulaires dirigées sont fondamentales, aussi bien en physiologie qu'en pathologie. Durant le développement embryonnaire, les cellules de la crête neurale migrent sur de larges distances, de manière directionnelle, afin d'atteindre certains sites spécifiques de l'embryon et de s'y différencier. En pathologie, l'exemple typique est celui des disséminations de métastases : les cellules cancéreuses s'échappent de la tumeur primaire et migrent sur de très longues distances jusqu'à atteindre des sites secondaires non aléatoires.

Dès lors, la cellule doit briser sa symétrie, polymériser un front de migration, et surtout maintenir cette polarité sur des échelles de temps suffisamment importantes pour produire un mouvement sur une longue distance (en excluant les longueurs parcourues avec le flux sanguin).

Dans ce contexte, la *chimiotaxie*, moyen par lequel une cellule acquiert une polarité en présence d'un gradient chimique et largement étudiée *in vitro*, représente une hypothèse de choix pour expliquer ces phénomènes de migration individuelle. Cependant, la présence de gradients

chimiques et leur quantification ne sont pas toujours montrées *in vivo*; et lorsqu'elles le sont, il est rarement démontré que ces gradients sont la cause directe des migrations dirigées.

Dans cette étude, nous avons montré qu'il est possible de produire un mouvement directionnel sur de larges distances (plusieurs centaines de micromètres) sans gradients chimiques. Pour ce faire, nous brisons la symétrie de l'environnement cellulaire grâce à la micro-impression. Les cellules, placées sur des motifs asymétriques avec des séparations variables et contrôlées, se polarisent et montrent une migration directionnelle forte (80% des mouvements cellulaires peuvent être rectifiés). Nous avons appelé ce mode de migration, la *ratchetaxie*.

Nous avons montré que le processus de rectification était gouverné par la dynamique de nucléations des adhésions focales, les sites d'ancrage cellulaire au substrat. En effet, l'inférence de force a montré que l'asymétrie des distributions de forces est corrélée avec la direction du mouvement.

De manière surprenante, le phénomène de rectification n'est pas linéaire. Cette observation est la conséquence d'une aire de nucléation saturante au-delà de laquelle il n'y a plus d'adhésions focales formées. Cette saturation induit cette dynamique bien particulière de la rectification et c'est la compétition entre le régime linéaire et le régime saturé qui détermine le biais dans le déplacement.

Enfin, les résultats expérimentaux ont pu être reproduits grâce à un modèle théorique simple, fondé sur des arguments géométriques et uniquement sur des quantités accessibles aux mesures expérimentales. Nous avons pu prédire de nouveaux résultats qui ont été, par la suite, testés avec succès lors de nouvelles expériences.

Pour conclure, nous avons élucidé dans ce travail les mécanismes qui gouvernent la migration cellulaire par *ratchetaxie* et prouvé qu'une rectification efficace peut avoir lieu sans gradients chimiques, simplement en modifiant l'environnement cellulaire.

Contributions: Supervision du projet et idée: Daniel Riveline (IGBMC, Strasbourg); Expériences et analyses – Simon Lo Vecchio (IGBMC, Strasbourg); Conception de la théorie – Raphaël Voituriez (LPTMC, Paris); Écriture du code des adhésions focales – Vincent Vigon et Laurent Navoret (IRMA, Strasbourg); Initiation du projet – Raghavan Thiagarajan et David Caballero (ISIS/IGBMC, Strasbourg).

RATCHETAXIE EN CANAUX ET ANISOTROPIES DU CYTOSQUELETTE

Émilie Le Maout*, Simon Lo Vecchio*, Praveen Kumar Korla, Jim Jinn-Chyuan Sheu, Daniel Riveline

Ce projet s'inscrit dans la continuité du précédent et vise à élucider l'efficacité et les mécanismes de la *ratchetaxie* en 3D, dans des canaux micro-fabriqués mimant les petits capillaires sanguins. Le canal est régulièrement constitué de petits 'goulots d'étranglement' périodiques qui constituent des asymétries locales et à travers lesquels la cellule doit se déformer pour passer. Ce contexte permet d'approcher les conditions *in vivo* où les cellules cancéreuses circulantes

présentent des phénomènes d'extravasation et de migrations directionnelles dans un réseau capillaire étroit et confiné.

Nous avons montré que la brisure de symétrie initiale et la déformation cellulaire au point d'entrée déterminent totalement la direction de la migration. En effet, après son entrée dans le canal, la cellule 'ignore' les autres asymétries locales et migre de manière directionnelle. A 'toit ouvert' cependant, la rectification locale du mouvement suit la brisure de symétrie des motifs comme dans le sujet précédent.

Lors du passage aux goulots, le cytosquelette se réorganise et de fortes anisotropies sont visibles aux points de compression : l'actine, la myosine et la kératine s'organisent pour déformer le noyau et permettre le passage de la cellule. Des cellules défectueuses en kératine (mutation retrouvée dans certains cancers oraux) échouent à passer les goulots et présentent une distribution homogène de la protéine, soulignant l'importance des anisotropies dans la migration confinée.

Enfin, en présence transitoire de gradients chimiques, l'effet de brisure de symétrie locale est rétabli. A l'arrêt du gradient, les cellules peuvent déformer leurs noyaux dans un sens, mais sont bloquées en moyenne dans l'autre sens du ratchet.

Ces résultats décrivent les mécanismes de brisure de symétrie et de migration dirigée dans un contexte de confinement, en 3D, ressemblant aux situations rencontrées *in vivo* dans des vaisseaux sanguins de la taille des cellules, avec des portées potentielles en physiologie et en pathologie.

Contributions: Supervision du projet et idée: Daniel Riveline (IGBMC, Strasbourg); Design et réalisation des expériences – Émilie Le Maout (IGBMC, Strasbourg); Expériences sur les adhésions focales – Simon Lo Vecchio (IGBMC, Strasbourg); Expériences sur les Cal27 – Praveen Kumar Korla et Jim Jinn-Chyuan Sheu (National Sun Yatsen University, Taiwan); Analyse des résultats – Émilie Le Maout et Simon Lo Vecchio (IGBMC, Strasbourg).

COUPLAGE ENTRE RHOA ET POLARITÉ CELLULAIRE LORS DES MOUVEMENTS COHÉRENTS

Simon Lo Vecchio, Marcela Szopos, Laurent Navoret, Olivier Pertz, Daniel Riveline

Lors du développement d'un organisme, la morphogenèse implique des mécanismes physiques qui sont essentiels pour expliquer l'élongation, les contractions et les migrations. Les épithélia se réarrangent de manière complexe et le cytosquelette d'acto-myosine ainsi que les voies de signalisation des Rho GTPases imposent les lois d'interactions entre cellules : les contractions et extensions dictent les dynamiques spatio-temporelles à l'échelle d'une cellule unique, mais également aux échelles multi-cellulaires.

Pendant le développement, de larges flux migratoires collectifs, impliquant des dizaines ou des centaines de cellules, émergent, entraînant des changements de formes importants. Chez l'organisme modèle *Drosophila Melanogaster* par exemple, quelques dizaines de cellules se mettent spontanément à migrer de manière collective et directionnelle, lors du développement et l'élongation de la chambre à œuf. Ce phénomène de rotation émergeant et spontané, assez peu

compris, se retrouve dans la morphogenèse des acini mammaires ou des structures tubulaires.

Le but de ce projet est de reproduire et de maîtriser *in vitro* et *in silico* les dynamiques de brisure de symétrie spontanée observées *in vivo*, afin de comprendre et d'extraire les lois d'interactions entre cellules et l'émergence de mouvements collectifs au sein des systèmes multicellulaires. Grâce à la biologie cellulaire, la micro-fabrication, la micro-impression et des modèles théoriques, nous avons réussi à reproduire ces mouvements collectifs sur un système simple d'anneaux cellulaires aux dimensions contrôlées. Cette configuration proposée par Alan Turing dans son article sur la morphogenèse constitue la réalisation la plus simple d'une brisure de symétrie pour un système multi-cellulaire.

Nous avons trouvé qu'il existait une taille seuil au-delà de laquelle le système comportait un nombre trop grand 'd'individus' pour spontanément obtenir une « cohérence » (c'est-à-dire un mouvement directionnel de l'ensemble des cellules), mais en-dessous de laquelle, le système brisait spontanément sa symétrie et acquérait une « cohérence » globale. Cette taille, appelée *longueur de cohérence* et extraite expérimentalement, correspond à environ 15 cellules.

D'autre part, nous avons montré que l'émergence de ce mouvement était le résultat d'une compétition interne entre les polarités cellulaires et que la cohérence était possible grâce à l'auto-assemblage de larges câbles d'acto-myosine aux interfaces, agissant comme des contraintes permettant d'éviter la dispersion de la cohorte cellulaire. Des perturbations locales de ce câble entraînent la fuite locale des cellules.

Les divisions cellulaires, mais aussi la densité locale sont des paramètres également déterminants dans la mise en place des mouvements cohérents : les divisions, par exemple, génèrent deux cellules filles avec des polarités opposées dans l'anneau. De ce fait, une des deux cellules doit relaxer sur la polarisation moyenne afin d'entraîner la cohérence. D'autre part, une densité cellulaire faible était associée le plus souvent à une cohérence globale moins élevée et parfois à des cassures spontanées de l'anneau.

Enfin, nous avons analysé la voie de signalisation Rho et son activité par sonde FRET afin de déterminer le couplage entre la chimie et la mécanique. Nous avons observé une corrélation entre les niveaux d'activation de RhoA et l'apparition du mouvement directionnel. Mais nous avons surtout mis en évidence que l'activité de RhoA pouvait être reliée de manière univoque avec les vitesses cellulaires. Enfin, les câbles acto-myosine internes et externes sont 'Rho' actifs.

Un modèle théorique nouveau, fondé sur celui de Vicsek, a permis de reproduire *in silico* ces observations expérimentales. La théorie repose sur les interactions entre polarités et inclut les deux câbles d'acto-myosine comme des frontières libres, contraignant les cellules. Ces deux caractéristiques suffisent à reproduire les observations expérimentales et nous ont permis de mieux cerner l'émergence spontanée de la cohérence.

Pour conclure, ce projet nous a permis de sonder les phénomènes de brisure de symétrie, spontanés, à l'échelle multicellulaire, et d'en extraire les règles essentielles. La cohérence résulte d'une synchronisation entre plusieurs paramètres : l'organisation des polarités cellulaires à l'intérieur de l'anneau, la longueur de cohérence inhérente au système multi-cellulaire, les câbles d'acto-myosine comme contraintes actives aux bords.

Contributions : Supervision du projet et idée: Daniel Riveline (IGBMC, Strasbourg); Expériences et analyses – Simon Lo Vecchio (IGBMC, Strasbourg); Conception de la théorie – Laurent Navoret (IRMA, Strasbourg) et Marcela Szopos (MAP5, Paris); Construction du biosenseur FRET et expertise – Olivier Pertz (ICB, Berne).

ÉMERGENCE DES MOUVEMENTS COHÉRENTS DANS DES SYSTÈMES 3D MULTICELLULAIRES

Simon Lo Vecchio, Gaëtan Jardiné, Michaël Ryckelynk, Pascal Didier, Olivier Pertz, Daniel Riveline

In vivo les cellules migrent dans des environnements 3D complexes. Pour essayer de comprendre si les mécanismes d'émergence de cohérence répondent aux mêmes règles que celles trouvées dans notre travail sur les anneaux 2D, nous avons essayé d'analyser ces dynamiques sur des sphéroïdes multicellulaires.

Ce projet, dont les résultats préliminaires sont détaillés dans ce manuscrit, visent à extraire les mouvements cellulaires collectifs en géométrie sphérique, les corréler aux activités des petites GTPases Rho et de comparer l'ensemble avec les phénomènes de cohérence 2D observés sur les anneaux.

Nous avons généré des sphéroïdes cellulaires grâce aux propriétés d'auto-organisation des cellules épithéliales MDCK : dissociées et cultivées dans des matrices de Matrigel, les cellules se divisent et s'organisent en sphéroïdes « creux » avec une seule monocouche cellulaire au contact d'un *lumen*. Des tests ont été aussi réalisés en montage micro-fluidique.

Afin d'observer ces ensembles de cellules, nous avons développé un montage optique de microscopie à feuillet de lumière. Ce type d'imagerie permet d'obtenir le mouvement des cellules sur tous les plans de la sphère avec une photo-toxicité basse et un taux d'images par seconde élevé. De plus, il permettra à terme de pouvoir effectuer des imageries FRET et d'analyser les activités des GTPases sur toute la surface de la sphère.

Nous présentons l'émergence de mouvements cohérents avec brisure de symétrie spontanée dans les sphéroïdes de cellules également. La vitesse de ces mouvements semble supérieure à celle observée sur les anneaux de cellules : en 3D, les cellules ont une vitesse de rotation d'environ 40-50µm.h⁻¹ contre 20-30µm.h⁻¹ sur la géométrie 2D. Ce résultat suggère qu'il existe des différences dans les modes migratoires des deux systèmes, peut-être simplement liées aux frottements avec les surfaces respectives (fibronectine sur l'anneau, Matrigel pour les sphéroïdes). Les lamellipodes cryptiques pourraient être impliqués de cette diminution de vitesse sur les anneaux cellulaires. En effet, la présence de lamellipodes dans nos sphéroïdes n'a pas été confirmée dans nos expériences, ce qui suggère que les cellules organisent leur mouvement de manière différente par rapport aux anneaux sur la surface plane.

Enfin, nous avons observé l'arrêt des rotations à mesure que les sphéroïdes grandissent, lorsque le diamètre atteint à peu près 45μm. Ces résultats indiquent que les règles établies par la longueur de cohérence multi-cellulaire semblent être conservées dans des contextes 3D.

En conclusion, ce projet nous permettra de mieux comprendre comment émergent les mouvements collectifs cohérents dans des environnements proches de ceux rencontrés *in vivo*

(comme les acini mammaires ou la chambre à œuf de *Drosophila Melanogaster*). Ces dynamiques seront comparées à celles des petites GTPases Rho permettant ainsi de corréler signalisation et mécaniques cellulaires.

Contributions: Supervision du projet et idée: Daniel Riveline (IGBMC, Strasbourg); Expériences et analyses – Simon Lo Vecchio (IGBMC, Strasbourg); Encadrement et expertise sur le montage optique – Pascal Didier (LBP, Strasbourg); Expertise en microfluidique – Michaël Ryckelynck (IBMC, Strasbourg); Construction du biosenseur FRET et expertise – Olivier Pertz (ICB, Berne).

THESIS SUMMARY

During development or during some physiological and pathological processes, cells often migrate directionally over lengths comparable to many cell sizes. To do so, cells need to break their symmetry and keep this generated polarity over time and space. This active process is driven by the activation of small Rho GTPases shaping up the dynamics of the acto-myosin cytoskeleton and generating sub-cellular structures such as focal adhesions, lamellipodia or filopodia among many cytoskeleton structures.

Even though migration of adherent cells on flat and homogeneous substrates is well characterized, complete understanding of the mechanisms leading to directional motion is still lacking. These phenomena, observed *in vivo*, are often associated with the presence of chemical gradient in the cell micro-environment. However, characterization and quantification of these gradients are rarely done *in vivo* and the causality between direction of motion and the presence of a long-range gradient is often lacking.

These directional migrations also emerge at the multicellular scale. In development, cohorts of tens of cells spontaneously break symmetry and undergo large coherent motions. Even though these phenomena can share similarities with single cell motions, extrapolation from one system to the other can be challenging: new properties emerge at the multicellular scales and these specificities need to be addressed separately in order to extract simple interacting rules and generic features setting collective motion.

This interdisciplinary PhD work, at the interface between Biology and Physics, aims at providing simple rules governing symmetry breaking processes and directed migrations, at the single cell level and a the multicellular scale.

COLLECTIVE DYNAMICS OF FOCAL ADHESIONS REGULATE DIRECTIONS OF CELL MOTION

Simon Lo Vecchio, Raghavan Thiagarajan, David Caballero, Vincent Vigon, Laurent Navoret, Raphaël Voituriez, Daniel Riveline

Directed cell motion is fundamental in various physiological and pathological processes. During development, cells from the neural crest migrate over large distances in a directional manner in order to reach specific sites of the embryo and differentiate. In pathology, metastasis spreading represents one of the canonical examples: cancer cells escape from the primary tumor and migrate over millimeter to centimeter length scales to reach specific secondary sites.

Therefore, cells need to break their symmetry to polymerize a leading edge, and to sustain this polarity over timescales sufficiently long to generate directed motion over large distances (excluding lengths travelled with the blood flow).

In this context, acquisition of polarity by chemical gradients in the cell micro-environment – namely chemotaxis – has been the most popular paradigm to explain directed migrations in vivo. Even though this phenomenon has been extensively studied in vitro, the existence of chemical gradients and their quantification in vivo are rarely demonstrated. If they are, they are not always proven to cause the directed motion.

In this study, we report that directed cell migration can be generated over hundreds of micrometers without any chemical gradients. To do so, we break the symmetry of the cell microenvironment using micro-printing methods of the extra-cellular matrix protein fibronectin. Cells are seeded on asymmetric adhesive regions with gaps of controlled/varying dimensions, cells polarize, and exhibit rectification (with up to $\sim 80\%$ of the cells migrating to one preferential direction on average). This phenomenon has been coined *ratchetaxis*.

We showed that the bias in cell migration is driven by the collective dynamics of cells anchoring zones – the focal adhesions. Indeed, force inference on focal adhesions distributions correlates with direction of motion, suggesting that focal adhesions distribution alone can predict directionality.

Surprisingly, rectification is a non-linear process. This result is a direct consequence of a saturating nucleation area above which there is no new focal adhesions generated by protrusions. This saturation drives the rectification dynamics and the competition between the linear regime and the saturating one sets the bias in direction.

Finally, experiments are reproduced with a simple theoretical model based on geometrical arguments and measurable parameters. We predicted new behaviors on different geometries for motifs and gap distances, and we successfully tested them with new experiments.

To conclude, we provide the mechanisms governing cell migration through ratchetaxis and evidence that efficient directed motions can be generated without any chemical gradient by simply tuning geometry of the cell micro-environment.

Contributions: Project supervision and idea: Daniel Riveline (IGBMC, Strasbourg); Experiments and data analysis – Simon Lo Vecchio (IGBMC, Strasbourg); Theory – Raphaël Voituriez (LPTMC, Paris); Focal adhesions force inference code – Vincent Vigon and Laurent Navoret (IRMA, Strasbourg); Project initiation – Raghavan Thiagarajan and David Caballero (ISIS/IGBMC, Strasbourg).

RATCHETAXIS IN CHANNELS: CELLS IN CONFINEMENT MOVE DIRECTIONALLY.

Emilie Le Maout*, Simon Lo Vecchio*, Praveen Kumar Korla, Jim Jinn-Chyuan Sheu, Daniel Riveline

This project aims at probing the efficiency of ratchetaxis in 3D micro-fabricated channels. They are designed with regularly spaced bottlenecks producing local asymmetries through which cells need to deform their nuclei in order to migrate. This type of configuration can be associated to *in vivo* contexts where cancer cells exhibit extravasation processes and directed migration into narrow and confined capillaries networks.

We show that the initial broken symmetry at the entry point totally sets direction of migration. Indeed, cells seem to 'ignore' cues from the local asymmetries and migrate in a directed manner. However, when confined in the x-y plane only, ratchetaxis operates and migrations are rectified towards the direction of local anisotropies.

During passage through bottlenecks, cell cytoskeleton reorganizes and exhibits strong anisotropies at the squeezing point: actin, myosin and keratin distributions correlate with nucleus deformation and cell passage. Defects in keratin – a mutation found in various oral squamous cancers – lead to blockage in channels and impair passage through the bottlenecks. In addition, mutated keratin distribution is homogeneous highlighting the importance of anisotropies at the bottleneck to generate proper migration.

Finally, chemical gradients can influence migration in closed configuration. After their removal, cells can or cannot pass on average the constriction zones depending on the respective orientations of chemical gradients and ratchets motifs. This suggests a polarization effect associated to chemical cues.

Altogether, we describe in this work mechanisms breaking symmetry and leading to directed migration in 3D confined environment mimicking some conditions encountered *in vivo* such as small blood vessels in capillary networks.

Contributions: Project supervision and idea: Daniel Riveline (IGBMC, Strasbourg); Design and experiments – Émilie Le Maout (IGBMC, Strasbourg); Experiments on focal adhesions – Simon Lo Vecchio (IGBMC, Strasbourg); Experiment with Cal27 cells – Praveen Kumar Korla and Jim Jinn-Chyuan Sheu (National Sun Yatsen University, Taiwan); Data analysis – Émilie Le Maout and Simon Lo Vecchio (IGBMC, Strasbourg).

TURING RINGS: SPONTANEOUS ROTATIONS AS AN INTERPLAY BETWEEN POLARITY AND RHOA ACTIVITY

Simon Lo Vecchio, Marcela Szopos, Laurent Navoret, Olivier Pertz, Daniel Riveline

During development, morphogenesis involves physical mechanisms essential to explain elongation, contractions and migrations. Epithelia undergo complex rearrangements and the actomyosin cytoskeleton together with its associated Rho signaling pathways set interacting rules between cells: contractions and extensions dictate the spatio-temporal dynamics at the single cell level but also at the multicellular scale.

In this context, large scale collective migrations involving tens or hundreds of cells emerge throughout the developing organism leading to important shape changes. In *Drosophila* Melanogaster egg chamber elongation, a group of cells undergo spontaneous rotation and starts migrating in a collective and directed manner. This phenomenon of spontaneous rotation also occurs in various other morphogenesis processes such as the development of mammary acini or tubular organs.

This project aims to reproduce and master *in vitro* and *in silico* the dynamics of spontaneous symmetry breakings observed *in vivo* in order to understand and extract interaction rules between cells leading to collective coherent motion in multicellular systems. With cell biology, microfabrication, micro-printing and theoretical models, we reproduced these collective motions on a simple system of cellular rings.

We report and confirm the existence of a length above which the system cannot spontaneously be "coherent" (i.e. a directional motion of the whole cellular cohort), but below which the system does spontaneously break its symmetry to undergo a global coherent motion. This typical length, called the coherence length is extracted from experiments and corresponds in our systems to about 15 cells.

We also show that the emergence of global coherence is a direct consequence of an internal tugof-war between single cell polarities. In addition, coherent motion is facilitated by the presence at the boundaries of two acto-myosin cables, acting as internally driven constraints maintaining the cellular cohort together. Local perturbations of these cables lead to local escape of cells.

Cell divisions but also local cell density are found to be determinant in the onset of coherence: daughter cells generated by divisions acquire in majority of cases opposite polarities and therefore act as polarity breakers. Indeed, one of the two cells needs to relax on the mean polarity in order to promote coherence. On the other hand, a cell density too low decreases the levels of coherence and can also challenge continuity of the multicellular ring with spontaneous breakages.

Finally, we probed RhoA activity by FRET sensors in order to determine the coupling between signaling pathways and mechanics. We report a correlation between RhoA activity levels and the appearance of spontaneous rotations but more importantly we show that RhoA activity is correlated to cell velocities within the ring. Finally, RhoA is active in the inner and outer acto-myosin cables, and this reinforces the active roles of these cellular boundaries on cell polarity and cell motion.

A new theoretical Vicsek-based model allowed us to reproduce *in silico* the experimental results. Theory mainly explored interactions between cell polarities and the impact of the two acto-myosin cables considered here as free boundaries constraining cells within the ring. These two characteristics were sufficient to fit experimental data and to reproduce the emergence of coherent motions.

To conclude, this study identified the spontaneous symmetry breaking at the multicellular scale. Coherence length is inherent to epithelial cells, acto-myosin cables act as internally driven active constraints, and the interactions between single cells polarity within the ring are key. These ingredients are sufficient to recapitulate quantitatively the phenomena leading to global coherence.

Contributions: Project supervision and idea: Daniel Riveline (IGBMC, Strasbourg); Experiments and data analysis – Simon Lo Vecchio (IGBMC, Strasbourg); Theory and simulations – Laurent Navoret (IRMA, Strasbourg) and Marcela Szopos (MAP5, Paris); FRET biosensor design and expertise – Olivier Pertz (ICB, Berne).

EMERGENCE OF COHERENCE IN 3D MUTLICELLULAR SYSTEMS

Simon Lo Vecchio, Gaëtan Jardiné, Michaël Ryckelynk, Pascal Didier, Olivier Pertz, Daniel Riveline

In vivo cells migrate through complex 3D environments. In order to know whether onsets of coherence follow the same rules set with 2D rings, we analyzed these dynamics on multicellular spheroids.

We report in this manuscript preliminary results of this project which aims to extract collective cells motion on a spherical geometry together with its associated Rho activity. These results will be further compared to those obtained on 2D configurations.

We generated multicellular spheroids by simple self-organisation of MDCK cells: dissociated and embedded into Matrigel matrices, cells divide and spontaneously self-assemble into hollow spheroids with a single monolayer of cells and a lumen. Tests were also performed with microfluidic designs.

In order to track cells dynamics in 3D, we developed a custom light-sheet optical set-up. This type of imaging modality allows to extract cellular motion in all the spheroid planes with a low photo-toxicity and with a high images per second rate. In addition, this set-up will be upgraded and used further in the project to perform FRET acquisition and to analyze GTPases activity over the full spheroid surface.

We report the emergence of global coherent motions with spontaneous symmetry breaking in multicellular spheroids. Velocity of these motions seems to be higher than the ones observed on cellular rings: in 3D, cells rotate with a speed of about 40 to $50\mu m/h$ whereas they migrate with an average velocity of 20 to $30\mu m/h$ on 2D geometries. This may be the result of differences in friction. Cryptic lamellipodia could be responsible for this decrease in velocity on cellular rings through interactions with the printed fibronectin. Indeed, lamellipodia in spheroids were absent in our experiments, suggesting that cells spontaneously organize their motion differently with Matrigel.

Finally, we observed arrest of rotation as the spheroids grew (here, when the diameter was about $45\mu m$). These findings indicate that the rules established by the coherence length seem to be still valid in 3D contexts.

Altogether, this project will provide new insights in the emergence of collective coherent motion in 3D environments close to situations encountered *in vivo* such as mammary acini or the *Drosophila* egg chamber. These cellular dynamics will be also compared to small Rho GTPases activity in space and in time in order to correlate Rho signaling and cell mechanics.

Contributions: Supervision of the project and idea: Daniel Riveline (IGBMC, Strasbourg); Experiments and analysis – Simon Lo Vecchio (IGBMC, Strasbourg); Supervision and optics – Pascal Didier (LBP, Strasbourg); Microfluidics – Michaël Ryckelynck (IBMC, Strasbourg); Biosensor FRET – Olivier Pertz (ICB, Berne).

TABLE OF CONTENTS

REMERCIEMENTS	3
RÉSUMÉ DES TRAVAUX DE THÈSE	5
THESIS SUMMARY	11
TABLE OF CONTENTS	
MOVIE CAPTIONS	21
LIST OF ABBREVIATIONS	23
1. PHD MOTIVATIONS	24
2. INTRODUCTION	
2.1 SYMMETRY BREAKING IN LIVING MATTER: FIRST THOUGHTS	
2.2 SINGLE CELL MOTILITY: A BIOLOGICAL DESCRIPTION	
2.2.1 Cytoskeleton components and sub-structures	
2.2.1.1 Actin	
2.2.1.2 Actin Binding Proteins (ABP)	
2.2.1.3 Myosin motors	
2.2.1.4 Microtubules	
2.2.1.5 Intermediate filaments	
2.2.1.6 Filopodia and Lamellipodia	
2.2.1.7 Focal Adhesions	
2.2.2 Rho Family: signalling pathways	
2.2.2.1 RhoA signalling	
2.2.2.2 Rac signaling	
2.2.2.3 Cdc42 signaling	
2.2.3 Migration on 2D flat surfaces	
2.2.4 Spatio-temporal regulation of small GTPases	
2.3 PHYSICS OF CELL MIGRATION	
2.3.1 Active gels theory	
2.3.2 Mechanics of cellular migrations	
2.3.2.1 Integrin-based migration	
2.3.2.2 Adhesion-free migration	
2.3.3 Persistent Random Walks	
2.4 BIOLOGY OF COLLECTIVE MOTIONS	
2.4.1 Cell-cell junctions	
2.4.1.1 Adherens junctions	
2.4.1.2 Tight junctions	
2.4.1.3 Inter-cellular communications through junctions mechanosensing	
2.4.2 Rho dynamics in epithelia	
2.5 PHYSICAL DESCRIPTION OF COLLECTIVE MIGRATIONS	
2.5.1 Coarse-grained hydrodynamic description	
2.5.1.1 Navier-Stokes equations	
2.5.1.2 Velocity fields in migrating epithelia	
2.5.2 Discrete description: the Vicsek model	
2.6 DIRECTIONALITY	
2.6.1 Biological relevance	
2.6.1.1 Single cell directed motion	
2.6.1.2 Directed collective motion	
2.6.2 Chamical gradients	56

2.6.3 Guidance through local asymmetries	
2.6.4 Alignment and directional flows driven by confinement	60
2.8 PhD question	62
3. MATERIAL AND METHODS	64
3.1 MICRO-FABRICATION	
3.1.1 Photomask	
3.1.2 Photolithography	
3.1.3 Soft lithography	
3.2 MICRO-PRINTING	
3.2.1 Patterns production	
3.2.2 Passivation	
3.3 CELL CULTURE	
3.3.1 Mesenchymal cells	
3.3.2 Epithelial cells	
3.3.3 Generation of MDCK spheroids	
3.3.4 Transfections	
3.3.5 Generation of new stable cell lines	
3.3.5.1 MDCK RhoA-BS/E-cadherin-DsRED and MDCK RhoA -dBS/E-cadherin-D	
3.3.5.2 NIH 3T3 VASP-GFP	
3.4 PREPARATION OF SAMPLES AND EXPERIMENTS	
3.4.1 On micro-patterns	
3.4.3 Gradient formation	
3.4.4 Hydrogels preparation	
3.4.4.1 Agarose and Phytagel	
3.4.4.2 Alginate	
3.4.5 Oleic acid preparation	
3.5 IMMUNOFLUORESCENCE	
3.6 MICROSCOPY	
3.6.1 Standard time-lapse microscopy	
3.6.2 Reflection Interference Contrast Microscopy (RICM)	
3.6.3 Confocal microscopy	
3.6.3.1 FRET acquisition	
3.6.3.2 Laser ablation	78
3.6.4 Spinning-disk	
3.7 IMAGE ANALYSIS	78
3.7.1 Focal adhesions and forces mapping	78
3.7.2 Trajectories	78
3.7.3 Particle Image Velocimetry (PIV)	
3.7.4 Coherence length	
3.7.5 FRET analysis	
3.7.6 Tissue Miner	
3.7.6.1 Cell elongation	
3.7.6.2 Cell orientation	
3.7.6.3 T1 transition	81
4. COLLECTIVE DYNAMICS OF FOCAL ADHESIONS REGULATE	
DIRECTIONS OF CELL MOTION	82
4.1 Introduction	
4.2 IMPROVED RECTIFICATION OF CELLS ON RATCHET-LIKE PATTERNS	
4.2.1 Description of the configurations	
4.7.7. UHANHIVINO AIRECHANAHIV	X 1

4.2	T and the state of	
4.3	FOCAL ADHESIONS DYNAMICS	85
4.3	Visualisation of FAs and controls	85
	3.1.1 Overexpression of FAs proteins and migration	85
	3.1.2 VASP-GFP and immunofluorescence	
	3.1.3 FAs dynamics on ratchet-like patterns	
	3.1.4 Testing with RICM	
4.3	Tr 8	
4.4	THEORETICAL MODEL	
4.4		
4.4	Camination of the William meessage at east a more remaining	
4. 4	r r g · · · · · · · · · · · · · · · · ·	
	EXPERIMENTAL TESTS AND VALIDATION OF THE MODEL	
4.5	Design of new configurations and predictions	
4.5	T	
4.6	DISCUSSION	
4.7	CONCLUSIONS	97
5. RA	CHETAXIS IN CHANNELS: CELLS IN CONFINEMENT MOVE	
	TONALLY.	98
5.1	Introduction	
5.2	DESIGN OF THE DIFFERENT CONDITIONS	
5.2		
5.2		
5.2		
5.3	MIGRATION IN RATCHET-LIKE CHANNELS	
5.3	Quantification of the bias	
5.3	V 1	
5.3	1 6	
5.4	ANISOTROPIES OF CYTOSKELETON COMPONENTS	
5.4 5.4	ActinFocal adhesions.	
5.4 5.4		
5.4 5.4		
	CHEMICAL GRADIENTS AND <i>RATCHETAXIS</i>	
5.5 5.5		
5.5		
5.6	DISCUSSION	
5.7	Conclusions	
		107
	RING RINGS: SPONTANEOUS ROTATIONS AS AN INTERPLAY	
BETW	EN POLARITY AND RHOA ACTIVITY	110
6.1	Introduction	110
6.2	OBTAINING COHERENT MULTICELLULAR SYSTEMS	
6.2	Dynamics of different ring configurations	
6.2		
6.2	·	
6.2		
6.2		
6.3	CELL MECHANICS	
6.3	Distribution of polarities inside the ring	
6.3	•	
	3.2.1 Tight junctions acquisition and segmentation	

6.3.2.2	Stretch	117
6.3.2.3	Alignment of polarities	118
6.3.2.4	Tangential alignment	118
6.3.2.5	Density	119
6.3.2.6	Cell divisions	120
6.3.2.7	T1 transitions	121
6.4 A	cto-myosin cables: internally-driven constraints	122
6.4.1	Immunostainings	122
6.4.2	Laser ablation experiments and tension measurements	123
6.4.3	Local perturbation of the cable: caldesmon transfections	123
6.5 R	hoA activity	124
6.5.1	Controls of the biosensor	125
6.5.2	Spatial localization of RhoA	126
6.5.3	FRET levels and coherence	126
6.5.4	RhoA activity and velocity	127
6.5.5	Reaction-diffusion patterns of RhoA	129
6.6 Thi	EORETICAL MODELLING: A VICSEK-BASED APPROACH	130
6.6.1	Description of the model	131
6.6.2	Experimental measurements of the model parameters	133
6.6.2.1		
6.6.2.2	Polarity relaxation	134
6.6.2.3	Polarity precedes velocity	134
6.6.2.4	Single cell velocity	136
6.6.2.5	Acto-myosin cables tension	136
6.6.2.6	Active force	136
6.6.2.7	Orders of magnitude taken from the literature	136
6.6.3	Simulations	137
6.7 D IS	CUSSION	138
6.8 Co	NCLUSIONS	141
7. EMERO	GENCE OF COHERENCE IN 3D MULTICELLULAR SYSTEM	5143
7.1 INT	RODUCTION	143
	RMATION OF MULTICELLULAR SPHEROIDS	
7.2.1	Microfluidics devices.	
7.2.1.1	Principles	
7.2.1.2	<u>*</u>	
7.2.1.3	<i>y</i> 8	
7.2.1.4		
7.2.2	Self-organization	
7.2.2.1		
7.2.2.2		
7.3 Ho	ME-MADE LIGHT-SHEET MICROSCOPY TO OBSERVE 3D MOTIONS	
7.3.1	Principles	
7.3.2	Tests with Open-SPIM	
7.3.3	Optical set-up	
7.3.4	Issues and troubleshooting	
	NAMICS OF SPHEROIDS.	
7.4.1	In phase contrast microscopy	
7.4.2	Through light-sheet microscopy	
	NCLUSIONS AND PERSPECTIVES	
1.0	NULLISIUMS AIND PERSPEULIVES	
	SSION AND CONCLUSION	

10.	APP	ENDIX	175
10.1	l Dr	RUG EXPERIMENTS FOR MULTICELLULAR RINGS	175
	0.1.1	Inhibition of RhoA activity (80µm)	
10	0.1.2	Increase in RhoA activity (80µm)	
10	0.1.3	Calcium switch (80µm)	
10	0.1.4	Calyculin A (300µm)	177
10	0.1.5	ML-7 (300μm)	
10	0.1.6	CK666 (300µm)	
10	0.1.7	Trypsin-EDTA (300μm – pipette)	
10.2	2 M	ULTICELLULAR ELLIPSES	
10.3	3 M	ICRO-PRINTING WITH INK JET	179
10.4		RAMETERS FOR NUMERICAL SIMULATIONS	
10.5		ABLE OF DRUG CONCENTRATIONS	
10.6		ST OF CONSTRUCTS	
10.7		ST OF PRODUCTS	
10.8		AS MAPPING – PYTHON CODE	
10.9		UBLISHED AND SUBMITTED ARTICLES	
10.7	, 10	DLISHED AND SUDMITTED ARTICLES	

MOVIE CAPTIONS

Movie S1: NIH3T3 fibroblast migrating on a fibronectin line (75% OL). hh:mm, scale bar = $50\mu m$.

Movie S2: NIH3T3 fibroblast migrating on connected triangles (25% OL). hh:mm, scale bar = $50\mu m$.

Movie S3: NIH3T3 fibroblast migrating on fibronectin triangles separated by $16\mu m$ gaps. hh:mm, scale bar = $50\mu m$.

Movie S4: NIH3T3 fibroblast migrating on fibronectin triangles separated by 22μm gaps. hh:mm.

Movie S5: NIH3T3 fibroblast fluctuating within a single motif and 'unable' to migrate to the neighboring motifs (45µm). hh:mm.

Movie S6: Dynamics of focal contacts (VASP-GFP). Cell migrates on fibronectin triangles separated by $22\mu m$ gaps. hh:mm, scale bar = $15\mu m$.

Movie S7: Nucleation of subsequent rows of focal adhesions in a wave-like manner.

Movie S8: NIH3T3 fibroblast migrating on fibronectin teardrops separated by $24\mu m$ gaps. hh:mm, scale bar = $50\mu m$.

Movie S9: NIH3T3 fibroblast migrating on fibronectin teardrops separated by $27\mu m$ gaps. hh:mm, scale bar = $50\mu m$.

Movie S10: NIH3T3 fibroblast migrating on equilateral triangles separated by $22\mu m$ gaps. hh:mm, scale bar = $50\mu m$.

Movie S11. NIH3T3 cell in ratchet. hh:mm, scale bar = 15μ m.

Movie S12. NIH3T3 cell in straight channel. hh:mm, scale bar = 15μ m.

Movie S13. NIH3T3 cell moving along the direction ratchet (closed). hh:mm, scale bar = $15\mu m$.

Movie S14. NIH3T3 cell moving against the direction ratchet (closed). hh:mm, scale bar = $15\mu m$.

Movie S15. Nucleus deformation during passage. hh:mm, scale bar = 15μ m.

Movie S16. NIH3T3 actin distribution during motion. Z planes in μ m from the bottom surface z=0. hh:mm, scale bar = 10μ m.

Movie S17. NIH3T3 focal contact distribution during motion. Z = 0 (up) and upper plane $z = 5\mu m$ (bottom). hh:mm, scale bar = $10\mu m$.

Movie S18. Reorganization of keratin during passage. hh:mm, scale bar = 10μ m.

Movie S19. Fusion keratin cell blocked by the ratchet. hh:mm, scale bar = 10μ m.

Movie S20. NIH3T3 cell passing after removal of BCS gradient (visible in red on the left when present). hh:mm, scale bar = $20\mu m$.

Movie S21. NIH3T3 cell blocked after removal of BCS gradient (visible in red on the right when present). hh:mm, scale bar = $20\mu m$.

Movie S22. 1000µm MDCK ring. hh:mm.

Movie S23. 300µm MDCK ring. hh:mm.

Movie S24. 180µm MDCK ring. hh:mm.

Movie S25. 80µm MDCK ring. hh:mm.

Movie S26. 80µm ring with MDCK stably expressing ZO1-GFP. hh:mm.

Movie S27. Acto-myosin cable assembly at the single cell level. hh:mm, scale bar = $25\mu m$.

Movie S28. Laser ablation on the acto-myosin cable. Fluorescence signal corresponds to MRLC-GFP. hh:mm.

Movie S29. Laser ablation on the cadherin junctions. Fluorescence signal corresponds to E-cadherin-GFP. hh:mm.

Movie S30. 80µm MDCK ring with cells transfected with Caldesmon-GFP. hh:mm.

Movie S31. $80\mu m$ MDCK ring expressing RhoA FRET biosensor. hh:mm, scale bar = $50\mu m$.

Movie S32. Reaction-diffusion simulations on a ring.

Movie S33. Vicsek-based model simulating the collective behaviour of a 80 µm ring.

Movie S34. Vicsek-based model simulating the caldesmon mosaic experiment.

Movie S35. MDCK spheroid in phase contrast. hh:mm, scale bar = $20\mu m$.

Movie S36. MDCK spheroid image with a custom light-sheet microscope. hh:mm, scale bar = $20\mu m$.

Movie S37. Inhibition of RhoA activity ($80\mu m$ ring). hh:mm, scale bar = $50\mu m$.

Movie S38. Inhibition of RhoA activity (300 μ m ring). hh:mm, scale bar = 50 μ m.

Movie S39. RhoA activator ($80\mu m \text{ ring}$). hh:mm, scale bar = $50\mu m$.

Movie S40. Chelation of calcium with 2mM EDTA ($80\mu m \text{ ring}$). hh:mm, scale bar = $50\mu m$.

Movie S41. Calyculin A incubation (300 μ m ring). hh:mm, scale bar = 100 μ m.

Movie S42. MDCK ring treated with ML-7 (300 μ m ring). hh:mm, scale bar = 100 μ m.

Movie S43. Inhibition of Arp2/3 complex by CK666 (300 μ m ring). hh:mm, scale bar = 100 μ m.

Movie S44. Local breakage induced by trypsin-EDTA delivery with micro-pipette ($300\mu m$ ring). hh:mm, scale bar = $100\mu m$.

Movies are available on https://seafile.unistra.fr/u/d/7bb4954c0e1944bf9342/.

LIST OF ABBREVIATIONS

	Name
BCS	Bovine Calf Serum
CC	Cross Correlation
CW	Clockwise
CCW	Counter Clockwise
DMEM	Dulbecco's Modified Eagle's medium
FA	Focal Adhesion
FBS	Foetal Bovine Serum
FN	Fibronectin
FRET	Fluorescence Resonance Energy Transfer
MCP	Micro-Contact Printing
MSD	Mean Squared Displacement
PBS	Phosphate buffered saline
PDMS	Poly(dimethylsiloxane)
PIV	Particle Image Velocimetry
RBD	Rho Binding Domain
RICM	Reflection Interference Contrast Microscopy
WT Wild Type	

1. PhD MOTIVATIONS

Motion is a fundamental characteristic in Nature. Aristotle described living matter in "Physics" as objects having an intrinsic principle of *motion*, not by accident, but by essence: "Nature is a principle or cause of being moved and of being at rest in that to which it belongs primarily, in virtue of itself and not accidentally." (Physics, Book II, chapter 1). Even though nowadays this description of living matter does not seem to be accurate, this puts forward *motion* – in a broad definition – as a remarkable property of living matter.

As a former medical student, I had many histology lectures. This was the opportunity to look under the microscope at tissues and cells; an instantaneous photograph of a living system. However, I had the feeling that something was missing. Among the beautiful variety of cells and shapes we were looking at, I was wondering how these assemblies could arise. In other words, dynamics, *motion* was lacking. Cells probably had to move, individually or collectively, change their shapes, they would potentially encounter obstacles or sense various cues from their surrounding environment. How these 10 micrometers-sized objects could migrate over such large distances without losing tracks? How a collection of cells can get organized and coordinated?

In Petri dishes, migration is random, somehow similar to a Brownian motion at a larger scale. But under certain conditions, certain signals, provided by its micro-environment or by its neighbors, cells can move directionally. This remarkable feature is key in Biology: shaping an organism, healing a wound or, in pathology, invading secondary organs during metastasis spreading.

These observations and the questions they triggered led me to study cell motility. Specifically, the present PhD work investigated the rules that set a direction. How a cell, starting from a circular, isotropic shape, breaks its symmetry, and how this broken symmetry can be sustained through space and time. We learnt generic properties at the single cell level but also at the multicellular level.

2. INTRODUCTION

The introduction of the present work will be divided in several parts, going from the description of symmetry breaking in Physics and the associated concept of polarity (2.1) to the description of single cell and multicellular behaviors (2.2-2.5) and the emergence of directionality (2.6). Description of cellular migrations will be systematically divided into two main aspects: a Biological description, with the molecular components involved in the phenomenon together with the main regulatory pathways, and a Physics characterization of the observed phenomena. Finally, the Introduction will be concluded by the questions aimed to be answered by the present PhD work.

2.1 Symmetry breaking in living matter: first thoughts

Symmetry breaking has been a long-standing concept in physics and is key to understand one system's fate. In his 1972 paper, Anderson described symmetry in physics through the concept of invariance and uniformity (Anderson, 1972). As such, isotropy, uniformity, or invariance cannot translate into the transformation of a system's state: symmetry has to be broken. This phenomenon can happen at many levels and can be the result of small fluctuations changing randomly the fate of the system (see Figure 2.1a) or can be directed by more complex processes (Figure 2.1b, (Chauwin et al., 1995; Prost et al., 1994; Rousselet et al., 1994)).

An intuitive way to think about symmetry breaking as a way to direct fate is the thought experiment made by Feynman in his "ratchet and pawl" paper (Feynman et al., 1963; Magnasco and Stolovitzky, 1998). The ratchet is a tooth wheel, confined in a closed box (see Figure 2.1c). It is jingling, hit by thermal fluctuations but the average motion of the wheel is zero. One way to tune the system's fate into a directed motion is to implement a hook, preventing the motion of the wheel in one direction but letting the wheel turn in the other one. This simple and intuitive idea conveys the importance of a broken symmetry and the need to go away from isotropy.

The "ratchet and pawl" and its wheel motion are mainly driven by differences in temperatures between the two compartments (see Figure 2.1c). Therefore, the phenomenon follows classical laws of thermodynamics. However, living matter cannot be described in such a way: at the nanometre scale of a molecular motor, temperature is constant, friction forces dominate and inertia is negligible (Jülicher et al., 1997; Purcell, 1977). Living matter is therefore fundamentally out-of-equilibrium in a sense that energy needs to be consumed to generate work. Breaking symmetry requires then orchestration of many molecular actor in order to occur and its maintenance in space and time implies continuous energy consumption.

One way to translate the idea of a broken symmetry into a measurable read-out is to introduce the concept of *polarity*. Polarity, \vec{p} , is a vector with a given amplitude, an orientation and a direction. \vec{p} gives the anisotropy of the system and can be measured in many ways on many scales: shape can be given as an input as well as differences in spatial concentration of a

molecule, or even the average orientation of filaments constituting a gel. Therefore, \vec{p} does not have any fixed molecular definition and can be whatever quantity that is anisotropically distributed in a system. For instance, at the molecular scale, one might consider the following expression of \vec{p} :

$$\vec{p} = \begin{pmatrix} \int_0^{2\pi} d\theta (A(\theta) - B(\theta)) \cos \theta \\ \int_0^{2\pi} d\theta (A(\theta) - B(\theta)) \sin \theta \end{pmatrix}$$
 (2.1)

with A and B the normalized concentrations of two molecules along a circular contour. Any anisotropy in the distribution of A and B will lead to a polarity.

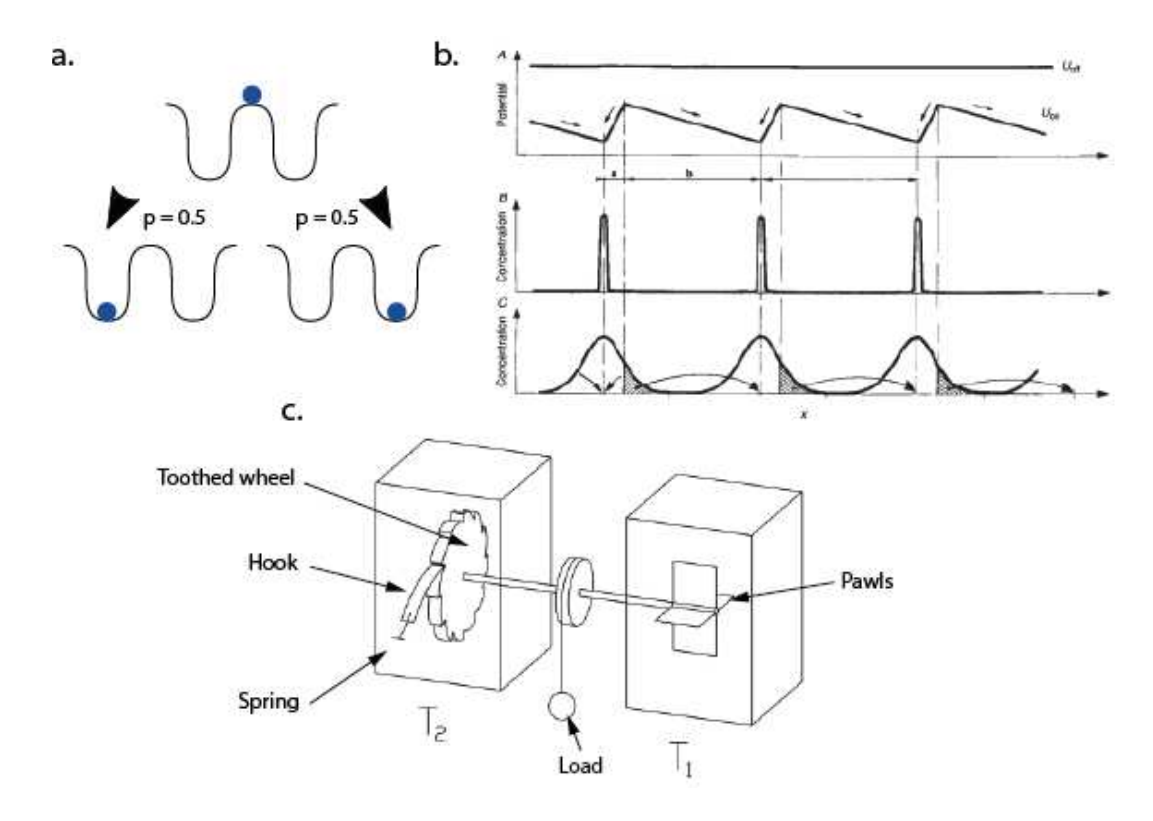


Figure 2.1. The concept of symmetry breaking. (a) A particle in a double-well potential. Fluctuations randomly break the symmetry of the system and direct the particle towards one potential well with equal probabilities. (b) Particles directed with asymmetric pumping (Rousselet et al., 1994). The particle is drifting between two states (change is induced by electrodes) with different potential. B corresponds to the concentration of the particle in the asymmetric potential, whereas C corresponds to the particle concentration in the flat potential. Induced oscillations between these two states deterministically direct particle motion and break the symmetry. (c) Ratchet and pawl experiment thought by Richard Feynman (Feynman et al., 1963). T1 and T2 corresponds to two different temperatures in the boxes.

At the cellular scale, cellular extensions can also trigger a polarity in the direction of the growth of these structures. The two definitions – the molecular one and the phenotypical one – will be used throughout the manuscript depending on the experimental read-out.

The fact that \vec{p} can be described by many ways leads to a large heterogeneity of definitions that are sometimes contradictory in Biology. For instance, cell polarity given by distributions of given proteins as a marker can lead to a different polarity than the one given by the shape of the cell or set by the cellular motion. However, despite these considerations, emergence of polarity as a consequence of symmetry breaking and memory of this polarity appear as a generic feature necessary to produce persistent and directional behaviours in living systems.

In the following sections, we will describe how polarity can arise from a mesoscopic ensemble of various molecular actors and how this phenomenon translates into many different biological processes such as cellular motion.

2.2 Single cell motility: a biological description

Throughout the work, we will detail symmetry breaking processes happening at the cellular level. Therefore, a biological description of the system is necessary to provide insights on molecular actors contributing to the process. In the present work, we used mammalian cells to study the mechanisms of symmetry breaking and directionality.

2.2.1 Cytoskeleton components and sub-structures

Cell architecture is maintained by a polymeric network, self-assembled and out-of-equilibrium: the acto-myosin cytoskeleton, combined with intermediate filaments and microtubules, are fundamental in the emergence of a broken symmetry.

These molecular actors do not operate individually in the cellular micro-environment: collections of thousands of molecules at the micrometre scale drive biological processes. However, individual properties of molecules set interaction rules for the ensemble and their understanding allows to predict how the mesoscopic structures emerge and evolve. Therefore, in this section, we will detail individual characteristics of the major cytoskeleton components and the mesoscopic dynamics of their ensembles.

2.2.1.1 Actin

Actin is a globular protein of approximately 42kDa that can be found in the cytoplasm (Elzinga et al., 1973). In its monomeric form, globular actin (G-actin) can assemble with other units of G-actin to nucleate helical polar filaments of filamentous actin (F-actin) (Nürnberg et al., 2011) (see Figure 2.2). A pool of G-actin binds to ATP molecules, leading to conformational changes allowing the binding to other G-actin units. This pool constitutes the centre of nucleation for the new filament.

Interestingly, there is an asymmetry between the polymerization rates of the two ends of the filament defining the polarity of the structure (Kuhn and Pollard, 2005; Pollard and Mooseker,

1981). The "+" end (also called "barbed" end) corresponds to the fast polymerizing end while the "-" end (also referred as the "pointed" end) correlates with unstable F-actin and constitutes as such the effective depolymerizing end. This property is fundamental since it breaks the symmetry at the filament scale. Consequences such as directional growth of protrusions or actin monomers directional flows can produce cellular polarities at the mesoscopic scale. For specific conditions, actin filaments reach steady state when polymerization rates are tuned in such a way that there is not net growth or shrinkage (Schaus et al., 2007). This phenomenon, leading to force generation without changes in filament length, is referred to as treadmilling.

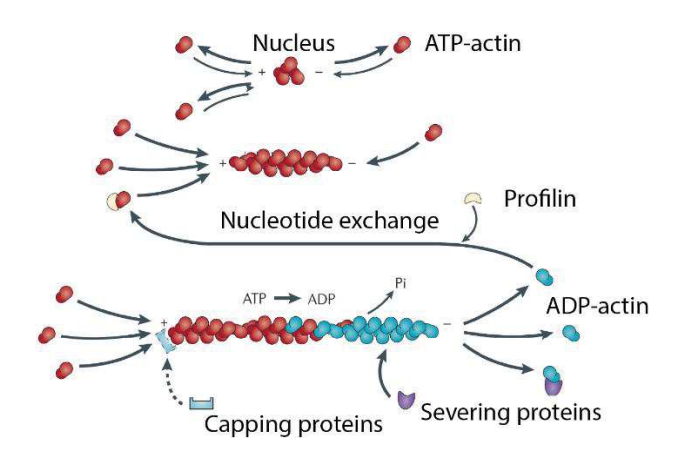


Figure 2.2. Actin dynamics. Actin polymerization from G-actin monomers (adapted from (Nürnberg et al., 2011)).

2.2.1.2 Actin Binding Proteins (ABP)

Actin filaments are regulated by actin-associated proteins specifically binding to actin. Level of expressions and localization of these ABPs modulate the spatio-temporal dynamics of actin filaments and are therefore important to tune cell polarity.

The first class of ABP are actin nucleators such as Arp2/3 or formin (Evangelista et al., 2003; Svitkina and Borisy, 1999; Winder and Ayscough, 2005). Both proteins are leading to an increase in polymerization. Formin binds to the "+" end of the filament and enhances elongation. It promotes actin nucleation and filament growth at speed that can exceed the one exhibited during spontaneous growth (Courtemanche, 2018). On the other hand, Arp2/3 controls branching of actin filaments: under the control of the Wiskott-Aldrich syndrome family proteins (WASP), Arp2/3 binds to actin and constitutes a new nucleation core. From this new core, actin is nucleated and a new filament grows at a well-defined angle of 70° leading to branched filaments.

These processes of polymerization are tightly controlled by another class of ABP: the capping proteins. Capping proteins like CapZ binds the "+" end of the filament and prevent assembly or disassembly of actin monomer, stabilizing the filament (Winder and Ayscough, 2005).

Altogether, ABPs are proteins that can tune actin assembly and disassembly dynamics. Previous works showed *in vitro* the influence of ABPs activities in the variability of reconstituted actin networks behaviours (Abu Shah and Keren, 2014; Malik-Garbi et al., 2019; Reymann et al., 2011). In the context of symmetry breaking, biased distributions of these proteins and sustained activity might translate into emergence of cell polarity as well.

2.2.1.3 Myosin motors

Myosin is a cytoplasmic protein responsible for contraction in mammalian cells. There are 18 classes of myosin, but the most studied myosin is the *conventional myosin* – the myosin II originally found in muscle (Aguilar and Mitchell, 2010; Cheney et al., 1993; Pollard and Korn, 1973). It is composed of two heavy chains, constituting the backbone of the protein, and four light chains: two *regulatory light chains* (RLC), and two *essential light chains* (ELC) (Aguilar and Mitchell, 2010; Cooke, 1989). They assemble into two myosin heads (Aguilar and Mitchell, 2010; Cooke, 1989).

These myosin heads upon phosphorylation by Myosin ATPase acquire conformational changes leading to binding to actin filament (see Figure 2.3a) (Boraas et al., 2018). After binding, Rho Kinase phosphorylates the Myosin RLC and the consumption of ATP leads to force generation of the myosin head moving on the actin filament (Drug et al., 2002; Kimura et al., 1996). Myosin motion on actin is sustained by a cycle of phosphorylation and binding/unbinding of the myosin head (see Figure 2.3a) (Boraas et al., 2018).

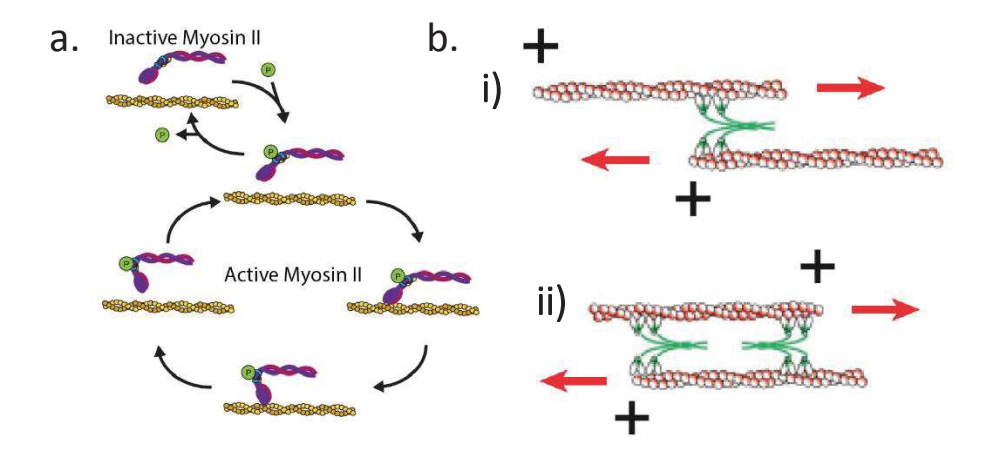


Figure 2.3. Myosin dynamics. (a) Myosin binding and unbinding cycle leading to myosin motion on actin filament (adapted from (Boraas et al., 2018)). (b) i) Contraction lead by myosin heads of two polar actin filaments. ii) Extension of acto-myosin with two actin filaments with opposite polarities (Kreten et al., 2018).

Stress generation arises when the two myosin heads are bound to different actin filaments leading to specific dynamics depending on the filaments polarities (see Figure 2.3b) (Kreten et

al., 2018): contraction (i) and extension (ii) drives stress production at the molecular and at the cellular scale. Therefore, myosin is indispensable for force generation and as such holds a key role in the physics associated with cellular mechanics.

Ensembles of 10-30 acto-myosin filaments in bundles constitute the stress fibres (Pellegrin and Mellor, 2007). These are contractile structures and are connected to the cellular zones of adhesion (Pellegrin and Mellor, 2007) (see below).

2.2.1.4 Microtubules

Microtubules are polymers composed by tubulin dimers. Each dimer is polarized and self-assembled with two monomers of α and β -tubulin (Amos, 2004; Valiron et al., 2001). This polarity translates into a global structural polarity of the filament where one end is only constituted of α -tubulin – the "-" end – and the other one of β -tubulin – the "+" end (Amos, 2004; Valiron et al., 2001) (see Figure 2.4a). Therefore, symmetry is also already broken at the filament scale.

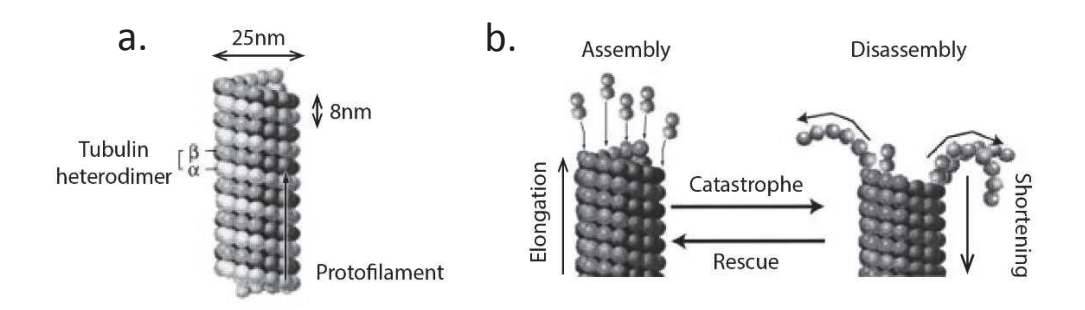


Figure 2.4. Microtubule polymerization. (a) Microtubule filament structure, composed of heterodimers of beta and alpha tubulin. (b) Dynamics of assembly and disassembly of microtubules. Sudden events of shrinkage are called "catastrophe". Adapted from (Valiron et al., 2001).

The filament is highly dynamic: GTP hydrolysis drives the nucleation of tubulin dimers during the *nucleation phase* (Valiron et al., 2001) (see Figure 2.4b). Then the filament grows upon addition of dimers at the "+" end, while the "-" end is stabilized with the centrosome – the MicroTubule Organizing Center (MTOC). This is the *polymerization phase*. Then the microtubule reached a steady state leading to a constant length of the dynamic filament (Valiron et al., 2001).

Microtubules are highly unstable, and this dynamic instability translates into sudden events of shrinkage called *catastrophe* (Gardner et al., 2013) (see Figure 2.4b).

These filaments play a key role in various physiological processes: in cell division, protein transport, in setting cell polarity and during cell motility (Bhabha et al., 2016; Kaverina and Straube, 2011; Meunier and Vernos, 2012).

2.2.1.5 Intermediate filaments

Intermediate Filaments (IF) constitute another class of filaments, less dynamic (they do not exhibit treadmilling for instance), highly stable, and with no polarity (Lowery et al., 2015; Robert et al., 2016). It exists 6 types of IFs, and all of them are cytoplasmic except the type V composed by nuclear lamins (Lowery et al., 2015).

Lamins assemble to create the nuclear envelop and more specifically the lamina (Houben et al., 2007). This structure is indispensable to ensure the proper structure and integrity of the nucleus and its mechanical properties allow strong deformation of the nucleus during cell motion (Houben et al., 2007).

More generally, IFs such as keratins, maintain cytoskeletal integrity and cell shape (Kirfel et al., 2003). Keratin filaments are hetero-polymers composed of type I and II keratin IFs and they are the most abundant in epithelial cells (Kirfel et al., 2003). They protect cells from mechanical stresses as they can be deformed and stretched over multiple times their initial length (Herrmann et al., 2007).

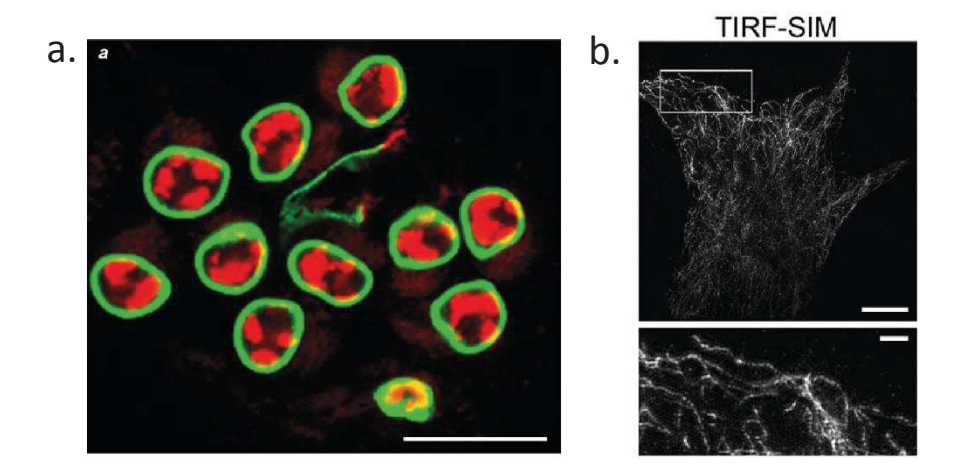


Figure 2.5. Intermediate filaments in cells. (a) Lamina visualization through confocal microscopy. DNA in red (DAPI), lamina in green (anti Lam-Dm0) (Fabbretti et al., 2016). Scale bar = 20μ m. (b) Keratin filaments with super-resolution microscopy (Robert et al., 2016). Scale bar = 5μ m (insert 1μ m).

The main components of the cell cytoskeleton have been described in the past sections. We now focus on the formation of the cellular substructures, essential for the emergence of cell polarity and cellular motion.

2.2.1.6 Filopodia and Lamellipodia

Lamellipodia refer to the very thin leading edge of the cell containing a branched actin network (see Figure 2.6 and (He et al., 2015)). It is mainly polymerized and branched upon the local

activation of Arp2/3 with high actin turnover (He et al., 2015; Nürnberg et al., 2011; Raz-Ben Aroush et al., 2017; Svitkina and Borisy, 1999). This dynamic structure, also rich in focal adhesions, is associated to adherent cell migration and its presence is often considered as a good polarity marker when cells have a "triangular" shape.

On the other hand, filopodia are small actin-rich cellular extensions, finger-like (see Figure 2.6b and (Machesky, 2008; Mattila and Lappalainen, 2008)). They are found at the leading edge and they go beyond the lamellipodium. Apart from their role in cellular motion, they are also involved in sensing and cell to cell communication (Machesky, 2008; Mattila and Lappalainen, 2008). Their growth is mainly driven by the action of formins and not Arp2/3 like the lamellipodium (Svitkina, 2018).

This translates into differences in structures: while lamellipodia are composed of a highly branched network, formins are constituted of straight actin bundles. Therefore, the actual picture associates formins to filopodia and Arp2/3 to lamellipodia. However, previous studies provided evidences that Arp2/3 might contribute to filopodia formation and conversely formins (such as mDia) are also necessary to lamellipodia growth (Korobova and Svitkina, 2008; Yang et al., 2007).

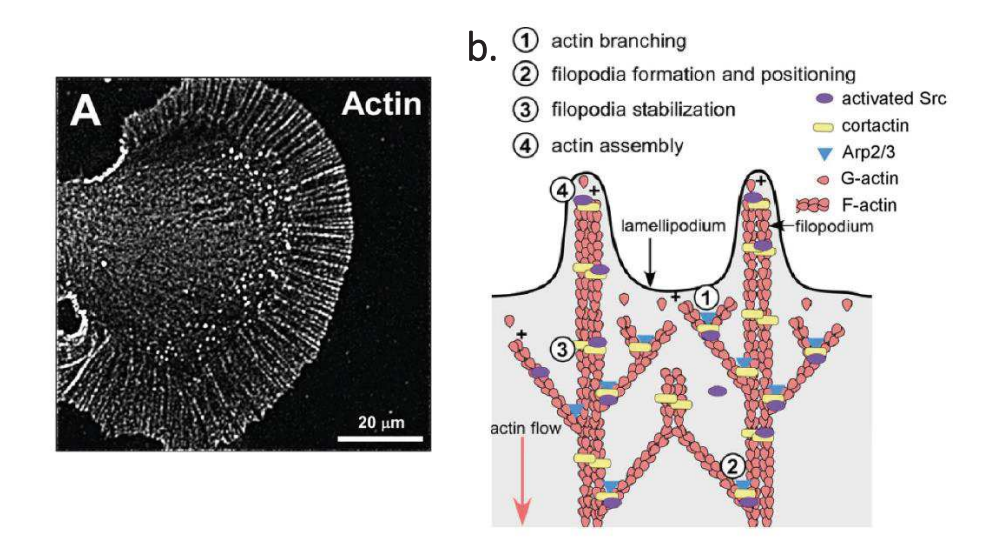


Figure 2.6. Lamellipodium organization. (a) Fluorescent Speckle Microscopy image of an Aplysia growth cone exhibiting a "gigantic" lamellipodium (adapted from (He et al., 2015)). (b) Scheme of a leading edge describing lamellipodium structure with branched actin network and showing the filopodium composition with straight F-actin bundles (adapted from (Nürnberg et al., 2011)).

2.2.1.7 Focal Adhesions

Focal Adhesions (FAs) are protein complexes constituting the cellular anchoring zones with the extra-cellular matrix. They are connected to the acto-myosin network through stress fibres and to the surface with inter-membranous integrins and the extra-cellular matrix (such as fibronectin for instance) (see Figure 2.7a and (Petit and Thiery, 2000; Wehrle-haller, 2012)).

It has been demonstrated that FAs can act as mechanosensors but also as local force transmitters (Balaban et al., 2001; Gardel et al., 2010; Riveline et al., 2001). Upon local mechanical stimulation along the inside of a cell, FAs dynamically undergo directional elongation with constant matter density as shown by Figure 2.7b (Riveline et al., 2001). It has also been shown that FAs apply a constant force per unit area of 5.5nN.μm⁻² for various cell types and on different substrates (Balaban et al., 2001).

Altogether, the plane of interaction with FAs constitutes the plane of force transmission between the cell and the substrate in adherent cells. FAs dynamics is indispensable to produce firm cellular anchors but also to detach at specific locations during cell migration (see 2.2.3). FAs can be seen as the link between the substrate and the acto-myosin cytoskeleton, playing a key role in mechanosensing and in cellular motion.

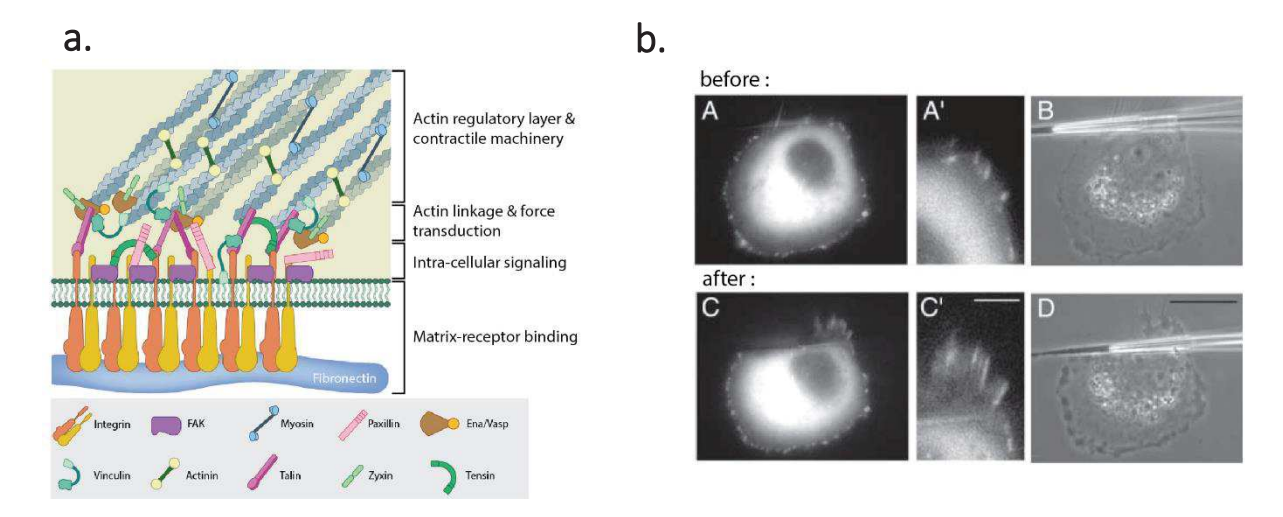


Figure 2.7. Focal adhesions structure and dynamics. (a) Focal Adhesion (FA) scheme with the intracellular part connected to the acto-myosin network and the integrin bound to the extracellular matrix. (b) Local mechanical stimulation on SV-80 cells. FAs are visualized through vinculin-GFP. FAs are shown before (A-B) and after (C-D) and exhibit elongation at constant density upon stimulation. From (Riveline et al., 2001).

The structures presented so far in the sections above are out-of-equilibrium, highly dynamic (seconds to minutes), and tightly regulated: their kinetics are controlled by key master regulators. These regulation pathways will be presented in the next section.

2.2.2 Rho Family: signalling pathways

In the early 90s, A. Hall *et al* described in two pioneer studies that RhoA and Rac1 activations were associated with shapes and cytoskeletal changes (Ridley and Hall, 1992; Ridley et al., 1992). This would also lead to different migratory phenotypes. These studies opened the door to new ways of envisioning the cell cytoskeleton with another layer of regulation: it is not only

a self-assembled polymeric network driven by its own dynamics and interaction rules. Instead, cytoskeleton kinetics are also dictated by key master regulators and their modulations might lead to different network configurations and dynamics.

The main – canonical – regulators for acto-myosin and cell motility are small GTPases from the Rho family: RhoA, Rac1 and Cdc42 (Schwartz, 2004). These GTPases are dependent on the action of GEFs (Guanine nucleotide Exchange Factors) and GAPs (GTPase Activating Proteins) (Bos et al., 2007). Both are changing the conformation state of the GTPase by the addition or the deletion of one phosphate on the guanine. In the following, we will only focus on the subsequent effects of GTPases activation without describing the dynamics associated to the GEFs and GAPs.

2.2.2.1 RhoA signalling

It is well established that RhoA is a key regulator for actin stress fibres and acto-myosin contractility (Kimura et al., 1996; Ridley and Hall, 1992; Riveline et al., 2001; Schwartz, 2004) (see Figure 2.8a). RhoA, a small GTPase of about 29kDa, is sequestered in its non-active form, in the cytoplasm by Rho guanine dissociation inhibitors (RhoGDIs) (Hodge and Ridley, 2016; Koo et al., 2015) (see Figure 2.8b). Dissociation of the complex RhoA-RhoGDI translocates RhoA to the membrane where the GTPase can be activated (Hodge and Ridley, 2016; Koo et al., 2015).

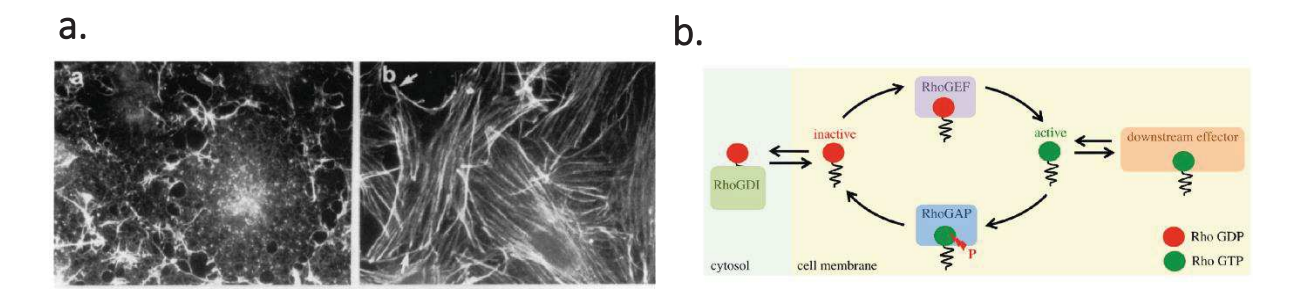


Figure 2.8. RhoA downstream effects and dynamics. (a) Swiss 3T3 cells treated with Val14RhoA before (left) and after (right). Actin filaments are stained with FITC-conjugated phalloidin. Incubation with Val14RhoA led to strengthening of actin stress fibres and change in phenotype. From (Ridley and Hall, 1992). (b) Activation cycle of RhoA GTPases with sequestration in the cytosol by RhoGDIs and translocation to plasma membrane and activation by the GEFs. From (Koo et al., 2015).

Upon activation, RhoA modulates ROCK (the Rho Kinase) which in turns phosphorylates the Myosin RLC leading to an increase contraction in the acto-myosin network (Kimura et al., 1996; Schwartz, 2004) (see Figure 2.9). ROCK also stimulates FAK (Focal Adhesion Kinase) promoting FAs growth, as well as profilin and cofilin, two ABPs, leading to actin network remodelling (Schwartz, 2004).

In the canonical view of cell motility, RhoA is assumed to be located and activated at the cellular rear, contracting the back of the cell. This leads to the motion on the substrate (Ridley, 2015). However, this framework has been challenged with the usage of new biosensors, showing a more subtle interplay between RhoA and migration, especially with a high activation at protrusions and lamellipodia edges through potential activation of formins (mDia) (MacHacek et al., 2009; Martin et al., 2016; Pertz et al., 2006; Ridley, 2015). This will be detailed in the section 2.3.4.

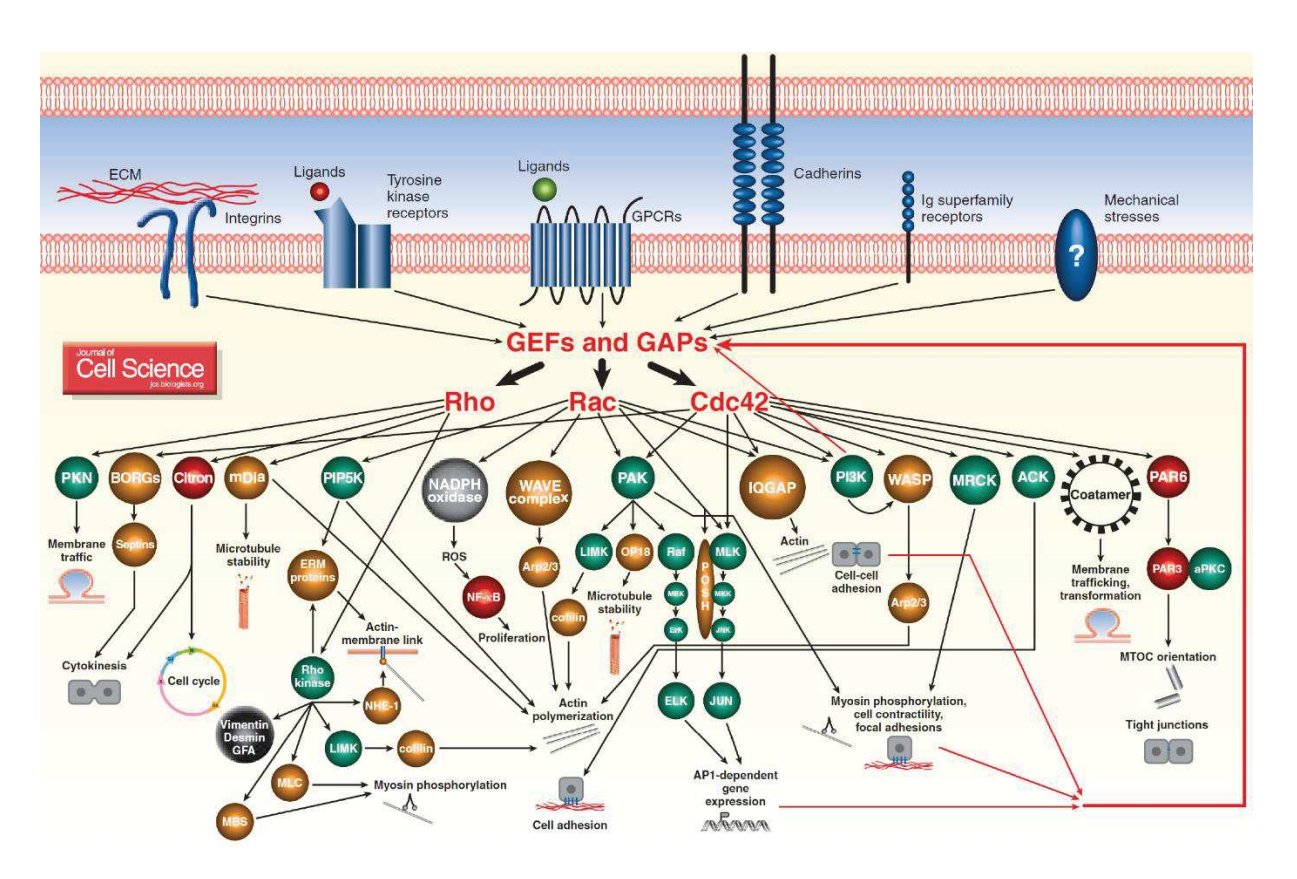


Figure 2.9. Rho Family signalling pathway. RhoA, Rac1 and Cdc42 signalling pathways. GTPases are activated by GEFs and GAPs upon external stimuli and they activate in turn specific downstream regulators. From (Schwartz, 2004).

2.2.2.2 Rac signaling

Rac1 is commonly associated with the growth of lamellipodia (Ridley, 2015; Ridley et al., 1992). More generally, it plays a key role in cytoskeletal reorganization by activating many actin-related pathways such as WAVE (activates Arp2/3), PIP5k (actin polymerization), PAK1 (cofilin) and many others (Hodge and Ridley, 2016; Schwartz, 2004) (see Figure 2.9). Therefore, Rac1 is found to be highly active in lamellipodia driving the branching process by activating Arp2/3 complex and actin nucleation through Formin-Like proteins (FMNL) (Kühn and Geyer, 2014).

2.2.2.3 Cdc42 signaling

Originally discovered for its role during cell cycle in *S. cerevisiae* (Nurse et al., 1976), Cdc42 is known to be a key regulator of filopodia formation in the context of cell motility (Ridley, 2015). Cdc42 targets formins (such as mDia and other FMNL) triggering nucleation of straight actin bundles in the filopodia (Kühn and Geyer, 2014).

2.2.3 Migration on 2D flat surfaces

The orchestration of structures and molecular actors detailed above can lead to the net displacement of a cell on a substrate. We will present here some elements about how motion can happen at the single cell level.

Even though the analysis of cells on 2D homogeneous flat surfaces remains far from biological conditions (Bissell, 2017), it gave over decades numerous information on the migration process. Typically, cell motion can be divided into 4 distinct steps (Mattila and Lappalainen, 2008) (see Figure 2.10a): (i) the cell acquires a front-rear polarity and grows a lamellipodium at the leading – front – edge through the mechanisms detailed in 2.2.1.6. The lamellipodium nucleates FAs and pulls on the substrate (ii) leading to contraction and cell body translocation (iii) and finally the retraction of the cellular rear.

The high actin turnover allows this cycle to repeat, producing a net displacement of the cellular body over large distances at speed of about $10\text{-}60\mu\text{m/h}$ (Maiuri et al., 2012). This turnover also contributes to the motion by the generation of forces mediated by actin centripetal flows (Callan-Jones and Voituriez, 2016) even though this feature cannot explain and capture all the phenomena (Godeau et al., 2020).

In the absence of external cues, the first step of the cycle – the acquisition of the front-rear polarity – is random. The cell is first isotropic (see Figure 2.10b) and then breaks its symmetry through stochastic – and amplified – fluctuations of acto-myosin concentrations or signalling molecules (Altschuler et al., 2008; Copos and Mogilner, 2020; Dyche Mullins, 2010; Yam et al., 2007). This leads to the growth of a leading edge (see Figure 2.10b).

Attachment on the substrate is mediated by FAs. Friction plays a key role in cell migration: it has been shown that it exists a non-linear relationship between friction and cell velocity (Palecek et al., 1997; Szewczyk et al., 2013). A friction too high down-regulates velocity until complete blockage of motion. Interestingly, this phenomenon also occurs for low frictions (like gliding), suggesting the need of an actual friction between the cell and the substrate for migration to happen (Palecek et al., 1997).

Growth of FAs, lamellipodia and filopodia, therefore the whole migration cycle detailed above, are under the tight regulation of the small GTPases from the Rho family described in 2.2.2.

Then, activity of these molecular actors should be probed spatially and temporally in order to understand the organization of motion.

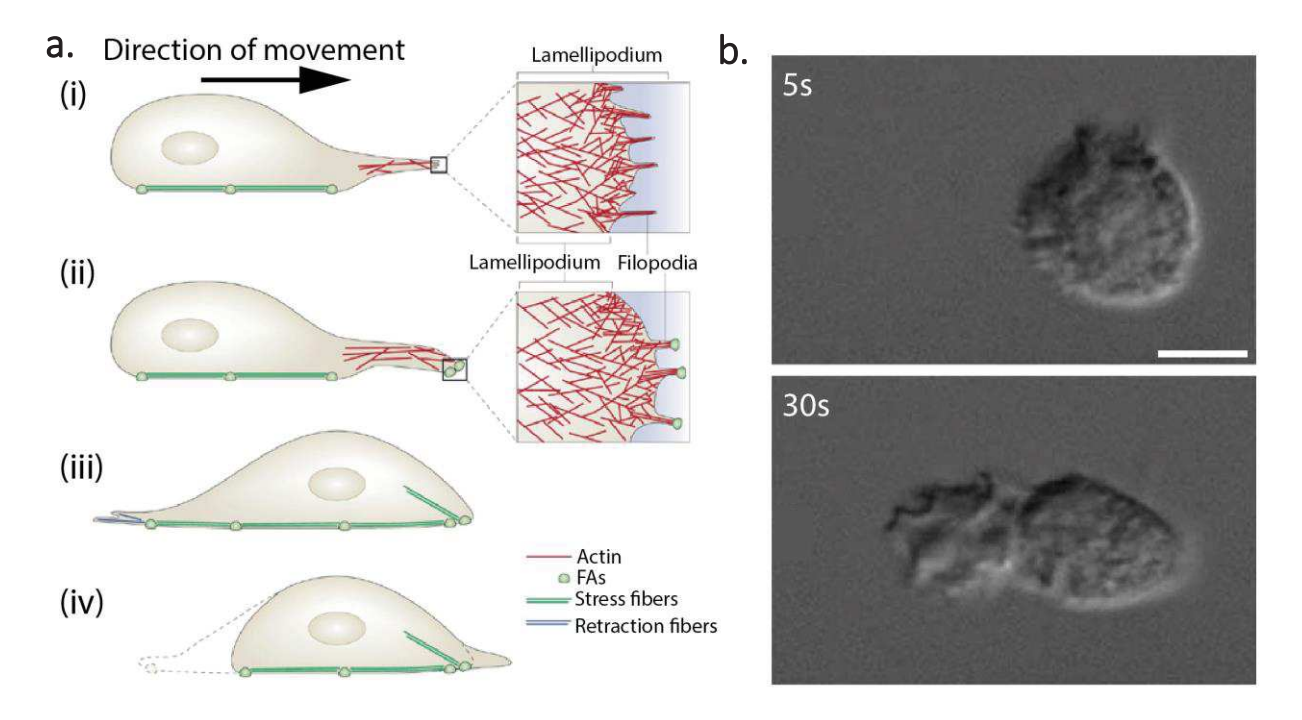


Figure 2.10. Lamellipodium growth and cellular motion. (a) Canonical migratory cycle. (i) front-rear polarity/lamellipodium growth (ii) nucleation of FAs (iii) body translocation (iv) contraction and rear retraction. From (Mattila and Lappalainen, 2008). (b) Example of a neutrophil cell before polarity acquisition (up) and after establishment of a front-rear polarity (bottom). Scale bar = 5μ m. Adapted from (Wang, 2009).

2.2.4 Spatio-temporal regulation of small GTPases

The recent usage of biosensors based on Fluorescence Resonance Energy Transfer (FRET) allows to probe acutely the interplay between the spatio-temporal dynamics of Rho GTPases and the cell motility (MacHacek et al., 2009; Martin et al., 2016; Pertz, 2010; Pertz et al., 2006). Activity and not only localization can be probed. These studies challenged the classical view of GTPases patterns where RhoA is mainly located at the rear of the cell, responsible for contraction, Rac1 at the lamellipodium and Cdc42 at the filopodia.

The results show that RhoA, Rac1 and Cdc42 can control their downstream regulators at the subminute timescale and at the micrometre scale (MacHacek et al., 2009; Martin et al., 2016; Pertz et al., 2006). All three GTPases are activated at the leading edge. More specifically, RhoA is present at the rear, indeed responsible of its retraction, but also present in a small activation band at the tip of the lamellipodium, promoting protrusions growth. This leading-edge activation decreases monotonically within 2µm to reach then the baseline level and RhoA cycles with a similar periodicity of the protrusion-retraction cycle with almost no time lag. This provides evidence that RhoA is indeed correlated with the growth of cellular extensions. Interestingly, upon activation of PDGF (platelet growth factor), protrusions and lamellipodia

grow without any RhoA activity at the leading edge. In fact, PDGF is a Rac1 strong activator and Rac1 has been shown to be an antagonist of RhoA. This feedback could explain this unexpected result, and this suggests that different signal cues could lead to different activation patterns.

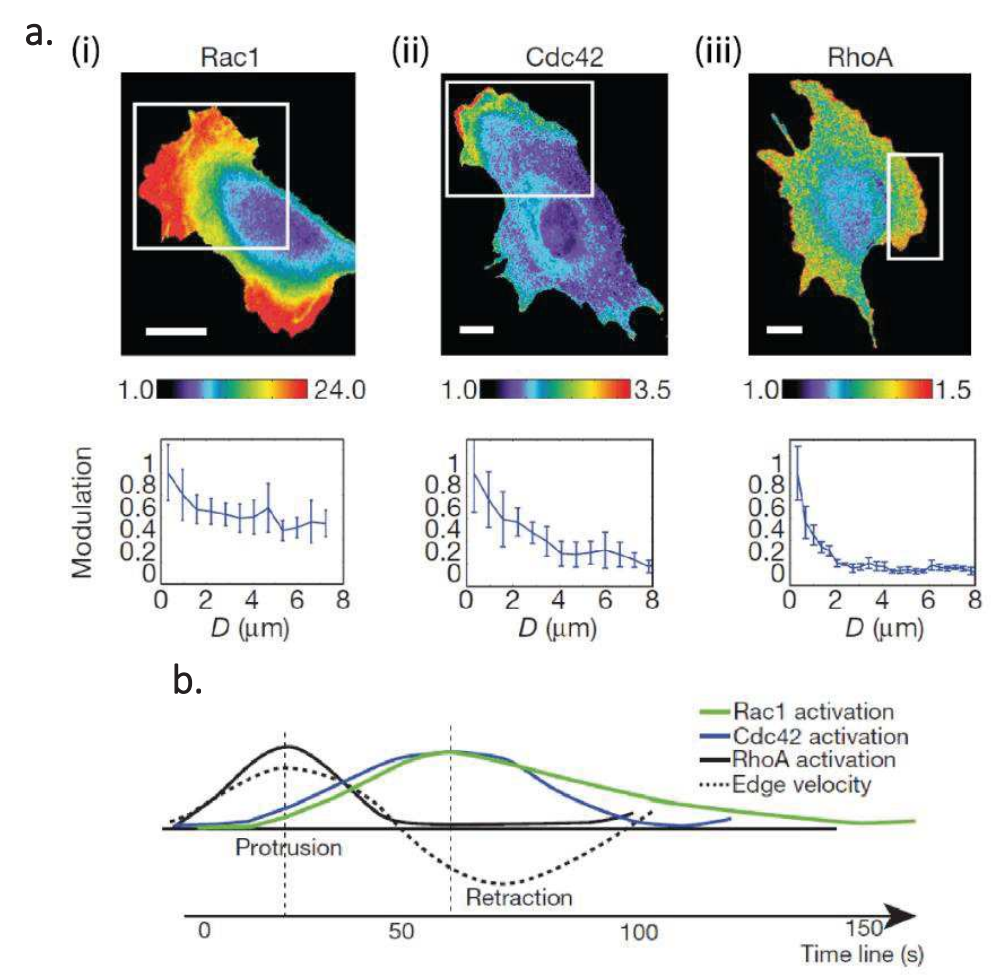


Figure 2.11. Rho GTPase spatio-temporal dynamics. (a) Ratiometric maps of RhoA activity acquired with FRET biosensors (up) together with the ac tivity profile from the leading-edge to the center of the cell (bottom). (i) Rac1 activity (ii) Cdc42 activity (iii) RhoA activity. (b) Temporal sequence of activations of GTPases together with the protrusion-retraction cycle. RhoA activation is concomitant to filopodia growth while Rac1 and Cdc42 activate after the protrusion phase. Adapted from (Martin et al., 2016)

Cdc42 is also present at the leading edge but is activated with a 40s delay relative to protrusions and 1.8µm away from the lamellipodium edge.

Rac1 is localized at a broader region on the lamellipodium but shows the same kind of activation patterns that Cdc42: it exhibits a delay relative to protrusions growth and is first activated away from the lamellipodium edge. Moreover, its activation peak correlates with the decrease of RhoA activity, giving more evidence that Rac1 plays an antagonist role with RhoA.

Altogether, the FRET analysis made on RhoA, Rac1 and Cdc42, shows that their coordination is more subtle than previously described. Especially, when there is no external cue, the delay

activation of Rac1 and Cdc42 with the protrusion growth indicates that their primary role may not be in initiating protrusion as hypothesized before, but they regulate protrusions by tuning adhesion dynamics.

These results, obtained with FRET biosensors on the subminute timescale, underline the importance of feedbacks mechanisms between GTPases as well as the highly dynamics behaviour they exhibit over short time and length scales. Perturbations of Rho pathways together with their description and the quantification of cellular read-outs (myosin intensities, velocity fields, shapes) could shed light on the coupling between signalling and mechanics.

2.3 Physics of cell migration

However, explicit link between GTPases activity and cellular motion/behaviour is not straightforward. Even though they correspond to emergence of specific cellular structures (filopodia, lamellipodia, stress fibres and FAs), GTPases activities eventually translate into generation of stress, friction with the substrate and changes of the acto-myosin network architecture. These phenomena need to be integrated into a consistent framework with predictive power and cannot be extracted from GTPases activity only.

Therefore, physical descriptions of the acto-myosin gel and its properties through space and time can lead to predictions. In this section, we will introduce first the active gel theory, then how this acto-myosin gel, driven out-of-equilibrium, dictates cell motion in 2D and 3D. Finally, we will provide a physical description of the canonical cell trajectory.

2.3.1 Active gels theory

Cells and its associated cytoskeletal polymeric gel can be seen as an *active gel*. The gel is assumed to be mainly constituted by out-of-equilibrium acto-myosin and is driven by the dynamics of these two proteins and the emergent properties of the mesoscopic ensembles (Kreten et al., 2018; Kruse et al., 2004, 2005; Prost et al., 2015). The theory is valid for any molecular motors with their polymeric partners and crosslinkers.

Due to the physical properties of acto-myosin, the gel is visco-elastic: upon mechanical stretch, it exhibits a first, fast, elastic response, described by an elastic modulus E of 10^3 - 10^4 Pa (Wottawah et al., 2005). On larger timescales (100s-1000s), the gel behaves like a viscous material, driven by its Maxwell relaxation time $\tau = \frac{\eta}{E}$ where η corresponds to the viscosity (in Pa.s) and E (in Pa) to the elastic modulus (Joanny and Prost, 2009). The Maxwell time has been measured for cellular aggregates and is typically around 45min (Guevorkian et al., 2010).

The mechanical properties described above are associated with an *activity* of the gel. This "active" description is derived from the dynamics and the kinetics of actin and myosin. In order for actin to polymerize, elongate or depolymerize and for myosin to slide on actin filaments, detach and bind to it, molecules of ATP need to be consumed. ATP hydrolysis (conversion of

ATP to ADP and inorganic phosphate) generates $\sim 10~k_BT$ (where k_B is the Boltzmann constant and T the temperature) and this energy contributes to the processes described in section 2.2. And because at this scale friction dominates and inertia is negligible – living matter operates at *low Reynolds number* (Purcell, 1977) – hydrolysis of ATP is essential to produce sustainable forces and stresses. Therefore, the system is fundamentally out of thermodynamic equilibrium.

Hydrodynamics description of active gels by Kruse *et al.* derived an expression of the stress σ given by this type of gel (Kruse et al., 2004, 2005). It includes, as a first term, the classical hydrodynamic definition of a shear stress in a fluid given by $\sigma = 2\eta u$ where u corresponds to the velocity field gradient ($u = \Delta v$). This canonical definition of hydrodynamic stress σ misses two properties of an acto-myosin active gel: the polarity of actin filaments, which can lead to different dynamics (contraction or extension, as we described in section 2.2.1.3) and ATP hydrolysis, providing the activity inherent to the active gels. Filaments polarity is described as an orientational field h (decomposed into h_{\perp} and $h_{//}$) derived from filaments orientations which constitutes another fundamental property of acto-myosin gels. Finally, the out-of-equilibrium nature of the gel, *i.e.* hydrolysis of ATP and energy fluxes, is embedded into the difference of chemical potentials of ATP, ADP, and P_i . This is given by: $\Delta \mu = \mu_{ATP} - \mu_{ADP} - \mu_{Pi}$. $\zeta \Delta \mu$ corresponds to the active stress. Finally, this yields to the expression of stress in active gels:

$$\sigma = 2\eta u + vh - \zeta \Delta \mu \quad (2.2)$$

This constitutive equation led to successful predictions of active gel behaviours, from actin asters formation and actin flows to myosin clusters. However, this equation does not take into account any regulation. As seen earlier, myosin can be active or inactive depending on its phosphorylation state, and this can be driven by RhoA GTPases. In the current active gel framework, myosin is assumed to be always active, leading to contraction and stress generation. Therefore, integration of both frameworks, GTPases regulation and gel activity, would need to be done.

In addition, $\zeta \Delta \mu$, considered as the "active" term of the equation, is hardly accessible from experiments and a robust associated value still needs to be characterized.

Despite these two features lacking so far experimental descriptions, active gels physics successfully captured the phenomena associated to acto-myosin and led to predictions and understanding of cellular features and behaviours.

2.3.2 Mechanics of cellular migrations

At low Reynolds number, inertia is negligible and force balance is equal to zero (Tanimoto and Sano, 2014). Therefore, symmetry has to be broken at the cellular scale in order to produce motion. This is achieved through active gel and its generation of traction forces. Force dipoles, either extensive or contractile, generated by these traction forces can lead to cellular motion

(Bergert et al., 2015; Schwarz and Safran, 2013; Tanimoto and Sano, 2014). In this work, we did not go through such analysis of multipolar developments but we did consider the interactions between acto-myosin and the substrate. In this section, we will detail the two different models describing cell migration: (i) adhesion-based migrations (also called integrinbased) and (ii) adhesion-free (also called friction-based) migrations.

2.3.2.1 Integrin-based migration

On 2D flat surfaces, and in some cases of 3D migrations (in collagen matrix or equivalent, when fibres are associated with anchoring zones), cells adhere on the substrate and generate FAs.

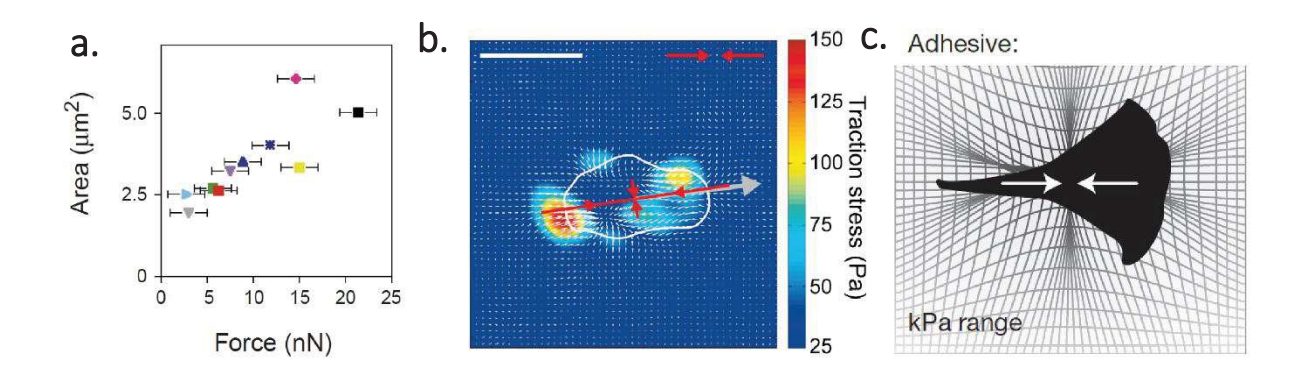


Figure 2.12. Adherent cells "pull" on the substrate. (a) Measurements of forces applied by FAs of different areas allowed to extract a force-area relationship. From (Balaban et al., 2001). (b) Traction force microscopy showing force distribution exerted on the substrate by the cell. Red arrows show direction of force dipoles while grey arrow indicates cell motion direction. From (Tanimoto and Sano, 2014). (c) Scheme representing an adhesive cell with a contractile force dipole. The cell "pulls" on the substrate to migrate. From (Bergert et al., 2015).

Complexes FA-stress fibres generate a constant force per unit area $f/A = 5.5 \pm 2 \, nN$. μm^{-2} (Balaban et al., 2001) (see Figure 2.12a). Collection of FAs exerts centripetal forces: cells "pull" locally on the substrate (Bergert et al., 2015; Schwarz and Safran, 2013; Tanimoto and Sano, 2014) (see Figure 2.12b-c). This is mainly this framework that will be used throughout the different projects presented in this manuscript.

2.3.2.2 Adhesion-free migration

When cells are confined with passivated walls (preventing adhesion), the cellular migration is mostly independent of such adhesion molecules. Therefore, it is rather the coupling between the wall, the cell membrane, and the actin flow that generates friction and propulsion of the cell body (see Figure 2.13a). Indeed, patterns of assembly-disassembly and polarity of actin filaments give the ability to the active gel to flow. This flow, from the leading edge to the centre

of the cell is called *retrograde flow*. Cellular motion is therefore dependent on the flow and the cell velocity v is linked to the flow speed V (see Figure 2.13a):

$$v = \alpha V$$
 (2.3)

The force associated with this friction is at the piconewton level, several orders of magnitude lower than the one produced by integrin-based motions. In addition, the resulting force dipole is extensile (see Figure 2.13b,c), opposite to the integrin-based migration type. Cells "push" on the walls (Le Berre et al., 2013; Hawkins et al., 2009).

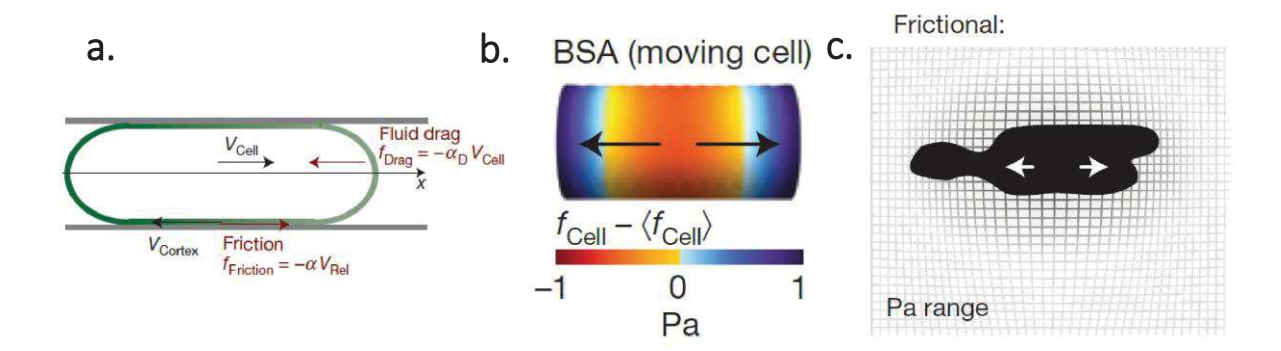


Figure 2.13. Non-adherent cells in 3D "push" on the walls. (a) Extensile force dipole exhibited by cells in micro-channels in a friction-based type of migration. (b) Cell cortex is modelled with active gel Eq (2.2). V_{cortex} corresponds to the retrograde flow while V_{cell} is associated to cell motion. $V_{Rel} = V_{cell} + V_{cortex}$. Cell migrates if the friction α generated by the flow compensates the drag α_D . (c) Scheme representing a cell with an extensile force dipole and the pressure range (Pa). All panels from (Bergert et al., 2015).

Altogether, these two types of migrations even though they exhibit differences can be modelled with the active gel framework exposed in 2.3.1. In all cases, force balance is satisfied and $\sum \vec{F} = 0$.

2.3.3 Persistent Random Walks

As a consequence of the phenomena described so far in 2.3.1 and 2.3.2, cells eventually move on substrates. Physical description of these trajectories allows to determine cellular behaviours and can lead to predictions.

Without external cues, on a 2D flat surface, cells exhibit a particular behaviour called *Persistent Random Walk* (PRW). Experimental observations were the following: after acquisition of front-rear polarity, cells start migrating over tens of micrometres without stopping. This is the *persistent* phase, happening during a characteristic time, the *persistence time* τ_n .

After a persistent motion, cells stop, depolarize, and acquire another front-rear polarity, starting another persistent migration. Since the acquisition of polarity is random, the average of all the

trajectories leads to no net displacement ($\langle x_t - x_0 \rangle = 0$). The overall motion is random.

The physical description of this migration is somehow an incremental derivative of the equation describing Brownian motion. The fundamental feature added to it is the presence of a persistence time τ_p as a term embedding a cell "memory" of the trajectory.

Therefore, the description of the PRW, originally written by Fürth, yields to the following expression (Fürth, 1920; Selmeczi et al., 2008):

$$\langle d(t)^2 \rangle = 2n_{dim} D\left(t - \tau_p \left(1 - e^{-\frac{t}{\tau_p}}\right)\right)$$
 (2.4)

Where $d(t) = \langle x_t - x_0 \rangle$ and n_{dim} corresponds to the number of dimensions. This physical description of a "random walker" with persistence successfully matched experimental observations and reproduced faithfully trajectories of migrating cells.

This PRW is the canonical migratory behaviours: in the absence of external cues, symmetry breaking is random, and the broken symmetry is not sustained over large times: there is no directed motion *per se* (see Figure 2.14). This indicates that emergence of polarity is not sufficient to produce a long-range directed motion. Instead, polarity needs to be kept, "memorized" by the cell. Section 2.6 will detail further this aspect.

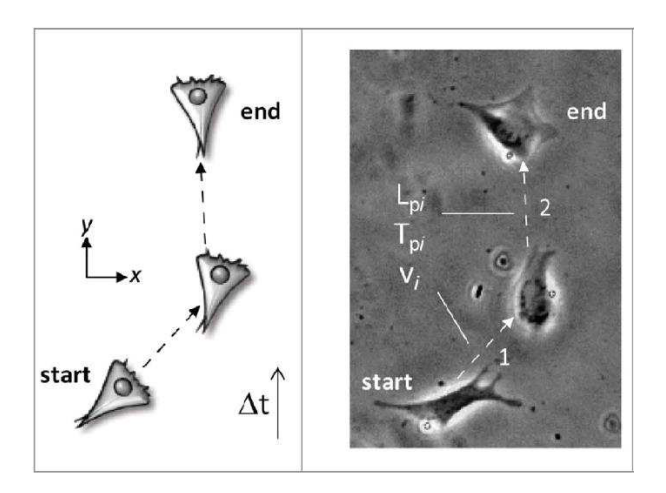


Figure 2.14. Cells migrate randomly with persistence on flat surfaces. Scheme of a PRW (left) and phase contrast images of a mouse fibroblast (NIH3T3) migrating on a flat surface. $Lp = persistence \ length$, $Tp = persistence \ time$, V = velocity. From (Caballero et al., 2015a).

In this section, we showed that single cells can be successfully described and modelled with active gel theory. A switch in migration can happen depending on the cellular microenvironment: on flat substrate, adherent cells "pull" locally while in confined channels, without adhesion, cells "push" on the walls. Finally, the canonical way of describing single cell trajectories is the PRW. This type of motion exhibits alternance between phases of persistent

motion and periods of pause and repolarization. On large timescales, the net displacement is zero.

In the next section, we will go to a different scale: we will focus on collective motion and how this kind of migration can emerge and can be predicted.

2.4 Biology of collective motions

We described, so far, motions of single cells and the regulation by the small Rho GTPases. If epithelial cells motions share many similarities with single cell migration (generation of FAs, stress fibres and the presence of a regulation by Rho GTPases) collective motion cannot be considered as a sum of moving units. Instead, cells interact with each other through cell-cell junctions and transmit forces and mechanical cues between neighbours. Collective motions are an emergent property of the living matter and cannot be guessed from extrapolation of single cell behaviours.

In this section, we will introduce the biology associated with epithelia and molecular components specifically involved in these cellular assemblies as well as what is known about their regulation by the small GTPases such as RhoA.

2.4.1 Cell-cell junctions

Cell-cell junctions are key molecular components in an epithelium as they ensure its integrity and allow cells to communicate and transmit mechanical cues between them. They are transmembranous protein complexes, connected to the acto-myosin network. Analogy can be made with the formalism described in 2.2.1.7 with FAs.

2.4.1.1 Adherens junctions

Adherens junctions are a type of cell-cell junction found in epithelial and endothelial tissues. It is a calcium-dependant protein complex, essentially made of catenin and cadherin (see Figure 2.15a) (Cao and Schnittler, 2019). Adherens junctions are divided into two domains. The first one is intracellular, mainly composed of catenins, and connects the junction to the acto-myosin network. The other one is intercellular, based on calcium-depend cadherin and connects the two adjacent cells between them. This type of structure resembles the one described for FAs in 2.2.1.7: an intra-cellular part, connected to the acto-myosin network, and a trans-membranous region.

These proteins complexes are essential to create a stable epithelium and ensure the proper mechanical properties of the tissue (Friedl and Gilmour, 2009; Ladoux and Mège, 2017; Lellouch et al., 2018).

2.4.1.2 Tight junctions

Tight junctions correspond to the most apical cell-cell junctions in epithelial and endothelial cells. They are formed by the inter-cellular proteins occludins, claudins, and by the Junction Adhesion Molecules (JAMs) (Niessen, 2007) (see Figure 2.15b).

They play a key role in holding cells together at their apical sides, but they also prevent leakage of small molecules and ions in the space between cells.

Figure 2.15c-d shows the distribution of the two proteins in a stained MDCK epithelium.

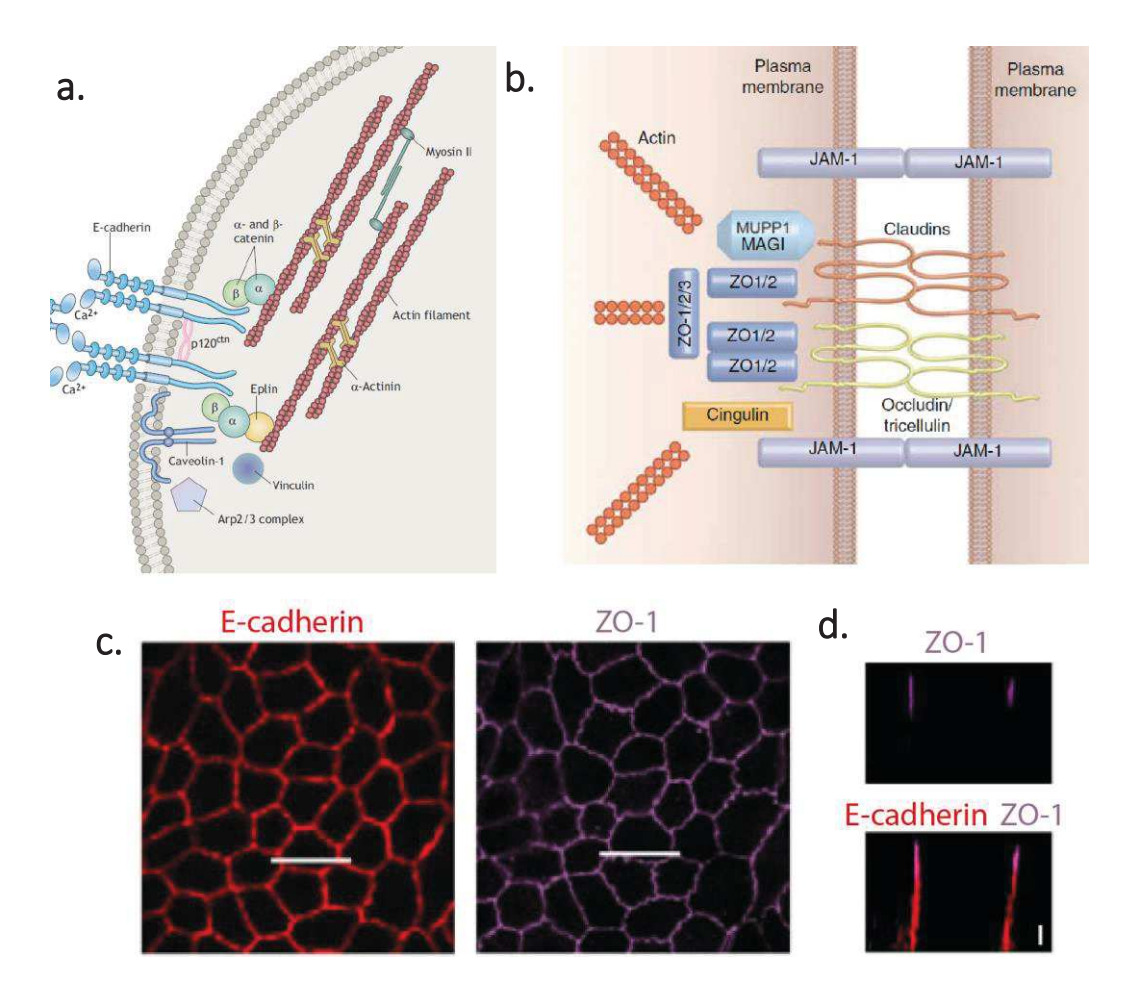


Figure 2.15. Cell-cell junctions architecture. (a) Scheme describing the structure of an adherens junction. Trans-membranous cadherins, forming homodimers, connect the two cells. The catenins bind the junction to the acto-myosin network. From (Cao and Schnittler, 2019). (b) Tight junction organization on the apical side of the cell. Trans-membranous occludins, claudins and JAMs are structuring the junction. From (Niessen, 2007). (c) Distribution of E-cadherin and ZO-1 in MDCK epithelium. Scale bar = 10μ m. (d) x-z profile of the epithelium presented in (c). ZO-1 is apically distributed whereas E-cadherin are medial and basal. Scale bar = 5μ m. (c) and (d) are adapted from (Chen and Chen, 2009).

2.4.1.3 Inter-cellular communications through junctions mechanosensing

It has been shown that epithelial cells interact with their neighbours in order to transduce forces and activate different kinds of regulatory pathways. This fundamental feature is mainly mediated by the junctions between cells, especially by the cadherin junctions, as detailed below.

Figure 2.16a shows how individual cells engage focal adhesions on the substrate and generate traction forces, as described in sections 2.2.1.7 and 2.3.2.2. In a multicellular context, traction forces are transmitted throughout the epithelium by the cadherin junctions that can undergo a conformational change (Ladoux and Mège, 2017) (see Figure 2.16b). This switch is mediated by α -catenin upon mechanical stimulation above 5pN (Le Duc et al., 2010; Huveneers and Rooij, 2013; Ladoux and Mège, 2017; Pannekoek et al., 2019): α -catenin molecule unfolds triggering the binding of vinculin to α -catenin (see Figure 2.16c,d). This property of junctions leads to the transduction of mechanical stimuli in the surrounding epithelial cells.

In addition, adherens junctions act as mechanosensors meaning that it exists a relationship between their extension and the applied force (Brevier et al., 2007; Delanoë-Ayari et al., 2004, 2011; Le Duc et al., 2010) (see Figure 2.16e). This property, described for FAs in section 2.2.1.7, holds true for these intercellular junctions. Indeed, upon mechanical stimuli and stretch of α -catenin, adherens junctions, tightly linked to the acto-myosin network, activate pathways related to actin remodelling (Huveneers and Rooij, 2013; Pannekoek et al., 2019) (see Figure 2.16d). This phenomenon is also governed by vinculin that mediates the recruitment of myosin II, also increasing the tension at junctions in response to stress (Le Duc et al., 2010).

However, if the stretch of α -catenin molecules and its consequences are well defined *in vitro*, the extrapolation of the principles to the mesoscopic ensemble constituted by thousands of α -catenin molecules should be taken with cautious. Emergence of new properties and behaviours could appear when an ensemble is pulled compared to the single molecule.

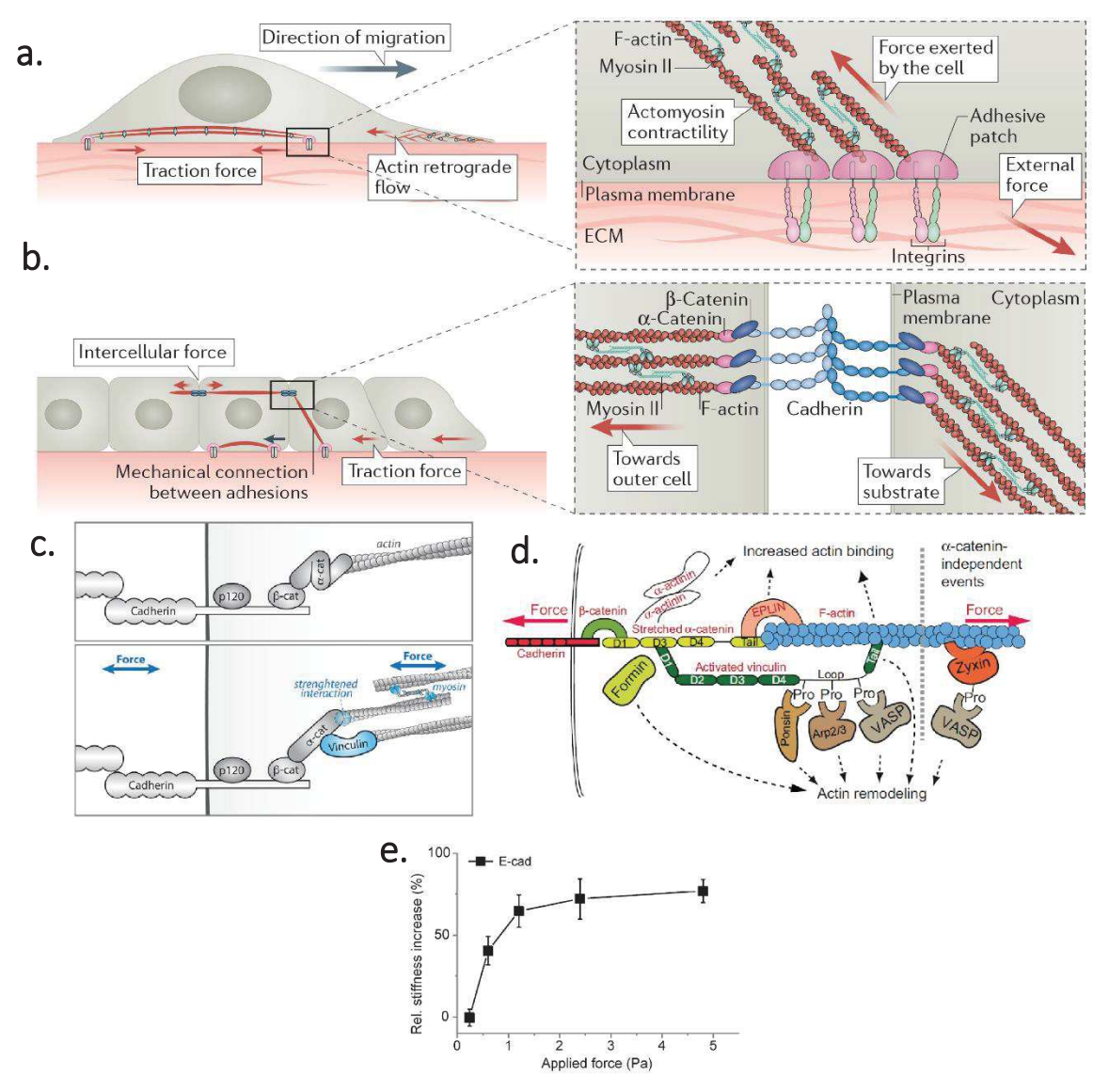


Figure 2.16. Mechanical coupling between epithelial cells goes through cell-cell junctions. (a) Single cell migration on substrate with forces transmitted by the FAs as described in section 1.5.1. (b) Migration of a multicellular system. Epithelial cells are connected through adherens junctions and forces are transduced and transmitted to neighbouring cells through these protein complexes. From (Ladoux and Mège, 2017). (c) Upon mechanical stimuli, α-catenin unfolds and binds to vinculin. From (Pannekoek et al., 2019). (d) This phenomenon activates various pathways involved in actin remodelling. From (Huveneers and Rooij, 2013). (e) It exists a relationship between E-cadherin stiffness and the applied force, indicating a role of mechanosensor. From (Le Duc et al., 2010).

A typical example and consequence of this intercellular communication is the "contact inhibition" phenomenon (Puliafito et al., 2012). At high confluency and crowding, group of cells exhibit, locally, a strongly decreased velocity as well as a very slow mitotic rate (Puliafito et al., 2012). This local phenotypical shift appears above a critical cell area reflecting mechanical stresses in the epithelium. Inter-cellular communication, hypothesized to be mediated by adherens junctions, activates in return pathways such as MAPK, known to be involved in cell cycle, or YAP, a mechano-sensing pathway (Puliafito et al., 2012). So far, the

complete scheme of regulating pathways activated upon contact inhibition is still lacking but the consequent effects such as the decrease in velocity and mitotic rate are well described (Abercrombie and Heaysman, 1953; Puliafito et al., 2012).

This example shows that inter-cellular communication, mediated by the acto-myosin cytoskeleton firmly anchored to the cellular junctions, ensures that any change in individual cell mechanical properties can be transduced to the neighbouring cells.

2.4.2 Rho dynamics in epithelia

The precise description of the three GTPases spatio-temporal activity detailed in 2.2.4 in a migrating epithelium is still lacking. Indeed, GTPases activities are often assumed to be an extrapolation of the behaviours described in (MacHacek et al., 2009; Martin et al., 2016; Pertz et al., 2006). If quantified in an epithelium, it is often described at the single cell level and then extended to the whole epithelium whereas new dynamics could emerge in the ensemble. Description and integration of RhoA activity over the whole epithelium would need to be done.

Nevertheless, the predominant role of RhoA activity at epithelial junctions and boundaries together with its role in epithelial mechanics has been described over the last years as detailed below.

In the context of acute mechanical stimuli, it has been shown that RhoA activity significantly increases at cellular junctions of endocarcinoma cells Caco-2 (Lellouch et al., 2018; Nestorbergmann et al., 2018) (see Figure 2.17a). This phenomenon involves many molecular actors such as MyoVI, $G\alpha12$ and p114RhoGEF and it exists a clear link between adherens junctions and this signalling cascade activating RhoA (Lellouch et al., 2018; Nestor-bergmann et al., 2018). This mechanical feedback is fundamental to preserve cell-cell junctions and therefore epithelium integrity. Also, the junctional activation is consistent with the fact that RhoA is a small GTPase mainly activated at the cell membrane (Koo et al., 2015).

In a migrating epithelium, the presence of leader cell pulling and driving the collective motion of the colony is determined by the presence of an increased RhoA activity (Reffay et al., 2014) with a spatial localization somehow similar to the one described for single mesenchymal cells (MacHacek et al., 2009; Martin et al., 2016; Pertz et al., 2006) (see Figure 2.17b). While inhibition of Rac1 does not impair collective migration and leader cell formation, knock-down of RhoA inhibits the normal migratory phenotype. In epithelial cells pulled by the leading edge, it is shown that mechanical stimuli are transmitted between neighbours through adherens junctions, by the mechanisms detailed above, and activate in return RhoA pathway and myosin phosphorylation (Ladoux and Mège, 2017).

Finally, in developing organisms, it has been shown in *Drosophila Melanogaster* that Rho pulses at cellular junctions leading to a ratchet-like mechanism where cells alternate between deformations and stabilizations in order to change their shape (Munjal et al., 2015). This

pulsatile behaviour is a result of acto-myosin dynamics (polymerization, contractility, transport) amplifying stochastic fluctuations of upstream signalling and does not come from a "pacemaker" property of Rho (Munjal et al., 2015). However, this stresses the intrinsic instability of Rho and the ability to produce self-organized patterns of Rho activity at cellular junctions. In contrast, some other works showed in *C. elegans* that RhoA could act as a pacemaker giving the tick for cortical acto-myosin (Nishikawa et al., 2017). This suggests that it exists a variety in behaviours depending on the biological system.

Altogether, it seems that RhoA activity mainly localizes at cellular junctions in an epithelium, consistent with the fact that small GTPases activate at the membrane (Koo et al., 2015). Their activation in response to mechanical stimuli or the ability to produce dynamical activation patterns is fundamental to morphogenesis and epithelia integrity. In addition, in moving epithelium, feedbacks exist between focal adhesions, adherens junctions and the other small GTPases (see Figure 2.17c). Higher RhoA activities correlate with the formation of leader cells and thus appear to drive collective cell migration.

However, these single cell activities within the epithelium might or might not be the same throughout the whole monolayer (differences in density, boundary effects) and collective properties may emerge. Therefore, analysis integrating the whole collection might be necessary to find out the interplay between GTPases and epithelia dynamics.

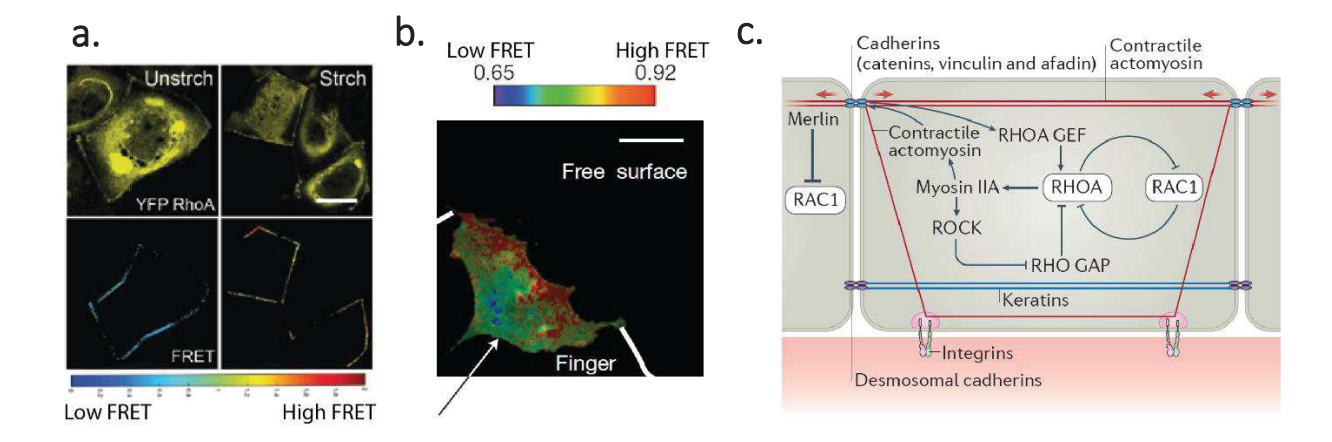


Figure 2.17. Single-cell RhoA activity in epithelia. (a) Caco-2 epithelial cells expressing a RhoA biosensor under mechanical stretch. Upon stimuli, RhoA activates at junctions (right) compared to the basal unstretched state (left). From (Nestor-bergmann et al., 2018). (b) Leader cell from a MDCK epithelium. Strong RhoA activity is present at the leading edge, correlating with the formation of a migrating "finger". From (Reffay et al., 2014). (c) RhoA activates upon adherens junctions stimulation (Ladoux and Mège, 2017).

2.5 Physical description of collective migrations

For the same reasons detailed in the introduction of the section 2.3, activity alone of GTPases cannot predict epithelium motion. Physics associated with a collective migration can either

describe it as a continuum driven by active gels theory, or by discrete models where interactions between cells are described without investigating the activity *per se*. In the next sections, we will describe both approaches.

2.5.1 Coarse-grained hydrodynamic description

2.5.1.1 Navier-Stokes equations

The Physics associated with a hydrodynamic description of a multicellular ensemble considers the system as a continuum driven by active gel physics. The large-scale dynamics of the system is deduced from the evolution of continuous variables such as density $\rho(\mathbf{r},t)$ or velocity $\mathbf{v}(\mathbf{r},t)$ (Shaebani et al., 2020). The most common description is derived from incompressible Navier-Stokes equations, at low Reynolds number (Shaebani et al., 2020):

$$\rho(\partial_t + \boldsymbol{v}.\nabla)\boldsymbol{v} = -\nabla P + \nabla \cdot \boldsymbol{\sigma} + \boldsymbol{f} \quad (2.5)$$
$$\nabla \cdot \boldsymbol{v} = 0 \quad (2.6)$$

where σ corresponds to the stress tensor, decomposed into active stress σ_a (derived from active gels equations), reversible stress σ_r and dissipative stress σ_d . P represents the pressure and f the force density.

2.5.1.2 Velocity fields in migrating epithelia

In this context, knowledge of v is fundamental. In a migrating epithelium, velocity fields can be obtained by a cross-correlation between the collection of cells – considered as a continuum – at a time t_n with the same system at the time t_{n+1} (see Figure 2.18a). The cross-correlation product gives the displacement of the objects in the field of view and, divided by the time step, gives the velocity direction and amplitude at each position. This computation, known as Particle Image Velocimetry (PIV), is now widely used in the field of Biological Physics in order to extract velocity from a multicellular system (see Figure 2.18b) (Comelles et al., 2019; Petitjean et al., 2010).

Velocities can be incorporated into Eq. (2.5) but also contribute to derive the stress from Eq. (2.2). Indeed, as described in section 2.3, one part of the stress is derived from the knowledge of u, the velocity field gradient.

In addition, another feature, not directly linked to the active gel physics but extensively used in the present work, can be extracted from the velocity fields: the *coherence length*. The coherence length is basically the length over which the velocity vectors are correlated over space. To extract this length, a simple spatial correlation of the velocity (along the radial direction r or the tangential one θ , see (Garcia et al., 2015)) given by:

$$C_{v}(\delta r, t) = \frac{\langle \vec{v} (\vec{r} + \delta \vec{r}, t) . \vec{v} (\vec{r}, t) \rangle}{\langle v(\vec{r}, t)^{2} \rangle}$$
(2.7)

The coherence length ξ is then extracted by fitting $C_v(\delta r, t)$ with an exponential decay $e^{\frac{-\delta r}{\xi}}$. This coherence length is fundamental to evaluate directionality in a multicellular system and how cells inside an epithelium migrate collectively.

Altogether, hydrodynamics description of an epithelium provides important readouts about its collective behaviour. Derivation of stresses, velocities and densities allows to describe and predict the phenomena. However, this is a continuum model and therefore it does not consider cells as individuals and ignore their interactions. In the next section, we will see how discrete approaches can provide other information and readouts.

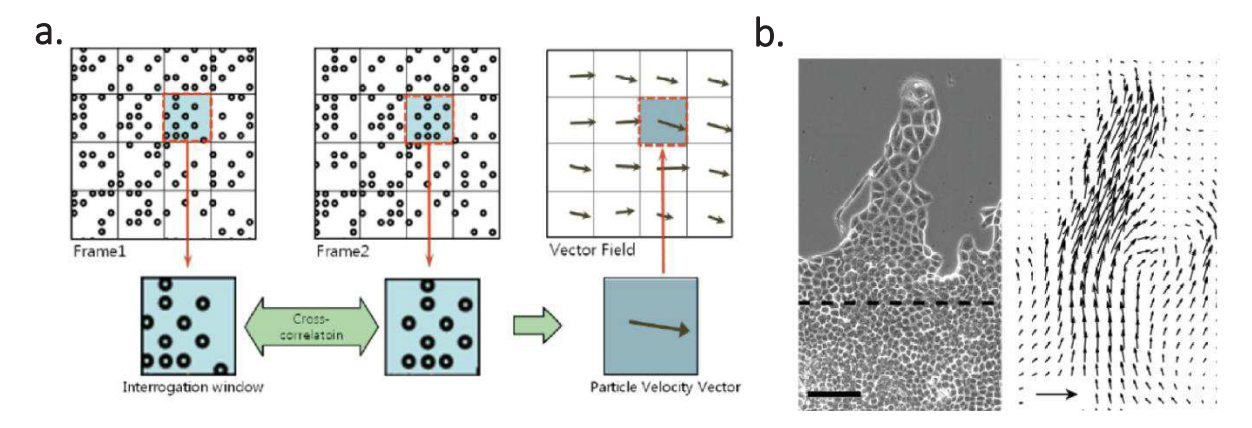


Figure 2.18. PIV generates velocity fields of collective motions. (a) Scheme of the PIV algorithm: interrogation windows are compared and cross-correlated through time in order to extract velocity vectors (Choi et al., 2011). (b) A PIV velocity field applied to a migrating epithelium of MDCK cells. Scale bar: 100µm. From (Petitjean et al., 2010).

2.5.2 Discrete description: the Vicsek model

The hydrodynamic description detailed above considers the ensemble of cells as an out-of-equilibrium continuous visco-elastic fluid behaving according to the active gel physics. Here, we will see that we can discretize our system and consider each cell as an individual self-propelled particle. Because the following work mainly focus on the Vicsek model, we will not detail other discrete approaches such as the vertex or the Potts models. Indeed, the Vicsek model, detailed below, focuses on the emergence of collective features based on single-particle polarities and velocities which corresponds to the scope of this work (Shaebani et al., 2020).

Historically developed to model trajectories of self-propelled particles (Vicsek et al., 1995), Vicsek models have been used to describe successfully active matters such as bird flocks, fish shoals or collection of cells. Its universality and its simplicity made it popular in Biological Physics (Shaebani et al., 2020).

Vicsek model is minimal as it includes only few parameters and considers the individuals as self-propelled particles without describing the mechanisms by which they acquire their motion. In other words, activity is embedded into the spontaneous velocity of the particles.

The model describes how the velocity of a particle aligns with the one imposed by the neighbours (Vicsek et al., 1995). A particle i is migrating with a constant velocity v_i . θ_i defines the angle of the velocity vector. At each time point, the particle velocity tends to align with the average velocity of the ensemble in the neighbourhood of radius r. Therefore, we can define at each iteration:

$$\theta_i(t+1) = \langle \theta(t) \rangle_r + \Delta \theta$$
 (2.8)

 $\langle \theta(t) \rangle_r$ corresponds to the average orientation of velocities in the neighbourhood while $\Delta\theta$ describes the noise in the system. A new position with a new velocity can be then derived from Eq. (2.8):

$$x_i(t+1) = x_i(t) + v_i(t)\Delta t \begin{pmatrix} \cos\theta_i(t) \\ \sin\theta_i(t) \end{pmatrix}$$
 (2.9)

This simple set of two equations lead to the description of new phase transitions in collective motion. In this model, the two main parameters driving the phase diagram are the density of particles and the noise $\Delta\theta$ (see Figure 2.19). At high noise and low density, particles are on average non-aligned and move randomly (the average velocity $|v_a| = 0$). At high density and low noise, velocities align, and the collective motion gets organized: the system exhibits a spontaneous symmetry breaking of the rotational symmetry (Vicsek et al., 1995).

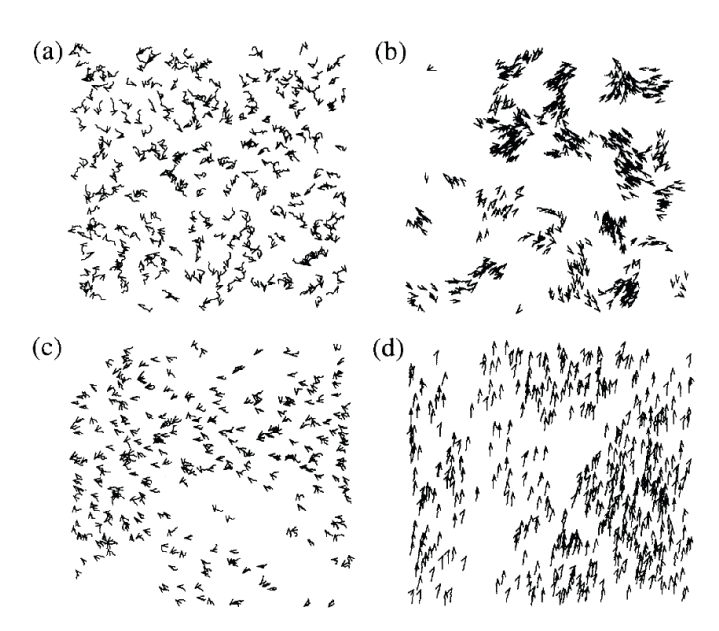


Figure 2.19. Emergence of collective behaviours in Vicsek model. (a-b) Simulations ran with small density and small noise at t0 (a) and after some time (b). Particles gather in small clusters and start behaving coherently. (c) For higher noise, particles move randomly in the field of view. (d) For high density and small noise, particles are all moving in the same direction (Vicsek et al., 1995).

This former model has been afterwards implemented with other terms in order to describe more faithfully certain types of behaviours. One could add some repulsion or attractive terms, or implement polarity, dissociated from velocity.

Altogether, Vicsek-based models are efficient to describe how global coherence can emerge from single cell polarities and how interactions between neighbours participate to this phenomenon.

2.6 Directionality

We saw in the previous section that cells can spontaneously break their symmetry and exhibit motion in random directions. The *persistent random walk* represents the canonical single cell behaviour. However, in some types of physiological and pathological contexts, cells can migrate from one localization to another in a directed manner; the PRW model does not recapitulate these observations: in fact, the broken symmetry needs to be sustained in time and space to produce long-range directed motions.

We will first describe relevant biological examples that will be key to bring the PhD motivations, and then different ways of triggering directed cellular motion.

2.6.1 Biological relevance

In physiology, directed migrations have been reported in key biological and pathological processes. We will detail in this section various realizations of directional cell motion at the single and at the multicellular scale.

2.6.1.1 Single cell directed motion

In vertebrates, migration of cells from the neural crest constitutes one of the most representative examples of directed single cell motion during development.

After gastrulation, more specifically during neurulation, multipotent cells from the neural crest undergo complete or partial Epithelial to Mesenchymal Transformation (EMT) and they dissociate from their original tissue (see Figure 2.20a) (Bronner and Le Douarin, 2012; Mayor and Theveneau, 2012). Upon EMT, they migrate to various places in the embryo to give raise to different tissues depending on their localization: melanocytes, bone cells, odontoblasts, enteric nervous system cells or smooth muscle (Bronner and Le Douarin, 2012; Mayor and Theveneau, 2012).

Cells funnel through the rostal portion of each somite and their direction of migration is associated with chemical gradients of EphB/EphrinB and semaphorin/neuropilin signalling together with interactions with the extra-cellular matrix (Mayor and Theveneau, 2012). This

way of directing motion, through differences in chemical compounds in the cell microenvironment, is called *chemotaxis* and will be detailed below, in section 2.6.2.

We described here one physiological example - among many others - of directed cell motion. However, this phenomenon can also be found in pathology. A canonical example of directed migration at the single cell level, involved in pathology, would be metastasis spreading (Stuelten et al., 2018).

In late stages of cancers, cells from the primary tumour escape and migrate directionally to different organs depending on the cancer type and the primary tumour localization (see Figure 2.20b) (Talmadge and Fidler, 2010). This motion over very large distances (for example, kidney cancer is often associated with metastasis in lungs (Agrawal et al., 2015)) is facilitated by the blood flows as the cancer cells often reach circulation. In order to invade secondary localizations, strong cues need to sustain the broken symmetry over sufficient times. Even if cancer cells could virtually invade all organs, specific cancers are associated with specific metastasis suggesting that different cancers cells react to external cues differently (Talmadge and Fidler, 2010).

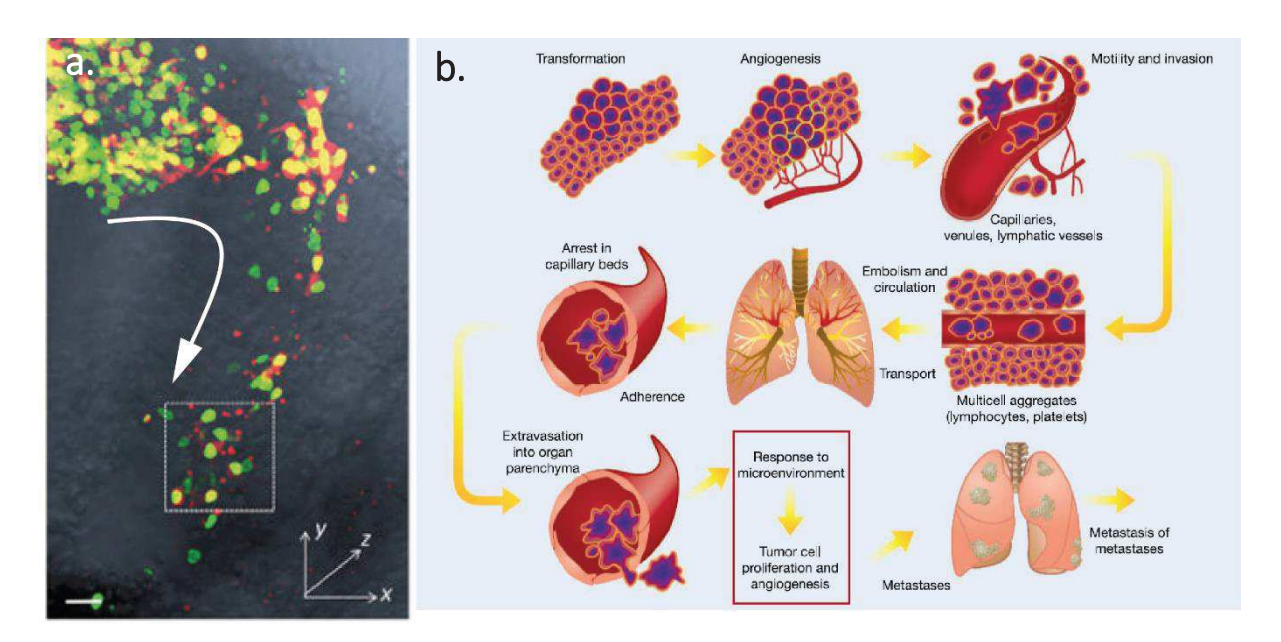


Figure 2.20. Cells move directionally in different physiological and pathological contexts. (a) Migration of cells from the neural crest (H2B-GFP and H2B-mCherry). The white arrow indicates the large-scale directed motion of single cells. Scale bar: 25µm. From (Li et al., 2019). (b) Typical picture of metastasis spreading. The red box highlights the "seed and soil" theory and the sequence where symmetry breaking and directed motion are prominent. From (Talmadge and Fidler, 2010).

Since 1889 and the work from Paget, the theory established to explain this phenomenon is the "seed and soil" hypothesis (Akhtar et al., 2019; Langley and Fidler, 2011; Paget, 1889). First, the cancer cells – the "seeds" – escape the primary tumour, reach the systemic circulation through extravasation in small blood vessels in order to migrate to the secondary tumour

localization – the "soil" (Akhtar et al., 2019; Langley and Fidler, 2011; Paget, 1889). The "soil" needs then to have specific characteristics so that the "seeds" get attracted and can grow in this region (Akhtar et al., 2019; Langley and Fidler, 2011; Paget, 1889). This theory shed light on the importance of the cellular microenvironment in directed migrations. Chemical gradients and chemical composition of the medium are often assumed to be one of the main triggers leading to this directed motion towards the "soil" such as the soluble gradients of CXCL12 in the trafficking of breast cancer cells or the haptotactic one of VCAM-1 in lungs (Langley and Fidler, 2012).

We saw different examples of directed single cell migrations without detailing the mechanisms leading to this directionality. In the next section, we will describe various examples of directed collective motion. Then, the following will explicitly detail the different ways to generate directionality.

2.6.1.2 Directed collective motion

Collection of cells – connected and interacting with their neighbours (with the biology described in 2.4) – can also undergo directed migrations *in vivo*.

In early *Drosophila Melanogaster* development, groups of cells are involved in large-scale organized motion. These *collective migrations* occur during oogenesis: upon egg chamber elongation, cells collectively rotate along the anterio-posterior axis (see Figure 2.21a) (Cetera et al., 2014). During the first hours, cells are not rotating, they fluctuate around their center of mass, exhibiting a very unstable behaviour (Cetera et al., 2014). The symmetry breaking and the transition to the rotational state is fast (minute timescale).

This motion is not well understood and interestingly also appears in various different processes: in tubular organ formation or in mammary epithelial acini groups of cells also exhibit this rotational behaviour (Tanner et al., 2012; Wang et al., 2013). The dynamics of this collective motion cannot be predicted from the single cell dynamics as this phenomenon is an emergent property of living matter.

In pathology, most of the epithelial cancer types exhibit collective cell migrations resulting into the invasion of surrounding tissues (Friedl and Gilmour, 2009). This process occurs *via* finger-like cellular assemblies with leader cells and followers (see Figure 2.21b). Remodelling and destruction of the extra-cellular matrix through proteases secretion together with probing and adhesion by filopodia and pseudopodia critically govern cancer invasion (Friedl and Gilmour, 2009). In addition, detachment from the tumour of cellular clusters can also occur and these structures can survive in the blood flow, leading to potential metastasis (Ku et al., 2007).

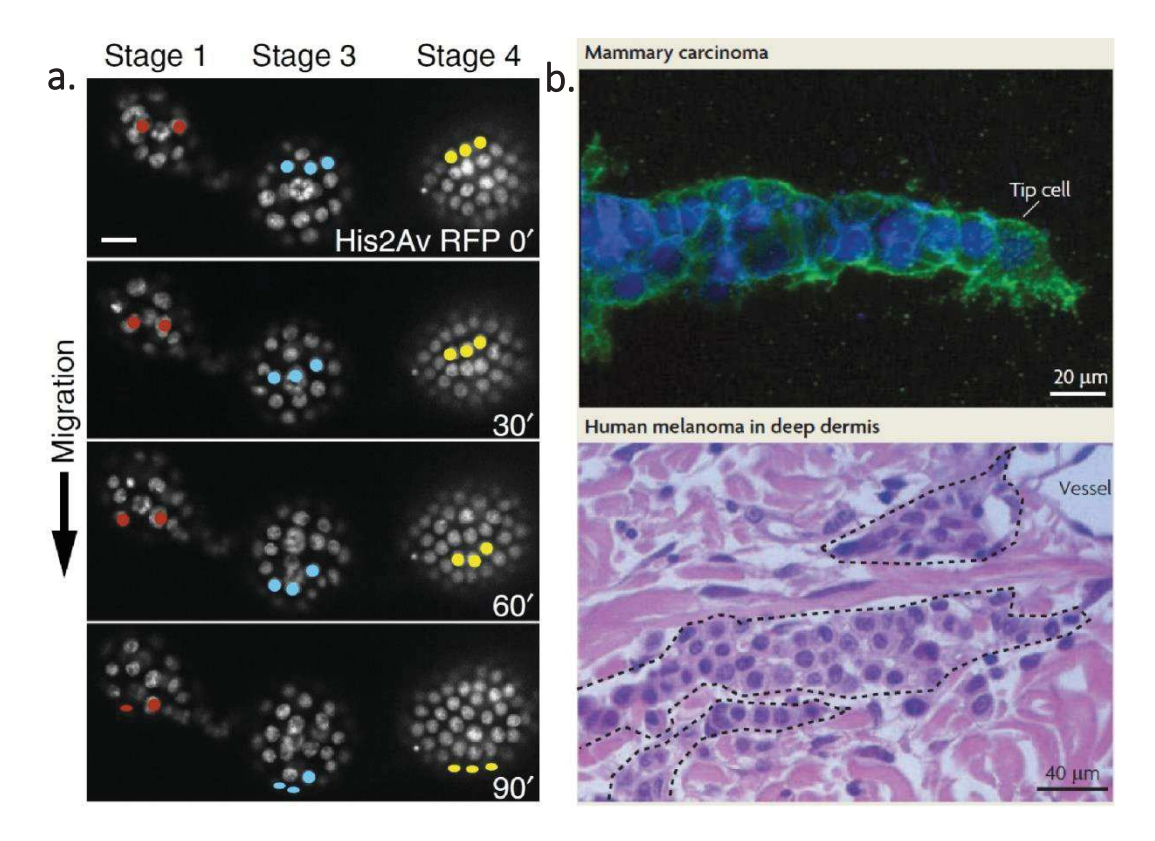


Figure 2.21. Collective directed motions in Biology. (a) Directed collective motion of Drosophila egg chambers cells. Cell nucleus is shown (His2Av-RFP). Colored dots mark the same set of nuclei at each timepoints. From (Cetera et al., 2014). (b) Two examples of collective cell migration during cancer invasion. MCF-7 mammary carcinoma exhibits a cellular strand composed of leader cells and followers (up, E-cadherin in green and DAPI). Bottom image shows a melanoma strand approaching a blood vessel on a histopathological slide. From (Friedl and Gilmour, 2009).

Altogether, we saw some examples of single and collective directed cell migrations happening *in vivo* during development or pathogenesis. In the following sections we will describe how this directionality can arise, focusing on roles of the cellular micro-environment.

2.6.2 Chemical gradients

As previously described in the context of cancer metastasis, chemical gradients constitute a well-established paradigm according to which cells acquire a front-rear polarity based on the direction set by the highest concentration of a given chemical (called *chemoattractant*). This way of breaking symmetry and imposing cell directionality has been so far the canonical way for explaining directed motion *in vivo* and especially during cancer spreading (see 2.6.1 and the "seed and soil" theory).

In organisms, chemical gradients are most of the time generated by a source, secreting a specific molecule (Kicheva et al., 2007, 2012; Kutejova et al., 2009). This chemo-attractant produced with a specific rate then undergoes diffusion, degradation or interactions with the

surrounding cells; all these events change the slope and the temporal dynamics of the gradient (Kicheva et al., 2007, 2012; Kutejova et al., 2009).

Rectification of cellular migrations by *chemotaxis* supposes a spatial sensing by the cells in order to encode the slope of the gradient and the direction towards which the cell will move. The sensing of chemical molecules is done through trans-membranous receptors (often G-proteins such as the $\beta\gamma$ complex in *Dictyostelium*), homogeneously distributed across the cell membrane and it is shown that cells can sense differences of less than 2-10% between front and rear (Van Haastert and Devreotes, 2004; Iglesias and Devreotes, 2008a; Zigmond, 1977).

The outcome of transducing chemotactic signals is the acquisition of a new polarity with the growth and the polymerization of a new lamellipodium together with filopodia, in the direction of the gradient. Signalling pathways are stimulated: in *Dictyostelium*, RhoA, Rac1, Cdc42, PAK or PTEN are often activated upon chemotactic stimulation and their activation increases the front-rear polarity, sustains it and even makes the cell more sensitive to chemicals (Van Haastert and Devreotes, 2004; Rappel and Loomis, 2009; Wang et al., 2011). This modulation of acto-myosin creates a feedback loop sustaining the broken symmetry in the direction of the gradient and then leading to firm directed migrations.

Various works done *in vitro* showed the efficacy of chemotaxis in breaking symmetry and promoting directed motion (Van Haastert and Devreotes, 2004; Rappel and Loomis, 2009; Xu et al., 2017; Zigmond, 1977). The pipette experiment delivering cyclic AMP (cAMP) with *Dictyostelium* represents the archetypal assay testing chemotaxis *in vitro*. In this experiment, *Dictyostelium* cells are stimulated with a high concentration of cAMP delivered by a micropipette in a petri dish. Cells polarize and migrate towards the tip of the pipette until all the cells reach the same point (see Figure 2.22a). Interestingly enough, upon treatment with Latrunculin A (Lat. A), cells fail to grow a lamellipodium, keeping their isotropic shape, but do not fail to polarize: an accumulation of polarity markers such as the pleckstrin-homology domain (PH) appears in the direction of the pipette(see Figure 2.22b) (Van Haastert and Devreotes, 2004). This means that the initial symmetry breaking event appears upstream of the lamellipodium formation. This also puts forward the apparent discrepancy between polarity markers: absence of a lamellipodium is not necessarily associated to a lack of polarity. In this context, it is rather the definition given in 2.1 – the anisotropy in protein concentration – which is relevant.

Chemotaxis is also reported in multicellular contexts where the directed collective migration is correlated with the presence of long-range chemical gradients. For example, in Zebrafish, a cluster of ~ 100 cells is involved in the formation of the lateral line primordium (Mishra et al., 2019). These cells are responding to a gradient of SDF-1 in their environment and the motion is critically dependent on the expression of the chemokine receptor 4 - CXCR4 (Mishra et al., 2019). Nevertheless, in cases of collective migrations, a major question remains: are all the migrating cells sensing the guidance signal or are some leader cells only transducing the chemotactic signals and then instruct the other cells by mechanical stimuli? This question is still open.

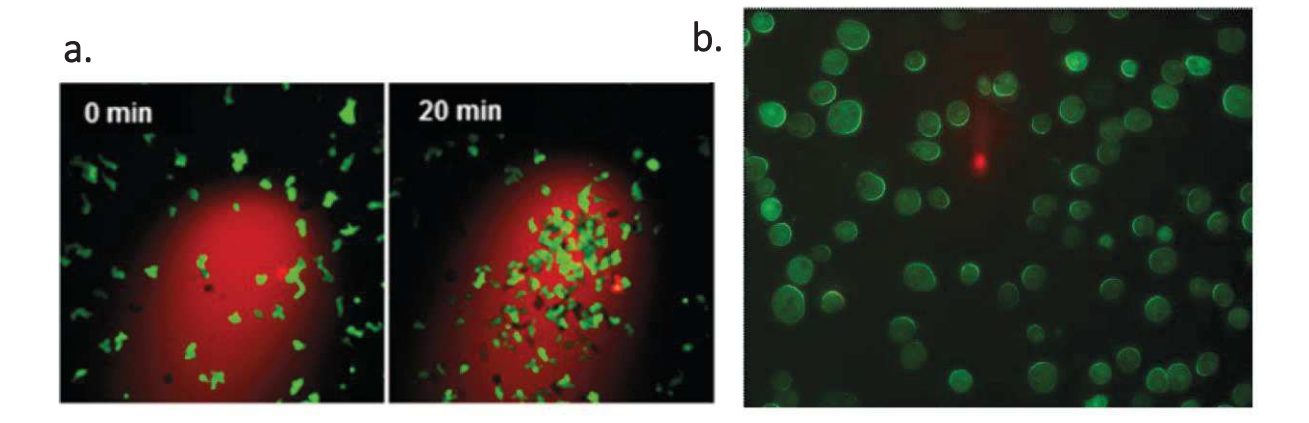


Figure 2.22. Chemical gradients orient Dictyostelium migration and polarity. (a) Dictyostelium cells migrating towards a spot a TRITC-cAMP. After 20min, cells aggregate on the delivery spot. From (Xu et al., 2017). (b) Cells expressing the pleckstrin-homology domain (PH) fused with GFP treated with latrunculin A, inhibiting actin polymerization and therefore motion. A broken symmetry is visible at the molecular scale: crescents of high density are forming in the direction of the cAMP hotspot (in red; Cy3-labelled cAMP). From (Van Haastert and Devreotes, 2004).

Regarding *in vitro* experiments, chemotaxis seems to be a good candidate to break symmetry in biological contexts. However, the systematic association of directed motion with chemical gradients might not be always true. Gradients are rarely quantified *in vivo* together with cell motility and if they are, they are rarely proven to be causal. Precise quantifications of the gradient slope in experiments (*in vivo* or *in vitro*) should be done in order to test the validity of the chemotaxis hypothesis. If two localizations exhibit different absolute concentrations of a given molecule, it has to be linked with the distance between the two spots and with the spatiotemporal dynamics of the molecule. Therefore, apparent differences in concentrations could lead to a gradient slope negligible at the cellular scale.

This leads to various works trying to find other ways to direct cell motion without the need of any long-range gradients. These works essentially focus on the importance of the extra-cellular environment and on how local asymmetries and constraints can direct cellular migrations.

2.6.3 Guidance through local asymmetries

The emergence of micro-fabrication and micro-printing created new *in vitro* assays probing the influence of the cellular micro-environment. These techniques open new ways to acutely tune environment geometry, substrate stiffness, elasticity, or cell density. This allows to manually break symmetry at the cellular scale and to probe the effects of this new generated polarity on directionality.

Many works proposed that breaking symmetry of the cellular environment could in return break symmetry of the cellular shape, protein distributions, cortex properties and then bias the overall

motion. Turning stochastic PRW motion into a deterministic one was the main focus of these studies.

Mahmud et al. proposed an assay where cells migrate on connected triangles made with microfabrication (Mahmud et al., 2009). These motifs – called "ratchets" – have a width comparable to the cell size, thus confining the cell and imposing its shape to the cells (see Figure 2.23). Remarkably, direction of motion was biased in the direction of the triangle. Interaction between the imposed geometrical cues and the cell lamellipodium/protrusions biases cell motion. This suggests that broken symmetries in the cellular micro-environment could translate into a strong bias in cell migration without the presence of any external chemical gradients.

Caballero *et al.* performed another experiment where cells move between fibronectin triangles separated by passivated adhesion-repellent regions on a flat substrate (see Figure 2.23b) (Caballero et al., 2014, 2015a, 2015b). Migrations were biased by the asymmetrical geometry and the stochastic probing of protrusions was shown to be key in the observed phenomenon. The broken symmetry changed the relative frequency of protrusions to the right and to the left sides of the cell but also the probabilities to adhere at the two ends of the patterns because available areas were different. The competition of these probabilities and its quantification would give an estimation of the final bias. FAs were also assumed to play a key role in the mechanism even though their visualisation and dynamic description were not performed. This rectification led by local asymmetries has been coined *ratchetaxis*. When the available motifs were of the same shape, the bias vanished, and the cells stochastically migrate between patterns with an overall displacement equal to zero. This further confirmed the observations and the conclusions made on the asymmetrical patterns.

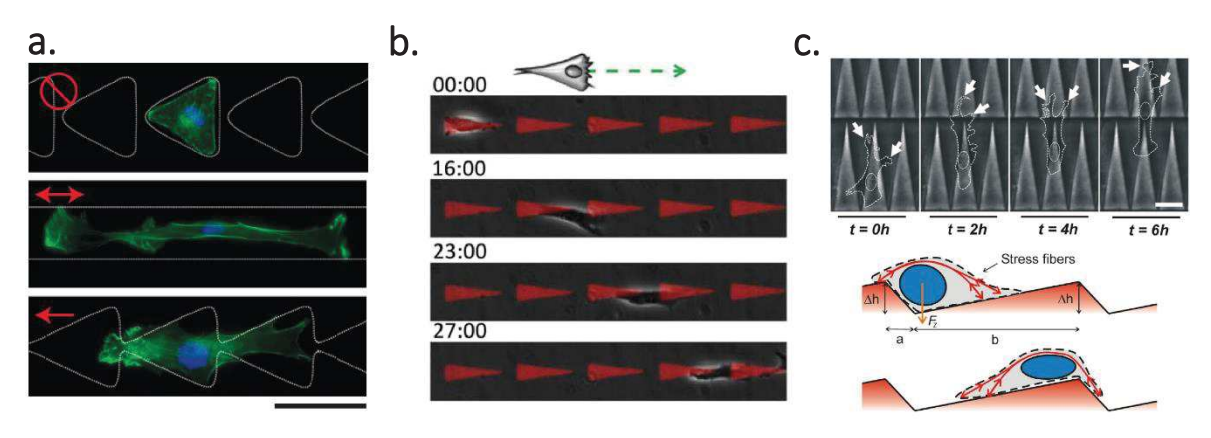


Figure 2.23. Topographical asymmetries direct single cell motion. (a) ratchet-like patterns made with micro-fabrication. Cells on patterns separated by physical gaps cannot cross the motifs and migrate (up). On lines, with no broken symmetry, the direction of migration is random (middle) whereas on asymmetric connected patterns, motion is biased (bottom). From (Mahmud et al., 2009). (b) Cell migrating on micro-printed fibronectin motifs (in red) separated by passivated regions. Cell can "hop" between motifs with a phenomenon driven by the stochastic probing for protrusions. From (Caballero et al., 2015a). (c) Topographical ratchet (up): migrations are biased towards the tip of the motifs. The direction is also related to the nucleus orientation with respect to the motif. From (Comelles et al., 2014).

Interestingly, directed migration was also possible on 3D topographical ratchets but through different mechanisms (see Figure 2.23c) (Comelles et al., 2014). While protrusions were the main regulator of bias in the 2D ratchets, the nucleus played an additional key role to the phenomenon on 3D ratchets. Indeed, mechanical interactions between topographical walls and cells nuclei were evidenced by biased distributions of staying probabilities as well as by precise quantifications of cells trajectories and nuclei shapes. Also, they showed that chemical gradients (haptotactic with grafted fibronectin) and ratchetaxis can compete or cooperate depending on their respective orientations.

Altogether, these works provide evidence that cellular migration can be directed by local asymmetries in the micro-environment without the need of any external chemical gradients: patterns with a length scale comparable to the cell size break the symmetry locally and impacts the overall motion. Moreover, the fact that nuclei are contributing to the rectification in the topographical ratchets suggests that the nucleus can be seen as the large organelle preventing or facilitating migration in opposite directions in 3D migration.

2.6.4 Alignment and directional flows driven by confinement

We showed in the previous section that geometrical constraints could promote bias in directionality and rectify migration in the context of single cell motion. Even though the test of asymmetrical patterns on collective migration has not been performed yet, it has been reported that geometrical constraints, especially confinement, can rectify collective migration. In this context, stress fibres and cytoskeleton assembly and organization are determined by the rules set by the micro-environment boundaries (Schuppler et al., 2016). This breaks the symmetry and imposes a long-range order in the migrating epithelium.

When placed onto fibronectin strips and chemically confined by the sides, cells adopt various migration modes depending on the width (*i.e.* the strength of the confinement) of the band (see Figure 2.24a) (Vedula et al., 2012). At low confinement, the migration front is slow and cells inside the migrating epithelium have no preferential orientation: polarity and orientation of stress fibres are not aligned (Vedula et al., 2012). Some vortices, swirling motions are also present.

However, at high confinements, cells exhibit larger velocities all across the epithelium (not only at the leading edge) as well as oriented stress fibres along the strip, a cell polarity and stretch parallel to the axis, and velocity vectors mostly aligned towards the same direction of migration (Vedula et al., 2012). The disappearance of swirling is also reported, suggesting a proper rectification along the axis of migration.

Confined on 2D fibronectin disks, epithelia exhibit the very same swirling motions together with large cellular flows until a specific diameter. Below this diameter, the size of the system is comparable to the "natural" coherence length of the cells and the cellular disk starts to rotate coherently in one direction (Deforet et al., 2014; Doxzen et al., 2013).

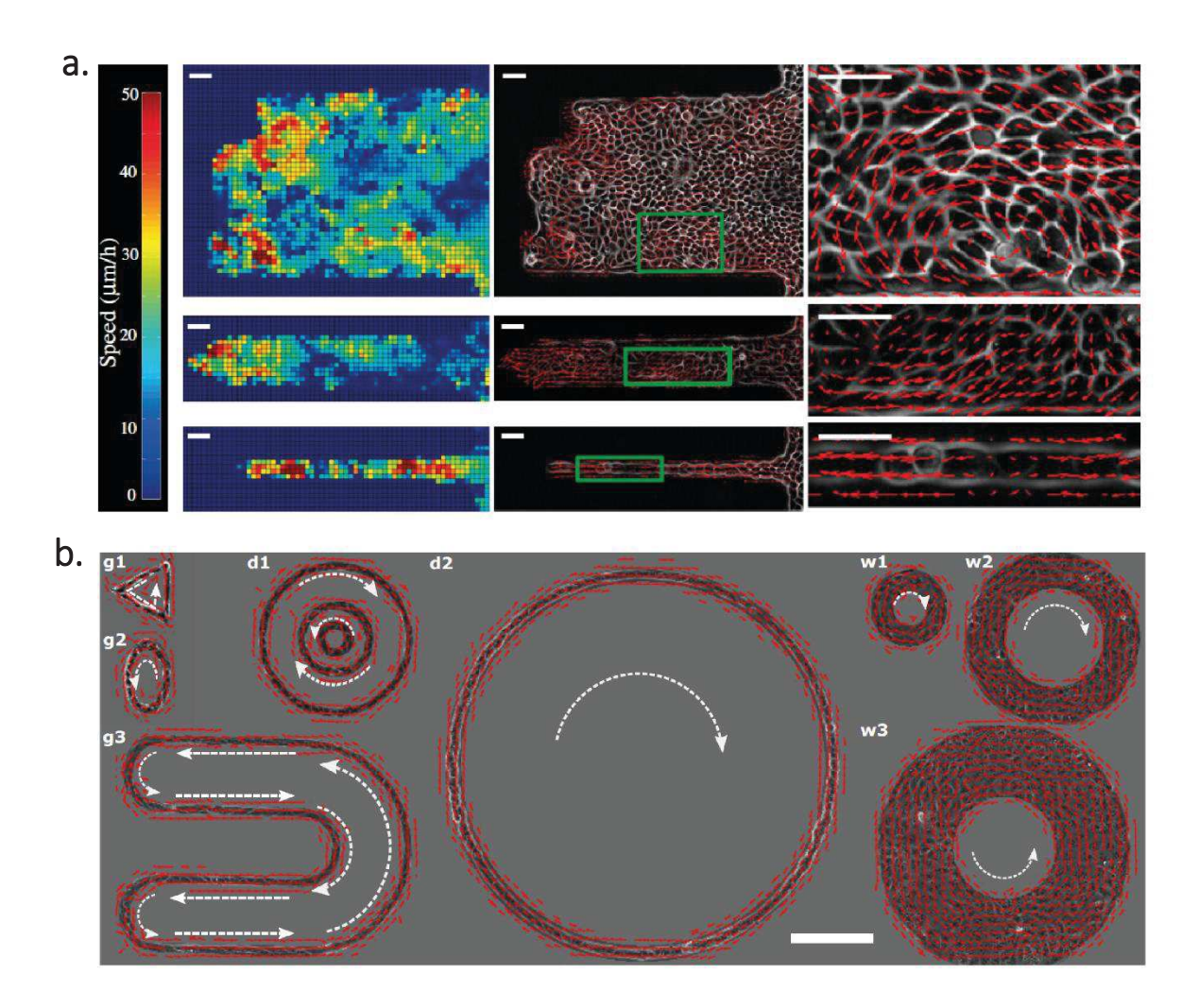


Figure 2.24. Confinement rectifies collective motion in 2D. (a) Velocity fields in migrating epithelia confined on a fibronectin strip. High fluctuations and large vortices are visible on the less confined epithelium while alignment of velocity vectors is prominent in high confinement although collective relaxations (as shown in the panel) can occur, suggesting a caterpillar-like behavior in this type of directed motion. Scale bars = 50μ m. From (Vedula et al., 2012). (b) Epithelial cells confined on large circular and triangular patterns. Cells acquire spontaneous rotation on every motif, independently of the "natural" coherence length of the system, as highlighted by the velocity fields overlaid on phase contrast images. Scale bar = 200μ m. From (Doxzen et al., 2013).

Similarly, when totally constrained over a ring-shaped pattern of a width corresponding to a cell size, epithelial cells exhibit spontaneous rotations (see Figure 2.24b) (Jain et al., 2020). However, this phenomenon in 1D appears on every sizes: extremely large rings (1mm in diameter) exhibit rotations even though their dimension is much larger than the "natural" coherence length of the cellular system used in the study suggesting that strong confinement (2D to 1D) can rectify motion over very large scales also confirming previous theoretical works (Soumya et al., 2015).

In this work, the authors showed a linear relationship between the size of the ring and the time corresponding to the onset of rotation, in agreement with the predictions from Soumya *et al* (Soumya et al., 2015). It has been shown that this trigger to coherence is critically governed by the integrity of the cadherin junctions: disruption by siRNA or with drugs lead to an abolition of rotational motion.

Altogether, we showed here that collective cell migration can be as well tuned and directed by simple boundary effects: strong confinements orient cell polarities, align stress fibres assembly and induce cellular flows in preferential directions.

More generally, this section 2.6 highlighted two major ways of directing cellular motion at the single or at the collective scale:

- (i) By biasing the chemical composition of the cellular micro-environment. This chemotactic effect is transduced by the cells and leads to the cell polarisation in the direction of the gradient slope.
- (ii) By breaking spatial symmetry locally or by boundary effects. Restricting anchoring zones and imposing cellular shape lead to biased cell motion.

2.8 PhD question

Throughout the introduction, we saw the necessity for living matter to break its symmetry in order to produce robust and significant motion. Intrinsically out-of-equilibrium, changes in shape, cytoskeleton, and coordination of molecular actors require consumption of energy.

What is evenly important that symmetry breaking is the maintenance, over space and time, of the emerging anisotropy: spontaneous symmetry breaking with low persistence leads, on average, to no displacement. This framework is well recapitulated by the Persistent Random Walk model. Therefore, external cues reinforcing the initial broken symmetry are expected to play a major role in directed motions. In a nutshell, polarity and memory of the generated polarity are essential.

We saw that these external cues, such as geometrical constraints governed by the cellular micro-environment, or chemical gradients can bias and rectify motion on large timescales. These motions are driven by components of the acto-myosin cytoskeleton and tightly regulated by the coordination of the small Rho GTPases.

Because collective motion is an emergent property of living matter, multicellular systems may not be considered as a sum of individual cells. Interactions between cells through adherens junctions, transduction and propagation of the substrate properties, changes in density and many other mechanisms contribute to the differences of dynamics observed between single cell and multiple cells. Considering this aspect, single cell directed motion and collective coherent

migrations, even though they share similarities, need to be studied separately, taking into account their own specificities.

Active gels recapitulate often the phenomena observed during experiment. However, myosin is assumed to be always active and experimental description of the active term $\zeta\Delta\mu$ is still lacking. Nevertheless, activity of upstream pathways such as RhoA is not sufficient to predict cellular behaviour since GTPases activity correlates with the emergence of subcellular structures but stresses cannot be derived from this feature only. Therefore, integration of both approaches needs to be done: active gels with regulation of myosin activity by the Rho GTPases. This could shed light on new behaviours.

In this PhD work, we extracted general rules leading to symmetry breaking and directionality in single and multiple cells systems. In chapter 4, we deciphered the mechanisms governing the rectification of single cell motion with local asymmetries – namely *ratchetaxis* (Caballero et al., 2015b) – and extract general features and theoretical models in order to understand and predict rectification in different micro-environments; we then tested in Chapter 5 if this paradigm of local asymmetries could be applied in 3D micro-environments mimicking *in vivo* confinement. In Chapter 6, we tried to understand how coherence in epithelia – a spontaneous symmetry breaking followed by a coordinated motion of the whole cell population – is set. Finally, we also show in Chapter 7 some preliminary results investigating emergence of coherent motion in 3D spheroids.

Altogether, the present work aims to provide general rules to understand and predict some symmetry breaking events happening *in vitro* and *in vivo* and how this broken symmetry can be sustained over time and space.

3. MATERIAL AND METHODS

In this chapter, we provide details relative to the protocols used in this PhD work. We will first introduce micro-fabrication and micro-printing – how to produce micrometre structures – then, the different types of cells cultured together with the generation of new cell lines. Preparation of samples and experiments will be detailed, followed by protocols of immunostaining. Finally, optical set-ups, imaging modalities, and image treatment/analysis will be described.

3.1 Micro-fabrication

Micrometer scale structures used to micro-print protein patterns or micro-fluidics chambers can be produced through a series of steps called *photolithography* (Le Maout et al., 2018; Théry and Piel, 2019). In this section, we will provide the detailed production pipeline.

3.1.1 Photomask

Photolithography is a process based on the emission of UVs through a layer of designed geometrical motifs called *photomask*. The photomask is an acetate sheet or a chromium one where the desired patterns are printed. This process can be done on various softwares such as AutoCAD or Clewin. Plastic masks are usually preferred for casual applications (> 10 μ m) while chromium masks offer a higher precision during UV exposure, reducing scattering of light, therefore leading to smaller structures (< 10 μ m).

3.1.2 Photolithography

This is the core process of micro-fabrication. The structures presented in the next sections are replica of a mould produced with photolithography. Briefly, we use silicon wafers on which an appropriate UV-polymerizable resin (SU-8) is spin-coated. Thickness of the SU-8 layer is chosen according to the size of the patterns in order to keep a proper aspect ratio (typically $l/h \ge 0.2$ and d < 20h). Then, the resin is exposed to UVs through the photomask previously described creating an illumination pattern and therefore controlling the cross-linked areas. After UV treatment, the non-polymerized SU-8 is washed out with acetone-based solvents, a step called "development", so that only the target patterns remain on the mould.

Here is the detailed protocol (see Figure 3.1):

- i) Silicon wafers are washed with acetone and isopropanol, dried with nitrogen gas, and heated up to 95°C during 1h to increase adhesion of the resin on the substrate.
- ii) SU-8 photoresist is spin-coated on the silicon wafer. Spin velocity depends on the height of the target patterns as indicated by the Table 3.1.
- iii) The resin is "pre-baked" at 65°C and 95°C during 1min and 3min, respectively.
- iv) Pre-baked SU-8, overlaid with the photomask, is exposed into a mask-aligner. Exposure time (and therefore deposited energy) depends on the thickness of the

resin (as shown by Table 3.1), in order to allow proper penetration and cross-linking all throughout SU-8. However, a too high exposure might be deleterious for the resin and some non-desired areas might be polymerized because of scattering. Also, a perfect contact between the mask and the resin needs to be ensured in order to prevent light scattering leading to ill-shaped patterns. The presence of visible interferences fringes can be a good read-out for a proper contact.

- v) Exposed resin is then "post-baked" at 65°C and 95°C during 1min and 3min, respectively.
- vi) At this stage, patterns are already slightly visible on the wafer. Polymerized and baked resin is now "developed" with an acetone-based solvent in order to wash out the non-crosslinked SU-8. Developing times depends on the patterns dimensions. Back and forth between the developing bath and the microscope are advised in order to see if there is no remaining non-polymerized resin on the wafer. Isopropanol is used to wash and inhibit developing solutions. A too long developing might be deleterious for the patterns. This step, with exposure, is critical.
- vii) The developed resin is then "hard-baked" at 200°C during 1h30. This step, though optional, leads to a slight dilatation of the resin, therefore removing microscopic cracks and improving patterns sharpness.
- viii) SU-8 moulds called *masters* are ready. They are stored in Petri dishes and can be used repeatedly.

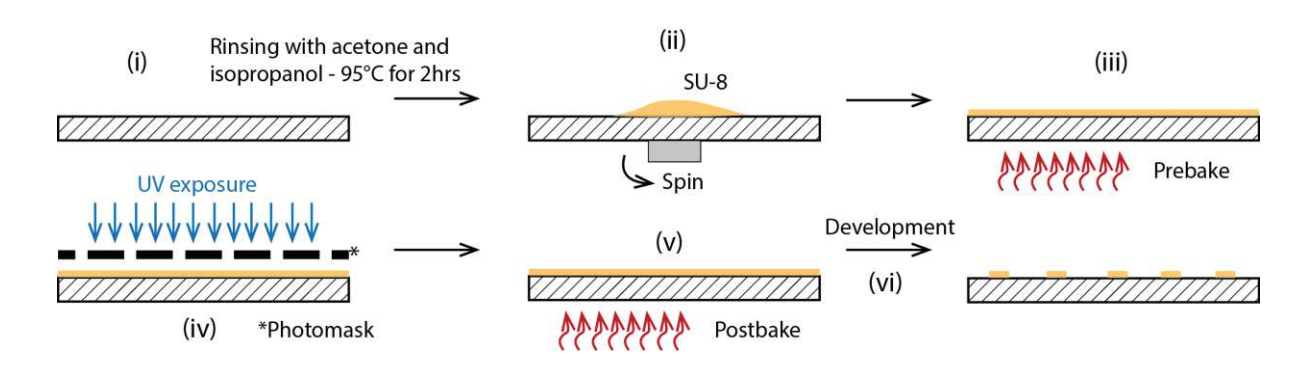


Figure 3.1 Main steps of microfabrication process. Details of all the steps are listed in 3.1.2.

Photoresist	Thickness (μm)	Spin- coating (rpm)	Prebake times 65°C/95°C (min)	Exposure energy (mJ/cm²)	Postbake times 65°C/95°C (min)
SU-8 2025	50	1700	2.5/7	160	1/4
SU-8 2025	40	2100	2/5	160	1/3
SU-8 2025	30	2800	1/3	152	1/3
SU-8 2015	30	1500	1.5/4	152	1/3
SU-8 2015	20	2200	1/3	145	1/2
SU-8 2015	15	3000	1/2	140	1/2

Table 3.1 Parameters used for microfabrication.

3.1.3 Soft lithography

Micro-structures used for microfluidics or micro-printing are replica extracted from the masters produced through photolithography. Poly(dimethylsiloxane) (PDMS), a silicone-like polymer, is poured on the masters, baked and polymerized at 65°C for at least 4h. After complete polymerization, blocks of PDMS containing the micro-structures can be removed from the masters and used for experiments. While masters can be used repeatedly, PDMS stamps and microfluidics chambers are single usage only.

Stiffness of PDMS can be tuned by changing the ratio crosslinker:polymer especially for traction-force microscopy experiments or any other experiments where the Young modulus needs to be tightly controlled. Standard usage recommends a ratio 1:9 (Théry and Piel, 2019).

3.2 Micro-printing

3.2.1 Patterns production

The protocol of micro-printing allows to produce micrometer scale patterns of a given protein on various substrates. Briefly, a PDMS stamp is inked with protein and placed, after surface treatments, on a substrate. Transfer of the protein leads to the production of patterns. Here, we provide the detailed procedure to print fibronectin on glass surfaces (see Figure 3.2).

- i) Glass coverslips are treated 10min with "Piranha" solution (hydrogen peroxide:sulfuric acid in a proportion 3:7). This step ensures a proper cleaning of the slides and makes the glass surfaces hydrophilic. Coverslips are rinsed with milli-Q water and sonicated 5min each to remove traces of acid which might be deleterious for cells viability. They are stored at 65°C during 10min.
- ii) Treated slides are put together with 100µL of (3-Mercaptopropyl)trimethoxysilane in a desiccator. Vacuum is generated and kept with a pump during 5min in order to

- disperse silane in the desiccator atmosphere. After 5min, the pump is turned off and the vacuum is kept during 1h. The silane will slowly deposit on the glass coverslips.
- iii) Functionalized slides are put (at least) 2h in the oven at 65°C. This important step leads to the destruction of the extra, non-reacting, silane molecules which are toxic for cells.
- iv) While coverslips are incubated in the oven, PDMS stamps, prepared with microfabrication, are surface-treated: they are washed and sonicated in ethanol 70% during 5min and dried 5min at 65°C. Then they are rendered hydrophilic with an oxygen plasma treatment (20s at 0.3mbar).
- v) After plasma activation, PDMS stamps are incubated with a 100μL drop of a 10μg/mL fibronectin solution during 45min.
- vi) After incubation, the fibronectin drop is removed with a 200µL pipette and the stamp is washed with PBS and dried at room temperature for 5min. This step is critical: a too dried stamp will not give any patterns (fibronectin will not be transferred) while a too wet stamp usually leads to spread, non-usable, patterns. Even though 5min is usually suitable, drying time depends on motifs geometry (especially spacing between motifs) and might also depends on humidity and temperature: a controlled atmosphere is then advised.
- vii) The stamp is placed face down on the functionalized coverslip and the set-up is kept in this configuration during 30min with 50g weight on top to ensure a proper transfer between the stamp and the glass substrate.
- viii) After transfer, the stamp is carefully removed with tweezers from the coverslip and the glass slide is directly immersed in milli-Q water to prevent drying. At this step, the patterned slide can be stored at 4°C and be used after 1 week.

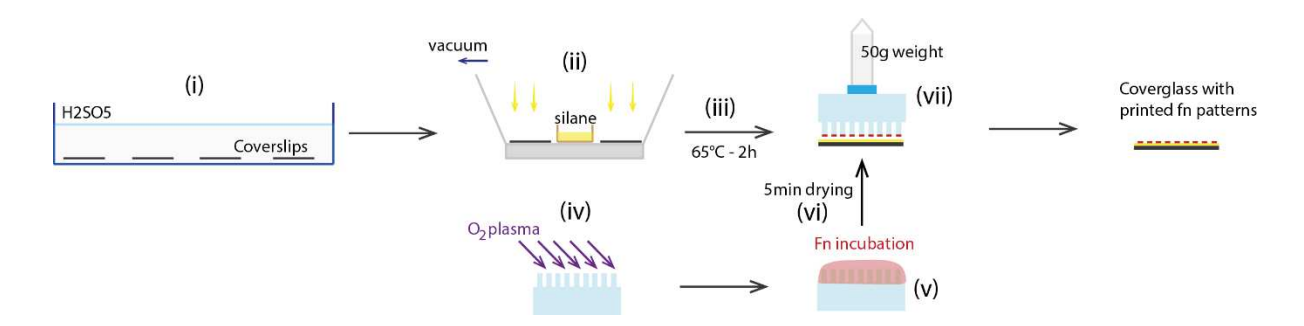


Figure 3.2 Protocol of microcontact printing. Steps are detailed in section 3.2.1.

3.2.2 Passivation

Before each experiment, the non-printed area is passivated with Poly-L-Lysine-graft-poly(ethylene glycol) (PLL-g-PEG), a brushed polymer that prevents sustained adhesions on the surface. This is done in order to have proper cellular patterns with cells seeding only on the motifs before wash-out.

The patterned coverslip is incubated, face down, on a drop of 100µL of 0.1mg/mL PLL-g-PEG

during 25min. Then, the glass coverslip is transferred to cell culture hood and rinsed 3 times with medium before usage.

3.3 Cell culture

All the following steps are performed under a sterile hood.

3.3.1 Mesenchymal cells

NIH 3T3

In routine, NIH3T3 mouse fibroblasts are cultured in high glucose Dulbecco's Modified Eagle's Medium (DMEM) supplemented with 10% Bovine Calf Serum (BCS) and 1% Penicillin-Streptomycin. For splitting, cells were detached from the Petri dish with Trypsin-0.25% EDTA incubation (3min), centrifuged at 500rpm during 3min and re-suspended in DMEM 10% BCS. Cells are kept at ~60% confluency in order to avoid any contact inhibition that would decrease cell motility during experiment.

HL60

HL-60 are neutrophil-like cells. They are grown in suspension in RPMI 1640 supplemented with $40\mu g/mL$ Gentamycin and 10% Fetal Bovine Serum (FBS).

3.3.2 Epithelial cells

MDCK II

Madin-Darby Canine Kidney (MDCK) cells are epithelial dog kidney cells widely used as a model system for collective motions. Cells are cultured in low glucose DMEM supplemented with 10% Foetal Bovine Serum (FBS). At 60-70% of confluency, cells are detached from Petri dishes with Trypsin-0.25% EDTA incubation (10min, cells are strongly adherent), centrifuged at 500rpm during 3min, and re-suspended in DMEM 10% FBS. Additional antibiotics may be added to the culture medium depending on the type of construct expressed by the cell as shown in table 3.2.

CAL27

CAL27 are epithelial cells extracted from squamous oral carcinoma. Cells were cultured in DMEM low glucose supplemented with 10% FBS and 1% Penicillin-Streptomycin. Detachment and splitting are achieved with the protocol used for MDCK cells described in part 1.3.2. Antibiotics treatment with G418 is added to the normal culture conditions for CAL27 K14-GFP and CAL27 V7-GFP (Table 3.2).

Cell line	Antibiotics	Concentration	
MDCK E-cadherin-DsRED	Geneticin (G418)	0.4 mg/mL	
MDCK RhoA-BS/E-	Hygromycin	0.2 mg/mL	
cadherin-DsRED			
MDCK RhoA-dBS/E-	Hygromycin	0.2 mg/mL	
cadherin-DsRED			
NIH 3T3 VASP-GFP	Puromycin	1μg/mL	
CAL27 V7-GFP	Geneticin (G418)	700μg/mL	
CAL27 K14-GFP	Geneticin (G418)	700μg/mL	

Table 3.2 Antibiotics and their concentration for the different cell lines used in this work.

3.3.3 Generation of MDCK spheroids

Cells are trypsinized and dissociated by harsh pipetting. They are diluted in 40µL of DMEM 10% FBS at a concentration of 3.10⁵ cells/mL. This solution is then mixed with 20µL of fresh Matrigel for a total volume of 60µL and a 1:3 ratio. The 60µL droplet of cells + Matrigel is then deposited on an autoclaved coverglass and incubated at 37°C for 30min. After incubation and polymerization of the gel, the coverglass is immersed in 2mL of DMEM + 10% FBS and can be stored many days. Medium is replaced every 2 days.

3.3.4 Transfections

Transient expression of fluorescently labelled proteins is essential for many experiments in order to visualise spatio-temporal dynamics and distributions of the protein of interest. When completed with an antibiotic resistance, cells can be selected by an antibiotic selective pressure.

In order to incorporate DNA plasmids into cells, positively charged liposomes are formed with a reagent called Lipofectamine. These liposomes containing DNA plasmids then fuse with the negatively charged plasma membrane of cells (Dalby et al., 2004). In this section, we will detail the standard transfection protocol we used for transfection of plasmids inside cells.

- (i) Cells are detached with trypsin treatment and split into a 6-wells plate 1-day prior transfection in order to reach 50% confluency the next day.
- (ii) For each well, 140μL of Opti-MEM and 10μL of Lipofectamine are mixed together in a 200μL Eppendorf.
- (iii) 149 μ L of Opti-MEM with 1 μ L of DNA (at a concentration of 1 μ g/ μ L) are mixed together in another 200 μ L Eppendorf.
- (iv) DNA mix is then poured into the Lipofectamine one.
- (v) The DNA-lipofectamine solution is kept at room temperature, under the hood, during 10min.
- (vi) Meanwhile, 10% serum medium is removed from the wells and replaced by 1% serum DMEM. This reduces toxicity from the lipofectamine.

- (vii) The mix DNA-lipofectamine is transferred into the wells and the plate is stored in the incubator at 37°C/5%CO2 during 4h-6h.
- (viii) After incubation, medium is removed, cells are washed with fresh 10% serum DMEM and stored in the incubator until the experiment day (usually the day after).

In our experiments, we used $10\mu L$ of lipofectamine and $1\mu g$ of DNA for a single well. This quantity is adjustable depending on the construct needed to be transfected. High toxicity can be balanced by reducing lipofectamine and/or DNA quantity. This will also cause a decrease in transfection efficiency.

3.3.5 Generation of new stable cell lines

Design of new cell lines was necessary in order to probe RhoA activity or FAs dynamics. In another context, introduction of a fusion protein found in oral squamous cancer allowed to identify its implication in cell motility.

3.3.5.1 MDCK RhoA-BS/E-cadherin-DsRED and MDCK RhoA - dBS/E-cadherin-DsRED

The RhoA biosensor (RhoA-BS) used in experiments is a FRET (Fluorescence Resonance Energy Transfer) based biosensor. Its design is shown in Figure 3.3, detailed in (Hodgson et al., 2010; Pertz et al., 2006) and its usage is described in section 3.6.3.1.

The biosensor plasmid contains an antibiotic resistance to Hygromycin B and its genetic insertion is driven by a Piggy-Bac (PB) transposon system. PB is a genetic engineering tool that allows the insertion of sequences into the cell genome. This process is made possible through the addition of a transposase together with the plasmid: the transposase cuts the transposons loci in the cell genome and the DNA repair machinery inserts the sequence from the plasmid instead. Although efficient for producing new stable cell lines, this protocol provides random insertions with a random number of copies.

MDCK II E-cadherin-DsRED, kindly provided by Dr. Sylvie Coscoy, are transfected with $10\mu L$ of lipofectamine and $1\mu g$ of DNA (0.5 μg of transposase + 0.5 μg of plasmid) with the protocol detailed in the section 1.3.5.

48h after transfection, sequences are inserted into the cell genome. Therefore, cells are selected with $200\mu g/ml$ of Hygromycin B for 1 week. After a week, cells are sorted with flow cytometry in order to remove both extremely high and low fluorescent cells. A subcloning step is then performed with selection of individual clones under the microscope. The individual clone is amplified, and the resulting cell line is used for experiments.

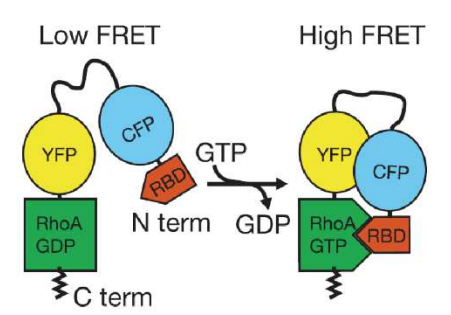


Figure 3.3 FRET biosensor. The CFP-YFP pair (more specifically mTFP1-Venus) acts as donor and acceptor, respectively. Upon activation, the molecule folds with binding to the Rho-Binding-Domain (RBD) and the fluorescence is transferred from the donor (mTFP1) to the acceptor (Venus). From (Pertz et al., 2006).

The very same protocol is applied for the generation of the MDCK RhoA -dBS/E-cadherin-DsRED cell line. The transfected construct is a "dead" biosensor (dBS). This biosensor is unable to interact with the RBD domain leading to no folding and no FRET. This provides a control condition to the WT biosensor (Pertz et al., 2006).

3.3.5.2 NIH 3T3 VASP-GFP

The VASP-GFP vector was kindly provided by Dr. Olivier Pertz (Institute of Cell Biology, Bern University, Switzerland). The construct is then expressed in lentivirus derived from pLenti CMV MVS. The viruses were added to a culture of wild-type NIH3T3 and cells were selected after 24h with 2 μ g/mL of puromycin.

3.3.5.3 CAL27 K14-GFP and V7-GFP

Gene segments of wild type keratin 14 (K14) and the fusion variant 7 were amplified from oral cancer cells by nested PCR and sub-cloned into pAcGFP1-N1 vector described in (Tsai et al., 2019). Because the main backbone of V7 is K14, K14 was utilized as the wild type control. The vector constructs were further transfected into CAL27 oral squamous cell line, purchased from the Bioresource Collection and Research Center (BCRC, Taiwan). The positive clones were enriched by cell sorting and maintained by G418 selection (700 µg/ml).

3.4 Preparation of samples and experiments

3.4.1 On micro-patterns

Prior experiments, cells are always kept at $\sim 50\%$ confluency in order to avoid any impairment of motility by contact inhibition (Abercrombie and Heaysman, 1953).

Cells are trypsinized and centrifuged at 500rpm during 3min. They are then diluted in DMEM 1% in appropriate dilutions: (i) for 2D *ratchetaxis* assays, NIH 3T3 are diluted in a low

concentration of 2000 cells/mL while (ii) MDCK on micro-patterned rings are diluted in very high concentration at 10⁶ cells/mL. 1mL of the cell dilution is then deposited on the patterned coverslip.

After 30min of incubation at 37°C for fibroblasts and 1h for MDCK, cells seeded on the non-adhesive regions are washed out with fresh medium. DMEM is removed and Leibovitz medium (L-15) is added to the sample. L-15 contains a CO₂ buffer that sustains a proper physiological pH during experiments without the need of any external CO₂ control and no effect on cell dynamics.

3.4.2 Inside micro-channels

This protocol has been designed and troubleshooted by Emilie Le Maout during her PhD work.

Open micro-channels are simply the PDMS blocks extracted from the master directly, facing up (see Figure 3.4 left). The completely closed configuration is the PDMS block facing down and plasma-bound on the glass coverslip (see Figure 3.4 right): micro-channels are activated together with the glass coverslip with O₂ plasma treatment during 30sec at 0.3mbar (the motifs facing up in the plasma chamber). Then, the PDMS block is bound to the glass slide by putting in contact the two activated sides. Finally, the complete micro-channels chamber is incubated overnight at 65°C in order to ensure a proper binding and prevent any leakage during experiments.

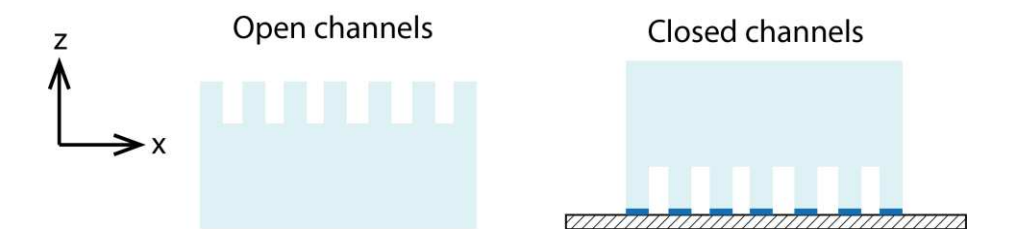


Figure 3.4 Micro-channels configurations.

NIH 3T3 and CAL27 were detached using Trypsin-0.25% EDTA, centrifuged 3min at 500rpm and re-suspended in L-15 with the appropriate concentrations: for the open-channels configuration, $100\mu L$ of a solution of 100,000 cells/mL is deposited on the PDMS motifs; for the closed-channels, a solution of 30,000,000 cells/mL is prepared and $20\mu L$ is injected in the chip reservoirs.

3.4.3 Gradient formation

This protocol has been designed and troubleshooted by Emilie Le Maout during her PhD work.

The PDMS chip is bound to the coverslip as described in the section 3.4.2 for closed microchannels (see Figure 3.5a).

Serum gradients for chemotaxis experiments are produced inside closed micro-channels (see Figure 3.5b). After binding of the chip and seeding of cells inside, the gradient is formed as follows:

- (i) Two 1 mL syringes filled with L-15 0.1% serum and L-15 10% serum are connected to flexible polymer tubing (Tygon). Tubes are cleaned with ethanol and then sterile L-15 before usage. Additional TRITC-dextran is mixed with the 10% serum solution. This will enable proper visualisation of the gradient.
- (ii) Tubing is connected to the two inlets of the microfluidics chip. Make sure that there is no bubble inside the tubes, this might cause irregularities in flows and detachment of cells in contact with air.
- (iii) The two solutions are then flowed with a rate of 10μ L/h inside the chip. A stable serum gradient will be formed after a couple of minutes.
- (iv) The gradient is visualised, and its slope can be quantified with the acquisition of the fluorescent signal.

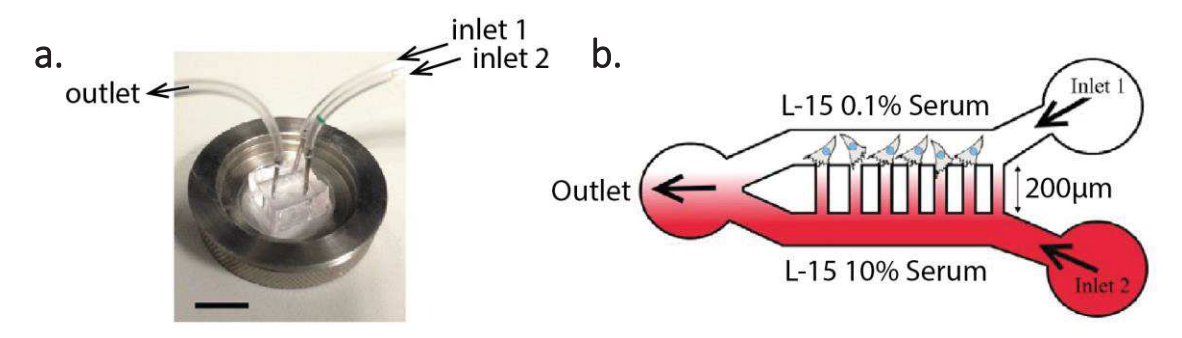


Figure 3.5. Generation of chemical gradients with microfluidics. (a) Experimental set-up. The microfluidic chip is connected to syringes through two inlets. (b) Scheme of the microfluidic chip with the formation of a serum gradient. Adapted from (Le Maout et al., 2018).

3.4.4 Hydrogels preparation

3.4.4.1 Agarose and Phytagel

Agarose, Agarose LMP and Phytagel powders are mixed with PBS 1X at the appropriate concentration (0.5% or 1%). The solution is then heated with a microwave oven until the powder is totally dissolved.

3.4.4.2 Alginate

Alginate polymerizes by addition of calcium ions in the solution. Therefore, alginate is dissolved in fresh Milli-Q water at the appropriate concentration (1% to 3%). To do so, the water is under constant agitation through magnetic steering and the powder is gently added to the water. The solution is steered until the complete disappearance of alginate clumps. The solution was filtered through a $0.2\mu m$ filter. Then, liquid alginate is desiccated to remove the air bubbles produced by the steering.

For microfluidics experiments, alginate is mixed with TRITC-dextran (0.5%) in order to visualize it under a microscope.

3.4.5 Oleic acid preparation

Dissolution of calcium into oleic acid has been done according to the protocol detailed in (Kim et al., 2009, 2011). 210mg of calcium chloride was dissolved in 5mL of 2-methyl-1-propanol by 3 cycles of 5min sonications. Then, the methyl propanol containing dissolved calcium chloride is mixed with oleic acid (50% v/v). In order to remove the solvent (2-methyl-1-propanol), the oleic acid solution is distilled overnight at 120° C. Finally, oleic acid containing calcium is filtered with a $0.2\mu m$ filter to remove any remaining debris. This solution can be stored at -20° C for further experiments.

3.5 Immunofluorescence

Immunofluorescence is the procedure by which proteins of the cell can be marked by specific antibodies in order to visualise them under a microscope. The protocol is divided into two steps. First, cells need to be fixed with fixating agents such as paraformaldehyde and then permeabilized with surfactants to enable penetration through the lipid bilayer of specific antibodies. Then comes the immunostaining *per se*: permeabilized cells are incubated with primary and secondary fluorescently labelled antibodies. We described here the full procedure:

Note: prior immunofluorescence, cells are seeded on a glass coverslip.

- (i) Medium is removed and cells are incubated during 10min with a solution of 4% paraformaldehyde-PBS.
- (ii) After fixation, cells are washed 3 times with PBS.

At this step, samples can be stored up to several weeks in PBS at 4°C.

- (iii) Triton 0.5X is added for 3min to permeabilize the lipid bilayer.
- (iv) Cells are washed 3 times with PBS.
- (v) A mix of 5% BSA-PBS is added to treated cells for 45min. Bovine Serum Albumin (BSA) will ensure a proper passivation to prevent non-specific binding of antibodies.
- (vi) Primary antibody is diluted in an appropriate concentration as shown by Table 3.3 in BSA-PBS.
- (vii) A piece of Parafilm is put on the bench and a 100μL drop of the primary antibody solution is deposited on it. The glass coverslip is then carefully flipped face down on the antibody drop and kept incubating at room temperature during 1h30.
- (viii) The glass coverslip is washed 3 times with PBS.
- (ix) The sample is incubated with secondary antibody (fluorescently labelled) with the same procedure detailed in (vii) and with concentrations given by Table 3.3.

(x) After a final washout with PBS, the glass coverslip is mounted on a microscope slide with a 10µL drop of PBS-glycerol solution (50%) and sealed with nail polish in order to prevent evaporation or leakage. At this stage and with good care (low light exposure) the slides can be stored at 4°C up to several months/years.

Compound	Target	Concentration
Phalloidin	Actin	1:200
Cy3 Anti-Mouse	Secondary antibody against mouse primary antibody	1:500
Mouse anti-paxillin	Paxillin	1:50
DAPI	Nucleus	1 μg/μL
Mouse anti phospho-myosin	Phosphorylated Myosin	1:100

Table 3.3 Chemicals used for immunostaining with corresponding targets and concentrations.

3.6 Microscopy

3.6.1 Standard time-lapse microscopy

Live observation of moving cells is usually done with an epifluorescence microscope. We used inverted Olympus CKX41 mounted on an optical breadboard and enclosed within a temperature-controlled box regulated at 37°C.

All the microscopes were used with phase contrast in order to get better images and cell contours. Therefore, phase rings need to be properly aligned and matching the corresponding objectives.

Fluorescence was provided either by a collimated optical fibre (Xcite device, mercury lamp) or directly from the source, carefully aligned between experiments (mercury arc lamp).

To prevent phototoxicity, two shutters are mounted on the optical path to control exposition with fluorescence or phase contrast. Images are acquired with a CCD Hamamatsu camera (C4742-95; pixel size: 6.45µm) synchronized with shutters opening. Control of the devices is done through custom scripts made on Micro-Manager.

Different objectives are used depending on the size of the desired feature to analyse. The numerical aperture (NA) sets the rules giving the resolution that can be achieved with a specific objective. In this work, we used 4x (Olympus, NA = 0.13), 10x (Olympus, NA = 0.25), 20x (Olympus, NA = 0.4), 40x air (Olympus, NA = 0.55), 40x oil (Olympus, NA = 0.9), and 60x oil (Olympus, NA = 1.45). Typically, 4x and 10x are used for single cell migration assays where large tracks need to be analysed as well as for large-scale collective motions. 40x and 60x objectives with high NA are used to image precise subcellular features such as focal adhesions or actin/myosin localization.

During long-term acquisition, proper humidification is ensured by beakers filled with water

inside the temperature-controlled box and evaporation is prevented by putting a clean Petri lid on the sample.

3.6.2 Reflection Interference Contrast Microscopy (RICM)

Reflection Interference Contrast Microscopy (RICM) is an interferometry technique that discriminates densities in regions in the close vicinity of the substrate. Therefore, it enables imaging of subcellular structures without the need of fluorescent labelling. This technique has been successfully used to image focal adhesions and organelles.

We did RICM with a custom-made modification of the previously described optical set-up (epifluorescence Olympus CKX41). We follow the protocol described by Curtis *et al* presented in Figure 3.6 (Curtis, 1964): we removed one filter set and used instead a 50% dichroic combined with a homogeneous white light source (arc mercury lamp). This gave interferences images from the surface in the absence of a polarizer.

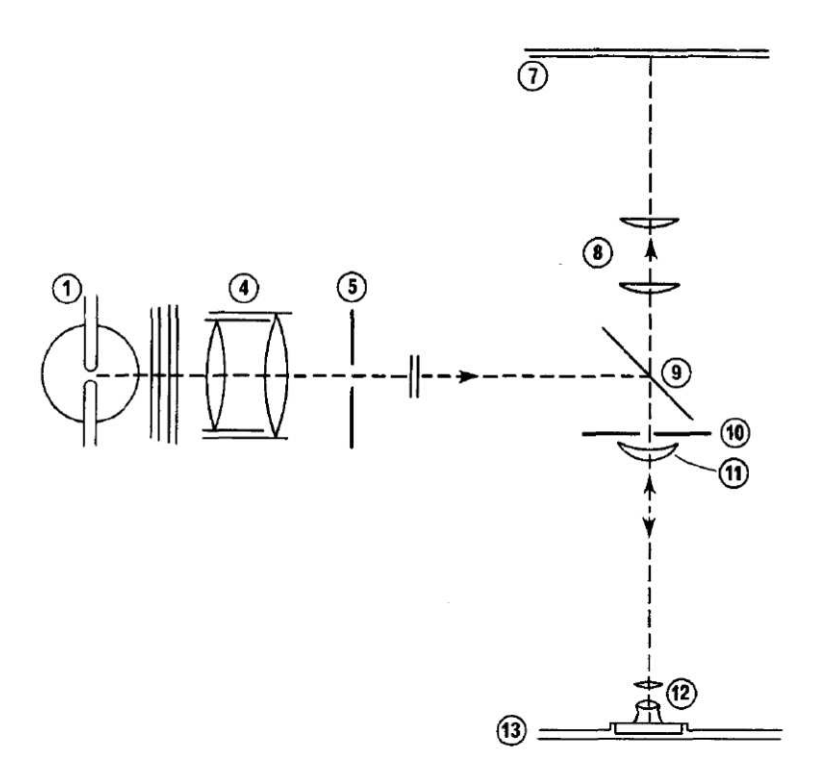


Figure 3.6 Montage used to perform RICM, as described in (Curtis, 1964). 1: mercury arc lamp; 4: collimating lens; 5: field iris; 7: photographic plate; 8: projection eyepiece; 9: half silvered mirror (50% dichroic); 10: aperture iris; 11: auxiliary lens; 12: objective (immersion); 13: slide with hanging drop culture. From (Curtis, 1964).

3.6.3 Confocal microscopy

Two confocal microscopes were used in this work, the Leica SP5-MP and the Leica SP8-MP, depending on the required utilization. SP8 was essentially used to image fluorescent stainings

and to acquire FRET images while SP5 was mainly used to perform laser ablation on actomyosin structures.

3.6.3.1 FRET acquisition

FRET is a way to quantify the proximity between two different fluorophores. A donor fluorophore, upon excitation, may transfer by non-radiative transfer a fraction of its energy to an acceptor fluorophore. The energy transfer efficiency is sensitive to the distance between the two fluorophores and proportional to $\frac{1}{R^6}$. Therefore, if the two molecules are closed enough, excitation of the donor fluorophore leads to the fluorescence emission of the acceptor.

In this work, we used a FRET biosensor quantifying RhoA activity. The biosensor has been designed by Pertz et al. ((Pertz et al., 2006) and Figure 3.3) and is constituted of the wild-type RhoA protein modified with the addition of two fluorophores: mTFP1 (CFP-analogue, donor) and Venus (YFP-analogue, acceptor). Upon activation, RhoA is translocated to the membrane and the interaction with the Rho-Binding-Domain (RBD) folds the protein. This conformational change increases the proximity between the CFP-YFP pair and leads to FRET between the donor (mTFP1) and the acceptor (Venus).

FRET measurements need many control steps in order to give robust read-out and the acquisition needs to follow some rules. We list here the procedure used the present PhD work with the SP-8 Leica inverted confocal microscope:

- (i) To increase section thickness and reduce noises in FRET signals, the pinhole needs to be open at the maximum.
- (ii) Quantification of the dark current noise is done before any acquisition. To do so, an average image is generated from 10 snapshots taken with the camera shutter closed. This characterization step needs to be done only once since the dark current is a property of the detector.
- (iii) Acquisition is done using two detectors at the same time. Therefore, detectors need to be aligned so there is no shift between the donor image and the FRET signal.
- (iv) The same gain should be used for all experiments and with values which are within the linear regime of the gain.
- (v) Because RhoA is mainly active at the membrane, the plane of acquisition was set according to the visualisation of cells lamellipodia.
- (vi) During acquisition, mTFP1 is excited at 458 nm and the simultaneous detection of the donor and acceptor is done through two Photo-Multiplier Tubes detectors (PMTs). The range for mTFP1 is set as 472-512nm and for Venus between 524nm and 544nm.
- (vii) After acquisition, an average image generated from 10 snapshots of a blank area (without any fluorescence) is taken with the same experiment parameters. This image will be used for illumination correction.

3.6.3.2 Laser ablation

Laser ablations made on acto-myosin were done with the Fluorescence Recovery After Photobleaching (FRAP) module of the Leica SP-5 inverted microscope. The sample was imaged and ablated through a 40x oil objective (NA = 1.25) and an 800nm infrared laser (80 MHz, pulsed). After laser characterization and tests, the following parameters were used for appropriate ablation:

- Offset = 62%
- Trans = 55%
- Gain = 100%

3.6.4 Spinning-disk

Spinning-disk microscopes are useful for fast imaging with high resolution and low phototoxicity. This was particularly useful to image focal adhesions dynamics with a high temporal resolution without bleaching and toxicity. The setup consists of an inverted Nikon microscope coupled with a spinning disk unit (Yokogawa CSU22). We used two lasers for acquisition: 488nm for GFP-like proteins and 560nm for mCherry derivatives. The Nikon Perfect Focus System (PFS) ensured a proper focus all throughout the experiments so that focal adhesions were acquired on the very same plane. Images were taken through a 63X oil objective (NA = 1.4) together with a temperature-controlled stage.

3.7 Image analysis

3.7.1 Focal adhesions and forces mapping

Images of NIH 3T3 expressing VASP-GFP are first thresholded in order to remove background signal from the cell cytoplasm. Then, binary images are analyzed through a custom-made Python script detailed in Appendix 10.6. Briefly, focal adhesions areas, orientations and barycenters of each focal adhesion are extracted and a force vector is associated in the direction of the focal adhesion and oriented centripetally (towards the cell center) as described in (Balaban et al., 2001; Riveline et al., 2001). Force amplitude is derived from the relationship found in (Balaban et al., 2001): each focal contact applies a force per unit area of 5.5nN.μm⁻². The full code is available in Appendix 10.6.

3.7.2 Trajectories

All trajectories analysed in the present work were generated using the Fiji plugins MTrack2 or Manual Tracking.

3.7.3 Particle Image Velocimetry (PIV)

Principles of PIV have been described in the introduction (section 2.5.1.2). We describe here the parameters used to run the algorithm.

We used PIVlab 1.4 to generate velocity fields. The interrogation window size d is selected according to the size of the features in the image. Therefore, we varied the window size from 32x32 to 64x64 with an appropriate displacement of the window equal to $\frac{d}{2}$.

We performed cross-correlation (CC) between interrogation windows of subsequent timepoints. CC led to better results in our experiments than the fast Fourier transform technique.

Before analysis, background is removed by the choice of appropriate ROI and masking. Then, we manually resliced the velocity histogram in order to remove all the artefactual velocity vectors (often coming from incorrect masking of the background).

3.7.4 Coherence length

Coherence length ξ was extracted from velocity fields with a custom-made Matlab code by computing the spatial correlation function of the tangential velocity v_{θ} as reported above in part 2.5.1.2:

$$C_{v_{\theta}}(\delta x, t) = \frac{\langle \overrightarrow{v_{\theta}} (\vec{x} + \delta \vec{x}, t) . \overrightarrow{v_{\theta}} (\vec{x}, t) \rangle}{\langle v_{\theta} (\vec{x}, t)^{2} \rangle}$$

Exponential decays are generated from the computations of $C_{\nu_{\theta}}$ and the intersections between the tangents at origin and x-axis give ξ . Because $C_{\nu_{\theta}}$ was not always converging to 0, we made linear fits on the 3 first points of $C_{\nu_{\theta}}$ in order to extract the tangent at origin.

For ξ_{max} , velocity fields were averaged over intervals of 10 frames and only the most coherent interval was taken.

3.7.5 FRET analysis

FRET images acquired with confocal microscopy (see section 3.6.3.1) were analysed with Biosensorpackage, a Matlab code provided by the Danuser lab (Vilela et al., 2014). Briefly, the analysis pipeline was done as follows:

- (i) Images are corrected for illumination inhomogeneities with the average blank image generated after acquisition (see section 3.6.3.1).
- (ii) Stacks are corrected for dark-current camera noise.
- (iii) Automatic threshold is done in order to extract signals only.
- (iv) Background is subtracted from images.

- (v) Generation of the ratiometric map: the donor signal is divided by the FRET one.
- (vi) Before analysis, a median filter (2 pixels width) is applied to smooth images.

Histograms of intensity values are manually resliced in order to remove very high and low outliers, resulting from artefactual ratios. Because they lead to virtual signal, nuclei are automatically thresholded using the machine-learning software Ilastik and removed from the ratio images.

Maps are analysed with a custom-made Matlab code discriminating the boundaries (actomyosin cables) from the cytoplasm.

3.7.6 Tissue Miner

Tissue Miner is a package from Jülicher Lab (Etournay et al., 2015, 2016). This allows to segment and extract single cell parameters for each time step (see Figure 3.7).

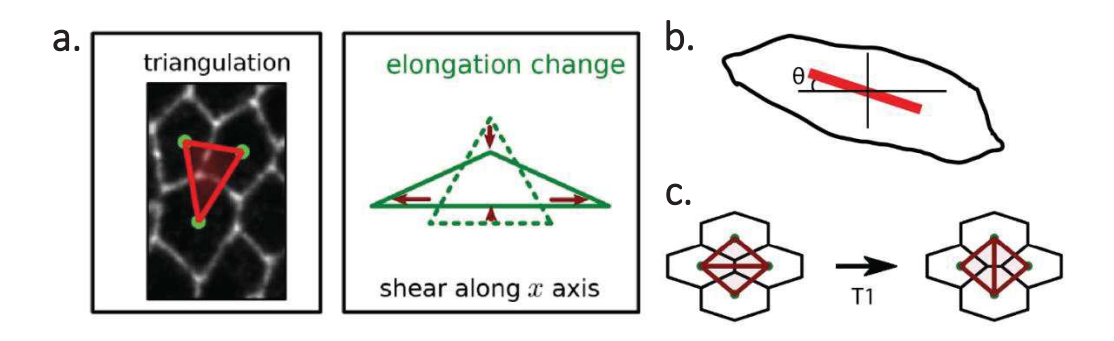


Figure 3.7. Segmentation to extract single cell parameters (a) Triangulation of the epithelial sheet (left) and an example of a triangle stretch (right) encoding cell elongation. Schematics defining cell orientation (b) and T1 transition (c). From (Etournay et al., 2016) and (Etournay et al., 2015).

3.7.6.1 Cell elongation

After triangulation, a nematic tensor \mathbf{Q} is defined to each triangle, characterizing its state of elongation (Figure 3.7a). Cell elongation per se is derived from the average of elongation tensors \mathbf{Q} of the triangles associated to the given cell.

3.7.6.2 Cell orientation

Cell orientation is defined as the angle between the long-axis after elliptical fit and an arbitrary framework (see Figure 3.7b).

3.7.6.3 T1 transition

T1 transitions are associated to neighbour exchanges as indicated by Figure 3.7c. They are extracted after triangulation.

4. COLLECTIVE DYNAMICS OF FOCAL ADHESIONS REGULATE DIRECTIONS OF CELL MOTION

NB: parts taken from the published article are in *italics*.

4.1 Introduction

As described in section 2.6.1, directed cell motion is fundamental in a variety of physiological and pathological processes (Machesky, 2008; Stuelten et al., 2018; Wijnholds, 2019). So far, chemical gradients have been the main hypothesis to explain this type of cellular migrations *in vivo* (Iglesias and Devreotes, 2008b; Roussos et al., 2014). However, along the point made in section 2.6.2, the presence of chemical gradients over large distances is rarely shown experimentally and if so, their precise quantification and description are often lacking. Therefore, how single cells acquire directed motion in the context of large-scale migrations remains elusive.

Because they constitute micrometre scale *adhesion interfacial* zones at the cell membrane between the extracellular matrix and cytoplasm with direct connection to acto-myosin stress fibres, Focal Adhesions (FAs) play a key role in cellular migration (Balaban et al., 2001; Goffin et al., 2006; Riveline et al., 2001). Moreover, the universal local force-area relationship derived from experiments on many cells and substrates opens the possibility to infer forces directly from the visualisation of FAs. Indeed, FAs elongate centripetally in the direction of the contact and apply locally a force per unit area of 5.5nN.µm⁻² (Balaban et al., 2001; Goffin et al., 2006). It has been shown that disruption of FAs by downregulation of their components involved in their nucleation decreases persistency and directionality of migrating cells (Chen et al., 2019; Juan et al., 2017; Rahman et al., 2016; Ray et al., 2017). Thus, quantitative description and connection between FAs distributions and the net bias in migration might lead to predictions for cell directionality with simple arguments based on geometry and FAs.

Previous works showed *in vitro* that local asymmetries in the cellular micro-environment could trigger directed motion without chemical gradients by a phenomenon coined *ratchetaxis* (Caballero et al., 2014, 2015b, 2015c; Comelles et al., 2014; Jiang et al., 2005; Mahmud et al., 2009; Sun et al., 2015). These studies are detailed in section 2.6.3. However, the main focus of these works was primarily the presence of a net bias and the existence of the rectification phenomenon without the elucidation of any cellular substructure driving the process. In Caballero *et al.* the role of stochastic probing of cell protrusions was highlighted and the function of FAs was hypothesized without their spatio-temporal visualisations.

In this context, we patterned ratchet-like adhesive regions and controlled the ability of cells to move along one preferential direction. We tested the interplay between geometry, focal adhesions dynamics and bias in cell migration. To this aim, we increased the inter-distance between motifs to probe the influence of gaps in directionality. We reported a non-linear increase of the net bias as a function of the gap distance and we showed that *ratchetaxis* can

efficiently rectify cellular migrations with almost 80% of cells going to the same direction in the most efficient configuration.

Furthermore, we reported that bias in direction of motion is mainly driven by the collective behaviour of FAs distributions and can be tuned and predicted by simple geometrical arguments describing the cellular micro-environment. In addition, a critical saturation area governs the bias: below this area, focal adhesions nucleate linearly with the accessible adhesive region, and above this area, nucleation saturates. It is the competition between these two dynamics that sets the bias.

Finally, we designed a theoretical model with a minimal number of parameters, all accessible by experiments, that recapitulates the phenomenon. We then tested and validated the model predictions with new sets of experiments.

4.2 Improved rectification of cells on ratchet-like patterns

4.2.1 Description of the configurations

With micro-fabrication and micro-contact printing (see 3.1), we patterned asymmetrical adhesive regions on glass substrates separated by gaps.

Designs of the motifs and setting of interdistances were done according to scaling arguments: Caballero *et al.* measured the typical average area of NIH 3T3 fibroblasts and reported a value of 1590 μ m². Thus, we adjusted the area of all the patterns to this value in order to impose shapes to cells and break their symmetry. Throughout the work we kept this area constant. In the same study, the authors also measured the mean protrusion length on Petri dishes and found out a value of 20.5 μ m. Gap distances were therefore tuned accordingly, and we varied interdistances from 13 μ m to 45 μ m together with overlapped configurations. More specifically, we probed the following conditions: 13 μ m, 16 μ m, 19 μ m, 20.5 μ m, 22 μ m, and 45 μ m. Two additional connected configurations were designed: 25% of overlapping between triangles, and a line of fibronectin without any broken symmetry.

4.2.2 Quantifying directionality

Cells were plated on adhesive patterns and they were able to adhere and migrate along the motifs (see Figure 4.1a-d, Movie S1-S4). The non-printed area was passivated with PLL-g-PEG (see (Le Maout et al., 2018)) so cells mainly probed the adhesive regions and do note migrate outside of the patterns. Cellular migrations were acquired over 48h with phase contrast microscopy and trajectories were decomposed into lattice units, *i.e.* steps between neighbouring motifs.

For each trajectory, the final position of the cell after 2 days was compared to its origin, defining a final bias. If the cell moved towards the tip of the triangle, the bias was set as "+", and "-" if it migrated towards the base of the pattern.

We reported a non-linear increase of the final bias as a function of the gap distance: while we did not observe any clear bias for $13\mu m$, $16\mu m$ and $19\mu m$, cells were strongly rectified on the $22\mu m$ configuration where almost 80% of the cells moved, on average, towards the "+" direction (Figure 4.1e). Notably, this direction of migration is opposite to the direction from the polarity set by the patterns. On larger gaps ($45\mu m$), cells were not able to migrate from one motif to another because the interdistance exceeded the maximum protrusion length (Movie S5).

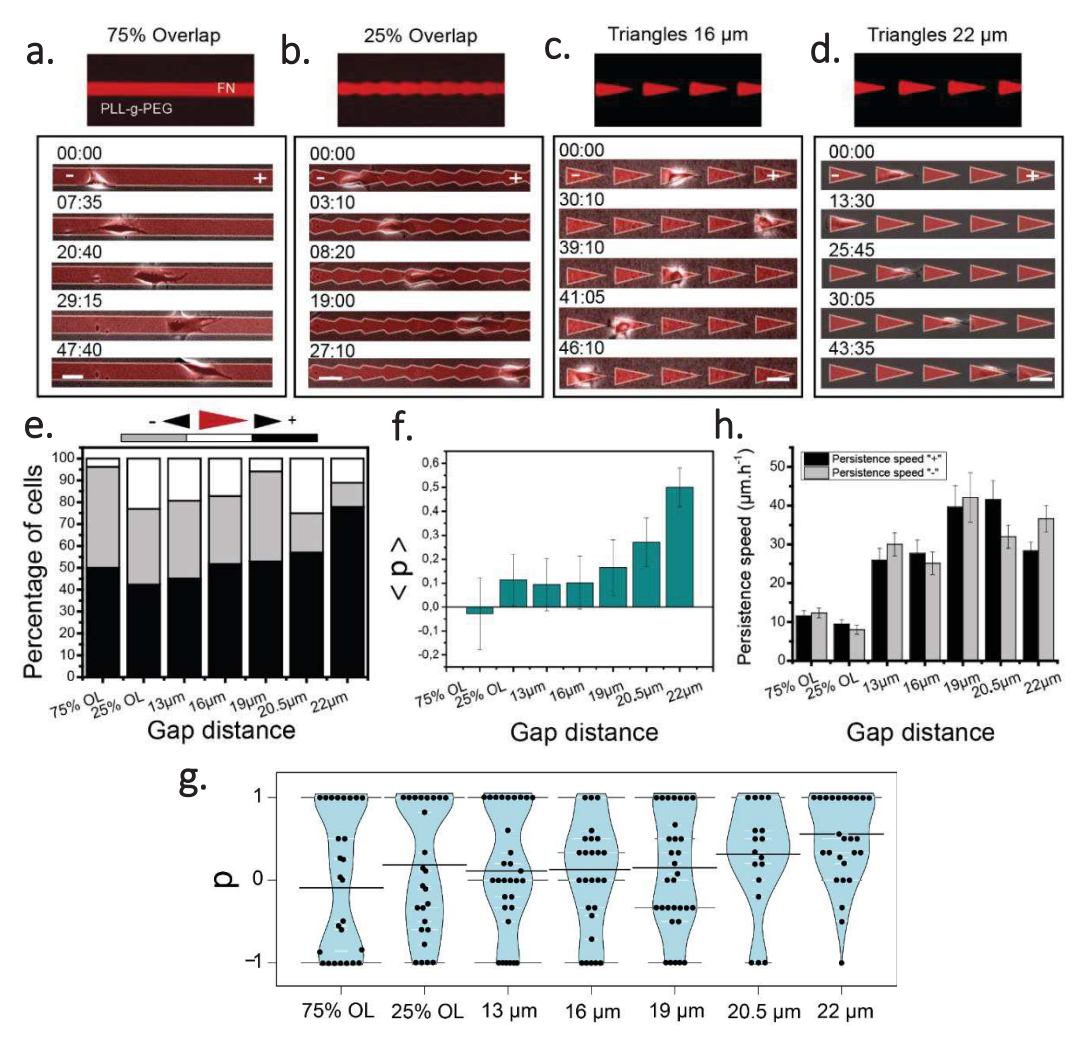


Figure 4.1. Cells move directionally on triangular patterns. (a-d) Cells are able to move from one motif to another on separated triangles, and crawl on connected ones. Time in hh:mm, scale bars: $50 \mu m$. (e) Final bias in percentage as a function of gap distance. (f) Average p given by Eq. 1 for each condition. (g) Complete p distributions for each condition (h) Persistence speed in $\mu m.h-1$. Data set: 25 < Ncells < 30 and Nbiological > 5 for 75% OL, 25% OL, $13\mu m$, $16\mu m$, $19\mu m$ and $22\mu m$. Ncells = 16 for $20.5 \mu m$. Data is shown as Mean \pm S.E. For (e) and (g), datasets are taken from Caballero et al. (Caballero et al., 2014). Adapted from (Lo Vecchio et al., 2020).

We next sought to describe all individual trajectories independently of the observation time. Therefore, we introduced and computed the mean bias per step p defined by:

$$p = \frac{N_{+} - N_{-}}{N_{+} + N_{-}} \tag{4.1}$$

where N_i corresponds to the number of steps performed in the i direction. This translates into a measurable and comparable readout the cellular behaviours on our assay. We averaged over trajectories the mean bias per step and the resulting $\langle p \rangle$ confirmed the behaviour observed with the final bias: we reported a non-linear increase of the bias until a maximum reached at 22µm of gap distance (p = 0.48±0.08) (Figure 4.1f). Distributions of p exhibited strong differences: cells behaviour on the fibronectin line was bimodal with peaks around p = 1 and p = -1, consistent with a stochastic persistent motion (Figure 4.1g). This feature progressively vanishes until a unimodal distribution for 22µm with a peak centred at p = 1. This suggests that simple geometrical features and local anisotropies in the cellular micro-environment could rectify and turn stochastic bimodality into a deterministic unimodal behaviour, and in the absence of chemical gradients.

4.2.3 Persistence speeds

Eventually, cells undergo persistent motion *i.e.* they migrate in the same direction without pausing. Their persistence speeds are reported in Figure 4.1h. Notably, cells were faster on separated triangles than on connected motifs, consistent with the fact that an increase in friction leads to decreased velocity (Palecek et al., 1997).

4.3 Focal adhesions dynamics

In order to elucidate the mechanisms leading to rectification of cells migrations by local asymmetries, we sought to observe FAs dynamics as they constitute the cellular substructure responsible for adhesion and force transmission.

4.3.1 Visualisation of FAs and controls

In this section, we will describe the different outcomes related to FAs visualisation.

4.3.1.1 Overexpression of FAs proteins and migration

We first tried to produce a stable cell line expressing vinculin-GFP, a protein from the FAs, with the CRISPR-Cas9 method in order to avoid overexpression and potential alteration of cellular dynamics. Unfortunately, cells engineered with this method did not exhibit strong fluorescent signals on FAs and light exposure rapidly bleached the fusion proteins. We also

reported coalescence of GFP leading to "dotty" distribution. Therefore, the generated cells were not suitable for live image acquisition.

On the other hand, cells stably transfected and overexpressing vinculin-GFP did not manage to migrate between neighbouring patterns (Figure 4.2). Instead, cells were "glued" to the adhesive regions, without moving out and dying after several hours (Figure 4.2). We hypothesized that this phenomenon was mainly the consequence of overexpression of a protein constituting FAs and therefore reinforcing the strength of the contacts. The same result happened with zyxin transfection.

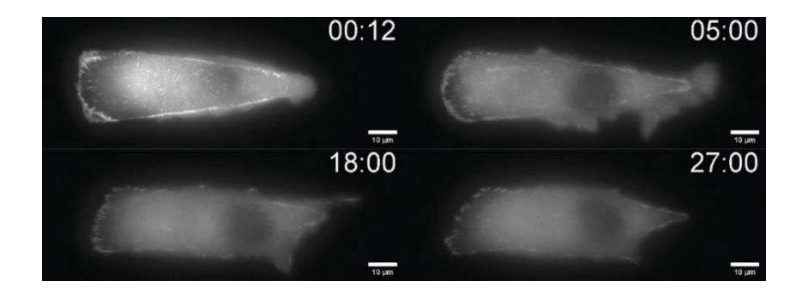


Figure 4.2. NIH 3T3 stably expressing vinculin-GFP. Cells were not able to move from one motif to another, possibly because overexpression of adhesion proteins. Scale bar = $10\mu m$. Time in hh:mm. (Lo Vecchio et al., 2020).

Finally, we found out that overexpression of VASP-GFP (Vasodilator-stimulated phosphoprotein), a protein from the FAs, was not affecting cellular dynamics, thus providing a good alternative for FAs imaging.

4.3.1.2 VASP-GFP and immunofluorescence

We next sought to confirm whether or not VASP was a reliable readout of FAs. To this aim, we compared with immunofluorescence the distribution of VASP-GFP with a paxillin-Cy3 staining, another protein from the FAs known to accurately co-localize (Figure 4.2). We reported an excellent match between the two distributions, confirming the relevance of VASP-GFP in our assays.

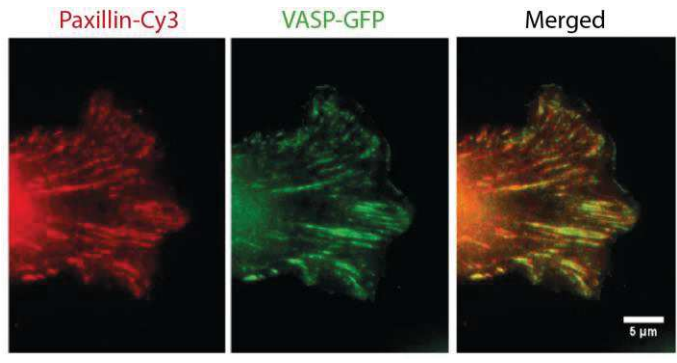


Figure 4.2. VASP-GFP is a good read-out for FAs. Immunostaining showing good colocalization between VASP-GFP and Paxillin-Cy3.

4.3.1.3 FAs dynamics on ratchet-like patterns

NIH 3T3 stably expressing VASP-GFP were seeded on patterns and were imaged through a spinning-disk microscope every 3min for 15h (Figure 4.3a, Movie S6). We observed that all protrusions, as soon as they touch fibronectin regions, nucleate FAs (Figure 4.3b).

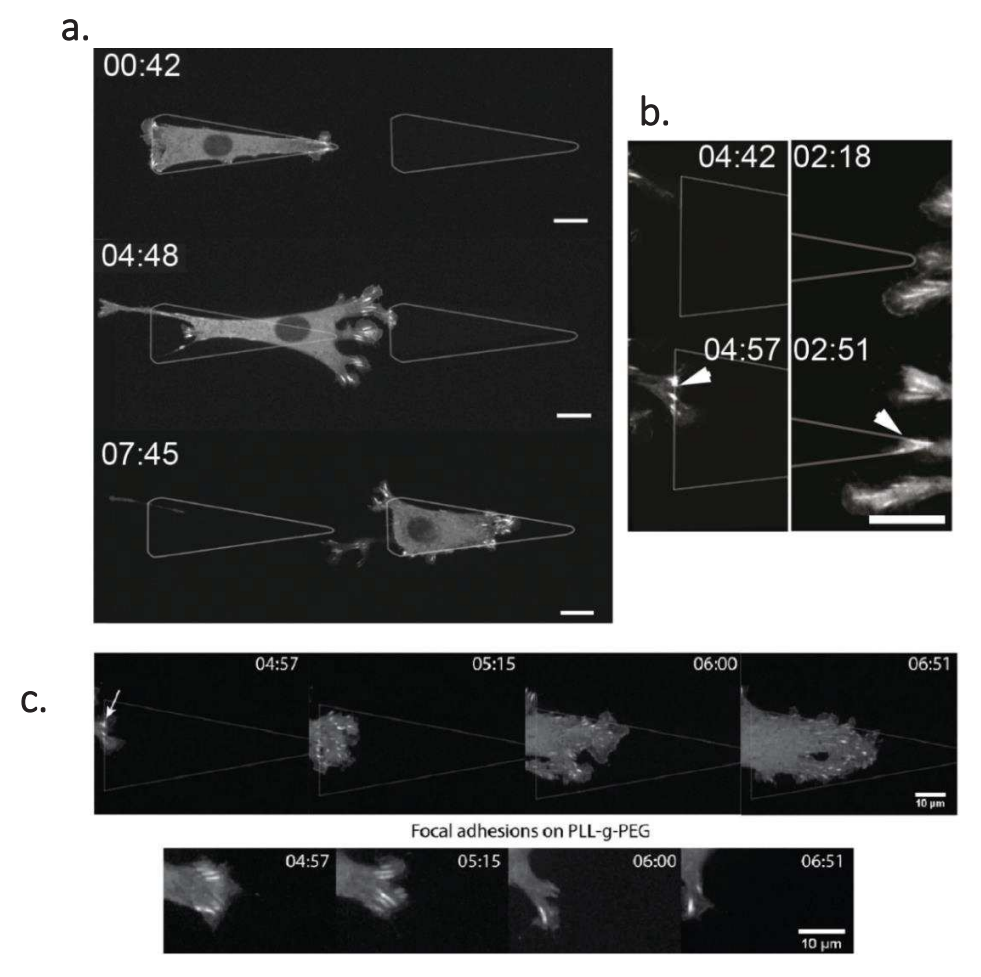


Figure 4.3. FAs dynamics on patterns. (a) Time-lapse images of an NIH3T3 cell stably expressing VASP-GFP. (b) Protrusions touching an adhesive motif imaged with fluorescence microscopy and RICM. Focal adhesions are nucleated right after contact with fibronectin motifs. Arrows indicate FA on patterns. (c) Protrusions come from the same cell at the same time points on both fibronectin triangles and on pLL-g-PEG. After a first docking line of focal contacts assembled on the edge of the triangle (white arrow), a wave of adhesion sites appears promoting migration towards this direction. On PLL-g-PEG (below), new contacts cannot be nucleated beyond the first row of focal adhesions, and this leads to retraction of the protrusion. Scale bars = 10µm. (Lo Vecchio et al., 2020).

This observation sheds light on the concept of "efficient protrusions" described by Caballero et al. Indeed, it was hypothesized that the bias observed in their experiment was the result of the differential probabilities of probing and docking on the neighbouring motifs. Therefore, some protrusions would probe the motifs without any docking -i.e. no FAs nucleated - while other protrusions, the efficient ones, would probe and dock. In our assays, we saw and

confirmed that every protrusion is efficient: when they probe an adhesive region, FAs are nucleated on a subminute timescale. We did not see any exception to this rule.

Then, when the first row of FAs nucleates on the neighbouring adhesive pattern, new contacts appear next in subsequent rows along the motif in a 'wave'-like manner (Movie S7). This phenomenon resembles waves of lamellipodial growth reported in previous works (Giannone et al., 2004). FAs growth on adhesive motifs is distinct from the protrusions on PLL-g-PEG. In this latter case, protrusion growth stops and retracts after nucleation of FAs (Figure 4.3c).

4.3.1.4 Testing with RICM

In order to rule out the influence of overexpression on the observed dynamics (especially concerning the efficient protrusions: the fact that all protrusions generate FAs could be a consequence of a higher protein pool) we tested with RICM our hypothesis (see methods) (Curtis, 1964).

With a proper focus on the surface, we observed dynamic high-density patches corresponding to FAs. On fixed samples, they co-localized with VASP-GFP (Figure 4.4a). During live acquisitions, the observed behaviour was similar to what we previously described with VASP-GFP: protrusions, as soon as they touch adhesive regions, generate FAs (Figure 4.4b). This simple experiment confirmed the results we had so far.

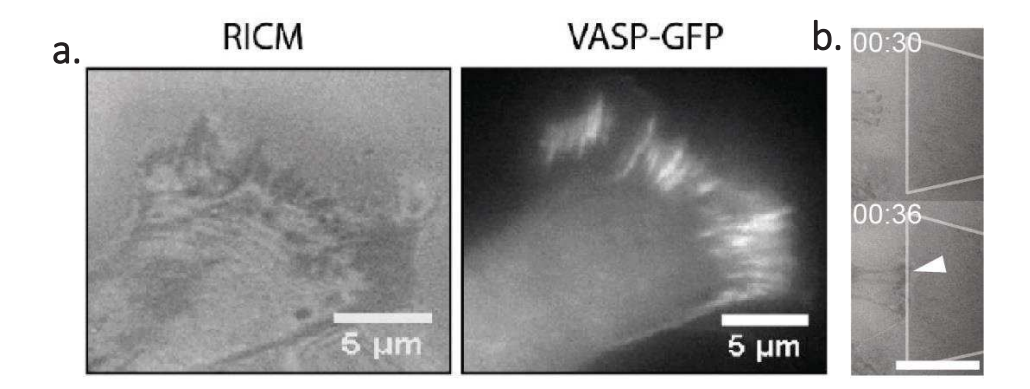


Figure 4.4. RICM confirms FAs dynamics on patterns. (a) Comparison between RICM and VASP-GFP on fixed samples. High density regions in RICM colocalize with VASP-GFP. (b) Time-lapse of a protrusion probing a triangular pattern: when the protrusion touches the adhesive area, new FAs are directly generated. Scale bar = 15μ m. Time in hh:mm. (Lo Vecchio et al., 2020).

4.3.2 Force mapping of FAs distributions

Considering the 22µm configuration as the most efficient one for directing migration, we specifically focused on this condition and asked whether or not FAs distributions and dynamics were sufficient to explain rectification.

To do so, we inferred forces directly on FAs (Figure 4.5b): each focal adhesion mediates a local force f_i exerted by the cell on the substrate along the long axis of the focal contacts, and its orientation points towards the interior of the cell. Its magnitude is deduced from the measured area of the FA by assuming a constant stress of 5.5 $nN.\mu m^{-2}$ (Balaban et al., 2001; Goffin et al., 2006).

While global force balance is verified at each time step ($\sum F_{ext} = 0$, inertia is negligible (Tanimoto and Sano, 2014)) local asymmetries in forces could be relevant. For simplicity, we take the scalar part of the vectorial sum. We reported that cells apply a large average force ($F_{cell} = \sum f_i$) of 130 nN.µm⁻² along the x-axis during motion, and that direction of this force correlates with direction of motion (Figure 4.5b-d). To satisfy force balance, a resistive friction force needs to be considered. Assuming viscous friction, and including the reported values of instantaneous velocity, the corresponding friction coefficient can be estimated as ~ 25 N.s.m⁻¹, consistent with reported values of friction of ~ 30 N.s.m⁻¹. This friction estimation matching experimental values further confirm the approach of inferring forces directly from the FAs distributions.

Since all protrusions nucleate FAs when they probe fibronectin patterns (we do not need to include any docking probability as in the "efficient protrusion" model), distributions of FAs and thus, bias in direction, should be critically governed by areas of available adhesive regions.

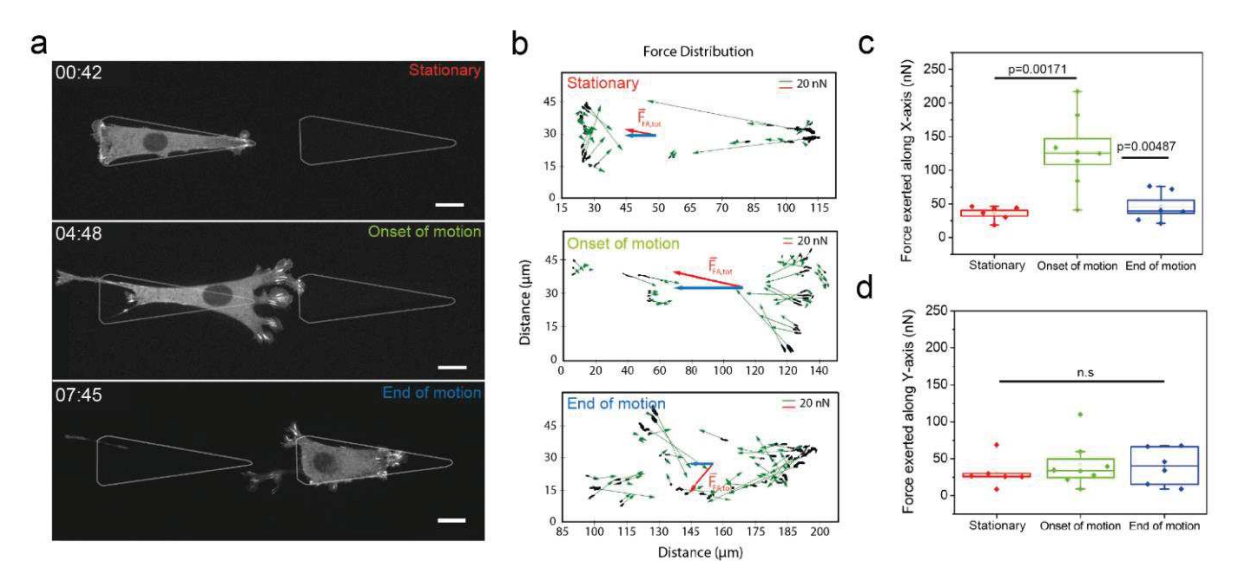


Figure 4.5. Force inference on FAs distribution correlates with direction of motion. (a) Time-lapse images of an NIH3T3 cell stably expressing VASP-GFP. Three time points are extracted for analysis: (i) during the stationary phase, (ii) at the onset of motion, and (iii) at the end of motion. (b) Force vectors map. Each focal adhesion is linked to a force vector oriented in the direction of adhesion zone (in green). Its amplitude is set according to the relationship $1\mu m^2$ corresponds to 5.5nN. The total force vector is displayed in red, its x component in blue. (c-d) Force exerted along x-axis and y-axis during the three time points. Statistical tests comparing distributions are done with a one-way ANOVA. $N_{biological\ repeat} = 4$, $N_{cells} = 8$. Scale bar = $15\mu m$. Time in hh:mm. (Lo Vecchio et al., 2020).

4.4 Theoretical model

4.4.1 Estimation of probed areas

We defined A_+ and A_- the areas probed in "+" and in the "-" directions, respectively. Theoretical estimates of these quantities are made considering the following scheme: a cell, spread on a triangular pattern, extend protrusions of average length λ over gaps of distance g to neighbouring motifs with known geometries (Figure 4.6a). Protrusions are assumed to be distributed, on average, over a half-disk whose centre is either the tip of the triangular pattern or the middle of the triangular base. The intersection between the neighbouring motif and this area represents the theoretical area probed by protrusions. With simple geometrical assumptions, we derived the expressions of A_+ and A_- as followed:

$$A_{-} = \frac{1}{2} \cdot (\lambda - g)^{2} \cdot \theta \qquad (4.2)$$

$$A_{+} = \left(B - (\lambda - g) \cdot \sqrt{\frac{1 - \sin \alpha^{2}}{\sin \alpha^{2}}}\right) \cdot (\lambda - g) \qquad (4.3)$$

where g, λ , θ and α correspond, respectively, to the gap distance, the protrusion length, the angle of the triangle tip and the angle at the base of the triangle (Figure 4.6a).

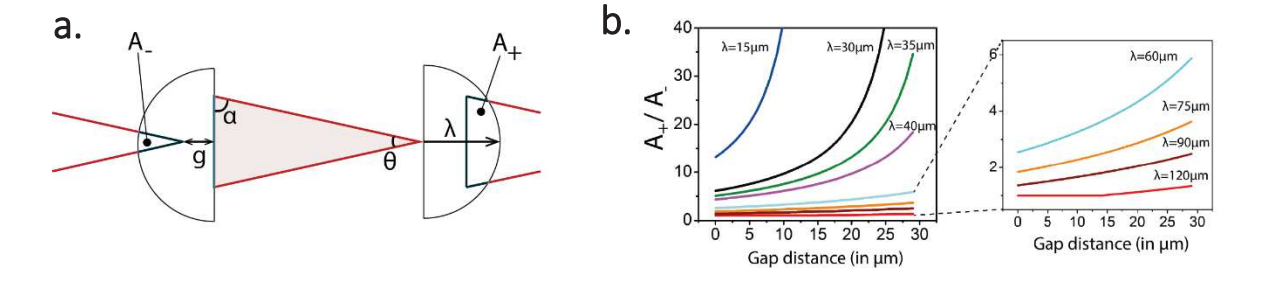
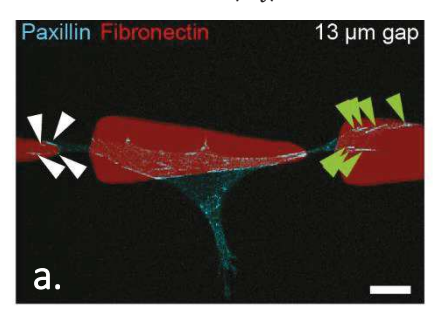


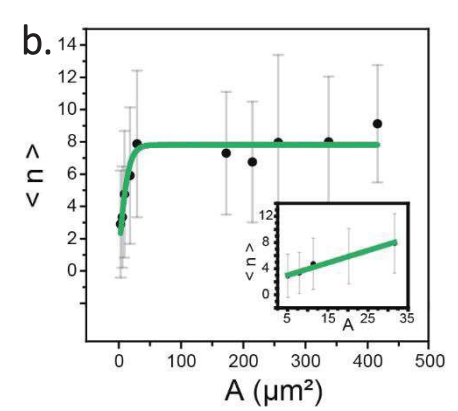
Figure 4.6. Theoretical estimates of areas probed by protrusions. (a) Geometrical arguments for estimation of theoretical probed areas. The cell spreads on the central pattern and sends protrusions to neighbouring regions. (b) Evolution of the ratio of probed areas for triangular patterns for various protrusion lengths.

Interestingly, analysis of the ratio $\frac{A^+}{A^-}$ is always greater than 1 and shows a monotonic behavior coupled to a strong divergence when the gap distance is close to the mean protrusion length λ resembling to the sharp increase observed in experiments (Figure 4.6b). When λ is large enough (i.e. close to the size of a pattern) ratio of probed areas goes back to 1. This result stresses the imbalance between the two probed areas and confirms the hypothesis that available adhesive areas determine the bias. To go further in this direction, we need to elucidate the relationship between FAs number $\langle n \rangle$ and the probed area A.

4.4.2 Quantification of FAs with accessible areas: a non-linear relationship

We first checked whether or not it exists a linear relationship between the two quantities $\langle n_i \rangle = \alpha A_i$ where n_i corresponds to the number of FAs and A_i to the theoretical probed area. We stained for FAs samples of cells during the initial probing phase for all the conditions (13µm to 22µm). We could have access to a high number of behaviours in few experiments and extract an estimation of $\langle n_i \rangle$.





We reported two different kinds of regimes: a linear increase for small A (corresponding to the probing of A_-) and a plateau for higher areas (corresponding to A_+). Therefore, the relationship between $\langle n \rangle$ and A is nonlinear and we could fit the typical saturating behavior with a hyperbolic tangent function $y = C * tanh(A/A_0)$ where A_0 translates the idea of a saturation area into a measurable readout. The fit also yielded to an estimation of A_0 and we found a saturation area of $16.43 \pm 2.22 \ \mu m^2$.

Figure 4.7. FAs nucleation saturates. (a) Immunostaining of NIH 3T3 during the probing phase. FAs are shown with arrows. (b) Average number of FAs as a function of the theoretical probed area. (Lo Vecchio et al., 2020).

4.4.3 Phenomenological expression of $\langle p \rangle$

The core hypothesis is that the direction of a step is dictated by the direction of the resulting force transduced by all FAs. Decomposing this resulting force into + pointing and - pointing forces, and projecting along the ratchet axis x, one has:

$$F_{x} = \sum_{i=1,n+} f_{xi} + \sum_{j=1,n-} f_{xj}$$
 (4.4)

Note that F_x is a random variable that depends on the fluctuating quantities n_i , which denote the number of FAs that transduce forces pointing in the i direction. The probability p+ of a step in the + direction is given in the model by the probability that $F_x>0$. Experimentally one expects a minimal threshold force that we neglect here for the sake of simplicity. While p+, as defined, in principle can depend on the full distribution of n_i and f_{xi} , it is controlled to linear order (small bias limit) only by the mean value of the resulting force, which is obtained from Eq. (4.4):

$$\langle F_{\chi} \rangle = \langle n_{+} \rangle \langle f \rangle - \langle n_{-} \rangle \langle f \rangle$$
 (4.5)

where $\langle f \rangle$ is the mean intensity of the force mediated by a single FA. Finally, the bias per step can be written as: $p \propto (\langle n_+ \rangle - \langle n_- \rangle)/(\langle n_+ \rangle + \langle n_- \rangle)$. If we consider $\langle n_i \rangle = \alpha A_i$. This yields to:

$$p \propto \frac{(A_+ - A_-)}{(A_+ + A_-)}$$
 (4.6)

which relates explicitly the bias to the local geometry. However, we tested linearity and we saw previously that we had instead a saturating behavior. Therefore, to go beyond the linear description of Eq. (4.6), we incorporated in the model A_0 , the saturation area, a phenomenological parameter representing the typical area over which nucleation of FAs saturates, as observed in immunostainings:

$$p = \frac{\tanh\left(\frac{A_{+}}{A_{0}}\right) - \tanh\left(\frac{A_{-}}{A_{0}}\right)}{\sum_{i=+,-} \tanh\left(\frac{A_{i}}{A_{0}}\right)}$$
(4.7)

The resulting prediction of p yielded an excellent agreement with experimental values, where notably the single fitting parameter A_0 was involved (Figure 4.8a). As expected, the linear description gave a poor fit (blue dashed line). Notably, the fit with the inclusion of saturation area A_0 yields $13.5 \, \mu m^2$, a value which is in excellent agreement with the value found in the < n > -A plot of $A_0 = 16.43 \pm 2.22 \, \mu m^2$. This further confirms the relevance of our hypothesis and the strength of our model.

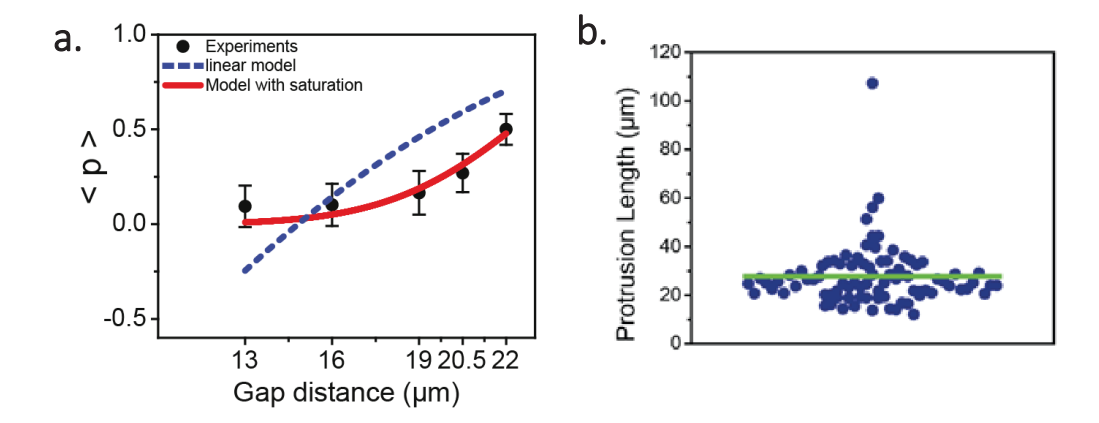
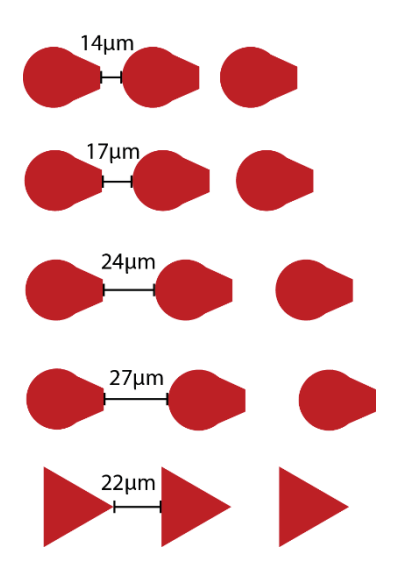


Figure 4.8. Model fits experimental data. (a) Experimental data fitted with the two phenomenological expression of $\langle p \rangle$. Parameters are set as followed: $\lambda = 28\mu m$, A_0 (free parameter) = $13.5\mu m^2$. The non-linear model recapitulates experimental results. (b) Protrusion lengths distribution measured on 5h temporal projections for 10 cells. $\langle \lambda \rangle = 27.85\mu m$.

4.5 Experimental tests and validation of the model

4.5.1 Design of new configurations and predictions

In order to test model predictions, we designed new configurations and computed the bias *a priori* with Eq. (4.6) to compare it with experimental results *a posteriori*.



To do so, we designed two new sets of patterns either with a different shape of with a different aspect ratio: (i) teardrops (TD) shaped motifs leading *a priori* to a reversal (majority of cells should now migrate in the "-" direction) with various gap distances from $14\mu m$ to $27\mu m$ and (ii) equilateral triangles, keeping constant the gap of $22\mu m$. Areas of patterns, as detailed in 4.2.1, remain constant at $1590\mu m^2$ in order to match cell area as detailed in 4.2.1.

Figure 4.9. New configurations designed to test model predictions.

The estimates of A_+ and A_- for the teardrops were derived using the same framework than previously and yielded:

$$A_{-} = \left(\frac{1}{\tan \phi} \cdot (\lambda - g) + b\right) \cdot (\lambda - g) \tag{4.8}$$

$$A_{+} = \lambda^{2} \cdot \arccos\left(\frac{d}{\lambda}\right) + R^{2} \cdot \arccos\left(\frac{d'}{R}\right) - (d + d') \cdot \sqrt{\lambda^{2} - d^{2}} \tag{4.9}$$

The predictions for the bias were the following:

- TD 14 μ m: p = 0 ($A_i \gg A_0$)
- TD 17 μ m: p = 0 ($A_i \gg A_0$)
- TD $24\mu m$: p = 0.0003829
- TD $27\mu m$: p = 0.2826317
- TE 22 μ m: p = 0.02235

4.5.2 Experiments

NIH 3T3 were seeded on the new patterns and they were able to migrate from one motif to another (see Figure 4.10, Movie S8-10). We computed the mean bias per step for each cell on every condition and reported the results in Figure 4.11.

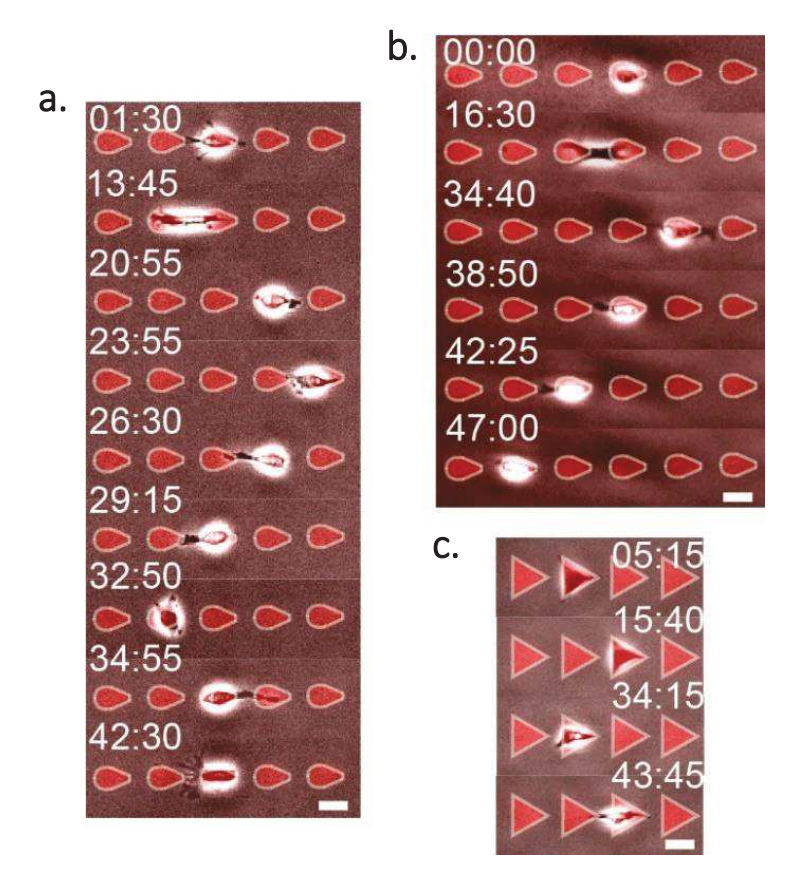


Figure 4.10. Experimental tests of the model predictions. (a-b) Cell moving on teardrops separated by $24\mu m$ and $27\mu m$ gaps respectively. (c) NIH3T3 on equilateral triangles separated by $22\mu m$ gaps. Scale bars = $50\mu m$. Time in hh:mm

We compared the value of $\langle p \rangle$ generated by experiments with the predictions made *a priori* with the model without free parameter. Experiments and model matched (Figure 4.11a) and the plot experimental $\langle p \rangle$ – theoretical $\langle p \rangle$ showed a linear relationship with only minor deviations confirming our former hypothesis and the strength of the model (see Figure 4.11b).

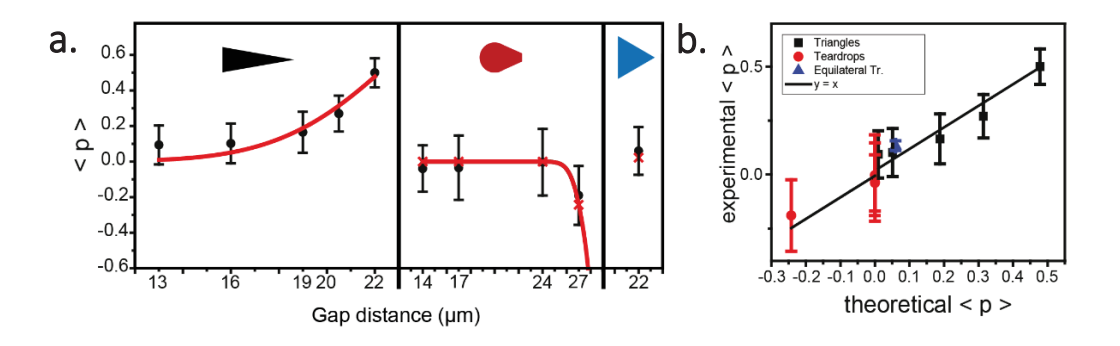


Figure 4.11. Theory predicted the new behaviours on patterns. (a) Experimental data together with model predictions without free parameters. Red crosses correspond to initial predictions. (b) Experimental $\langle p \rangle$ with theoretical $\langle p \rangle$. The linear relationship between the two quantities show the strength of the model.

4.6 Discussion

Altogether, this study showed that direction of cell motion can be tuned and predicted by simple geometrical features without external long-range gradients. We managed to design an optimal condition where 80% of cells move, on average, along the same direction (opposite to the polarity imposed by the triangular patterns). We reported, with force inference and theoretical modelling, that FAs distributions can explain direction of motion and that tuning of these distributions by simple geometrical arguments can rectify cellular migrations in predictable ways.

Interestingly, the number of FAs generated on an adhesive region is not linearly correlated to the available probed area: it exists a saturating area above which protrusions do not generate more FAs. This saturating behaviour explains the sharp increase in the mean bias per step we observed in experiments.

Finally, we managed to test the model and its predictions with new geometries, therefore confirming the strength of our hypothesis.

This ratchetaxis phenomenon can be summarized with the following scheme. If the area available on both sides is greater than A_0 , the cell will be able to create stable saturated anchoring zones on both sides, leading to $\langle F_x \rangle = 0$. Therefore, the bias will be poor even if A_+ >> A_- (13 μ m to 19 μ m conditions, see Figure 4.1). On the other hand, if one side goes close or below A_0 , the bias becomes stronger in the opposite direction.

Although simple, the model recapitulates faithfully the experimental results. Additional layers of complexity could be thought such as implementation of more accurate spatial distributions of protrusions. Indeed, we considered for the sake of simplicity the protrusions probing the same way both sides of the patterns. In reality, protrusions are more "focused" at the tip of the triangle and more spread out at the base. Therefore, it exists differences between the two ends that might contribute to a bias in the probing efficiency. If this feature does not seem to play a key role in our configurations (predictions and experiments successfully matched), the effect could be more prominent for other types of geometries that we did not probe here.

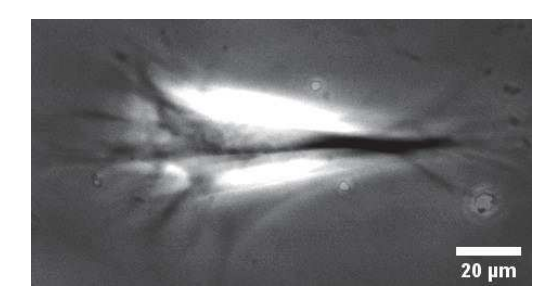


Figure 4.12 Projection of 10 cells after 2 hours of probing on a triangular pattern. Protrusions are distributed in a different way right and left.

Moreover, the protrusion length λ in the model is fixed and its value is deduced from the average length $\langle \lambda \rangle$ measured on triangles separated by 22µm. This parameter will contribute to determine the position of the sharp deviation of $\langle p \rangle$. However, we saw that the protrusion length might vary between conditions. Indeed, after analysis on 13µm and 22µm, it seems that this length adapts and scales to the topology of the environment: on short gaps (13µm) $\langle \lambda \rangle$ will be smaller than on larger gaps (22µm). The relationship between protrusion lengths and gaps is still not clear and we decided to fix λ in the model and to consider that the resulting mean bias per step $\langle p \rangle$ will be a consequence of largely distributed λ . Probably an implementation of a variable λ will be useful to predict precisely the net bias on more complex geometries but it will also allow to derive not only $\langle p \rangle$ but distributions of p as shown in Figure 4.1.

In addition, we observed in some cases a memory of polarity consistent with what was reported in (Caballero et al., 2014). This translates into a sustained broken symmetry during motion, and an increase in velocity throughout the migration between lattice units (reported, to be quantified). These preliminary results are shown in Figure 4.13. However, on the configurations we probed, our model did not need to incorporate such details to predict the average p. Nevertheless, this memory of polarity would be necessary in order to derive the full distribution of p, especially for conditions such as the fibronectin line: the bimodal distribution is a consequence of this memory.

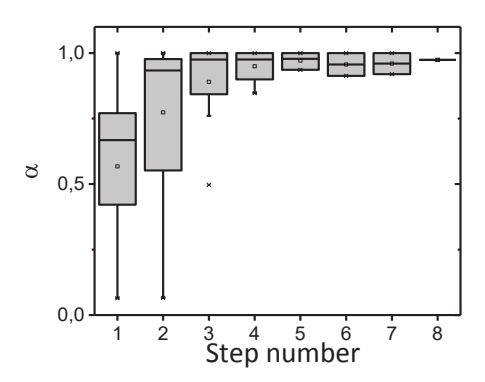


Figure 4.13 Memory of polarity increases polarization over time. Polarization as a function of the step number. Polarization α is defined as $\left|\frac{A_{s+}-A_{s-}}{A_{s+}+A_{s-}}\right|$ where A_{si} corresponds to the area occupied by the protrusions/the lamellipodia at each side of the cell. $\alpha=1$ means that the cell is fully polarized towards one preferential direction.

Finally, we think that the overlapped configurations might need to be considered apart from the separated patterns even if they do enter into the logics of the scientific test. Indeed, initial polarization and symmetry were not clear on these configurations. Instead, cells were randomly choosing direction and moving persistently along this direction, leading to a bimodal distribution. The fact that the initial direction is sustained might be a consequence of the wave of FAs described above as waves are usually a good mean to auto-amplify a broken symmetry. We did notice a slight influence of the patterns for the 25% overlap with a minor shift of the distribution towards positive values and we saw in some experiments cells probing the

boundaries of the motifs and funnelling towards the "+" end. However, this phenomenon was not clear enough to propose new statements.

4.7 Conclusions

Overall, this *in vitro* study stresses the importance of cellular micro-environment topology and this paradigm could be tested *in vivo* along lines recently suggested (Bajanca et al., 2019). Anisotropy in adhesive proteins patterning such as fibronectin comparable to the cell size could be relevant and potentially bias motion *in vivo*.

Although it exists other layers of complexity as discussed above, it seems that a minimal number of parameters can predict, on average, directionality: the protrusion length, the area probed by the cell, and the saturating area. These parameters are available from experiments and their full characterization can be done for future predictions.

5. RATCHETAXIS IN CHANNELS: CELLS IN CONFINEMENT MOVE DIRECTIONALLY

NB: This work was started and performed during the PhD work of E. Le Maout. I continued this study and finalized the remaining experiments.

5.1 Introduction

In the previous chapter, we described how cells can rectify their direction of motion in the presence of local asymmetries in their micro-environment topology. This study was done on 2D flat surface (Bissell, 2017). In this new chapter, we will try to test this *ratchetaxis* principle in 3D microchannels mimicking *in vivo* confinements.

In tissues or in capillaries, cells migrate *in vivo* in highly dense environments, therefore confining the cell and its components. Large organelles, the acto-myosin cytoskeleton, and the nucleus need to deform and to reorganize in order to allow cell passage through these small spaces with potential biological consequences (Le Berre et al., 2012; Halfmann et al., 2019).

It has been shown that micro-fabrication of micrometre size channels allows to probe these new behaviours. Interestingly, cells migrate in a different mode of migration when confined in channels with passivated walls: they "push" on sides (Bergert et al., 2015; Hawkins et al., 2009; Liu et al., 2015). This motion, driven by friction generated by actin flows, is an emergent behaviour under confinement.

However, it is not clear yet how the cell cytoskeleton and its large organelles such as the nucleus deform and reorganize in order to pass through very narrow spaces in the cellular path. This type of local asymmetries can be found in small veins and in venules where microscopic venous valves (MVV) are present (Caggiati et al., 2006) introducing 'bottlenecks' in the migratory path. These local squeezing points, breaking micro-environment symmetry, could also potentially bias direction of migration, in way similar to *ratchetaxis* but in 3D environments. This kind of phenomenon could be relevant for Circulating Tumour Cells (CTCs) getting trapped in small blood vessel as detailed in previous works (Rejniak, 2016; Yamauchi et al., 2005).

In addition, in some squamous cancers, cells are known to be defective for keratin, an intermediate filament essential to shape the scaffold surrounding the nucleus (Tsai et al., 2019). Defects in these structures and their implications in motility in confined spaces have not been reported.

In this work, we showed that local asymmetries direct cell motion when cells are confined in open channels. When fully confined, polarity is "locked" and the direction of motion depends only on the entry point: cells do not repolarize and are not biased by cues provided by the micro-environment topology.

We next sought to characterize the dynamics of cytoskeleton components such as actin, focal adhesions, and the keratin array surrounding the nucleus during passage through bottlenecks. We report anisotropies in distributions of cytoskeletal proteins with actin bundles located at the bottom and the top of the cell between which the nucleus can be deformed. Focal contacts are mainly located at the channel wall specifically at the junctions between ratchet units. The keratin array also exhibits an asymmetric distribution where keratin accumulates at the rear of the nucleus potentially to facilitate deformation.

Finally, we combined cell migration through asymmetric micro-channels with chemical gradients. We observed that cells could migrate after removal of the gradient only when anisotropies were directed towards the direction of the highest chemical concentration. Otherwise, cells would stop.

Altogether, this work provides new reports on ratchetaxis in 3D confined environment.

5.2 Design of the different conditions

5.2.1 Scaling arguments

In order to probe the mechanisms leading to cell deformation and passage through confined spaces, we need to design 3D environments that efficiently confine cells keeping migration feasible: if the confinement is too low, cells migrate in their usual way; if the confinement is too high, cells are totally squeezed and cannot move or even enter the micro-channels.

Therefore, we designed different conditions with various bottleneck sizes and angles, and we characterized cellular motion inside. Channels are designed with periodic asymmetries in order to mimic cell blockage in small veins. Results are reported in Figure 5.1: the best balance between optimal confinement and sustained migration was obtained for the condition 'a16i4' where a corresponds to the tip angle and i to the opening width.

Two sets of configurations were considered to evaluate potential effects of full confinement: open channels, where cells are only confined by sides, and closed channels where cells are totally confined. Each time, the control experiment was a straight channel, without anisotropies, whose width corresponds to the bottleneck width.

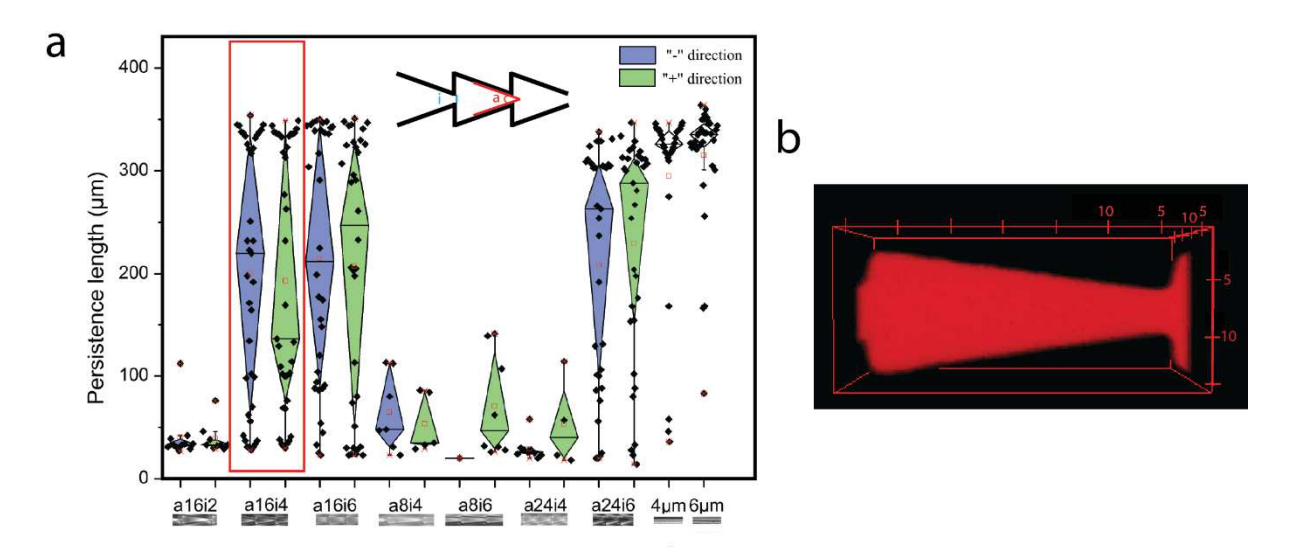


Figure 5.1. Scaling arguments for micro-channels design. (a) Persistence length as a function of the ratchet configuration. i corresponds to the opening width (in μ m) while a is associated to the opening angle. At very high confinements, cells do not move as they cannot pass through the narrow bottleneck (a12i2). For elongated geometries (a = 8), cell motion is also impaired. Motion was possible in condition a24i6 but the confinement was weak (large opening angle and width). (b) One lattice unit of the ratchet, filled with TRITC-Dextran, imaged with spinning-disk. Units in μ m.

5.2.2 Partial confinement: open micro-channels

The first condition aims to confine cells only by the sides in order to impose a broken symmetry in the x-y plane. This consists in asymmetric channels of PDMS without any closure on the top as shown in Figure 5.2a-b. Cells are seeded in the centre of the array and they can enter and migrate freely in both directions of the channels (Figure 5.2b, Movie S11). They are systematically compared with straight channels (Movie S12).

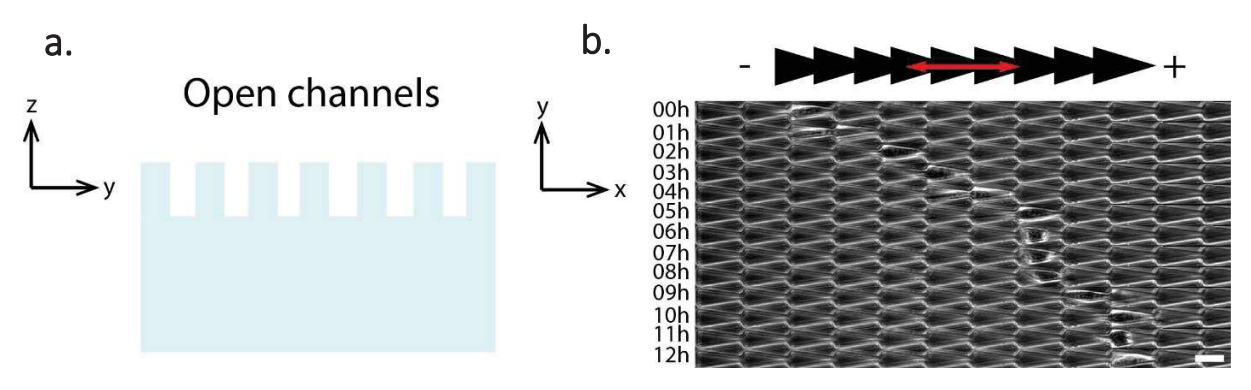


Figure 5.2. Cells migrate in open channels. (a) Schematic representation of the configuration probed (see MM 3.4.2). (b) NIH3T3 migrating in open ratchet-like channels. In this particular example, the cell moves towards the "+" direction. Scale bar = 15 μ m.

5.2.3 Closed micro-channels: a total confinement

In this configuration, a full confinement in x-y and z is imposed to the cell as shown in Fig.5.3 a-b. Cells are seeded into reservoirs and they enter the closed micro-channels either by the "-" end or by the "+" end and migrate (Figure 5.3b, Movie S13-14).

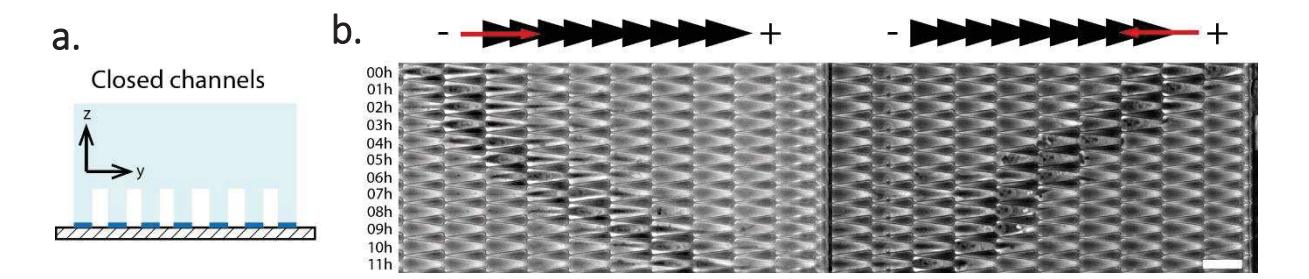


Figure 5.3. Cells migrate in closed channels. (a) Schematic representation of the closed configuration (see MM 3.4.2). (b) NIH3T3 migrating in closed ratchet, facing the "+" direction (left) and the "-" direction (right). Scale bar = $30 \mu m$.

5.3 Migration in ratchet-like channels

5.3.1 Quantification of the bias

In order to compute the net bias in the direction of migration, we used the mean bias per step $\langle p \rangle$ already introduced in chapter 4 (Eq. 4.1). We compared back-to-back migrations in a straight channel, as a control, and motion in ratchet-like asymmetric channels. Results are reported in Figure 5.4.

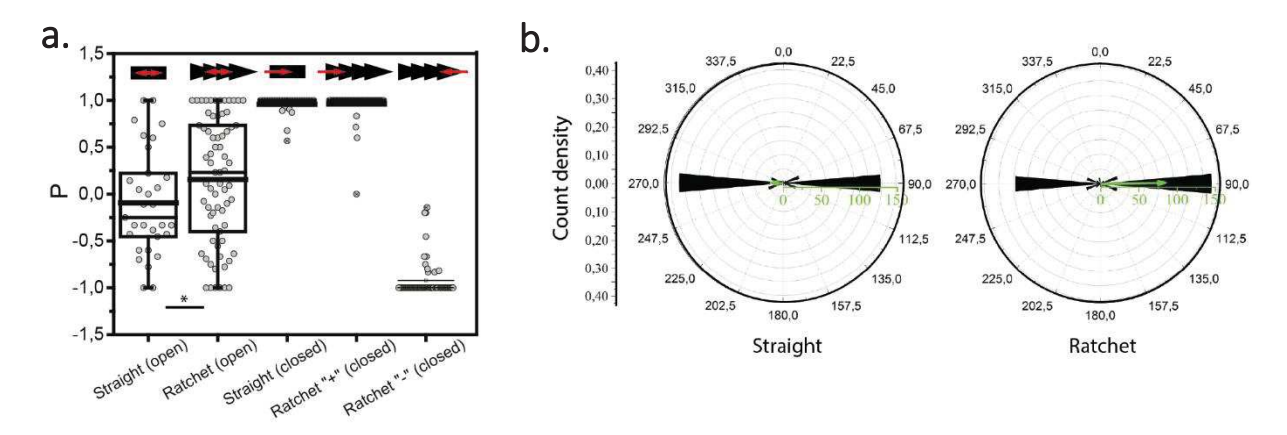


Figure 5.4. Cell motion is biased in ratchet channels. (a) distribution of p as a function of the configuration probed. Bias is seen in open configurations whereas polarity is "locked" in closed ones leading to distributions peaked around +1 and -1. (b) The bias observed in open channels is further quantified with the mean displacement vector, showing an increased magnitude towards "+" direction in ratchets compared to the straight channel.

In open channels, a significant net bias can be seen in the direction of the ratchet asymmetries ("+" direction) compared to the straight channels. This was also confirmed with the computation of the net displacement vector, exhibiting differences between the two conditions.

However, when totally confined, cells exhibited a different migratory behaviour: polarity was "locked", and direction of motion was only depending on the entry point. This led to $\langle p \rangle$ distributions peaked at +1 if the entry point was directing towards the ratchet direction and peaked at -1 otherwise. The straight channels gave the very same results. These results suggest that at high confinements, cells are not biased by topological cues and cannot repolarize inside micro-channels.

5.3.2 Velocity profiles comparison

Instantaneous speeds were computed for each time step and velocity profiles could be extracted (Figure 5.5a). Comparison of these between straight channels and ratchet-like channels exhibited differences. Indeed, in straight channels cell motion is decomposed into phases of pauses and migrations, with various times and speeds whereas cellular motion in ratchet-like channels is constituted of consecutive increase in velocity corresponding each time to passage from one lattice unit to the other.

5.3.3 Squeezing of the nucleus

The velocity profile found for ratchet-like channels might be the consequence of cytoskeleton deformations and especially from nucleus deformation that seemed to be, in our experiments, the large organelle preventing passage. Indeed, Figure 5.5b shows a time-lapse sequence of a NIH 3T3 nucleus (stained with DAPI) deforming before each step towards the next lattice unit (Movie S15). This phenomenon also happened with another cell type such as HL60 (Figure 5.5b, right). Therefore, we can assume that large deformations occur at the bottlenecks and that reorganization of cytoskeletal components may allow or not the cell passage.

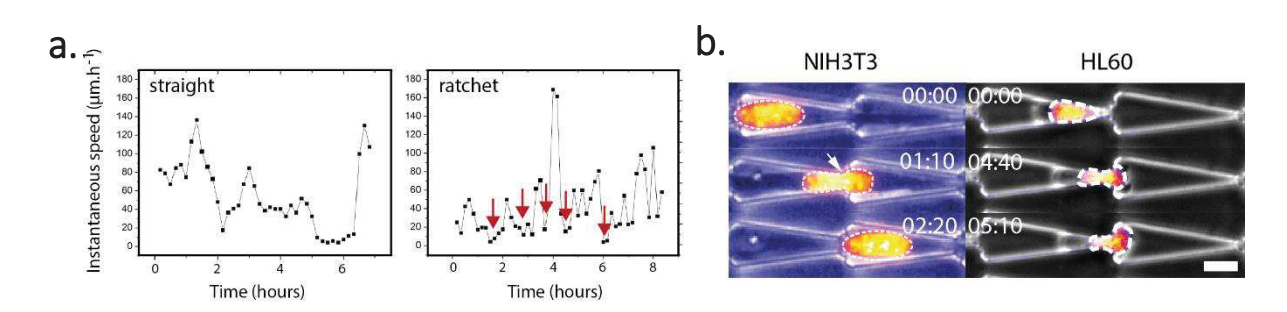


Figure 5.5. Nucleus compression and cell passage. (a) Instantaneous speed as a function of time. In ratchet-like channels, cells exhibit "bursts" of velocity and stops (red arrows) corresponding to passage from one lattice unit to another. (b) Nucleus deformation for NIH3T3 and HL60 passing through ratchet bottleneck. Scale bar = $10 \mu m$.

5.4 Anisotropies of cytoskeleton components

We next sought to visualize various cytoskeleton components and to correlate their dynamics with cell passage through bottlenecks.

5.4.1 Actin

NIH 3T3 were first transfected with lifeact-mcherry in order to visualize actin dynamics live in micro-channels (Figure 5.6a, Movie S16). We observed two actin stress fibres bundles located at the ventral cellular side but also dorsally, consistent with previous studies (Comelles et al., 2014). We also saw some local accumulation of actin at the bottleneck during cell passage. The nucleus is positioned and deformed between the two actin bundles as shown by the immunostaining with phalloidin and DAPI in Figure 5.6b.

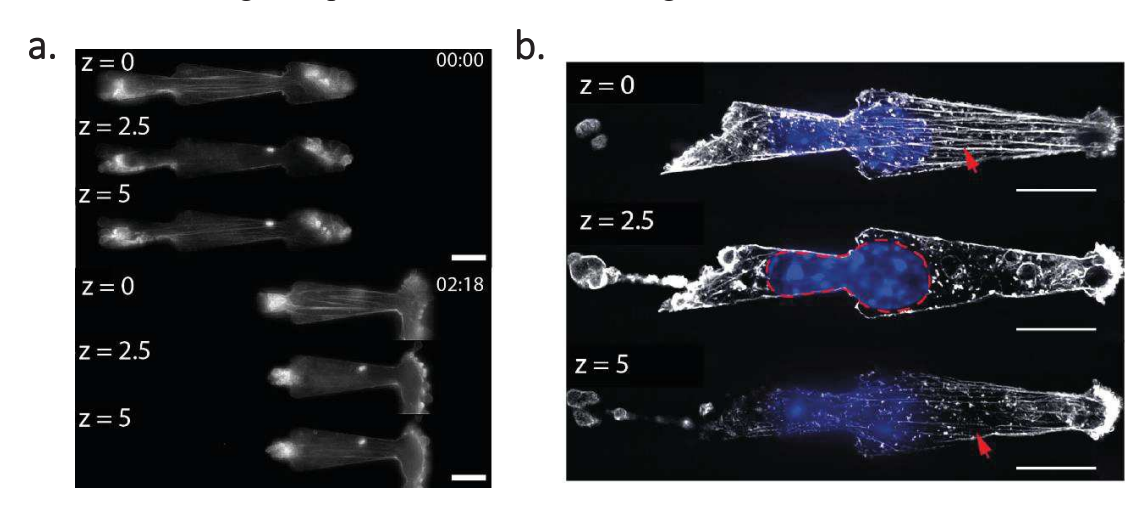


Figure 5.6. Actin bundles assemble at the ventral and dorsal sides. (a) NIH3T3 transfected with lifeact-mCherry. Actin bundles are visible ventrally and dorsally as well as accumulation at the bottleneck during migration. (b) Immunostaining of a cell in a ratchet-like channel. The nucleus (DAPI) is deformed and the two actin bundles are visible (phalloidin 488).

5.4.2 Focal adhesions

We visualized FAs using NIH 3T3 cells stably expressing VASP-GFP as detailed previously in Chapter 4. We report a biased distribution of FAs: FAs are generated mainly at the interface between channel walls and the glass substrate during protrusion growth (see Figure 5.7, Movie S17) and then, they accumulate at the bottleneck. Less FAs were visible at the contact zone between the channel "roof" and the cell body. The fact that FAs nucleate more on glass could be the consequence of fibronectin deposition from the serum potentially promoting FAs growth.

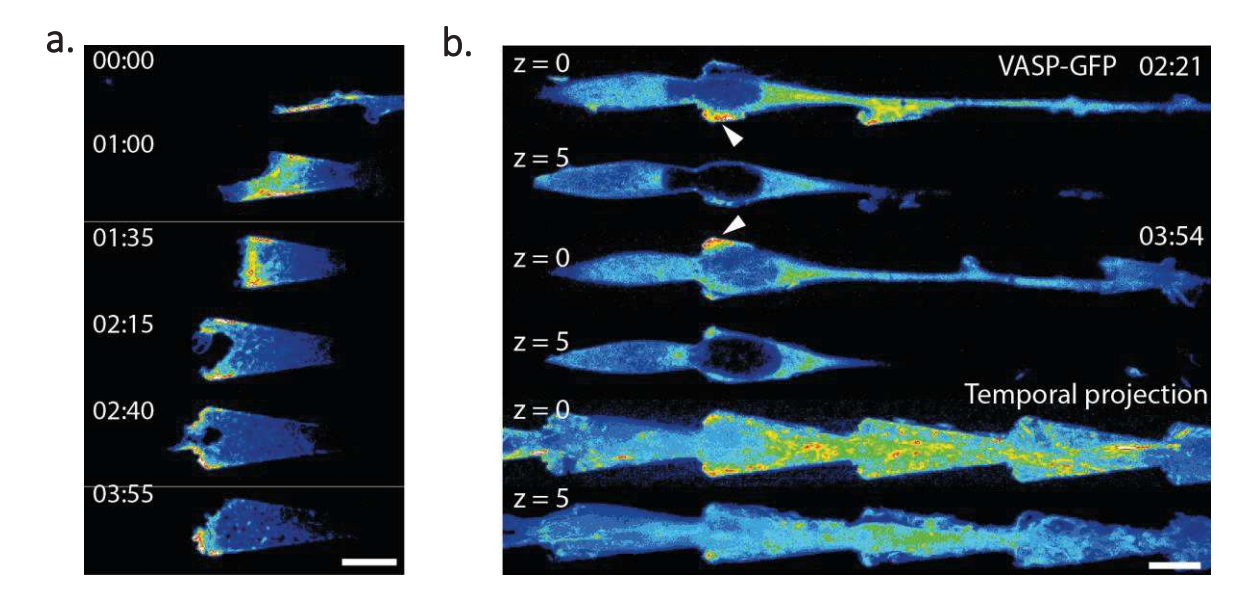


Figure 5.7. FAs accumulates around the bottleneck. (a) NIH3T3 protrusion growing in a closed channel. FAs accumulate at the channel wall and at the bottleneck. (b) FAs localize at the bottleneck and at the protrusion, more on the glass substrate at $z = 0\mu m$ than on the "roof" at $z = 5\mu m$. Scale bar = 15 μm .

5.4.3 Keratin

Defects in keratin cytoskeleton have been reported to be involved in some squamous cancers and this mutation is also related to the severity of the disease (Tsai et al., 2019). Therefore, intermediate filaments, and more specifically keratin, could be important in cellular deformations during migration in confined spaces. To test whether or not defects in keratin array are relevant or not, we used the cell line with the keratin variant CAL27-V7, found in squamous cancers, and compared it to the wild-type cells.

On flat surfaces, CAL27 cells, being epithelial, did not undergo any motion (Figure 5.8a). However, migration was possible inside micro-channels, consistent with the fact that 3D motion differs from 2D migration.

In ratchet-like micro-channels, we observed a highly dynamic keratin network in wild-type CAL27 cells, exhibiting firm and visible flow. We also report that the keratin array around the nucleus reorganizes during cell passage through the bottleneck: initially, keratin is homogeneously distributed around the nucleus whereas during passage, keratin exhibits an anisotropic distribution with accumulation at the rear of the nucleus (Figure 5.8b-c, Movie S18). A measurement of the polarity, as defined in Chapter 2 (section 2.2, eq. (2.1)) can confirm this observation. With the mutant cell line, keratin was ill-organized and did not exhibit strong anisotropies in distribution such as the wild-type cells (Figure 5.8d-e). Instead, cells were arrested at the bottleneck and sometimes we reported fracture of the nucleus (Figure 5.8f, Movie S19). We did not see any motion from one lattice unit to the other, suggesting that intermediate filaments, and in this particular case keratin, could be essential to deform the nucleus and allow cell passage in confined spaces.

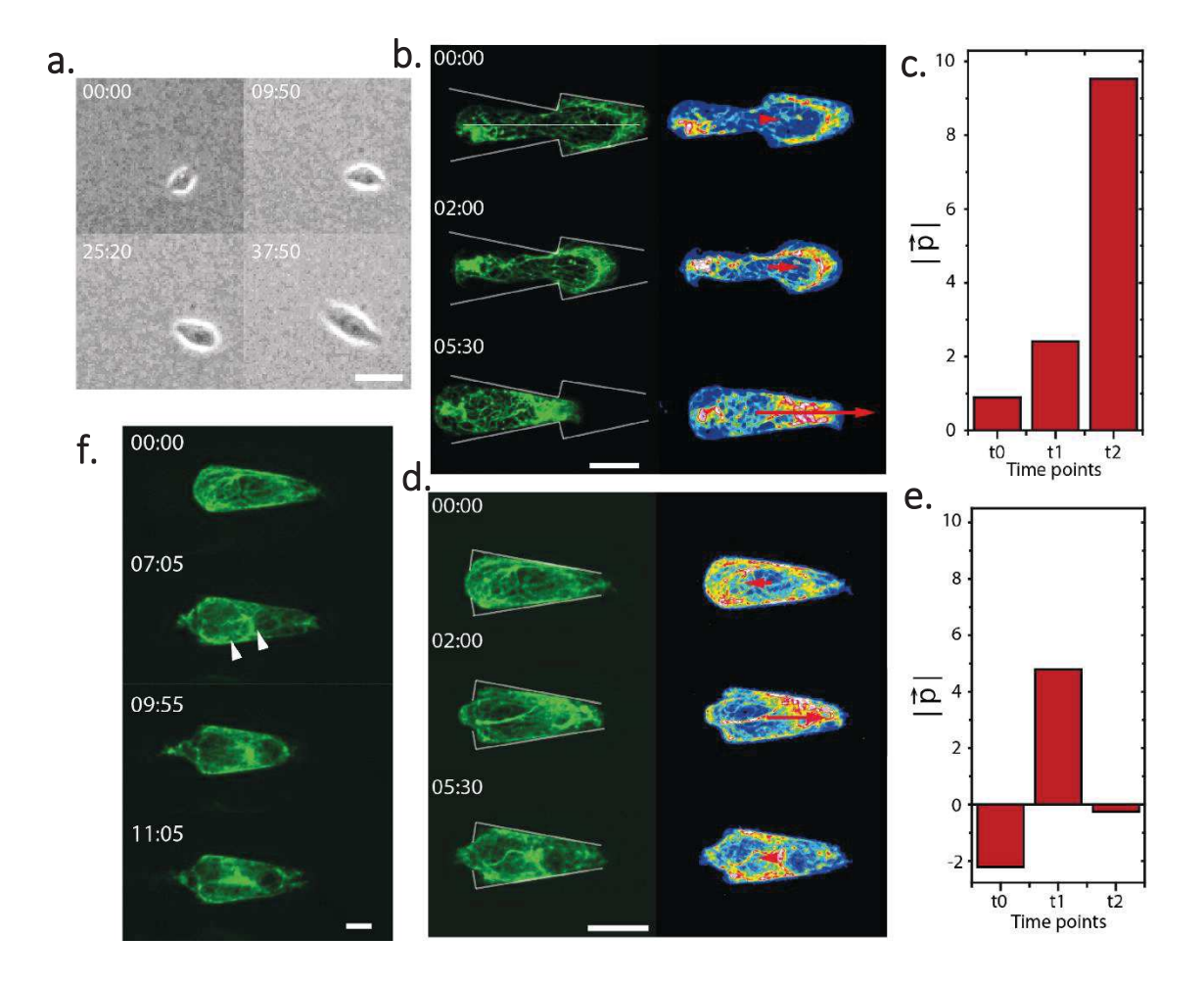
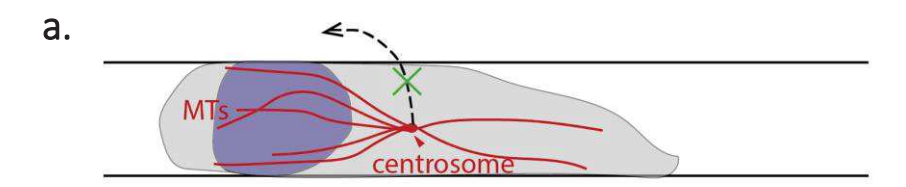


Figure 5.8. Keratin defects impair cell motion in confined ratchets. (a) CAL27 on flat glass coverslip. Cells are not able to migrate. (b) In microchannels, cells can move from on lattice unit to another. WT cells (K14-GFP) exhibit an anisotropic keratin array, accumulating at the rear of the nucleus during cell passage. Norm of the polarity vector (red arrow) is shown in (c) and shows the anisotropy. Cells expressing fusion protein found in squamous cancer (V7-GFP) do not exhibit the same keratin array and do not exhibit strong anisotropy (d-e). (f) We reported fracture of the nucleus at the bottleneck for the mutant cells. Motion was not possible in the channels. Scale bar = $15 \mu m$ for (b-d) and $5 \mu m$ for (f).

5.4.4 Centrosome positioning

We made the hypothesis that cells could not repolarize in micro-channels because the microtubule array and specifically the axis centrosome-nucleus would be "locked". We transfected cells with pACT-mKOI and we could image the centrosome, appearing as a dot during live acquisitions. The axis centrosome-nucleus indeed corresponded to the direction of motion during the course of our experiments.



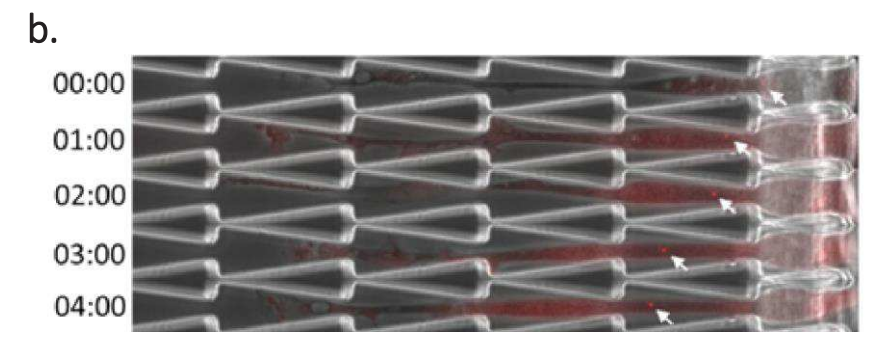


Figure 5.9. Axis nucleus-centrosome correlates with direction of motion. (a) Scheme representing the idea of a "locked" microtubule array where the centrosome-nucleus axis cannot change its orientation because of confinement. (b) NIH3T3 transfected with pACT-mKOI. The centrosome appears as a fluorescent dot (white arrow) but vanishes with time. Time in hh:mm.

5.5 Chemical gradients and ratchetaxis

It has been shown that chemical gradients (haptotactic) can compete and cooperate with topological cues (Comelles et al., 2014). Therefore, we next sought to compete local topological cues with chemical gradients in micro-channels.

5.5.1 Migration of cells through serum gradients

We designed an assay were cells are exposed to serum gradients. Serum solutions of 0.1% and 10% are flowed in two opposite reservoirs. After few minutes, a stable gradient is formed and its profile can be extracted with the visualisation of TRITC-dextran, mixed with the solutions. This is reported in Figure 10a. Cells are able to migrate and sense the direction of the chemical gradients as shown in the montage Figure 10b.

5.5.2 Competition between topological cues and *chemotaxis*

We next combined motion in closed channels with chemotaxis to see the potential interplay between topological and chemical cues.

In the two configurations probed (cells migrating towards the "+" end or towards the "-" end, with the gradient in the same orientation), cells were always migrating towards the highest serum concentration, suggesting that for this specific condition (strength of the gradient slope), *chemotaxis* oriented cells motion (Figure 5.10c-d).

However, we observed two different behaviours depending on the orientation of the ratchet-like channels (Figure 5.10c-d, Movie S20-21). After gradient removal, cells migrating in the direction opposite to the ratchet direction stopped their motion and paused for hours. On the other hand, cells migrating in the direction of the ratchet could continue their migration without stopping. Overall, two hours after gradient removal, cells in the ratchet direction ("+") travelled an average distance of $78\mu m$ whereas cells in the opposite direction ("-") travelled only $39\mu m$ (Figure 5.10e). To quantify further the phenomenon: when we aligned all the trajectories sequences with respect to the gradient removal, we observed that the ratio of velocities for each case α_+/α_- is about 10 (Figure 5.10f). Altogether, these results suggest that polarity induced by gradient could be distinct from the polarity set by topology.

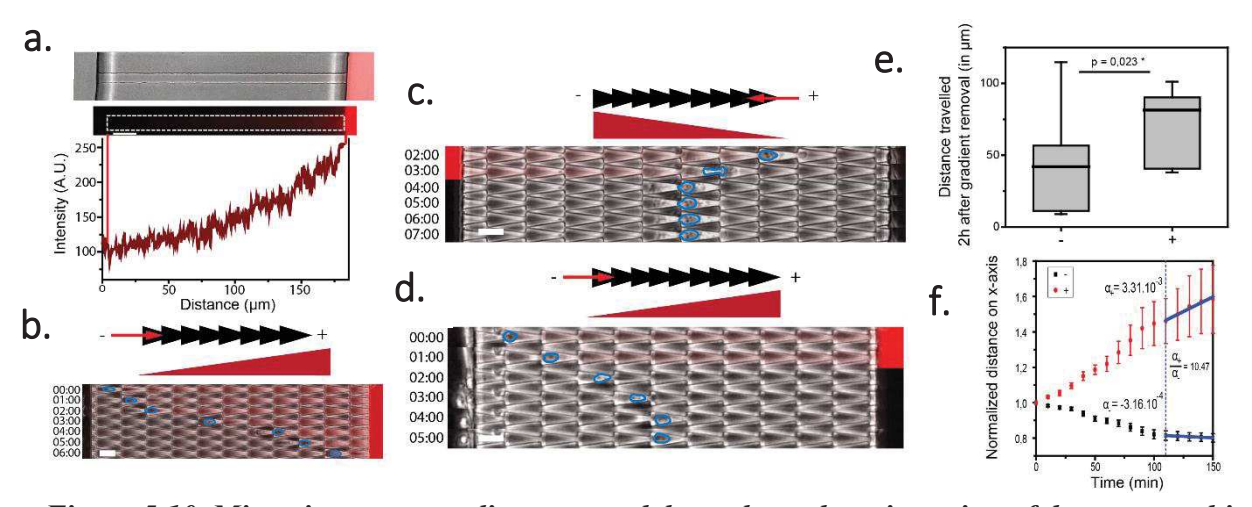


Figure 5.10. Migration upon gradient removal depends on the orientation of the topographic cue. (a) Serum gradient generated in straight closed channel and its visualization and quantification with TRITC-dextran. (b) NIH3T3 moving in the direction of the serum gradient and in the "+" direction of the ratchet. (c) Cell migrating towards the gradient and against the ratchet direction. After gradient removal, the cell stops migrating. (d) Cell migrating towards the gradient and towards the ratchet direction. After gradient removal, the cell continues to migrate in the same direction. (e) Distance travelled 2h after gradient removal. Significant differences are seen between the two orientations: migration is favoured when cells migrate towards the "+" direction. (f) Distance travelled after gradient removal. All sequences are aligned and their displacement is analysed with the respect to the gradient removal (dashed blue line). Slopes are extracted and cells migrate better in the ratchet direction.

5.6 Discussion

In this work, we described mechanisms of cellular motion in confined micro-environments. We report that *ratchetaxis* operates when planar x-y polarity is broken, *i.e.* when cells are confined by the sides only. In this context, local asymmetries bias direction of migration towards the direction of the anisotropy.

However, when fully confined in x-y-z, cell polarity is "locked", and direction of migration is totally defined by the entry point of the micro-channels. Such mechanisms of a locking polarity could be relevant *in vivo* during extravasation processes where cells migrate through very narrow capillaries with confinements comparable to our experiments (5µm) (Chambers et al., 2002; Labelle and Hynes, 2012; Rejniak, 2016; Yamauchi et al., 2005). In such cases, motion would be directed all throughout the confined path, as we report in our experiments. However, the mechanism by which polarity is locked remains unknown. We hypothesize that repolarization is impaired because the axis nucleus-centrosome does not have any degree of freedom to reorganize and set another defined polarity to the cell. We tested this hypothesis by tracking nucleus-centrosome axis in live experiments. In the time-frame of our experiments, the axis nucleus-centrosome indeed matched with direction of motion.

We also show that nucleus needs to deform in order to pass through $5\mu m$ width bottlenecks and this induces a typical migration with consecutive bursts of instantaneous velocities at each step from one lattice unit to another. This nucleus deformation correlates in time with the reorganization of many cytoskeleton components:

- (i) Actin foci were found specifically at the bottleneck and stress fibres organized into bundles found ventrally and dorsally, potentially allowing nucleus deformation.
- (ii) FAs during protrusion growth and cell passage were mainly located at the interface between channel walls with accumulation at the bottleneck.
- (iii) We also investigated whether or not defects in keratin network, as reported in some squamous cancers, could alter migration in micro-channels. We report accumulation of keratin at the rear of the nucleus when the cell passes through the bottleneck for wild type cells. However, mutation of the protein leads to an isotropic distribution of keratin, frequent fragmentation of the nucleus, and arrest of cellular motion.

These anisotropies in distributions of cytoskeleton components may lead to anisotropy in forces. Indeed, as described in Chapter 4 for FAs, these structures generate forces per unit area that could be inferred from their localization. The fact that they distribute mainly at the bottleneck could lead to anisotropic stress generation. We hypothesize that this is needed for the nucleus to deform and pass through the bottleneck.

This fusion was reported in medical cases (Tsai et al., 2019). Therefore, further studies need to be addressed *in vivo* in order to see whether or not arrest of cell migration in narrow capillaries is indeed directly linked to cancer aggressiveness. In this context, it is known that initial arrest in the capillary is critical for tumour cells to metastasize through extravasation processes (Chambers et al., 2002; Labelle and Hynes, 2012).

Then, we combined ratchet-like micro-channels with chemical gradients. We saw two distinct migratory behaviours after gradient removal depending on the direction of the topographical anisotropy. Cells exhibited persistent motion upon gradient removal when they were migrating towards the ratchet direction ("+") but they stopped their motion if the motion was directed

against the ratchet direction ("-"). We hypothesized that exposure to the chemical gradient would reinforce cortical tension in the direction of the motion. This would lead to different effects upon removal, conditioning the passage or not depending on the orientation of the topographical anisotropy.

This kind of ratchet-like micro-channels could be relevant to mimic small capillaries with local asymmetries created by small venous valves and could be extended to broader usage. Indeed, the classical assay to quantify the sensitivity of cells to chemical gradients is the Boyden chamber (Boyden, 1962). This historical assay places cells into a chemical gradient generated between two reservoirs. A porous physical barrier separates the two reservoirs and cells can migrate through the pores. However, pores size represents only a fraction of a cell size and this can lead to results of efficiency that could be far from the actual *in vivo* effect. Our assay could be seen as an alternative to test long range motion in this context.

5.7 Conclusions

In this work, we propose ratchet-like micro-channels mimicking small capillaries with $5\mu m$ width bottlenecks.

We show two ways of rectifying direction of cellular motion by breaking local symmetry: either by planar x-y anisotropies or with a full confinement. The latter case is the most efficient. The broken symmetry of the entry point is kept over the full trajectory with no change in polarity and is not biased by the topological cues from the ratchet. This "locking" effect might be important in *in vivo* situations were confinement is high, during extravasation for example.

We also provide the dynamics of various key players from the cytoskeleton such as actin, FAs or keratin. In all the cases, they accumulate at the bottlenecks and exhibit anisotropic distributions. We propose that this facilitates the passage through these narrow regions while enabling deformation and passage of the nucleus. Stress fibres anchored at focal adhesions at the wall would press in the relevant directions to elongate the nucleus accordingly.

Finally, analogy with the previous chapter on 2D *ratchetaxis* can be made as we report here a way to induce a polarity and to bias cell directionality only with topological features. This again stresses the importance of the micro-cellular environment in cell migration and directed motion.

6. TURING RINGS: SPONTANEOUS ROTATIONS AS AN INTERPLAY BETWEEN POLARITY AND RHOA ACTIVITY

6.1 Introduction

In development, morphogenesis is associated with large scale directional flows of cells. In *Drosophila Melanogaster*, cells from the egg chamber acquire a coherent motion leading to a spontaneous rotation along the chamber shell (Cetera et al., 2014). This symmetry breaking followed by a sustained global motion is reminiscent of the dynamics observed in mammary acini where this type of spontaneous coordination appears (Tanner et al., 2012; Wang et al., 2013). It has been shown that perturbations in this collective motion impairs proper morphogenesis (Tanner et al., 2012; Wang et al., 2013). So far, the mechanisms leading to symmetry breaking and to coherent motion remain elusive.

In past chapters, we saw how spontaneous individual directed migrations could be generated by topological cues. These directed motions, as detailed in section 2.7.1 and in respective introductions, are fundamental in biological contexts. However, going from the analysis of single cell dynamics to the behaviour of a directed collective migrations might be challenging. Communications between cells through adherens junctions together with the mechanical and chemical feedbacks happening in the epithelial layer lead to emergence of new phenomena.

Acto-myosin cytoskeleton and its Rho signalling pathways set interacting rules between cells: contractions and extensions drive the spatio-temporal dynamics at the cell scale but also at the multicellular scales. Therefore, the emergence of multicellular coherent motions has to be dependent on the crosstalk between mechanics and signalling. In addition, if the interplay between Rho activity and the acto-myosin cytoskeleton is documented at the single cell level, it is not yet fully characterized at the multicellular level. Extrapolations from single cells are often made whereas collective effects in Rho activity may as well contribute in tissues.

In this work, we extracted some general mechanisms and features leading to spontaneous symmetry breaking and to coherent motion in epithelia. To this aim, we generated multicellular rings a simple periodic configuration already proposed by A. Turing in 1952 where reaction-diffusion patterns were supposed to appear and to lead morphogenesis (Turing, 1952).

By varying rings diameters, we could measure the coherence length of our system. This allowed us to generate multicellular systems where global coherence and spontaneous rotations appear. Analysis of the cellular dynamics revealed that coherence is a non-linear, sharp process, with minor deviations between rings. Transition between the non-coherent and the coherent state appears in about 1 hour.

Then, we report that establishment of coherence is a direct consequence of a tug-of-war between single cells polarities happening within the ring. In addition, cell number and divisions were associated with different levels of coherence.

We also showed that an internally driven constraint, mediated by acto-myosin cables at boundaries is necessary to ensure proper collective motion. Local perturbations of the cables led to decrease in coherence and cell escape.

Next, we compared RhoA activity in the rings with the coherence dynamics. We found out that high cell velocity and coherence correlates with low RhoA activity. In addition, highest RhoA levels were located at the boundaries co-localizing with acto-myosin cables. We conclude that active Rho relate to boundaries acting as walls for cells, whereas it inversely correlates to velocity within the ring.

Finally, we recapitulated experimental results *in silico* with a Vicsek-based model describing polarities interactions and including free acto-myosin boundaries and parameters extracted from experimental measurements. And we deduce from this computational approach that coherent rotations result from a fine tuned interplay between cell polarity, alignment rules for velocity/polarity, and acto-myosin cables.

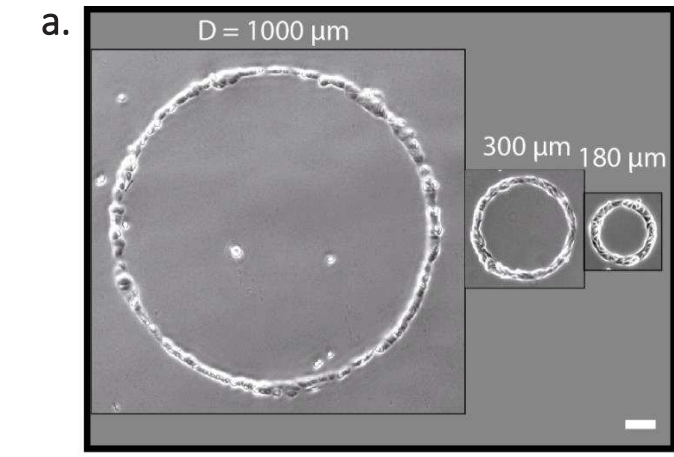
6.2 Obtaining coherent multicellular systems

6.2.1 Dynamics of different ring configurations

We needed first to identify the natural length over which cells can collectively migrate – namely the coherence length – characterizing our system. To this aim, we designed different micro-patterned fibronectin rings with various diameters as shown by Figure 6.1a while keeping the ring thickness constant.

Cells on the rings adopted different behaviours depending on the pattern size and exhibited rich dynamics (Figure 6.1b, Movies S22-24). Since cells were not confined by any chemical or mechanical constraint, they could migrate "in" and "out" of the pattern. On the largest configuration (1000µm diameter), local flows of cells were visible and finger-like extensions appeared all around the perimeter, consistent with the behaviour observed at free edges on normal migrating epithelia.

However, for smaller configurations (300 μ m and 180 μ m), this feature vanished, and cells exhibited migrations resembling to wound healing assays: cells first spread and migrate "in", closing the ring and leading to a disk-shaped colony, before spreading outwards. For the smallest configuration (180 μ m), we observed some global spontaneous rotations, indicating that the system size was close to the coherence length.



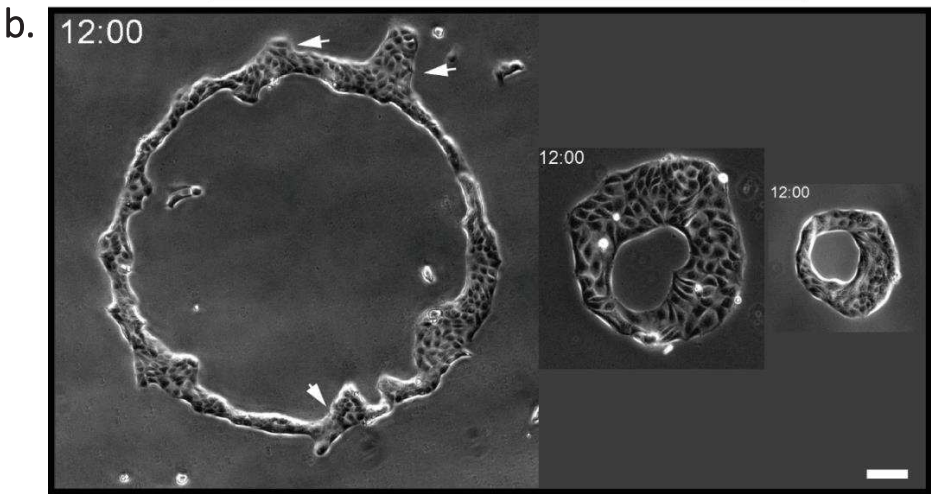


Figure 6.1. Ring behaviour depends on the system size. (a) Multicellular rings with various diameters. MDCK cells are plated on fibronectin rings. After washout, cells are able to migrate in and out (see 3.4.1). (b) After 12h, rings exhibit different behaviours. Finger-like extensions are visible on large rings ($1000\mu m$ diameter) while smaller rings "close" like wound healing assays (Begnaud et al., 2016; Brugués et al., 2014). Time in hh:mm, scale bar = $100 \mu m$.

6.2.2 Velocity fields and extraction of the coherence length

We next sought to quantify the motion of cells on the ring. To this aim, we computed for each time step the ring velocity field with Particle Image Velocimetry (PIV, see 3.7.3).

We could spot local flows of cells of similar length on every condition. These flows are characterized by their coherence length ξ , the length over which velocity vectors are correlated -i.e they point in the same direction. If ξ is equal to the ring perimeter, a global coherence is obtained. ξ varies between time steps: its value is very low when cell motion is not coordinated (usually at the beginning) and reaches a maximum ξ_{max} when cells acquire coherent motions. Therefore, we do not average ξ and we rather aim to extract ξ_{max} as a relevant measurement of the length over which cells can acquire a coherent motion.

In order to extract ξ_{max} we computed the correlation functions of the tangential velocity v_{θ} as defined in 3.7.4. Results are shown in Fig 6.2. The tangent at the origin allows to get values of ξ_{max} for each condition and we found out $\langle \xi_{max} \rangle = 330 \pm 15 \mu \text{m}$ with similar length for the different conditions (Figure 6.2c) suggesting that ξ_{max} is a property of our cellular system which does not depend on the system size.

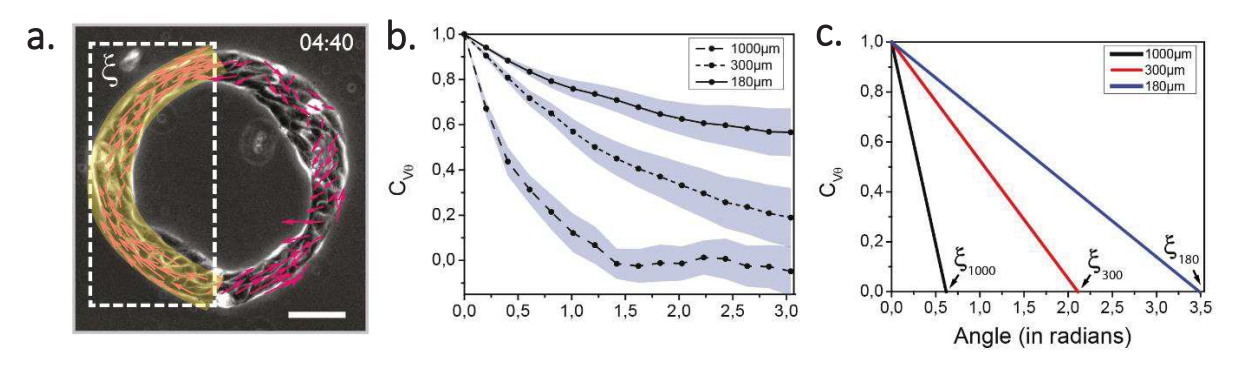


Figure 6.2. Coherence length characterization. (a) MDCK ring (300 μ m) with its associated velocity field. A coherence length ξ is highlighted: cell motion is correlated over this length. (b) Average correlation functions for the different configurations. (c) Tangent at the origins for the 3 systems. Intersects with y = 0 give the coherence length. Scale bar $= 50\mu$ m.

6.2.3 Rectification and coherence

Since the coherence length ξ_{max} is a generic property, we assumed that a new configuration with a perimeter equal or below ξ_{max} would exhibit global coherence in a majority of cases. Therefore, we designed another configuration with a diameter of 80µm resulting in a perimeter p of 250µm, below ξ_{max} .

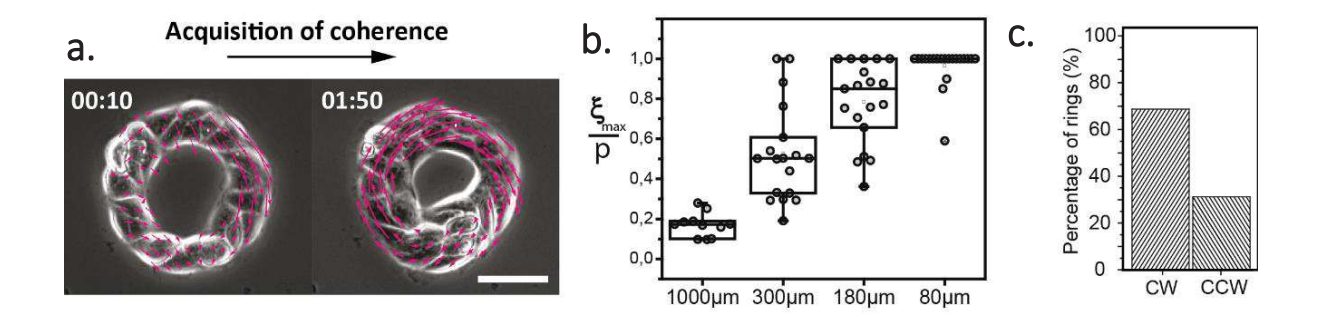


Figure 6.3. Generation of rotating rings. (a) Rings of $80\mu m$ in diameter undergo coherent rotation after a fluctuation phase. (b) Global coherence index as a function of the system size. Index increases with the decrease of the diameter. (c) Proportion of clockwise (CW) and counterclockwise (CCW) rotations. Scale bar = $50\mu m$.

We plated MDCK cells on the new patterns and we saw spontaneous rotations emerging suggesting that we successfully rectify collective motion of cells (see Figure 6.3a and Movie S25). To be quantitative, we defined for each condition an index of global coherence which is the ratio of the coherence length and the perimeter $\frac{\xi_{max}}{p}$ (Figure 6.3b). This ratio is equal to 1 when the ring exhibits a spontaneous rotation and is close to zero when the global coherence is low. We confirmed the behaviour observed in our experiments: the average coherence index increases as the perimeter decreases. We reached almost 100% of spontaneous rotations for the 80µm configuration.

Altogether, we managed to reproduce fully coherent system with the knowledge of ξ_{max} only.

6.2.4 Temporal description of coherence acquisition

Next, we sought to describe the temporal sequence of coherence acquisition. To do so, we computed for each time step the ratio $\frac{\xi}{p}$. When averaged out with all rings, we ended up with a linear progression of the ratio. (see Figure 6.4a) However, this linear trend does not reflect the actual behaviour. Indeed, because coherence does not appear at the same time on every ring, averaging all the sequences blurs the transition between the fluctuating state (*i.e.* random non-coordinated motion) and the global coherence state. Therefore, we aligned all sequences with respect to the coherence onset over a new pseudo-time and we found out that transition to the coherent state was a sharp process, happening in about 1 hour (Figure 6.4b).

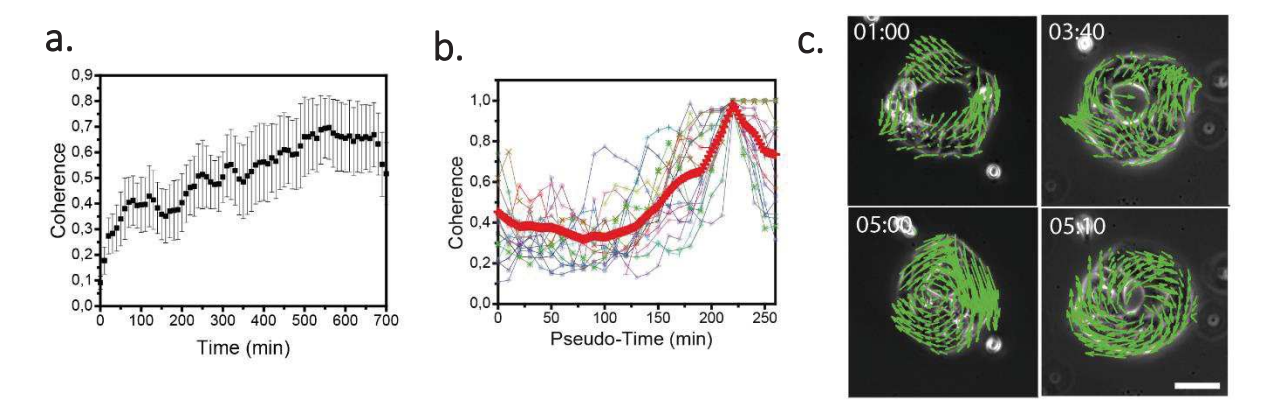


Figure 6.4. Temporal sequence of coherence acquisition. (a) Global coherence index $\frac{\xi}{p}$ averaged on all the rotating rings. (b) $\frac{\xi}{p}$ with sequences aligned on the onset of coherence on a new pseudo-time. (c) Two examples of coherence acquisition with velocity fields during the "fluctuating" state and during the coherent state. Time in hh:mm. Scale bar = 50μ m.

6.2.5 Coupling between ring velocity and persistence

Figure 6.4b shows the average temporal sequence of coherence acquisition. Among the different sequences, two ring populations emerged: rings that "transiently" rotate – they stop quickly after reaching $\frac{\xi}{p} = 1$, and rings that undergo persistent rotations. We sought to understand this phenomenon and we reported the existence of a coupling between the ring velocity and coherence duration (see Figure 6.5a). This relationship echoes the universal coupling between cell speed and persistence time (UCSP) (Maiuri et al., 2015) for single cell.

In addition, we observed an increase in velocity magnitude during coherence (see Figure 6.5b-c). We plotted the average cell velocities from the two phases of a rotating ring: when coherence did not appear or stopped, and during coherence (see Figure 6.5b-c). This could be the consequence of a potential positive feedback between velocity and alignment.

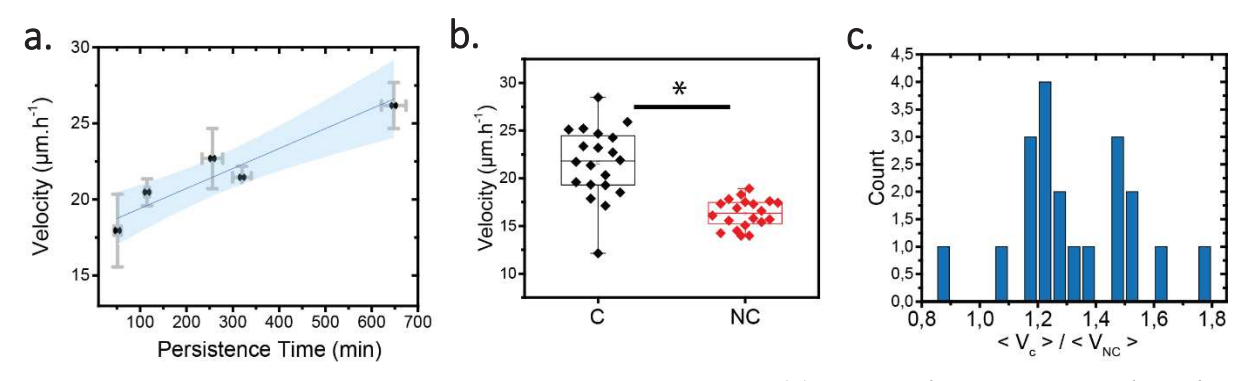


Figure 6.5. Coupling between persistence and velocity. (a) Ring velocity compared to the duration of coherence. N=20, data are binned for the corresponding persistence time. (b) Comparison of average cell velocities between the Coherence Period (C) and the Non-Coherent (NC) Phase. (c) Ratio of average velocities (coherence period over non-coherence period) for each rotating ring.

6.3 Cell mechanics

In order to decipher the emergence of a coherent rotation, we designed complementary strategies with labelling of lamellipodia and tight junctions in different experiments.

6.3.1 Distribution of polarities inside the ring

We first tried to understand how cell polarity was distributed within the ring at initial time points. To do so, we transfected transiently some cells with actin-GFP and mixed them with non-transfected cells. This created "mosaics" and allowed to localize lamellipodia, one readout of cell polarity that cannot be accessed in phase contrast images (Figure 6.6a, Movie S27). Cell polarities were distributed along the two tangential orientations, and only rare events of radial polarizations were seen (Figure 6.6b). This led us to hypothesize that tug-of-war between opposite polarities within the ring could potentially trigger the onset of coherence.

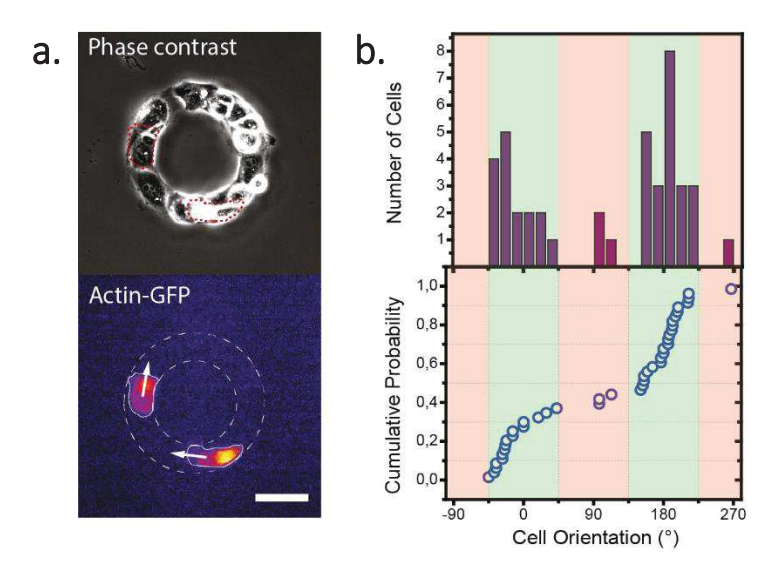


Figure 6.6. Cell polarity adopts a tangential bi-modal distribution. (a) "Mosaic" with actin-GFP transfected cells. Cryptic lamellipodia are visible and are used as polarity read-out. (b) Distribution of polarities for n = 20 rings. Radial polarization is almost absent. Scale bar = $50\mu m$.

6.3.2 Single cell properties within the ring

To go beyond this first observation, we aimed to extract single cell properties within the ring. This was achieved using intercellular junctions fluorescent proteins and images segmentation.

6.3.2.1 Tight junctions acquisition and segmentation

We used cells expressing ZO1-GFP, a tight junction protein, therefore present apically. ZO1 appeared to be more efficient for segmentation than the canonical cadherin-GFP proteins because the signal ratio junctions/cytoplasm was much higher. Also, good signals in cadherins are obtained only when cell packing is high and junctions denser, which was not the case in our ring experiments.

We acquired the ZO1-GFP rings with a confocal microscope (see Methods 3.6.3, Movie S27). We took z-stacks, from the glass coverslip to the very top of the epithelium, in order to capture all the tight-junctions. The final result is given by the maximal projections of all the planes.

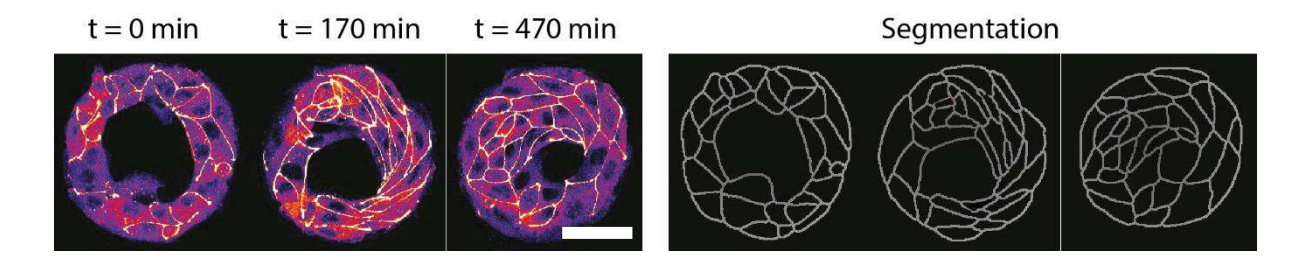


Figure 6.7. ZO1 allows cell segmentation. MDCK cells stably expressing ZO1-GFP (left) together with the associated segmentation (right) to extract single cell parameters. Scale bar = $50\mu m$.

Rings were treated on ImageJ and since many junctions were discontinuous, they were manually corrected. Watershed images were obtained through a Matlab custom code. Watersheds were then analysed through Tissue Analyser (see 3.7.6) and single cells parameters could be extracted.

6.3.2.2 Stretch

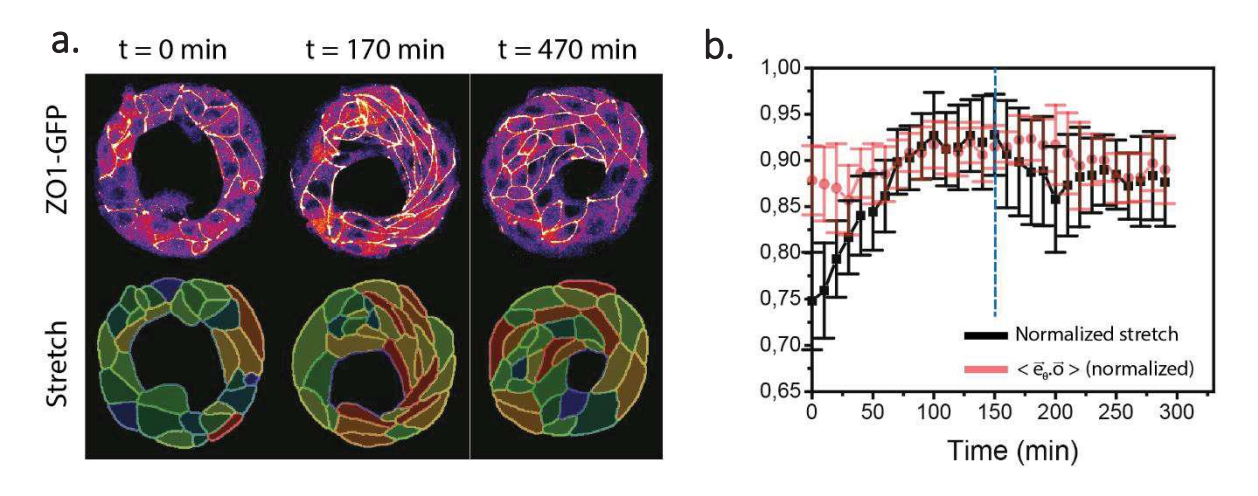


Figure 6.8. Stretch dynamics correlates with coherence acquisition. (a) Stretch map extracted from the visualization and segmentation of tight junctions. (b) Normalized Stretch aligned with respect to the coherence onset (dashed blue line). Tangential alignment (in red) is also shown (see 6.3.2.4).

A striking feature of the rotating rings with ZO1-GFP expression was the presence of cellular stretches appearing before the onset of coherence (see Fig 6.8a). This stretch can be quantified as detailed in 3.7.6. The stretch map in Figure 6.8a shows with a colour code the increase of stretch before the onset of coherence. The average stretch, aligned over a new pseudo-time with respect to the coherence acquisition (blue dashed line) shows a three-phases behaviour: (i) the stretch increases monotonically within few hours and reaches a plateau (ii) that lasts about 1h and (iii) the stretch decreases after the onset of coherence. This result can be seen as a marker of the internal tug-of-war between opposite polarities. Indeed, we hypothesized that two sets of opposite polarities are "pulling" in their associated directions. This potentially provoke a

cellular stretch, reported in our experiments. Then, when the tug-of-war is resolved the coherence starts and the cellular stretch is relaxed.

6.3.2.3 Alignment of polarities

To test the hypothesis of an internal tug-of-war between polarities we mapped cell polarities based on ZO-1 anisotropies as shown by Figure 6.9a. This polarity read-out gave us access to the percentage of aligned polarities. When we compared this value to the time of coherence onset, we saw a direct – linear – relationship. This result, combined with the stretch dynamics, indicates that two sets of opposite polarity could be in competition within the ring and this phenomenon might be determinant in the acquisition of coherence.

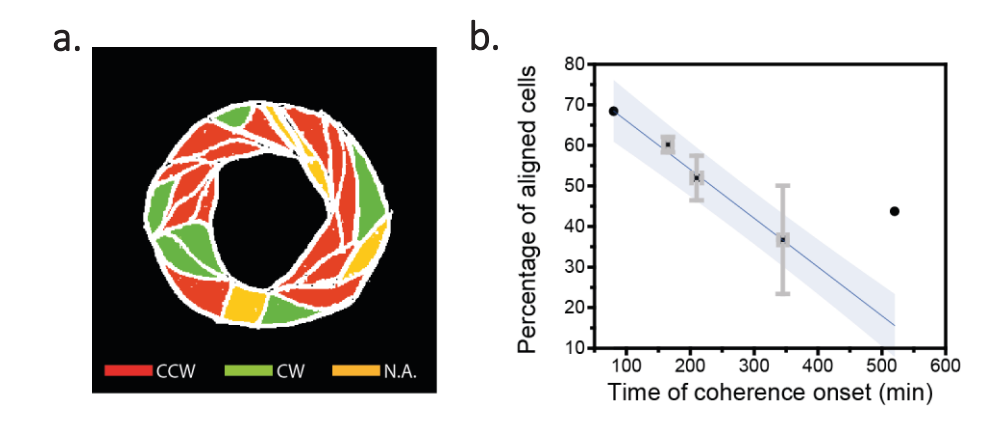


Figure 6.9. Coherence acquisition time depends on the percentage of aligned cells. (a) Clockwise (CW) or counterclockwise (CCW) polarities based on ZO1 anisotropies. N.A. refers to cases where polarity is uncertain/cannot be defined. (b) Percentage of aligned cells (based on the polarity described in (a)) as a function of the coherence acquisition time. Data are binned according to the corresponding time of coherence onset (n=10 rings). T_0 corresponds to the start of the experiment.

6.3.2.4 Tangential alignment

We next sought to quantify tangential alignment of cells within the ring before and after coherence. We defined the tangential alignment by the scalar product of the nematic orientation \vec{o} with the unit tangential vector \vec{e}_{θ} at the same position (see Figure 6.10a). This yields to the following expression:

$$Alignment = \langle \vec{o}. \overrightarrow{e_{\theta}} \rangle \qquad (6.1)$$

Cells are aligned tangentially when the scalar product equals to 1 and are radial when it is equal to 0. Alignment was always high, as shown by Figure 6.10b-c and did not vary much with respect to the coherence as reported in Figure 6.8b.

Interestingly, rings that did not undergo spontaneous rotations did not fail to align. No significant differences existed between the coherent and the non-coherent rings (Figure 6.10b-c).

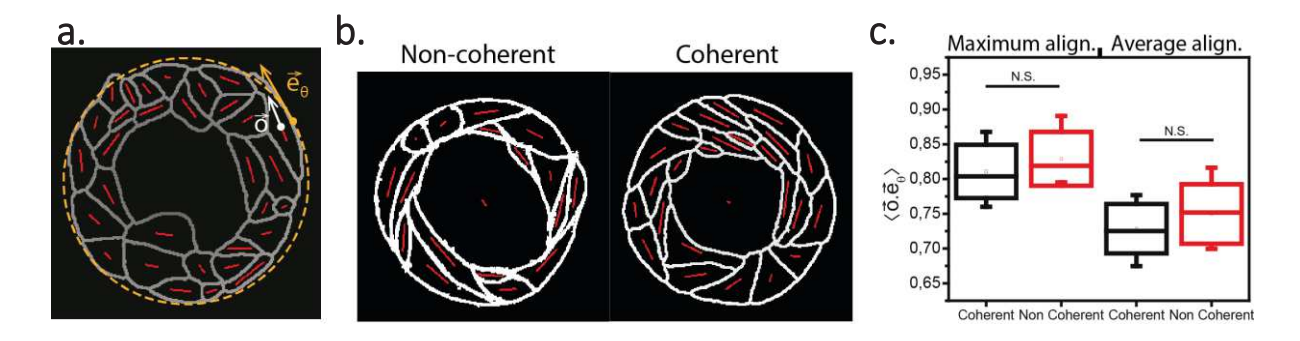


Figure 6.10. Non-coherent rings do not fail to orient tangentially. (a) Schematic definition of tangential alignment $\langle \vec{o}, \overrightarrow{e_{\theta}} \rangle$. (b) Cells orientations for non-coherent and coherent rings. In these examples, the non-coherent ring does not seem to fail to align tangentially. (c) Tangential alignment of coherent and non-coherent rings.

6.3.2.5 Density

We checked whether or not cell density could play a role in coherence. To this aim, we first computed the number of cells for each ring and compared it to the coherence. To have a better readout of coherence "intensity" we preferred here the integral of the ratio $\frac{\xi}{p}$. The results, shown in Figure 6.11a, shows a direct relation between cell number and coherence efficiency.

To confirm this first observation, we measured another read out for cell density. We transformed the segmented ring with a Delaunay triangulation (Barton et al., 2017), and we extracted the mean branch length of the network, as reported in Figure 6.11b-c. Low densities were associated with low coherence while higher cell densities corresponded to high coherence.

We made the hypothesis that low density could challenge continuity of the epithelium when coordinated motion tries to emerge. Indeed, we sometimes saw spontaneous ring breakages in regions where the local density was low (see 6.3.2.6). These phenomena impaired global coordinated motions.

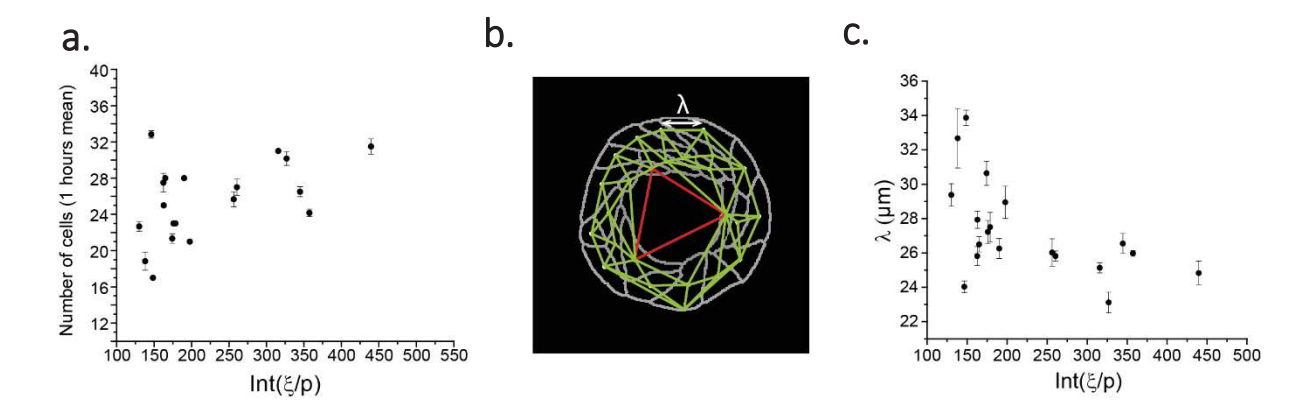


Figure 6.11. Cell density is associated with different coherence levels. (a) Number of cells in the ring (80 μ m) averaged over the first hour (to integrate early divisions) compared to the integral of the global coherence index. (b) Delaunay triangulation and definition of the branch length λ as another readout of cell density. Large artefactual branches (in red) are removed for analysis. (c) Branch length compared to coherence.

6.3.2.6 Cell divisions

We then investigated the role of cell divisions in the process of global coherence as divisions were reported in theoretical works to trigger interesting features, such as blockage or reversal of rotation (Siedlik et al., 2017; Soumya et al., 2015). In addition, we observed that cell divisions were associated to the formation of two opposite polarities within the ring (Figure 6.12a). This could potentially place divisions as polarity breakers.

Since cells were incubated at low serum concentration (1% FBS), cell divisions were decreased. Average rates of divisions for coherent and non-coherent rings were $0.34h^{-1}$ and $0.46h^{-1}$, respectively. However, these differences were not significant (Figure 6.12b; p = 0.084).

Nevertheless, differences appeared in the temporal sequences of divisions. Indeed, cells undergoing spontaneous rotations were associated with synchronous divisions, *i.e.* divisions occurred in very short time period (Figure 6.12c-d). On the other hand, non-rotating rings exhibited asynchronous and regular divisions all throughout the experiments (Figure 6.12c-d). We think that this regular introduction of polarity breakers might impede global coherence whereas initial "bursts" of divisions may be compensated afterwards.

In addition, spontaneous ring breakages also happened when divisions appeared in areas where local density was low: cell rounding associated with division into two daughter cells often challenged epithelium continuity in this configuration. This phenomenon is reported in Figure 6.12e. Lower attachment at the surface during cell rounding may contribute to this phenomenon also.

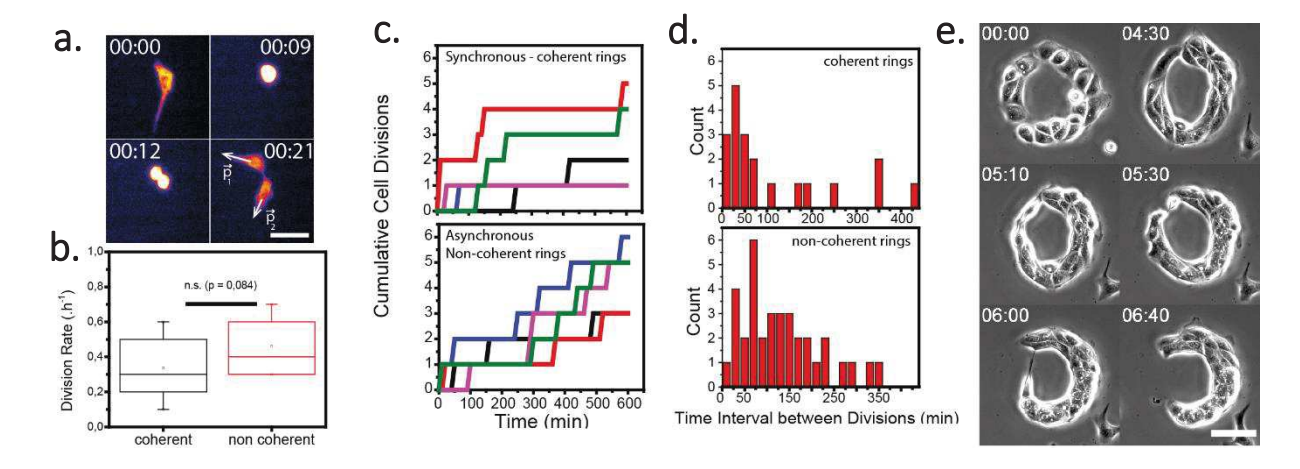


Figure 6.12. Divisions act as polarity breakers. (a) Cell division happening within the multicellular ring. Daughter cells have opposite polarities. Time in hh:mm. Scale bar = $20\mu m$. (b) division rates for coherent and non-coherent rings. (c) Cumulative cell divisions as a function of time for the two behaviors. Coherent rings exhibit "synchronous" divisions with afterwards large pauses without divisions. On the contrary, non-coherent rings are "asynchronous" and undergo constant divisions throughout the experiment. (d) Distribution of times between divisions showing a narrow peak at small values for coherent rings. (e) Cell division occurring in low density region induces breakage and impairs coherence. Time in hh:mm. Scale bar = $50\mu m$.

6.3.2.7 T1 transitions

Finally, we checked if neighbour exchanges – namely T1 transitions (Etournay et al., 2015, 2016) – could be a good read out of coherence.

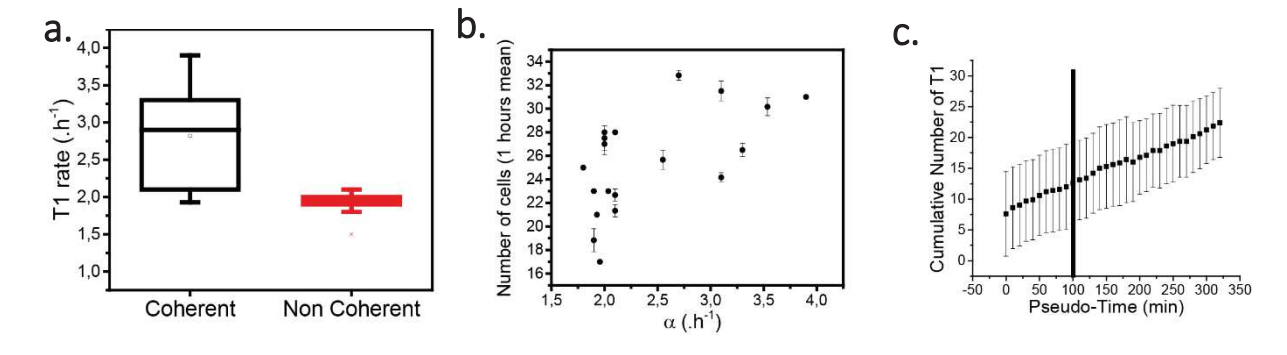


Figure 6.13. T1 rates in rings. (a) T1 rates for coherent and non-coherent rings. (b) Number of cells compared to the T1 rate (α). (c) Average cumulative number of T1 from sequences aligned with respect to the coherence acquisition (black line).

We computed T1 rates and compared it to the coherence (Figure 6.13a-b). We found out a direct link between the two quantities. However, it is not clear yet if these differences are a consequence of a difference in behaviours or if it is only related to the differences observed in cellular densities: since non-rotating rings are less dense, as reported before, lower rates in T1

could just be an epi-phenomenon. In addition, we did not see any change in T1 rate before, after, or at the onset of coherence (see Figure 6.13c).

6.4 Acto-myosin cables: internally-driven constraints

6.4.1 Immunostainings

We next sought to understand why cell polarities were distributed mainly along tangential orientations without any confinement. To this aim, we first stained 80µm rings for actin and myosin (Figure 6.14a). We observed the assembly of acto-moysin "cables" at the outer and inner boundaries, consistent with what was already reported at the free boundary of a migrating epithelium (Nier et al., 2015; Reffay et al., 2014). The presence of acto-myosin cables was not a consequence of the underlying fibronectin pattern and we also observed its assembly in MDCK colonies in normal culture conditions (Figure 6.14c). Also, it is important to notice that this cable is not an autonomous structure: this acto-myosin assembly is intra-cellular and is part of the cell (see Figure 6.14d, Movie S28).

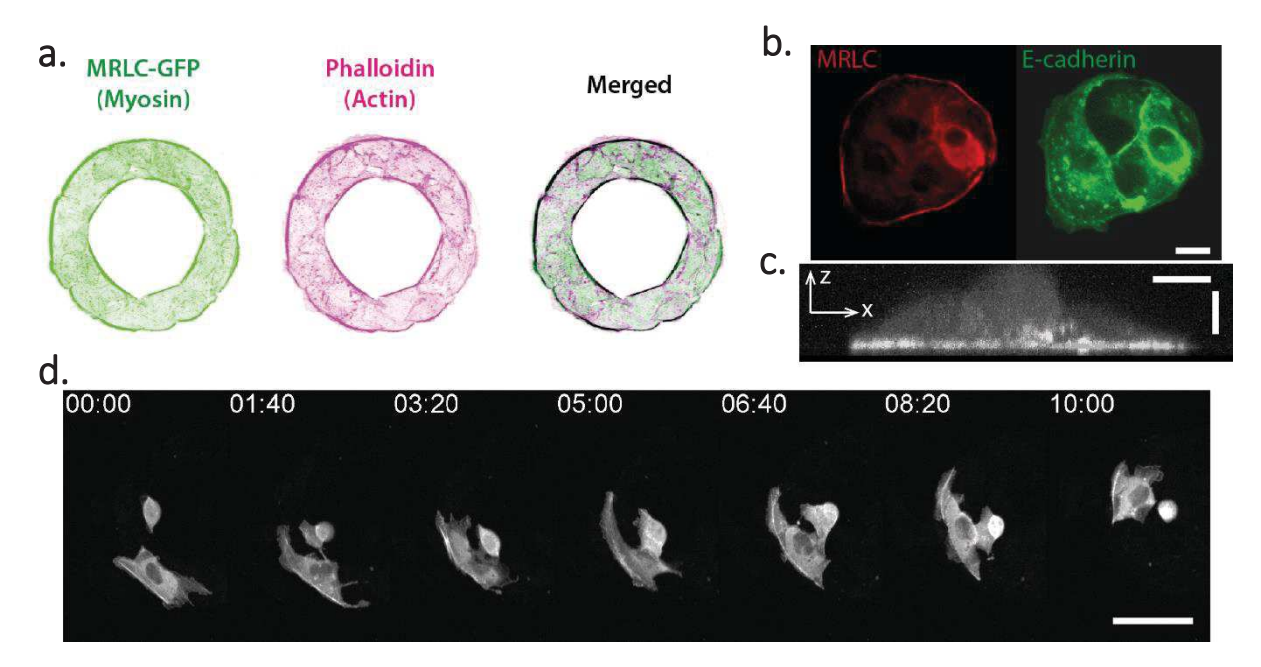


Figure 6.14. Acto-myosin cables assemble at boundaries. (a) Immunostaining performed on MDCK rings ($80\mu m$). An acto-myosin cable is visible at outer and inner boundaries. (b) The acto-myosin cable is also seen on regular MDCK colonies at the interface. Discontinuities in the cable are associated with the presence of lamellipodia. (c) The cable is a continuous structure. For (c-d) scale bars = $5\mu m$. (d) MDCK cell transfected with actin-GFP in for a mosaic experiment. Building and destruction of the actin cable can be seen as the cell migrates directionally (Movie S28). Scale bar = $25\mu m$.

6.4.2 Laser ablation experiments and tension measurements

To test whether or not these acto-myosin cables could act as mechanical constraints on cells, we performed laser ablation on the structures. Upon ablation, cables open and retract (Figure 6.15a, Movies S29-30). Comparison between the behaviour at the cadherin junctions and the acto-myosin cables revealed significant differences (Figure 6.15b). In addition, retraction velocity is informative of the tension stored in the cables and follows the equation (Mayer et al., 2010):

$$v = \frac{T}{\eta} e^{-\frac{t}{\tau}} \tag{6.1}$$

where T corresponds to the tension and η to the damping coefficient, related to the friction with the surrounding micro-environment (assumed homogeneous). Because η is not known, laser ablation provides relative measurements. Comparison between inner and outer cables did not give any significant differences (Figure 6.15c). We found $\frac{T_{in}}{\eta} = 0.69 \pm 0.064 \,\mu\text{m. s}^{-1}$ and $\frac{T_{out}}{\eta} = 0.71 \pm 0.023 \,\mu\text{m. s}^{-1}$ higher than the cortical tensions found in (Mayer et al., 2010) (in this work, $\frac{T}{\eta} = 10 \,\mu\text{m.min}^{-1}$). Therefore, we hypothesized that these two acto-myosin cables could act as internally driven constraints keeping the cellular cohort together and providing the adequate conditions for global rotation.

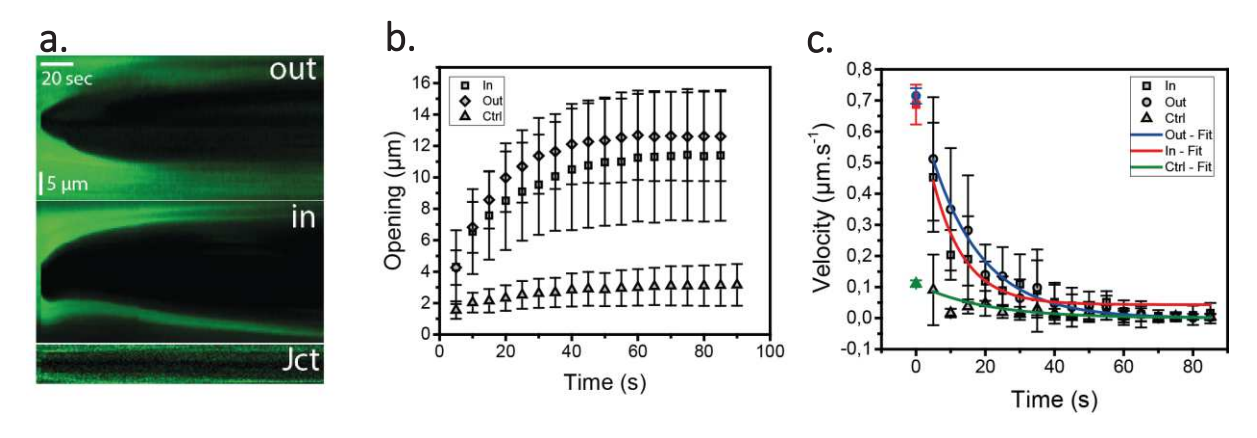


Figure 6.15. Acto-myosin cables are under tension. (a) Kymographs of laser ablation on inner and outer cables, and on cadherin junctions. (b) Opening distance after ablation. (c) Retraction velocity for the three systems. Initial tension is extrapolated from the exponential fits.

6.4.3 Local perturbation of the cable: caldesmon transfections

In order to test the role of acto-myosin cables we tried to locally perturb them. To do so, we transfected some cells with caldesmon, a calmodulin-binding protein that inhibits myosin ATPase activity and impair conformational changes of the myosin head (Helfman et al., 1999) (Figure 6.16a). The consequent effect could be considered as a knock-down of myosin activity.

Immunostaining of CaD and phosphorylated myosin showed co-localization indicating that the protein was properly functioning (Figure 6.16b, Movie S31).

Then, transfected cells were mixed with normal cells in proper dilutions so that we ended up with only 1-4 CaD-positive cells in the rings. In majority of cases, cells with defect in myosin activity did not exhibit a proper cable assembly and they escaped radially the ring with a "leader" cell behaviour (Figure 6.16b). As a consequence, we observed a decrease in average coherence in the group with local defective cells (Figure 6.16c). The fact that rings with transfected cells could still rotate in some cases could be explained partially by the level of expression of caldesmon after transfection. Indeed, Figure 6.16d shows that the coherent rings with transfected cells express less caldesmon, on average than the non-rotating rings.

Altogether, these results suggest that acto-myosin cables could act as internally driven constraints necessary to the proper initiation of coherence.

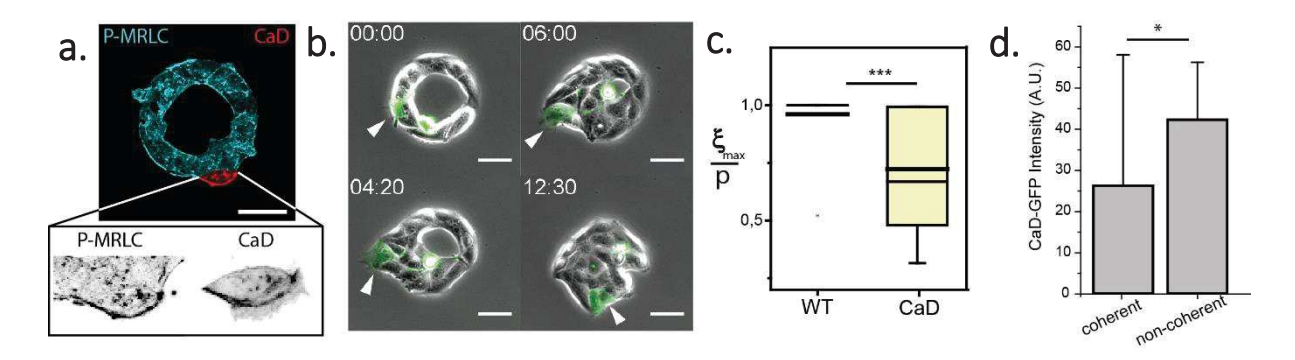


Figure 6.16. Local perturbation of cables lead to cellular escape. (a) Mosaic with a single cell transfected with caldesmon, a calmodulin binding protein inhibiting myosin activity (CaD). The inset shows co-localization between CaD and myosin suggesting a functional protein. CaD-positive cells often escape the ring and grow lamellipodia. (b) Cell expressing CaD escape the cellular ring and breaks coherence. (c) Comparison of coherent rings between WT and CaD groups. (d) The coherent rings with CaD cells exhibit lower CaD intensities, suggesting that levels of expression could tune further the phenotypes. Scale bars = $50\mu m$. Time in hh:mm.

6.5 RhoA activity

Because RhoA is essential in cell motility and shape changes (through myosin phosphorylation and actin polymerization, see (Arnold et al., 2017; Sit and Manser, 2011)), we decided to probe RhoA activity within the ring. We used a FRET biosensor, as described in Material and Methods (3.6.3.1).

6.5.1 Controls of the biosensor

We first checked if the FRET biosensor was a reliable tool to quantify RhoA activity in our assays. To do so, we incubated MDKC epithelia with activating and inhibiting drugs: RhoA activator II and C3-transferase (RhoA specific inhibitor). We compared the dynamics with normal epithelia without drug incubation. As expected, we observed an increase in the overall FRET intensity upon RhoA activation and a gradual decrease with inhibitor incubation (Figure 6.17a). In the control epithelium, we observed a slight decrease of the FRET intensity in the course of the experiment. Since we acquired every 10min only and did not observe any bleaching in CFP, we first attributed this decrease to spreading that could potentially feedback RhoA activity. However, tests with a fully confluent epithelium also gave the same kind of decrease ruling out this hypothesis. Further experiments have to be done to understand this phenomenon.

Next, we designed a new cell line expressing a modified FRET biosensor, unable to interact with the RBD domain therefore unable to fold. This construct, named "dead" sensor, is an additional control to see if our WT biosensor gives a reliable read out. When we imaged rings with either the WT cell line or the modified one, we saw significant differences (Figure 6.17b). Comparison between the two histograms of intensity values confirmed observations we made and exhibited a clear shift (Figure 6.17b).

Finally, we could assume that the FRET biosensor used in this study was an appropriate tool to probe RhoA activity.

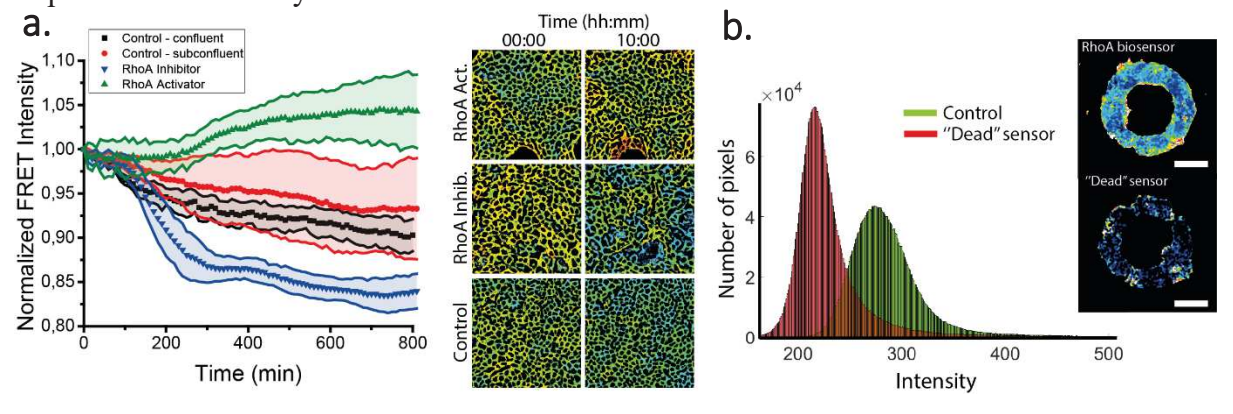
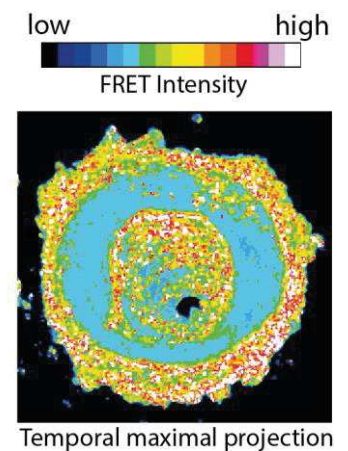


Figure 6.17. The FRET biosensor is reliable tool for RhoA activity. (a) Test of the biosensor with an activator and an inhibitor, compared with normal epithelia with various confluency. (b) Dead sensor and WT sensor intensity histograms. For the dead sensor, values are peaked around the lowest values of the WT sensor. Scale bar = 50μ m.

6.5.2 Spatial localization of RhoA



Highest RhoA activities were located at the inner and outer boundaries. Temporal maximal projections confirmed that high levels of RhoA co-localize with the acto-myosin cables (Figure 6.18, Movie S32). This further confirms the constraint applied by the boundaries. We could not spot any higher RhoA activity at the cell-cell junctions. This allowed us to consider the cellular ring as a continuum.

Figure 6.18. RhoA activity is higher at acto-myosin cables. Temporal projection of the FRET signal. RhoA activity mainly localizes at boundaries, where acto-myosin cables are present.

6.5.3 FRET levels and coherence

In order to quantify FRET levels, we segmented the ring in a way that cables are distinguished from the cellular "bulk" (Figure 6.19a). The ring is coarse-grained and in a first approach considered as a continuum. We extracted average FRET intensities for the whole bulk and cables. Even though we distinguish the cables and the "bulk", acto-myosin cables are parts of the cells and they are not autonomous entities external to cells.

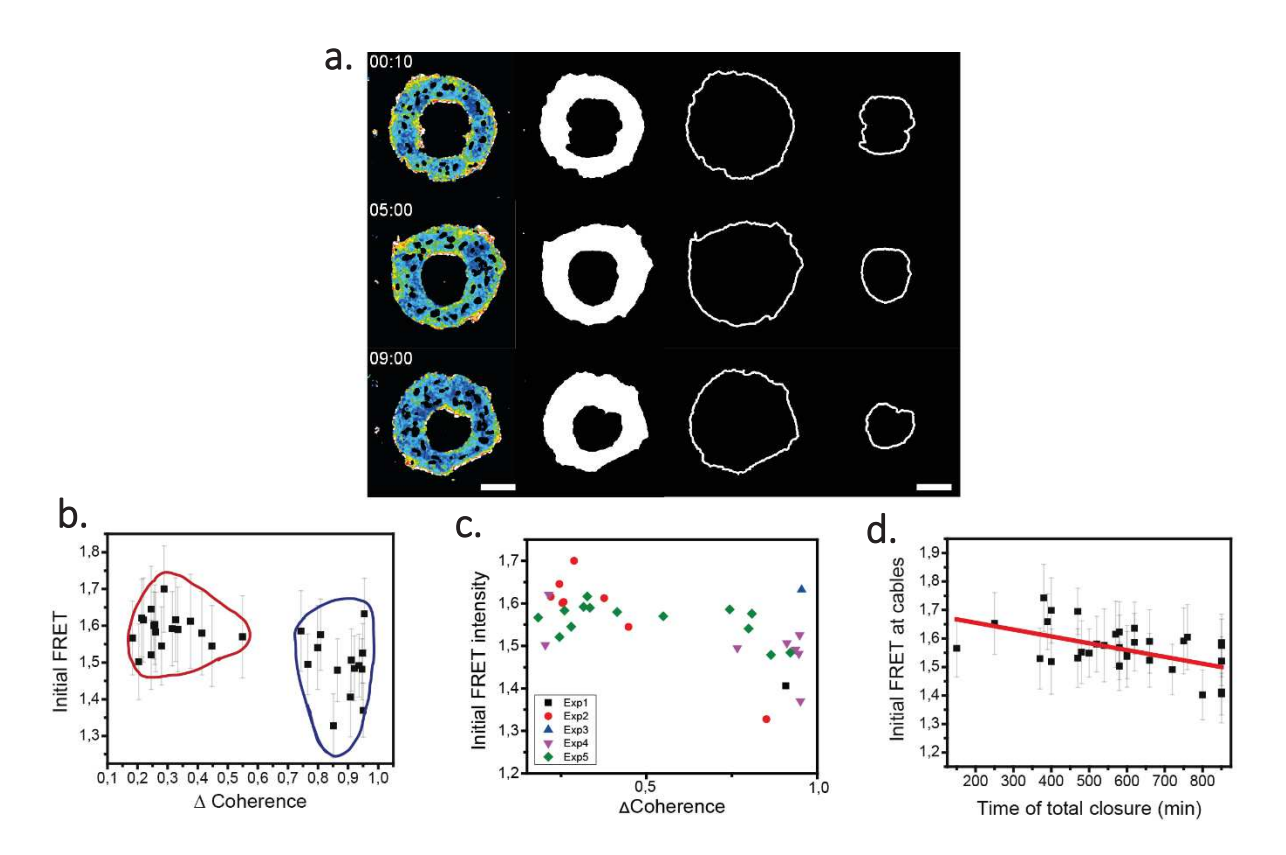


Figure 6.19. RhoA activity is associated with different coherence levels (a) Rings are segmented to separate cables activity and "cells" activity. Scale bar = 50μ m. (b) Initial FRET levels averaged over the full ring at t0 compared to the amplitude of the coherence together with the plot with a colour-code for experiments (c). (d) Initial FRET levels at cables compared to the time of ring closure.

We observed significant differences in FRET initial levels (at t_0) for the cells bulk. The results are reported in Figure 6.19b where FRET intensity (therefore RhoA levels) are compared to the amplitude of coherence Δ Coherence ($\frac{\xi_{max} - \xi_{min}}{p}$). Low FRET levels were associated with coherent rings whereas higher levels of FRET corresponded to non-coherent rings. We also made sure that this effect was not experiment dependent. Therefore, we plotted in Figure 6.19c the same graph than 6.19b with a colour-code for experiments.

Then, comparison between initial FRET levels at cables and closure time showed that highest cables activities are correlated with faster contraction and closure of the ring (Figure 6.19d).

Taken together, these first observations indicated that various RhoA levels are associated with different collective behaviours.

6.5.4 RhoA activity and velocity

Next, we observed that initial RhoA levels were also correlated to the overall velocity amplitude as reported in Figure 6.20a.

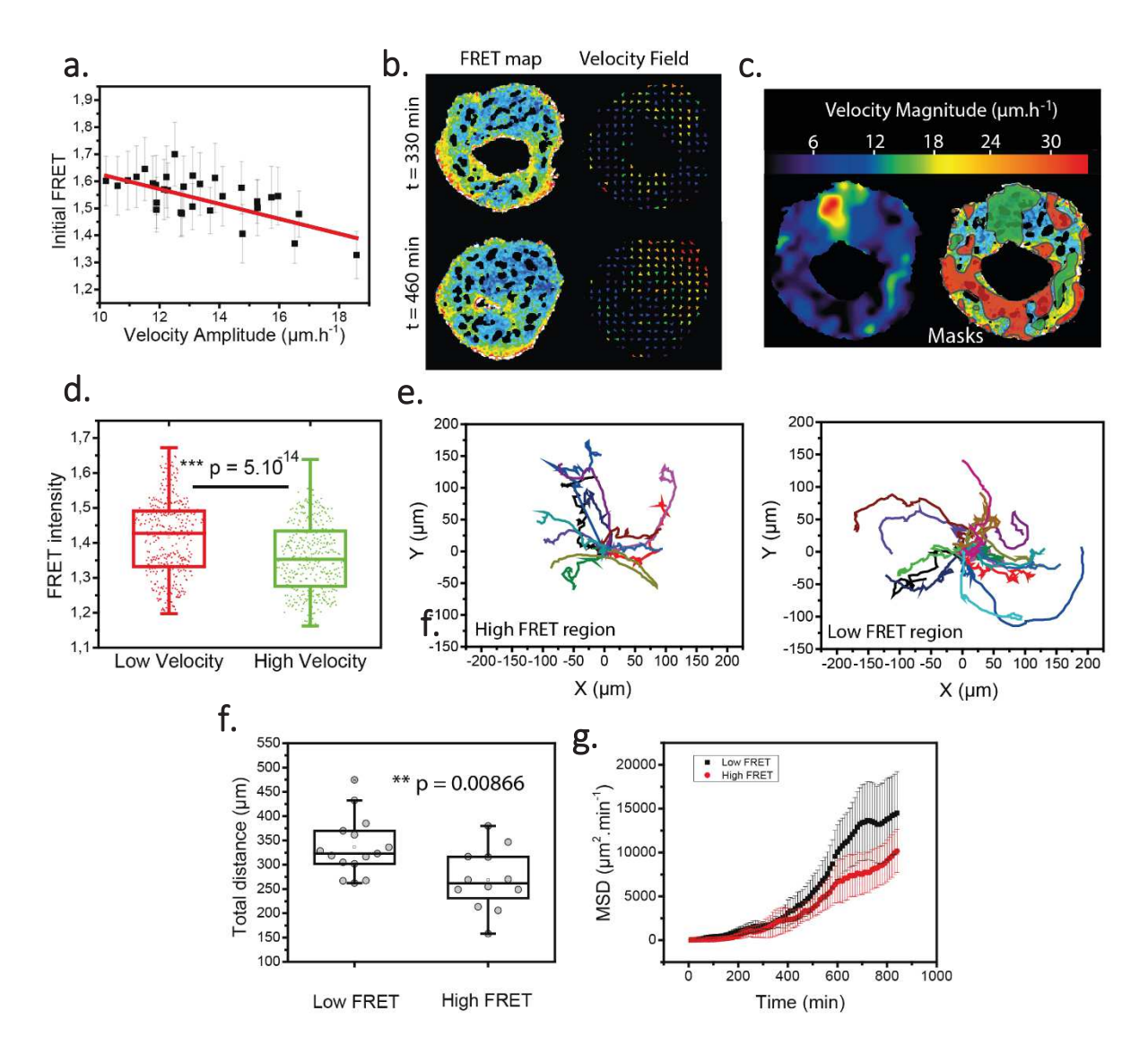


Figure 6.20. RhoA and velocity are anti-correlated. (a) Initial FRET velocity as a function of the mean ring velocity. (b) FRET map and velocity field (c) Velocity magnitude map. Regions in green correspond to high velocities and in red to low velocities. (d) Comparison between FRET levels and velocities for each ring at each time point. Differences are significative, tested with a one-way Anova. (e) Trajectories of nuclei. (f) Distance travelled by nuclei as a function of the FRET intensity. (g) Mean Squared Displacement of nuclei coming from high FRET and low FRET regions.

To test further this feature, we compared for each ring and each time point the FRET map with the velocity field (Figure 6.20b). More specifically, we extracted regions of high velocities ($> 15 \,\mu m.h^{-1}$) and low velocities ($< 7 \,\mu m.h^{-1}$) and we compared them with RhoA activity (Figure 6.20c). Data are reported in Figure 6.20d and confirmed the fact that high RhoA activity is associated with low velocity.

To go beyond this coarse-grained analysis, we also tracked single cell by analysis of their nucleus trajectory. We distinguished two populations: nuclei coming from high FRET regions

and those coming from low FRET regions. Mobility of nuclei coming from low FRET regions was higher than the one from nuclei in high FRET regions, especially during the coherent phase (the super-diffusive regime in the Mean Squared Displacement – MSD – plot). Details are provided in Figure 6.20e-g.

Altogether, we showed that in our assay, on the time and length scales we are probing, that RhoA mainly contributes to changes in velocity and strength of the acto-myosin cables. We did not report any Turing patterns comparable to those exhibited in *Xenopus* oocyte for example (Bement et al., 2015) but we observed strong accumulation at boundaries.

6.5.5 Reaction-diffusion patterns of RhoA

NB: computations and analysis are done with Rémi Berthoz, a Master Student in the team.

In his 1952 paper, Turing proposed a set of two differential equations dictating the spatiotemporal dynamics of an activator and an inhibitor (Turing, 1952). More specifically, he described the configuration of a ring of cells where appearance of reaction-diffusion patterns could potentially drive morphogenetic events. In addition, RhoA has already been reported to exhibit Turing patterns and actin polymerization was hypothesized to be the inhibitor (Bement et al., 2015).

Even though we did not report striking patterns in our rings, we wonder if the accumulation of RhoA activity at the boundary could be one of the realizations of the reaction-diffusion equations due to boundary effects.

We used the following set of equations, directly taken from Turing's original paper (Kondo and Miura, 2010; Turing, 1952):

$$\frac{\partial u}{\partial t} = F(u, v) + D_u \frac{\partial^2 u}{\partial x^2}$$
 (6.2)

$$\frac{\partial v}{\partial t} = G(u, v) + D_v \frac{\partial^2 v}{\partial x^2}$$
 (6.3)

where F(u, v) = au + bv + c - du and G(u, v) = au - dv.

We chose the classical Turing scheme of an activator-inhibitor couple as shown in Figure 6.21a. In this context, a corresponds to the production rate (dependent on the concentration of u), b – set as negative – to the inhibition of u by v, c to a constant production rate, and d to the degradation rate. All these parameters – except c – are homogeneous to T^{-1} . c is homogeneous to M. T^{-1} .

We set the boundary conditions as a barrier for diffusion. Briefly, species cannot diffuse out of the ring. This translates into a simple computational rule described in Figure 6.21b. All parameters of the reaction-diffusion equations remain the same throughout the ring: we did not bias the dynamics at boundaries by introducing variations in parameter values. In addition, the ring is considered as a continuum and we did not include cell-cell junctions.

Simulations generated ratiometric maps of the two species (see Figure 6.21c) where the ratio $\frac{u}{v}$ is plotted. We found out that boundary effects can lead to the presence of one species and the absence of the other at the ring boundaries specifically. Even though u and v can be virtually any compound that can diffuse and react within the cytoplasm, our results suggest that the large RhoA activity at boundaries could be explained by simple reaction-diffusion equations, as described by Turing in 1952.

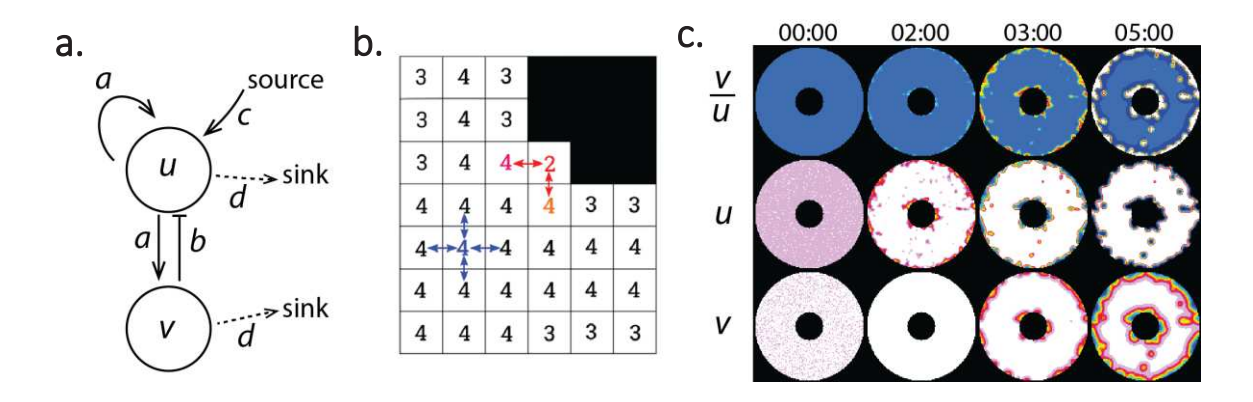


Figure 6.21. Boundary effects induce biased distributions of chemicals through reaction-diffusion. (a) Feedbacks within a classical couple of an activator and an inhibitor. Kinetics parameters are detailed in 6.5.5. (b) Connectivity map describing the boundary conditions. At boundaries, chemicals cannot diffuse outwards. (c) Evolution of the two species u and v together with their ratio. Time in mm:ss. Simulations from Rémi Berthoz.

6.6 Theoretical modelling: a Vicsek-based approach

Since we described in section 6.3 how single cell polarities and more generally single cell mechanics play a key role in setting coherent motion and because RhoA regulation is mostly embedded into cell velocity, we used a theoretical approach based on a Vicsek model. However, we did not use the classical approach described in section 2.5.2 with cell velocity only: we implemented cell polarity and cell-cell interactions of polarity as well as free boundaries modelling acto-myosin cables.

We will first describe the details of the model by presenting its constitutive equations then we will explicit how the free parameters have been measured experimentally. Finally, results, validation and new outputs from the model will be detailed.

6.6.1 Description of the model

Cells are considered as self-propelled particles of radius r_k and with a position X_k . The particle velocity V_k can be derived from the knowledge of X_k at each iteration and its orientation is governed by the direction of the polarity P_k (this assumption will be backed up by experiments in section 6.6.2). Altogether, this leads to the first set of equations:

$$\frac{dX_k}{dt} = V_k \qquad (6.4)$$

$$V_k = \mathbf{P}_{C_X} \cdot cP_k \quad (6.5)$$

where c corresponds to the particle velocity magnitude. In addition, \mathbf{P}_{C_X} defines the projection of the polarity vector onto the set of admissible velocities (to prevent overlap of particles) such as:

$$C_X = \{ V \in (\mathbb{R}^2)^N | \forall i < j, \ D_{i,j}(X) = 0 \rightarrow \nabla D_{i,j}(X). V \ge 0 \}$$
 (6.6)

where $D_{i,j}(X) = ||X_i - X_j|| - (r_i + r_j)$ corresponds to the distance between two particles.

Polarity P_k , associated to each particle, is assumed to dynamically relax on the mean polarity $\overline{P_k}$ of the neighbouring particles with a velocity $\mu > 0$ rad. h^{-1} . It relaxes also to the velocity direction $\frac{V_k}{\|V_k\|}$ with a velocity $\nu > rad$. h^{-1} . In addition, P_k is not still and undergoes random angular diffusion. Taken these assumptions together, this yields:

$$dP_k(t) = \mathbf{P}_{P_k^{\perp}} \circ \left(\nu \left(\frac{V_k}{\|V_k\|} - P_k \right) dt + \mu (\overline{P_k} - P_k) dt + \sqrt{2D} dB_t^k \right)$$

$$\overline{P_k} = \frac{\sum_{j, \|X_i - X_j\| \le R} P_j}{\left\| \sum_{j, \|X_i - X_j\| \le R} P_j \right\|}$$

$$(6.8)$$

Because acto-myosin cables were hypothesized to act as internally-driven constraints and were shown to be under tension, we next sought to model their action on particles. To do so, we considered the inner and outer cables as an ensemble of *N* small springs connecting each particle at the outer and at the inner boundaries. We can derive the global energy such as:

$$E(X) = \sum_{j=1}^{N} k_{b,j} \left(1 - e_j \cdot e_{j+1} \right) + \sum_{j=1}^{N} k_{st,j} \left(\left\| X_{j+1} - X_j \right\| - l_0 \right)^2$$
 (6.9)

$$e_j = \frac{X_j - X_{j-1}}{\|X_i - X_{j-1}\|} \tag{6.10}$$

The first term, associated to the bending modulus $k_{b,j}$, corresponds to the bending energy of the springs connecting the particle X_j to X_{j+1} and X_{j-1} . This is followed by the stretching energy and the associated stretching modulus $k_{st,j}$.

Considering this set of equations (6.9 and 6.10), acto-myosin cables exert on any boundary particles a force $F_{cable\ passive}(X_i)$. This force is given by:

$$(F_{cable_passive})_k = \begin{cases} -\nabla_{X_k} E(X), & if \ k \in I_{in} \\ 0 & else \end{cases}$$
 (6.11)

The bending and the stretching presented here represent the passive component of the actomyosin cables.

However, considering acto-myosin cables as passive elastic materials would not be consistent with their active properties, described in 2.2.1.1 and 2.2.1.3. Indeed, actin and myosin can be considered as an active gel, intrinsically out-of-equilibrium. In addition, FRET experiments showed high levels of RhoA at the boundaries suggesting a high activity at acto-myosin cables. These fundamental properties can be modelled by incorporating an active component to the force. This gives:

$$(F_{cable_active})_k = f.n_k + f.(sgn(t_k \cdot P_k)t_k - P_k)$$
 (6.12)

with f the active force and n_k the unit vector directing the force. This active force is set radial and does not depend on the bending nor the stretching moduli. It essentially translates the activity of acto-myosin cables. It is important to note that cables also have a nematic effect on the cells: as shown in Figure 6.14d cells migrate along the acto-myosin cable and are aligned tangentially. This is translated by the term $f.(sgn(t_k \cdot P_k)t_k - P_k)$ in Eq. 6.12 where t_k denotes the normalized tangent vector.

Incorporating forces exerted by acto-myosin cables into Eq. 6.7 yields to the final set of equations:

$$\frac{dX_k}{dt} = V_k \qquad (6.4)$$

$$V_k = \mathbf{P}_{C_X} \cdot cP_k \quad (6.5)$$

$$dP_{k}(t) = \mathbf{P}_{P_{k}^{\perp}} \circ \left(\nu \left(\frac{V_{k}}{\|V_{k}\|} - P_{k} \right) dt + \mu (\overline{P_{k}} - P_{k}) dt + \alpha \left(F_{cable_passive} \right)_{k} dt + \beta \left(F_{cable_avtive} \right)_{k} dt + \sqrt{2D} dB_{t}^{k} \right)$$
(6.13)

Decomposing Eq.6.13 into distinct phenomena gives:

 $dP_k(t)$ = Relaxation on the mean velocity direction + Relaxation on the mean neighbouring polarity + Force exerted by the cables + Angular diffusion of the polarity

This model allows us to probe with minimal number of parameters the interaction of single cell polarities and its subsequent emergence of coherence together with the action of acto-myosin cables.

In order to capture the phenomena observed in experiments, we next sought to measure experimentally the free parameters of the model.

6.6.2 Experimental measurements of the model parameters

6.6.2.1 Angular diffusion

We first measured cell polarity diffusion *D*. Because all the parameters included in the model previously described are single cell parameters, we analyzed the motion of individual MDCK cells on flat surface coated with fibronectin at the same concentration as the circular patterns.

Cell polarity orientation was set according to the cellular long axis. Its direction was defined in phase contrast either by the largest lamellipodium or by the direction of the anisotropy, as shown by Figure 6.22a.

Over time, P_k did not exhibit strong angular diffusion and three major behaviors emerged: (i) cells with still polarity with only minor deviations from the original polarity, (ii) polarity shifts at 180° and (iii) cells without polarity (excluded from the analysis). This is reported in Figure 6.22a.

Quantifications extracted from these observations yielded to an angular diffusion coefficient $D = 0.016 \, rad^2 \, min^{-1}$. This is derived from the angular Mean Squared Displacement (MSD) as shown in Figure 6.22b.

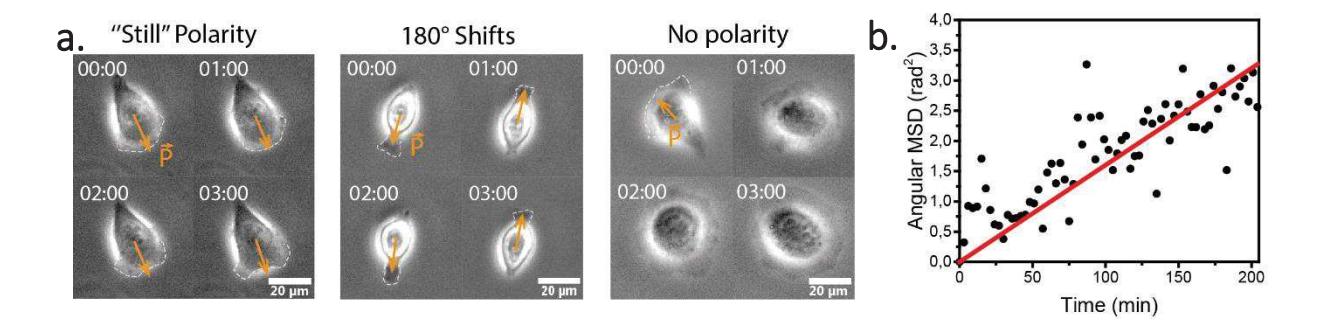


Figure 6.22. Angular diffusion of cell polarity. (a) Different type of behaviours of diffusing cell polarity. The lamellipodium taken for setting polarity direction is highlighted with a dashed line. Time in hh:mm. (b) Angular Mean Squared Displacement as a function of time. The slope from the linear fit gives D. $D = 0.016 \, rad^2$. min^{-1} . Time in hh:mm.

6.6.2.2 Polarity relaxation

Polarity P_k relaxes on the mean polarity $\overline{P_k}$ of the neighboring polarity with a rate $\mu > 0$. To extract relevant timescales for μ we first isolated canonical examples of polarity relaxation: in mosaic experiments, cells with a polarity opposite to the direction of rotation relax after a time τ on the direction of motion (assumed to be equivalent to $\overline{P_k}$) (see Figure 6.23). A first approximation would be to consider that $\mu = \frac{1}{\tau} \cdot \pi$. Therefore, we found that $\mu = 2.87 \pm 3.03 \, rad. \, h^{-1}$ (mean \pm SD) and this gave us an order of magnitude of μ .

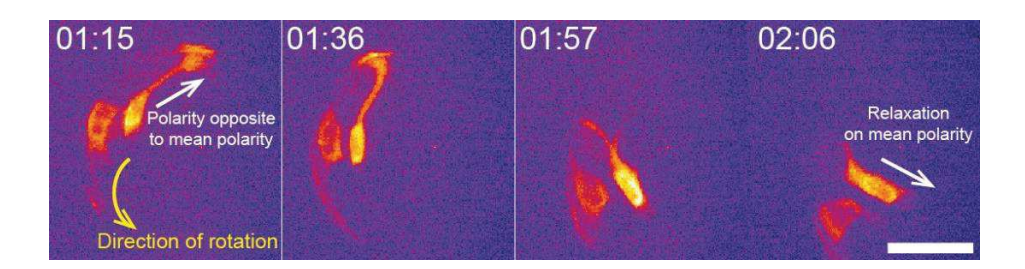


Figure 6.23 Cellular ring with actin-GFP transfected cells. Cells with polarity opposite to the mean polarity are tracked and their relaxation times are measured. Scale bar = $20\mu m$. Time in hh:mm.

In the following, we hypothesize that the relaxation on velocity direction follows the same rules, giving $\nu = \mu$.

6.6.2.3 Polarity precedes velocity

We saw in section 6.6.1 that the particle velocity V_k was governed by the polarity P_k such as $V_k = cP_k$ (Eq. 6.10). We tested this assumption. To do so, we isolated cells that are not already spread in mosaic experiments and therefore did not grow any cryptic lamellipodium (see Figure 6.24a). These cells then acquire polarity by polymerization of cryptic leading edge, and this

can be correlated to the appearance of a net displacement. Figure 6.24b-c reports the different cells analyzed.

We reported that cells first acquire a polarity with a growing cryptic lamellipodium before a net displacement – and therefore a velocity – can be seen (Figure 6.24a-c). This supports the assumption we made in the model.

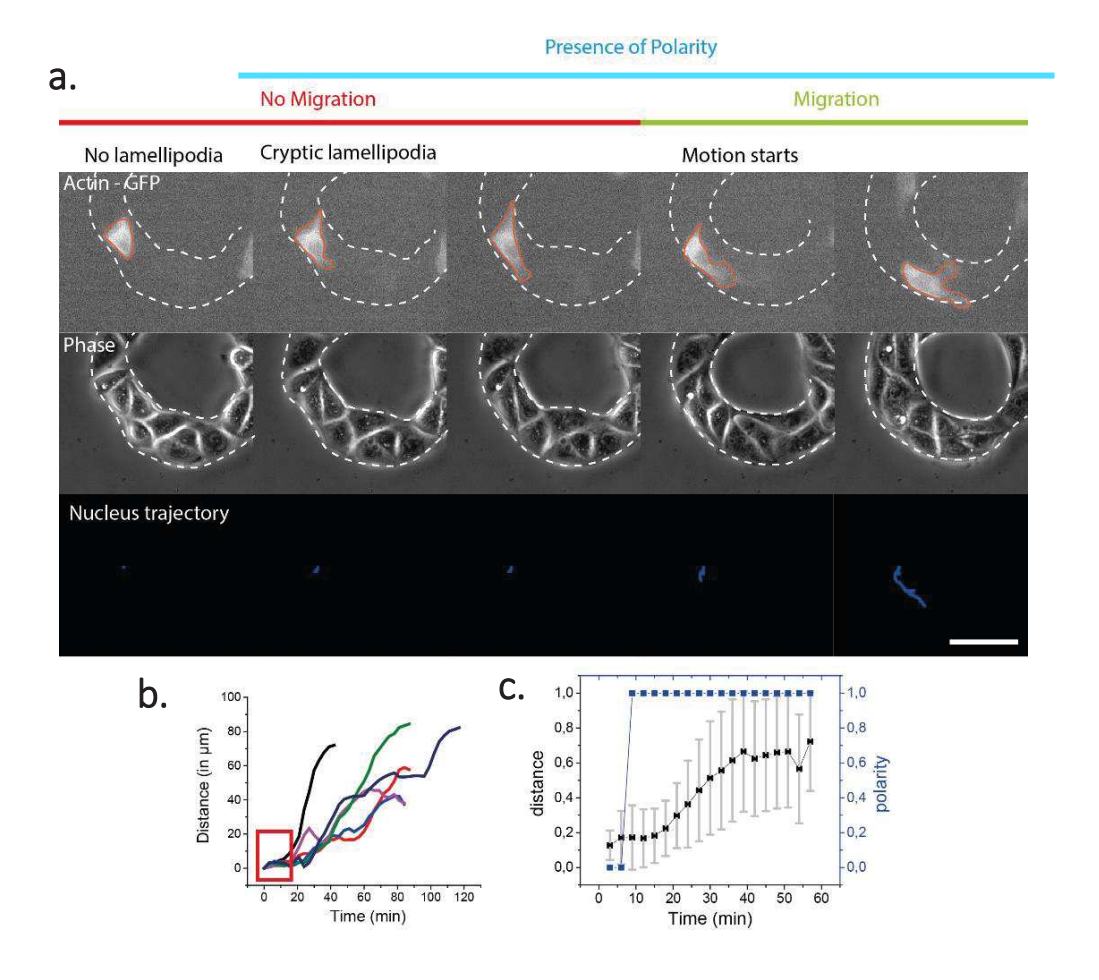
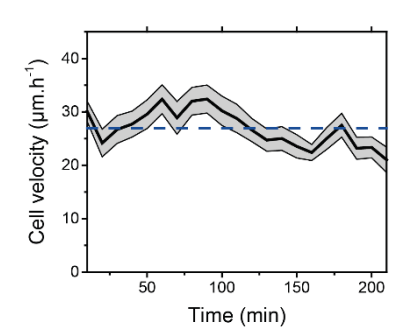


Figure 6.24. Polarity precedes velocity. (a) Non-spread cell transfected with actin-GFP within a ring ($80\mu m$). Growth of a cryptic lamellipodium (as a readout for cell polarity) is correlated with cell motion. (b) Displacement of centers of mass for n=5 cells. The red box indicates the period where there is not net displacement but where the polarity is set. (c) Displacement of centers of mass aligned with respect to the polarity acquisition (p=1, 0 else).

6.6.2.4 Single cell velocity



Because single MDCK cells on flat surface do not exhibit any motion, we measure single cell velocity during coherent motion. We found an average velocity $\langle c \rangle = 26.92 \,\mu m. \, h^{-1}$ (see Figure 6.25).

Figure 6.25. Average individual cell velocity measured during coherent motion.

6.6.2.5 Acto-myosin cables tension

Even though tension *per se* is not embedded in the model, extraction of cables tension allows us to see if there are differences in "strength" in the outer and the inner cables. This is necessary to tune the bending and the stretching modulus $k_{b,k}$ and $k_{st,k}$.

Laser ablation experiments done in 6.4.2 allow to derive the relative tension $\frac{T}{\eta}$ for each cable. Exponential fits of the retraction velocity (see Figure 6.15) gave the following values: $\frac{T_{in}}{\eta} = 0.69 \pm 0.064 \ \mu m. \ s^{-1}$ and $\frac{T_{out}}{\eta} = 0.71 \pm 0.023 \ \mu m. \ s^{-1}$. Therefore, considering the damping coefficient η constant and homogeneous in space, we assumed that $T_{in} = T_{out}$.

6.6.2.6 Active force

We defined the active force as a constant radial force exerted on the cells by the acto-myosin cables. This force has been set to 10 nN, consistent with previous works (Nier et al., 2015) and this is the order of magnitude of forces applied by stress fibres (Guthardt Torres et al., 2012; Yoshinaga and Marcq, 2012).

6.6.2.7 Orders of magnitude taken from the literature

Values of k_b and k_{st} associated to acto-myosin cables cannot be extracted from our experiments. Therefore, we took values reported in the literature for acto-myosin stress fibers (since cables are assumed to be composed of actin and myosin, mainly). Elastic modulus E has been measured to be equal to ~ 10 kPa in MDCK cells (Reffay et al., 2014; Roure et al., 2005; Schulze et al., 2017).

We assumed with scaling arguments that $k_{st} = E.d$ with d the section of the acto-myosin cable (taken as 500nm, from Alka Bhat PhD work). Therefore, we found that $k_{st} = 5.10^3 \ pN. \mu m^{-1}$.

In addition, we used similar scaling arguments to derive an order of magnitude for k_b . We considered that:

$$k_b = \frac{\pi}{4}.E.d^3$$

This is taken from (Broedersz, 2016) considering a 1D case (d^4 vanishes into d^3). This yields to $k_b = 10^3 \ pN$. μm

Altogether, we managed to directly measure or to derive from already published literature values for parameters in our model. This ensures that the comparisons between numerical simulations and experiments are relevant.

6.6.3 Simulations

Simulations were performed with the values set in the section above and available in appendix (10.4). We recapitulated rotations on rings with a diameter of 80µm within timescales comparable to our experiments (in hours) (see Figure 6.26a and Movie S33). Alignment of polarities through the relaxation on the mean polarity and velocity (µ and nu, respectively) generates a long-range order and leads to coherence. The absence of cables impairs coherent motion, leading to cells spreading everywhere on the field of view. Notably, absence of the active term also impairs coherence. This suggests that considering acto-myosin cables as active out-of-equilibrium structures is necessary to recapitulate the phenomena observed in experiments.

Then, we tried to reproduce the caldesmon experiment and the local cellular escape. To do so, we set $F_{cable} = 0$ for one particle within the ring: this is mimicking the decrease in myosin activity induced by the drug at the single cell level. This local perturbation recapitulates successfully the phenomena observed in experiments: the defective particle escapes radially, decreasing coherence of the ensemble. This is shown in Figure 6.26b and Movie S34.

In conclusion, the minimal number of features detailed in the model (*i.e.* alignment of polarities and the presence at the boundaries of active acto-myosin cables) generated results comparable to our experiments. Further simulations and quantification need to be done in order to provide a fair comparison between the two systems. Specifically, we will extract and compare the $\frac{\xi_{max}}{p}$ as a function of the ring diameter, as shown in Figure 6.3b. Timescales seem to be close between simulations and experiments (hours timescale) and this has to be confirmed with further and systematic quantification. Finally, the caldesmon experiment was reproduced and we aim at modelling different more drug experiments that are available in appendix (see 10.4).

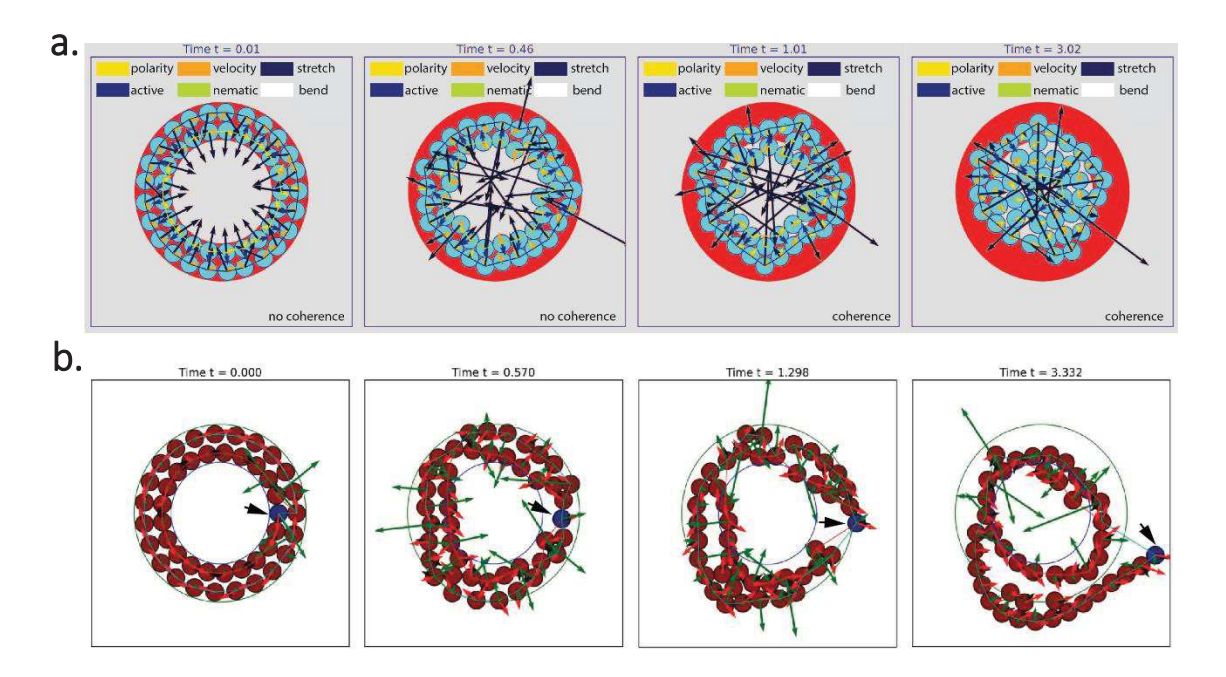


Figure 6.26. Simulations recapitulate coherence and drug experiments. (a) Simulation of an 80µm ring. Particles represent cells within the ring. Acto-myosin cables are represented by lines linking particles between them. Time in hours. (b) Caldesmon experiment reproduced in sillico. The blue particle (indicated by a black arrow) corresponds to a transfected cells with caldesmon. The cable force in this context is equal to zero. This leads to a radial escape with impairment of coherence. Time in hours. NB: the colour code is shifted in this preliminary representation.

6.7 Discussion

In this work, we extracted general features leading to spontaneous symmetry breaking and to coherent directed motion in epithelia. To do so, we micro-fabricated cellular rings, a simple periodic condition already proposed by Turing in 1952 and we analysed the collective dynamics.

Because cells were not confined onto their original pattern, we reported a variety of behaviours depending on the system size: (i) for very large diameters ($1000\mu m$), cells migrate inwards and outwards through finger-like extensions consistent with what is found at leading edges of migrating epithelia. (ii) On smaller diameters ($300-180\mu m$), cells first migrate inwards, closing the ring to a disk-shaped system and this resembles to wound healing assays. (iii) Rings undergo spontaneous rotations with a higher probability for the smallest configuration ($180\mu m$).

This latter observation confirmed the fact that epithelial cells have a natural coherence length under which global rotation is possible and above which global coherence is impossible. This is consistent with previous 2D works on disks or in epithelia (Doxzen et al., 2013) but in contrast with other studies (Jain et al., 2020). Indeed, when totally confined (physically or

chemically) within a ring-shaped pattern, cells always undergo global rotation, independently of the system size (Jain et al., 2020). Only the time to reach coherence will scale with the diameter (Jain et al., 2020). We hypothesized that confinement in this 1D configuration screens the effect of the coherence length with a mechanism of rectification distinct from ours even though they share similarities (see below). This behaviour under confinement is consistent with previous theoretical works (Soumya et al., 2015).

Our assay with different ring sizes allows to probe the natural coherence length of the cellular system. With PIV we extracted velocity fields and we were able to characterize the maximal coherence length for each ring. We found that this length was similar for all conditions and was equal to $\sim 315 \mu m$ (which correspond approximately to 15 cells). We could then rectify the motion of the rings: by designing a new ring geometry (80 μm) with a perimeter below the coherence length, we managed to have a condition where almost 100% of the rings were spontaneously rotating.

Analysis of the global coherence through time taught us that acquisition of coherence is a fast process, non-linear, happening within 1 hour. Interestingly, time of coherence acquisition as well as duration of rotation were random with no clear explanation at a first sight.

We observed a coupling between persistence of coherence (time of rotation) and the epithelium velocity. This coupling echoes the one found in single cell (Maiuri et al., 2015). Further investigation would need to be done in order to decipher the mechanisms leading to this phenomenon. Notably, velocity during coherence (20-30µm.h⁻¹) is in the same range than the one found in the rotation of follicle cells in the *Drosophila* egg chamber (~ 20µm.h⁻¹) (Cetera et al., 2014). It is interesting because it has been shown that this *in vivo* coherent motion was driven by lamellipodia and "crawling" on the egg chamber shell (Cetera et al., 2014). The phenomenon we describe here could be therefore extrapolated to this 3D context.

Next, we sought to understand how this coherent motion could take place and which features are necessary for its initiation. We found that single cell polarities were mainly oriented tangentially and this would lead to a potential tug-of-war between opposite polarities. This is backed up with single cell mechanics analysis showing: (i) an increase of the cellular stretch until the onset of coherence where the stretch drops; (ii) a relationship between the time of coherence acquisition and the percentage of aligned polarities within the ring.

In addition, we found that cellular density and divisions were important parameters in the onset of coherence. Indeed, low density challenges continuity of the monolayer and local breakages impairs coherence. More generally, low densities were associated with low coherence while higher densities were correlated with high coherence.

On the other hand, cell divisions act as polarity breakers: daughter cells within the ring exhibit in majority of cases opposite polarity cues. If divisions happen at the same time, as a synchronous "burst", rings undergo spontaneous rotations. Instead, divisions occurring at a constant path throughout the experiment were associated with low global coherence.

We saw that global coherence was sensitive to overexpression of proteins. Indeed, we used in this work a cell line over-expressing cadherins (MDCK stably transfected with E-cadherin-DsRED), known for their "stickiness". With the usage of a CRISPR-Cas9 ZO1-GFP cell line or with the FRET cell line (over expressing RhoA), we reported a decrease in the number of rotating rings, suggesting that the coherence length might be affected by the different levels of adhesion protein – as expected. Instead of ruling out the non-rotating rings, we took them as an advantage to probe differences between coherent and non-coherent rings.

Next, we reported two acto-myosin cables self-assembled at the inner and outer ring boundaries. This acto-myosin accumulation was also found at leading edges of epithelia and can be observed on normal MDCK colonies. We hypothesized that they could act as internally-driven constraints preventing cells to escape radially and providing proper conditions for coherence to appear. To test this idea, we ablated the cables and saw that the tension they exerted was much higher than the one between cells. We did not see any difference in tension between the inner and the outer cables. Then, we locally perturbed the cables by decreasing myosin activity of some cells in the ring and we saw that this was associated to radial escape and a decrease of the global coherence.

Along the same idea, we tested various drugs on the different types of multicellular rings. If the different drugs led each time to a different behaviour, drug experiments are difficult to analyse: dysregulating protein activity usually leads to a variety of consequences in the cell. For instance, disruption of cellular E-cadherin junctions by chelating calcium would also impair myosin activity and therefore cell motility. The fact that effects are various and combined made the analysis and the causality challenging. However, all the experiments are reported in Appendix (see 10.1).

As described in 2.2.2.1, RhoA activity is responsible of most of the cytoskeletal changes. In addition, it has been shown that this small GTPase can exhibit dynamical Turing patterns in the cell cortex (Bement et al., 2015). This led us to take RhoA as a good candidate to test Turing's framework on a multicellular ring (Bement et al., 2015).

We did not observe any classical Turing patterns within our rings. If the property described in (Bement et al., 2015) is universal to any acto-myosin cortex, this absence could be due to the imaging we used. Indeed, Bement *et al.* were using TIRF microscopy, therefore imaging the cortex in a very thin section of hundreds of nanometers. Instead, we used confocal microscopy with a pinhole opened at its maximum in order to increase the signal/noise ratio for the FRET analysis. The resulting optical section was $\sim 7\text{-}8\mu\text{m}$.

However, we reported an accumulation of RhoA activity at boundaries, co-localizing with actomyosin cables. Even though it is not the canonical Turing patterns (Bement et al., 2015; Kondo and Miura, 2010), we reproduced this behaviour with the set of reaction-diffusion equations described in the 1952 paper suggesting that boundary effects might bias distributions of activities.

We reported a correlation between RhoA activity and cell velocity as well as with global coherence. High RhoA activities were associated to low velocities whereas low RhoA levels led to higher velocities. This suggested that RhoA was mainly acting on the velocity V_k in the theoretical framework.

Finally, we recapitulated our experimental results with a Vicsek-based model integrating single cell polarities and their interactions together with free acto-myosin cables. Specifically, we found out that alignment of cell polarities and cables at boundaries acting as mechanical constraints on the cells are sufficient to reproduce coherent motion. If one of these two components is set to zero, coherence is impaired. In addition, we showed that the active part of acto-myosin cables is necessary to give raise to coherent motion. This is consistent with the fact that actin and myosin are intrinsically out-of-equilibrium and that RhoA is highly active at the cable localizations. Also, it is important to notice that our simulations recapitulate the phenomena observed in experiments with similar hours timescales. In addition, our model does not require cell-cell adhesion to promote rotation.

We next managed to reproduce the caldesmon experiments with our theoretical model. In this context, we set the force exerted by the cable to zero for one particle within the ring. This led to the radial escape of the particle, as observed during the mosaic experiment.

Further simulations with variations in the ring diameter and quantification of the ratio $\frac{\xi_{max}}{p}$ will allow to compare in a fair way experiments and results from the model. We also plan to test whether or not our theoretical model can recapitulate the drug experiments we made so far with the multicellular rings. This would confirm further the robustness of our predictions.

6.8 Conclusions

Altogether, we provide here a description of the establishment of global coherence in 2D multicellular systems.

This spontaneous symmetry breaking, followed by directional migration of the whole epithelium can be recapitulated with two minimal ingredients: interaction between single cells polarity and the presence of acto-myosin cables. Cell polarities are driven by the growth of cryptic lamellipodia and their alignment is responsible of the onset of coherence. In parallel, acto-myosin cables confine cells and prevent radial escape, thus providing good conditions for coherence initiation.

RhoA activity accumulates mainly at boundaries through reaction-diffusion processes as described by Turing in 1952. RhoA regulation is mainly embedded into active stress in cables and in cell velocity as it exists a direct relationship between FRET intensities and velocity field magnitudes.

All these assumptions were further tested with a Vicsek-based model integrating experimental observations together with measurements of their parameters. The recapitulation of the phenomena with the proper length and time scales provides good evidence that our assumptions are relevant.

7. EMERGENCE OF COHERENCE IN 3D MULTICELLULAR SYSTEMS

NB: This work has been done with the help from Gaëtan Jardiné and Marielle El Kazzy, two Master students from the lab. Stéphanie Baudrey and Michael Ryckelynk provided their help for the microfluidic part. Pascal Didier supervised the mounting of the light-sheet microscope.

7.1 Introduction

Spontaneous coherent motion, as described in Chapter 6, are found in a variety of *in vivo* contexts. We briefly highlighted two examples in 2.6.1.2: coherent angular motions during *Drosophila* egg chamber elongation and during mammary acini formation (Cetera et al., 2014; Haigo and Bilder, 2011; Tanner et al., 2012; Wang et al., 2013). Both examples happen in 3D micro-environments. If some similarities are shared between 2D and 3D contexts, we cannot directly extrapolate the framework detailed in Chapter 6 to the 3D multicellular case. Notably, these two examples highlight important divergences: even though the final result seems similar (the acquisition of a global coherent motion), the ways to achieve it are likely to be different. Indeed, in the *Drosophila* egg chamber, cells are growing lamellipodia on the basal membrane composing the chamber leading to migration mode related to adhesion (Cetera et al., 2014) (this would be related to some extent to the phenomena described in Chapter 6). In contrast, presence of lamellipodia and therefore of an adhesion-based migration in mammary acini is not clear (Tanner et al., 2012; Wang et al., 2013).

In this work, we tried to reproduce and imaged MDCK spheroids in order to investigate the emergence of spontaneous rotations in these systems. Three main questions are addressed: (i) will the coherence length argument be still valid in this context? (ii) Since adhesion on the surface might not be responsible for the collective migration, what would break the spheroid symmetry and lead to the rotation? (iii) Turing also proposed in 1952 the case of a multicellular 3D spheroid (Turing, 1952). Therefore, what would be the RhoA spatio-temporal dynamics in such a configuration?

We will detail in this chapter the preliminary results generated so far. Specifically, we will describe the different attempts to produce hollow MDCK spheroids either through microfluidics or using Matrigel matrixes. Then, we will detail a home-made optical set-up suitable for fast live imaging of spheroids and suitable for FRET acquisitions in 3D. Finally, dynamics of spheroids in standard bright field microscopy and in the new set-up will be shown.

7.2 Formation of multicellular spheroids

We tried to generate MDCK spheroids by two main approaches: either with microfluidics devices, in order to get reproducible, monodisperse spheres or by spontaneous self-assembly in Matrigel matrixes.

7.2.1 Microfluidics devices

7.2.1.1 Principles

Analysis of coherent motion in 3D requires the production of spheroids with a single layer of cells. Production of such "hollow" spheres can be done by encapsulating cells into shells of hydrogel as described in Figure 7.1. After encapsulation, cells would spread on the shell, divide, and create a continuous monolayer lining the capsule. This has been done previously with alginate shells and MDCK cells as well (Alessandri et al., 2013; Trushko et al., 2019).

Before going to the production of spheres, we wanted to get for the shell the best combination between optical properties, adhesion on the gel and polymerization conditions. Therefore, we tested various biocompatible hydrogels and compared them.

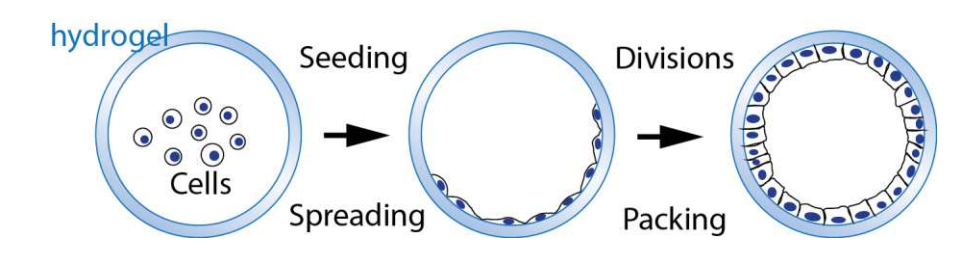


Figure 7.1. Cells encapsulation for generation of spheroids. Schematic view of the spheroid generation with hydrogel capsules.

7.2.1.2 Hydrogels characterization

Because they are all optically transparent and biocompatible, we tried agarose, low melting point (LMP) agarose, phytagel, and alginate (Jaeger et al., 2015).

The first point we focused on was the ability of cells to adhere on the gel. We tested the different hydrogels and found out that cell adhesion was impossible. In addition, adsorption on these substrates is extremely low (Silva et al., 2010; Zustiak et al., 2013). Therefore, we tried to directly mix the gels with different adhesive molecules in order to get better attachment. Despite these trials, most of the conditions tested led to no adhesion. Only alginate 1% + 30% FN led to adhesion, even though not optimal (spreading was slower).

The polymerization method constitutes another parameter important for the generation of capsules. Agarose and phytagel both polymerize at high temperatures (34-38°C for agarose and ~ 32°C for phytagel). Therefore, the microfluidics chip would need to be heated up to temperatures close to 40°C; otherwise clogging of the chip might occur because of gelling and increased viscosity. In addition, high temperatures for long periods might be deleterious for cells.

LMP agarose and alginate could be considered as alternatives. LMP agarose gels at temperatures below 25°C and alginate starts polymerizing upon calcium ions addition. Because LMP agarose solution starts being viscous between 25°C and 30°C, it would also need heating devices to ensure proper flows in the chip. Addition of a calcium-rich solution for alginate is the most convenient as it does not require any device to keep alginate fluid. The only critical point is to not put in contact calcium with alginate until the point polymerization is desired.

Altogether, we considered only alginate as a potential candidate for the formation of cell spheroids because it had the best attachment in experiments and because its gelling process was the most convenient.

Hydrogel	Adhesion	Viability	Polymerization
Agarose 1%	No	No	34-38°C
Agarose 1% + 50% Serum	No	No	34-38°C
Agarose 1% + Matrigel 10%	No	No	34-38°C
Agarose 1% + FN 30%	No	No	34-38°C
Agarose 0.5% + Polylysine 10%	No	No	34-38°C
Alginate	No	No	Upon Ca ²⁺ addition
Alginate 1% + FN 30%	Yes, partially (50%)	Yes	Upon Ca ²⁺ addition
Alginate 1% + Polylysine	No	No	Upon Ca ²⁺ addition
Phytagel	No	No	~ 32°C
Agarose LMP	No	No	

Table 7.1 Hydrogel characterization.

7.2.1.3 Description of the different set-ups

We used two different microfluidics approaches to produce alginate capsules: (i) "standard" microfluidics flow-focusing device, with micro-fabricated PDMS chip and monitoring under inverted microscope (inspired from (Kim et al., 2009, 2011)); (ii) "on bench" microfluidics, with HPLC capillaries and tubings (derived from (Alessandri et al., 2013)).

The first device is composed of three inlets (see Figure 7.2a): inlet (1) brings the DMEM solution with cells in suspension, while the alginate solution is flowed in (2). Calcium ions are injected at inlet (3). Calcium is dissolved into oleic acid, an oil phase. This is necessary as the droplet generation relies primarily on the contact between two immiscible phases. In this context, the couple cells-alginate (inlet (1) and (2)) constitutes the aqueous phase, and the

calcium solution (oleic acid, inlet (3)) the oil phase. This device has been produced with microdrill (in collaboration with IPGG, Paris) because the features present on the chip are around 150-200µm. In this regime, standard photolithography is less convenient as multiple layers need to be done to avoid issues in UV penetration.

Alginate flows will flank the central flow of cells without mixing as it has different velocity and viscosity. Oleic acid containing calcium ions is expected to generate droplets at the cross-junction because of geometrical constraints and by imposing tangential viscous stress to the central flow (Gañán-Calvo and Gordillo, 2001; Nooranidoost et al., 2016). After droplet generation, capsules are supposed to polymerize during their transportation in the oil phase containing calcium.

The second set-up tested was done with an assembly of various capillaries as shown in Figure 7.2b. The principle remains almost the same except that the oil phase is removed and spheres are instead falling into a saturated calcium bath, polymerizing capsules upon contact. Droplets are generated with proper flow rates leading to Rayleigh-Plateau instability. This instability breaks the aqueous jet into regularly spaced droplets with predictable size.

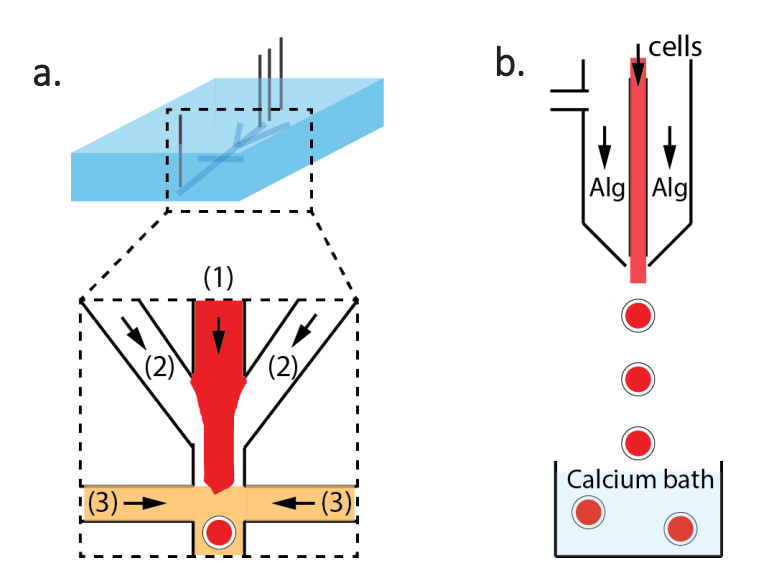


Figure 7.2. Two microfluidics approaches to generate alginate shells. (a) Microfluidics device (flow-focusing) to produce alginate capsules. (1) = cells; (2) = Alginate; (3) = Oleic acid (with calcium). (b) Alternative set-up to generate cellular spheroids. Alg = alginate.

7.2.1.4 Trials and observations

We successfully generated droplets with the flow-focusing device, as shown by Figure 7.3a-d. Alginate flows nicely flanked the central flow of cells (here, medium only) without mixing. Thickness of alginate flows can be tuned by adjusting the flow respective flow rates. Spheres of about 150µm were produced after contact with oleic acid flows.

Alginate was mixed with TRITC-dextran and could therefore be visualized. Figure 7.3c shows the fluorescence profile of the generated droplets. The two peaks (indicated by arrows) suggest

that a capsule is present, without alginate in the center. This was confirmed by imaging the droplets right after production under confocal microscope (Figure 7.3d).

However, after few hours at room temperature, we noticed after each experiment the fusion of the spheroids. With further investigation and micro-manipulation under the binocular, we figured out that our microfluidics device did not generate 3D capsules but instead some kind of alginate torus (Figure 7.3e). This led to the fusion of the aqueous phase on large timescales with deposition of the remaining alginate at the bottom of the collection tube.

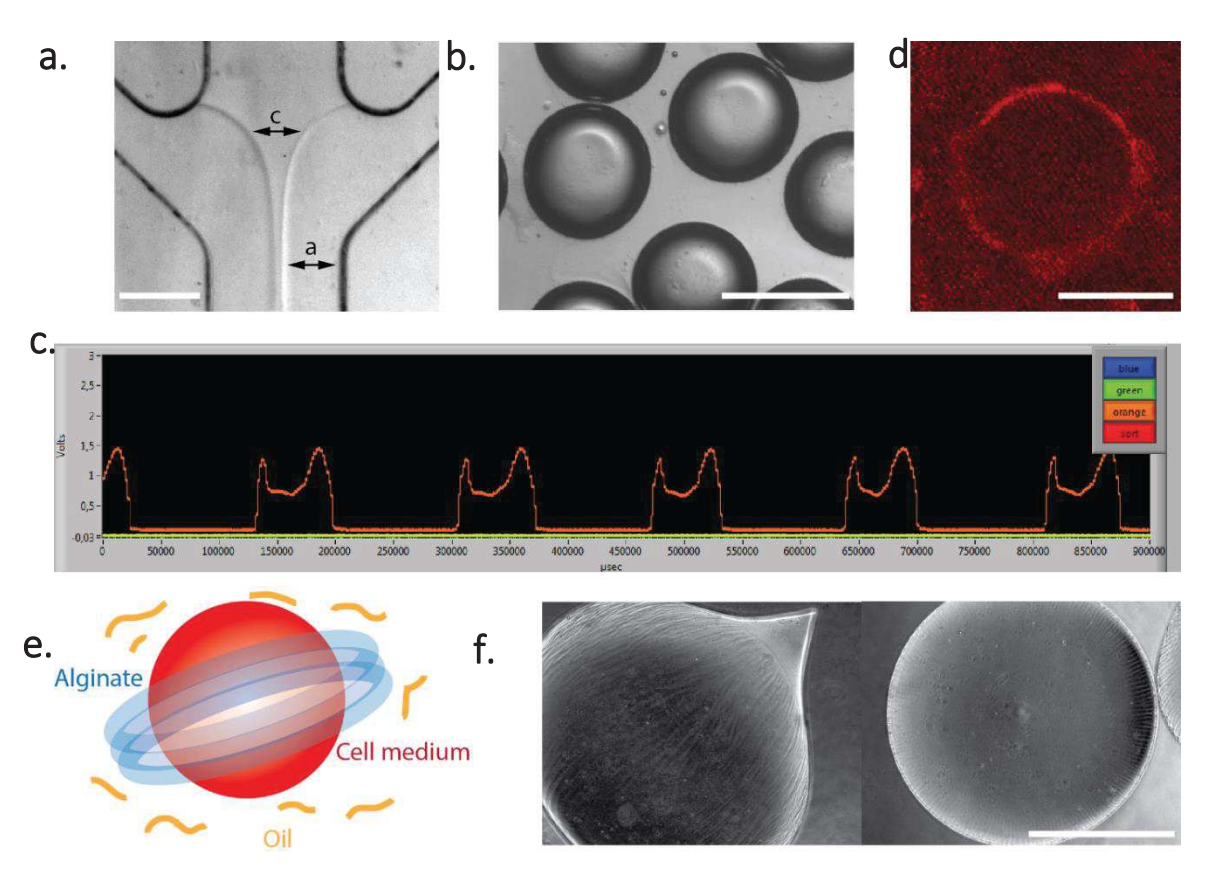


Figure 7.3. Alginate shells generated with microfluidics. (a) Microfluidics device for alginate shells generation. The central flow is the aqueous phase containing cell medium and the coflows are associated with alginate. c and a are adjustable by tuning respective flow rates. Scale $bar = 75\mu m$. (b) Droplets generated with the flow-focusing device shown in (a). Scale bar =150µm (c) TRITC-dextran signal for each droplet passing through the production channel. The two-peak profiles indicate that alginate surrounds the central droplet of cell medium. (d) Epifluorescence image of a droplet produced by the microfluidics device. A fluorescent ring is visible suggesting that an alginate shell might exist. Scale bar = 100µm. (e) Schematic view of the actual configuration. Because of the presence of an oil phase, the central flow of medium adopts a droplet configuration (typical of this water-in-oil emulsion) while alginate, polymerized in the production channel with the calcium, is assembled into a torus structure. This explains the results observed with micromanipulation under the binocular and the fusion of droplets in the Eppendorf with an alginate pellet. (f) Alginate droplets generated with the on set-up described in Figure 7.2b. The arrow indicates an alginate tail, a consequence of the Rayleigh plateau instability breaking the jet into regularly spaced droplets. Droplets are indeed alginate shells (this was checked by direct cutting with a blade and observation under the binocular). Scale bar = $1000\mu m$.

The second set-up relies on the generation of droplets by production of a Rayleigh-Plateau instability, breaking the jet into regularly spaced droplets with predictable sizes. In order to create such instability, flow rates need to be adjusted correctly. Results are shown in Table 7.2.

Even though we managed to create instability and generate droplets in some conditions, we faced various issues:

- Deviation of the jet and wetting at the capillary aperture, even with proper cut under the binocular and with PEG passivation. This suggested a non-straight interface at the opening and a defective hydrophobic coating.
- Flattening of the droplets at the contact with the calcium bath leading to alginate disks floating at the surface. This could be decreased by changing the distance between the tubings and the bath.
- With these two problems solved, we still did not end up with usable capsules: we generated hollow beads of alginate as reported in Figure 7.3f but with a size way too large to probe coherence in 3D (1500-2000 μ m). We did not manage to get Rayleigh-Plateau instability and stable droplets generation for lower diameters.

Altogether, even though microfluidics could provide in theory interesting advantages (production rate, monodispersity, reproducibility), we did not manage to generate reliable hydrogel capsules embedding cells and with relevant sizes in our assays. More straight forward technics were also tested in parallel, such as self-organization in Matrigel matrices.

Cells solution flow rate (mL/h)	Alginate flow rate (mL/h)	Presence of RP instability
90	30	No
90	65	No
95	60	No
95	75	Yes
100	65	Oscillation between jet and RP
105	65	Oscillation between jet and RP
110	75	Yes

Table 7.2 Flow rates associated with Rayleigh-Plateau instability (RP).

7.2.2 Self-organization

7.2.2.1 Spontaneous generation of spheroids in Matrigel

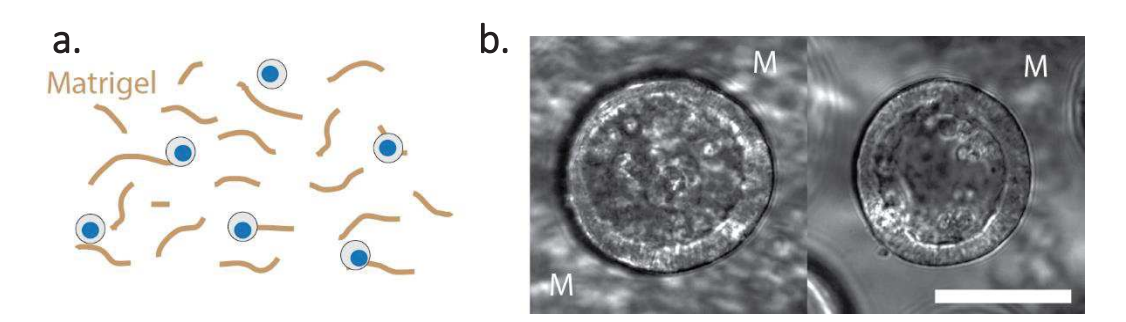


Figure 7.4. Self-organization of MDCK spheroids. (a) Schematic view of the initial timepoint for generation of multicellular spheroids. Cells are trypsinised and dissociated so that single cells are mixed in Matrigel. (b) MDCK spheroids after 10 days of culture. Scale bar = 50μ m. M = Matrigel.

MDCK cells in Matrigel matrixes spontaneously self-assemble into single-layered spheroids with a single lumen. Briefly, cells are trypsinized and mixed with Matrigel at a proper density to have isolated single cells in the gel (see Figure 7.4a and 3.3.3 for more details). After few days and divisions, well formed MDCK spheroids are generated as shown in Figure 7.4b.

7.2.2.2 Growth of spheroids

After self-organization, cells inside the spheroid continue to undergo divisions. Therefore, we can monitor the average spheroids size with the incubation time. This allows to get reproducible (even though distributed) spheroids from experiment to experiment. Figure 7.5a shows the evolution of the spheroids size over time: the first spheroids can be seen at day 3 and they exhibit then linear growth. Notably, the size at day 13 (quasi-maximal growth) does not depend on the initial cell density as reported in Figure 7.5b.

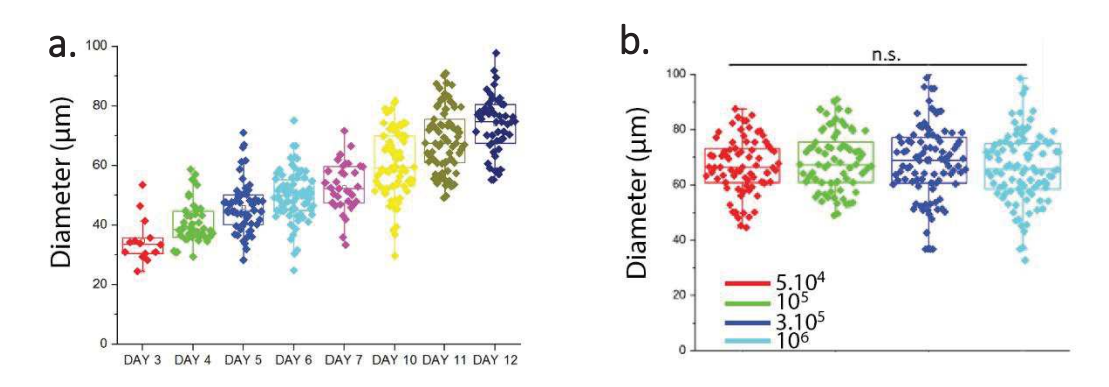


Figure 7.5. Growth dynamics of MDCK spheroids. (a) Evolution of spheroids size as a function of incubation time. Initial density was 3.10⁵ cells/ml. (b) Spheroids size as a function of the initial density (in cells/mL) at day 13.

7.3 Home-made light-sheet microscopy to observe 3D motions

We managed to generate multicellular spheroids, as described in the previous section. However, imaging their dynamics requires an optical set-up able to scan in 3D the sample, fast enough to reduce phototoxicity, and for large timescales (at least 12 hours). In addition, RhoA activity should be accessible by FRET acquisitions. In this context, we developed a home-made light-sheet microscope. We will first explain the principles and the rationale behind it, then detail the optical set-up *per se*, and finally we will expose the various issues and the way we troubleshooted it.

7.3.1 Principles

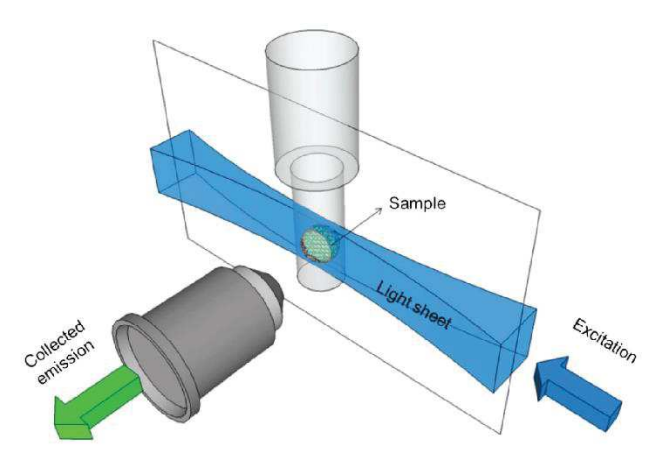


Figure 7.6. Basic schematic of a light-sheet microscope. Adapted from (Lvarez, 2018).

Light-sheet microscopy allows to image "slices" of a 3D sample through an illumination sheet generated by a cylindrical lens (Lvarez, 2018). Typically, an x-y sheet of a thickness z of 5-10µm can be generated through a 20x objective

with a typical numerical aperture of about 0.40. Scanning in z is then done by the translation of a motorized stage. We considered this imaging method because of its speed and its low phototoxicity compared to confocal microscopy.

7.3.2 Tests with Open-SPIM

Open-SPIM (Selective Plane Illumination Microscopy) is an open-access light sheet design (Girkin and Carvalho, 2018). Briefly, an illumination objective coupled to a cylindrical lens produces a light sheet, passing through the sample (Figure 7.7a). A water-dipping objective detects the emission. Both objectives are placed at 90° each. The sample is embedded and stabilized into an agarose tube as shown by Figure 7.7a. In order to image all the different planes the tube rotates during acquisition. All this acquisition system is set-up into a water tank.

We first tried this method in order to image multicellular spheroids. This set-up was available at Institut de Biologie Moléculaire des Plantes (IBMP, Jérôme Mutterer). We fixed lifeact-GFP mouse blastocysts as models to test the optical set-up. They were embedded into agarose 0.5% and images are reported in Figure 7.7c.

However, these optical set-ups presented many drawbacks: detection and illumination objectives were too close and space between them did not allow easy manipulation of the sample; embedment of the biological sample into agarose tubes does not allow any motion of cells inside the gel and could potentially trigger different effects as new constraints are applied; registration of images are necessary if the object is not totally in the rotation axis – this could lead to additional artefacts; curvature of the agarose tube induced strong aberrations on blastocysts close to the edges.

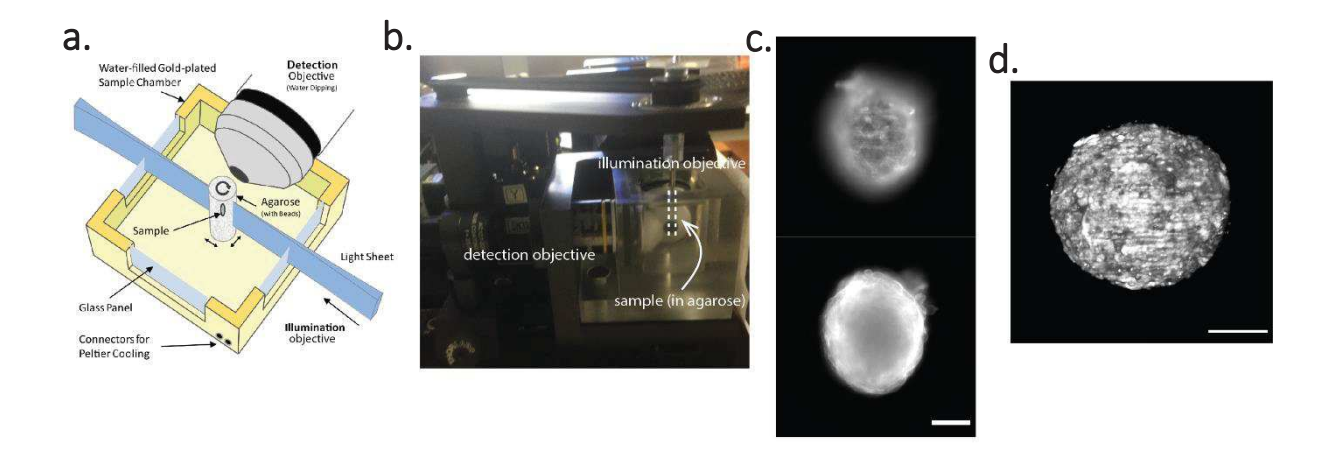


Figure *7.7.* Open-SPIM set-up. (a) Scheme ofthe optical montage (from https://imagej.net/SPIM Registration Method). The sample is embedded into an agarose tube and rotates during acquisition. (b) Images of the optical set-up. Two objectives (at 90°) are immersed in a tank filled with medium. The sample is imaged in an agarose tube rotating during acquisition. (c) Images of a mouse blastocyst acquired with open-SPIM. Fluorescence corresponds to lifeact-GFP. The upper plane (left) and the middle plane (right) are taken. Scale bar = $25\mu m$. (d) NIH3T3 spheroid imaged with a Leica SP8DLS. Cells are stained for actin with Alexa-488 phalloidin. Scale bar = $100\mu m$.

Finally, we also tried a Leica SP8DLS light-sheet (Figure 7.7d), but the system had the same limitations than the Open-SPIM.

Altogether, these results led us to consider a home-made light-sheet set-up fixing the issues detailed above.

7.3.3 Optical set-up

We designed a simple montage where an illumination sheet is produced by a cylindrical lens in the optical path.

A 488nm source (488) delivers the excitation light (Figure 7.8a-b). Each acquisition is triggered by the opening of the shutter (s). It goes through a first telescope, composed of two lenses (Ta-Tb) of different focal (50mm and 100mm respectively). This will enlarge the beam size in order to fill the entire cylindrical lens (CL). After passage through the cylindrical lens, the beam translates into a light sheet. This goes into the illumination objective (IO) which will focus the sheet in the sample.

In standard light-sheet set-ups, like the open-SPIM, the illumination and the detection objectives are in contact, at 90° . This creates difficulties to manipulate the sample and to find a proper mounting system to image it. In order to bypass this issue and to have an easy access to the stage and the sample, we used a large working distance objective. Indeed, the 10x objective (Mitutoyo, N.A. = 0.28) in our set-up has a working distance of 34mm. This allows to put the objective far away from the stage and to create space and comfort for sample manipulation.

Emission light then passes through the detection objective, here a water immersion 40x (DO) (N.A. = 0.8) and a GFP filter (400-700nm). Emission is corrected for chromatic and geometrical aberrations thanks to a tube lens (TL) and is detected by the camera (C).

We analyzed the profile of the light sheet to measure its thickness and to characterize homogeneity. In the actual configuration, the full width at half maximum (FWHM) is $\sim 12 \mu m$. The sheet is also quite homogeneous in x-y, as shown by the profile in Figure 7.8c-d.

Spheroids with MDCK cells stably expressing E-cadherin-GFP can be visualized through the optical set-up, as shown by Figure 7.8e, confirming the proper function of our light-sheet.

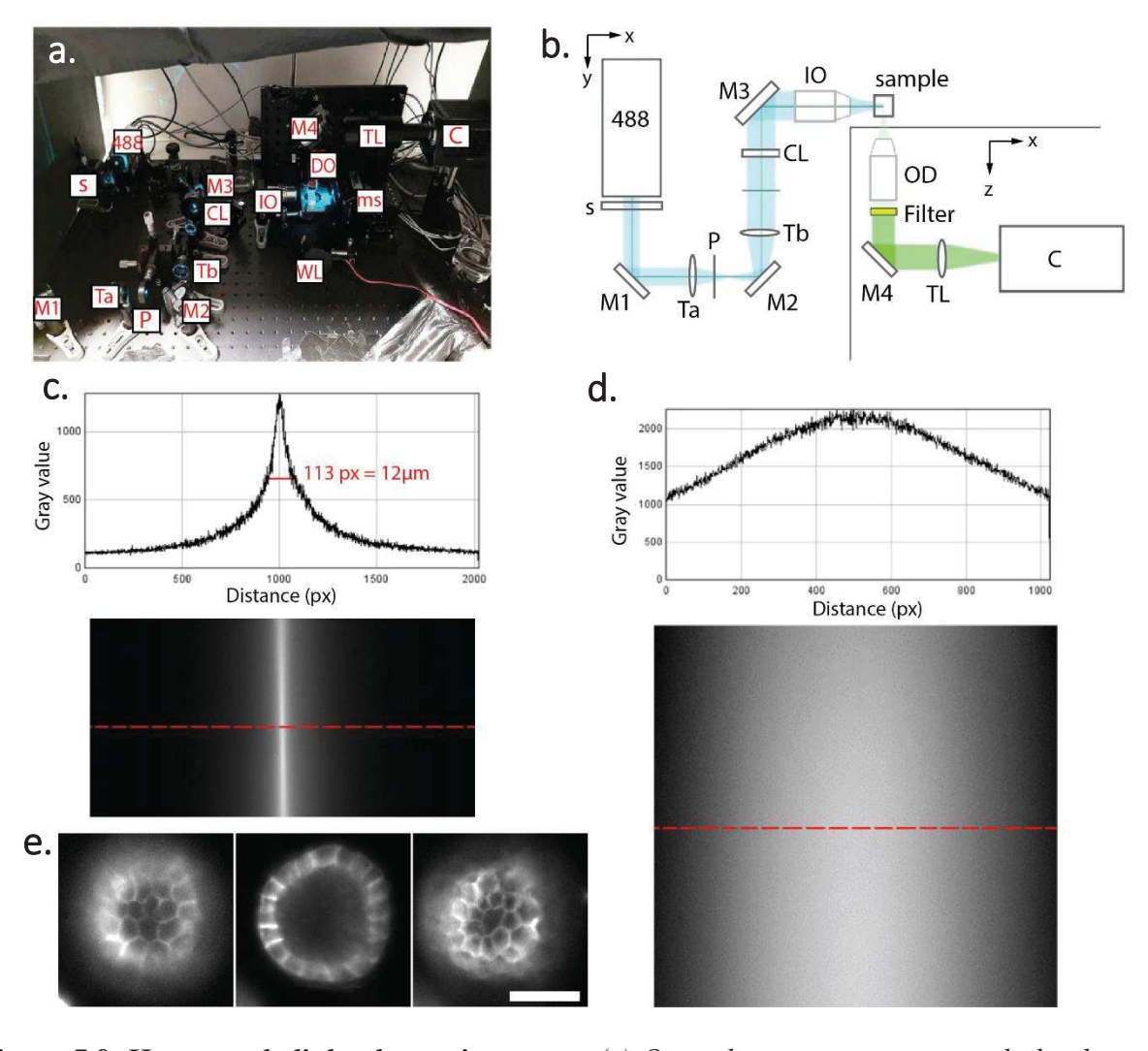


Figure 7.8. Home-made light-sheet microscope. (a) Optical set-up to generate a light-sheet. 488 = 488nm laser source; s = shutter; Mi = mirrors; Ta-Tb = Telescope lenses; P = pinhole; CL = cylindrical lens; IO = illumination objective; DO = detection objective; TL = tube lens; C = camera; ms = motorized stage; WL = white light source. (b) Schematic view of the set-up. (c) Fluorescence profile of the x-z plane of the sheet. Full width at half maximum (FWHM) gives an approximation of the sheet thickness. Here, FWHM $\sim 12\mu m$. (d) Fluorescence profile in the x-y plane. (e) MDCK spheroid (E-cadherin-GFP) imaged through the home-made light-sheet. left = bottom plane; middle = medium plane; right = top plane. Scale bar = $20\mu m$.

In order to image the FRET biosensor, an additional laser source (468nm) will be added to the set-up as well as a new motorized filter wheel between the tube lens and the camera.

7.3.4 Issues and troubleshooting

The first issue is related to the sample mounting. Indeed, for long timelapses of tens of hours, sufficient amount of medium needs to be available to compensate evaporation. In addition, a straight interface needs to be set with a refractive index not too far from water otherwise this would give deflection of the sheet and a poor image quality.

We designed a tank prototype for sample mounting, as shown in Figure 7.9a. The volume was sufficient to keep imaging during 10 hours. However, the tank positioning was critical in the quality of our acquisitions. As said above, having the illumination sheet not perfectly normal to the imaging window would cause dramatic drop in image quality as shown in Figure 7.9b. We will fix this issue by modifying the stage and inserting micrometric screws in order to stabilize and correctly adjust the tank for imaging.

Evaporation can be compensated for longer acquisition with the continuous addition of medium by a microfluidic pump. However, we experienced some minor drifts, possibly due to the flows created by the pump. In this context, we plan to make another kind of tank, shown in Figure 7.9c. Here, medium will be added in a separated compartment separated from the samples.

We also experienced z drift, due to thermal fluctuations. This was solved by heating up the whole system at 37°C and closing it in a box.

The fact that the light sheet thickness is around $10\mu m$ can be attributed to the cylindrical lens optical quality as well as a default in the lens alignment. Indeed, for the moment, the lens is not mounted on a x-y-z stage that would allow precise alignment. These two approaches will be probed in the future in order to go below $10\mu m$ of thickness.

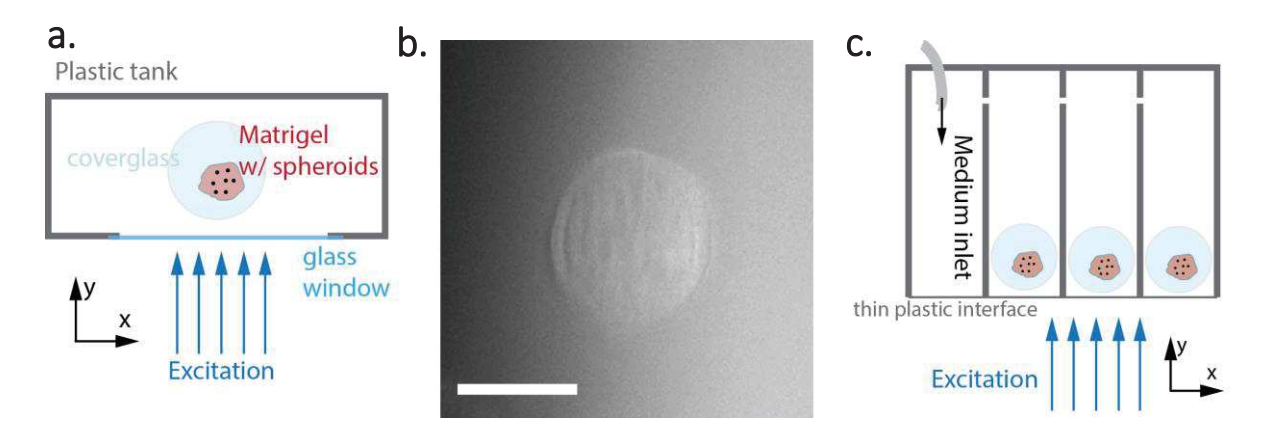


Figure 7.9. New designs for sample observation. (a) First tank prototype to image MDCK spheroids in Matrigel matrix. (b) Images acquired when the excitation sheet is not totally normal to the glass window. Scale bar = $50\mu m$. (c) Future tank, with multiple samples and an inlet for medium.

Finally, we can see in Figure 7.8e that it exists a halo around the spheroid. This fluorescent signal will be removed in the future by deconvolution methods. In this context, we will

characterize the Point Spread Function (PFS) by imaging in 3D fluorescent beads embedded into a Matrigel matrix.

7.4 Dynamics of spheroids

In order to capture phenomena of coherent motion in 3D, we tried to analyze MDCK spheroids dynamics with two approaches: first with standard phase contrast microscopy to test whether or not rotation could occur in our system and check dependency to the system size; then with light-sheet microscopy, to get the precise spatio-temporal dynamics.

7.4.1 In phase contrast microscopy

MDCK spheroids in Matrigel exhibited, as reported in (Chin et al., 2018), spontaneous rotation. This happens at very initial time points (already at 3-cells stage, data not shown) when the spheroid is small (~ 20µm) at a high speed of ~ 40-50µm.h⁻¹ and is sustained over days (see Figure 7.10a-b, see Movie S35). Notably, we reported an arrest of rotation when the spheroid size was increasing. This is reported in Figure 7.10a-b for one spheroid, when the spheroid size reaches ~ 45µm of diameter (for a perimeter of ~ 140µm) but this arrest was observed on almost all the samples. This suggests that the coherence length argument could be still valid in 3D and could be the limiting factor for spontaneous rotation to occur.

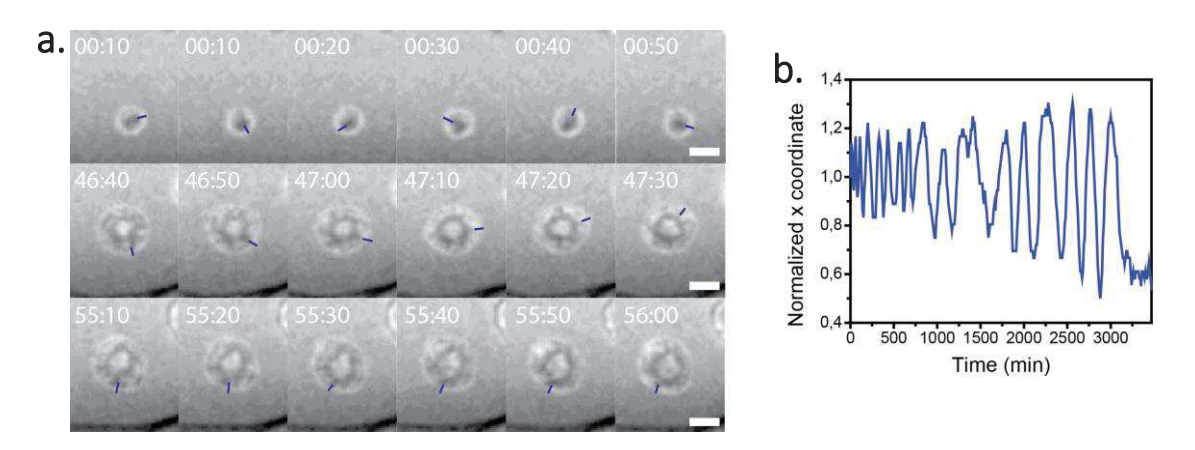


Figure 7.10. Spheroids undergo spontaneous rotations. (a) Timelapse images of a MDCK spheroid. Scale bar = $20\mu m$. Time in hh:mm. (b) Normalized x trajectory of a reference point in the spheroid. Spontaneous rotation occurs and stops when the spheroid reaches $\sim 45\mu m$ of diameter.

7.4.2 Through light-sheet microscopy

We next sought to analyse the motion of cells in 3D with our light-sheet microscope (Movie S36).

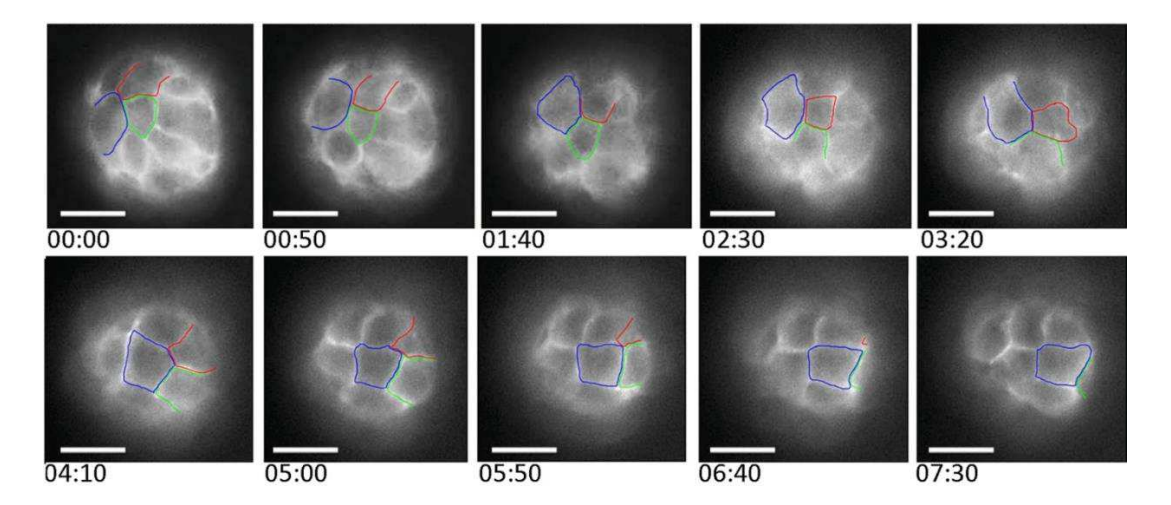


Figure 7.11. Light-sheet microscopy captures 3D rotations. Spontaneous rotation of one MDCK spheroid. Tracked cells are outline with colors. Scale bar = $20\mu m$. Time in hh:mm.

A preliminary result is shown in Figure 7.11. In this case, the MDCK spheroid undergoes spontaneous rotation, as highlighted by the group of three cells that were tracked. More experiments need to be repeated with all the z planes to provide a full description of the phenomena. Interestingly, we did not report any lamellipodia during the rotation, and this could make this kind of coherent behavior distinct from our 2D ring described in chapter 6 and from what is known during egg chamber elongation.

7.5 Conclusions and perspectives

We presented in this chapter the preliminary results regarding the analysis of coherent motion in 3D spheroids.

The first step of this project was to generate multicellular spheroids with a single layer of cells only. Among the different methods we could use, we decided to go for the spontaneous self-organization of MDCK cells into spheroids when dissociated in Matrigel matrices. Even though sizes are distributed and the production rate is lower than with a microfluidics flow-focusing device, the method was more convenient and reliable.

We reported the emergence of a global coherent motion in spheroids, appearing at early stages, when the spheroid is only $10\text{-}20\mu\text{m}$ size. The rotational speed seems to be higher than the one measured for the 2D configuration or even for the *Drosophila* egg chamber: rotations for spheroids reached $40\text{-}50~\mu\text{m.h}^{-1}$ while the collective motion reported in Chapter 6 and in the literature for the egg chamber was around $20\text{-}30~\mu\text{m.h}^{-1}$. A first explanation could be that the motion in the egg chamber and on the fibronectin rings is driven by lamellipodia whereas in the spheroids such cellular features were not visible. Therefore, friction might be higher and this could result in a velocity decrease. However, we still lack evidence and this hypothesis needs to be backed up by more experiments. In addition, it would be interesting to investigate how polarities emerge and align in this context and if the polarity argument detailed in Chapter 6 would be still present.

Also we observed an arrest of rotation as the spheroid grew. This could be a first hint suggesting that the coherence length argument is still valid in such 3D configurations. This will need to be confirmed with additional experiments and systematic comparison of the velocity profile with

the spheroid size. Therefore, we will be able to determine whether or not it exists a cut-off limiting the establishment or the sustain of a global coherent motion.

In order to precisely analyse collective motion in 3D we designed a home-made light-sheet microscope with an illumination objective having a large working distance. This new feature allows an easy mounting of the sample on the stage. Even though we faced minor issues (drift, medium evaporation, "straightness" of the observation window or thickness of the light sheet), the optical set-up is fully functional and provides images in different planes. Future improvements include: a deconvolution process with the knowledge of the PFS to get better images, replacement and alignment of the cylindrical lens to decrease the sheet thickness, and the addition of laser sources and filter wheel to perform FRET.

Having images of the entire 3D spheroids for each time step will allow in the future to make planar projections and to perform PIV on the datasets. Such analysis of the cellular flows are necessary in order to extract the coherence length ξ .

We did not for the moment make experiments with the FRET biosensor to investigate the activity of RhoA GTPases. This will be performed in the future, when the set-up will be finalized. This will allow us to compare the behavior of RhoA in 3D and in 2D. These results will be used to test Turing's hypothesis and predictions on 3D spheres.

Altogether, this project aims to provide an integrated picture of the emergence of coherent motion in 3D with the activity of small GTPases. Generic features leading these multicellular spheroids to spontaneously break their symmetry and undergo large-scale rotation will be extracted and compared with the 2D configurations probed so far. Similarities could be shared between the two systems and their presence could reflect universal properties of living matter to spontaneously organize into directional flows.

8. DISCUSSION AND CONCLUSION

This PhD work aimed to understand how single cells or multicellular assemblies undergo spontaneous symmetry breaking followed by directional motion. To answer this problem, we built different projects at different scales: (i) at the single cell level, we probed the mechanisms by which local asymmetries in the cellular micro-environment can trigger and rectify the migration without chemical gradients (Chapter 4); (ii) we tested whether or not this paradigm could be applicable in a 3D context, where cells migrate in micro-channels containing periodic "bottlenecks" and with chemical gradients (Chapter 5). We then tried to understand how directed motion could arise in collection of cells. (iii) In this context we analysed the emergence of spontaneous rotations in rings of cells (Chapter 6) and (iv) we tried to extract similar readouts for multicellular spheroids in 3D (Chapter 7).

At the single cell level, we reported that the distribution of focal adhesions and their dynamics was responsible for the bias when the cell experienced asymmetric adhesive regions on 2D surfaces. More specifically, we found a saturation area above which no more focal adhesions were generated. This translated into a non-linear increase of the bias as a function of the gap distance between adhesive patterns. We showed that this is the competition between the linear regime and the saturating one that sets the direction of motion. These observations were recapitulated into a theoretical model taking into account parameters accessible to experimental measurements. With this model, we predicted new behaviours and tested them experimentally with success.

In 3D, cells experienced the local asymmetries and a biased migration only when confined in x-y. When totally confined in x-y-z, cells exhibited persistent motion towards one direction without being biased by the presence of local asymmetries: the direction is fully set by the entry point in the micro-channel. To move along these narrow spaces (~ 5µm width) cells reorganize their cytoskeleton and recruit focal adhesions, stress fibres and keratin around these bottlenecks in order to squeeze the large organelle preventing passage: the nucleus. In addition to the nucleus compression, we also report that chemical gradients can generate different cellular responses depending on the direction of the topographical anisotropy: when cells migrated against the ratchet, motion after gradient removal was impaired. On the other hand, cell migration was less impacted when the motion was along the ratchet direction.

At the multicellular scale, cells on circular patterns spontaneously undergo large scale coherent motion resulting to the rotation of the cell monolayer. This happened when the ring perimeter was lower than the coherence length, a length above which global coherent motion cannot appear because the number of individuals in too high and below which global coherence rotations – can be initiated. We reported that this phenomenon was driven by the interaction between single cell polarities and by the assembly of two acto-myosin cables at boundaries. These cables act as internally driven constraints, preventing the cellular cohort to spread out. Finally, we probed RhoA activity in the ring and found out that it accumulates at boundaries, where acto-myosin cables assemble. Moreover, we reported that RhoA activity was mainly embedded into cell velocity: low RhoA levels were associated with high cell velocity. We recapitulated all these observations with a Vicsek-based model describing interaction between polarities and incorporating acto-myosin cables as free boundaries applying constraints on the cells. We found out that these two elements were sufficient to reproduce our experiments in sillico. Specifically, the model highlights the need of an active term driving the dynamics of acto-myosin cables, consistent with the high RhoA activity found at boundaries and consistent also with the out-of-equilibrium nature of acto-myosin. The model also recapitulated some of

our drug experiments, confirming the assumptions we made. Further simulations need to be generated in order to compare better experiments and theory.

We then tried to compare these phenomena to systems closer to what could be found *in vivo*. Therefore, we generated multicellular spheroids and we imaged them. We found out that collective rotations also occurred in these systems, consistent with previous works. Interestingly, these rotations stopped as the spheroids grew, suggesting that the coherence length argument detailed before could be still valid in this 3D configuration. Even though the final result looks similar *i.e.* the presence of rotation in both 2D and 3D systems, the mechanisms by which this motion is acquired are likely to be different. Indeed, we reported different rotational velocities in the two configurations and we did not see any lamellipodia in the spheroid case, indicating that different modes of migration are acting here.

The phenomena were distinct in the two scales we probed. At the single cell level, the broken symmetry was imposed by the micro-environment topology whereas at the multicellular scale we let the system spontaneously break its symmetry and undergo coherent motion. In both cases however, local broken symmetries translated into long-range motions: either through memory effects, in *ratchetaxis*, or by the alignment of the neighbouring cells on the generated polarity. In 2D and 3D *ratchetaxis* assays, the initial broken symmetry was pre-determined while it was totally stochastic in the multicellular rings and spheroids.

Our results also put forwards how local polarities can be amplified in multicellular systems: stochastic growth of lamellipodia within the colony can compete and align and eventually lead to a long-range motion. This kind of phenomenon could potentially be found *in vivo* in configurations where cells are confined or surrounded by internally-driven constraints (such as acto-myosin cables). In this context, the rotational motion of cells in the *Drosophila* egg chamber is interesting: cells exhibit cryptic lamellipodia and start rotating after a fluctuation period at speeds consistent with our 2D rings. Therefore, the claim we made on this latter configuration could be close to what is seen *in vivo*.

More generally, presence of local asymmetries with sizes comparable to the cell scale and readouts for cell polarity could be probed across space and time *in vivo* and then correlated with the emergence of directional migrations. These analysis could provide novel and alternative ways of envisioning directed motion *in vivo*.

Another point risen throughout this manuscript is the emergence of new properties when an ensemble of objects interact together: dynamics of FAs on the substrate and its saturating behaviour or the emergence of a coherent collective motion cannot be predicted by the analysis of their individual components. Interaction rules between each of the component often drive the appearance of new behaviours. Altogether, this highlights the importance to explore the dynamics of individuals and collections in different sets of experiments taking into account these specificities. Extrapolation from the single cell behaviour or from the protein dynamics to an ensemble of these objects might not always be valid and further experiments probing the collective dynamics should be done.

Finally, the cell cytoskeleton, out-of-equilibrium, governed the different phenomena: for single cells on ratchets, distributions of focal adhesions and their associated stress fibres were responsible for the bias while the alignment of cryptic lamellipodia of each cell in the multicellular ring translated into a long-range polarity driving the onset of coherence.

To conclude, this PhD work, at the interface between Physics and Biology, provided some generic features about symmetry breaking and directional migrations at the single cell level and at the multicellular scale. Specifically, it shows how a local broken symmetry, imposed by the micro-environment or triggered by stochastic single cell behaviours within a colony, can translate into a long-range motion.

9. REFERENCES

Abercrombie, M., and Heaysman, J.E.M. (1953). Observations on the social behaviour of cells in tissue culture. Speed of movement of chick heart fibroblasts in relation to their mutual contacts. Exp. Cell Res. 5, 111–131.

Abu Shah, E., and Keren, K. (2014). Symmetry breaking in reconstituted actin cortices. Elife 3, 1–15.

Agrawal, A., Sahni, S., Iftikhar, A., and Talwar, A. (2015). Pulmonary manifestations of renal cell carcinoma. Respir. Med. *109*, 1505–1508.

Aguilar, H.N., and Mitchell, B.F. (2010). Physiological pathways and molecular mechanisms regulating uterine contractility. Hum. Reprod. Update *16*, 725–744.

Akhtar, M., Haider, A., Rashid, S., and Al-Nabet, A. (2019). Paget's "seed and Soil" Theory of Cancer Metastasis: An Idea Whose Time has Come. Adv. Anat. Pathol. 26, 69–74.

Alessandri, K., Sarangi, B.R., Gurchenkov, V.V., Sinha, B., Kießling, T.R., Fetler, L., Rico, F., Scheuring, S., Lamaze, C., Simon, A., et al. (2013). Cellular capsules as a tool for multicellular spheroid production and for investigating the mechanics of tumor progression in vitro. Proc. Natl. Acad. Sci. U. S. A. *110*, 14843–14848.

Altschuler, S.J., Angenent, S.B., Wang, Y., and Wu, L.F. (2008). On the spontaneous emergence of cell polarity. Nature 454, 886–889.

Amos, L.A. (2004). Microtubule structure and its stabilisation. Org. Biomol. Chem. 2, 2153–2160.

Anderson, P.W. (1972). More is different. Science. 177, 393–396.

Arnold, T.R., Stephenson, R.E., and Miller, A.L. (2017). Rho GTPases and Actomyosin: partners in regulating epithelial cell-cell junction structure and function. Exp Cell Res *358*, 20–30.

Bajanca, F., Gouignard, N., Colle, C., Parsons, M., Mayor, R., and Theveneau, E. (2019). In vivo topology converts competition for cell-matrix adhesion into directional migration. Nat. Commun. 10, 1518–1535.

Balaban, N.Q., Schwarz, U.S., Riveline, D., Goichberg, P., Tzur, G., Sabanay, I., Mahalu, D., Safran, S., Bershadsky, A., Addadi, L., et al. (2001). Force and focal adhesion assembly: a close relationship studied using elastic micropatterned substrates. Nat. Cell Biol. *3*, 466-472.

Barton, D.L., Henkes, S., Weijer, C.J., and Sknepnek, R. (2017). Active Vertex Model for cell-resolution description of epithelial tissue mechanics. PLoS Comput. Biol. 13, e1005569.

Begnaud, S., Chen, T., Delacour, D., Mège, R.M., and Ladoux, B. (2016). Mechanics of epithelial tissues during gap closure. Curr. Opin. Cell Biol. 42, 52–62.

Bement, W.M., Leda, M., Moe, A.M., Kita, A.M., Larson, M.E., Golding, A.E., Pfeuti, C., Su,

K.C., Miller, A.L., Goryachev, A.B., et al. (2015). Activator-inhibitor coupling between Rho signalling and actin assembly makes the cell cortex an excitable medium. Nat. Cell Biol. *17*, 1471–1483.

Bergert, M., Erzberger, A., Desai, R.A., Aspalter, I.M., Oates, A.C., Charras, G., Salbreux, G., and Paluch, E.K. (2015). Force transmission during adhesion-independent migration. Nat. Cell Biol. *17*, 524–529.

Le Berre, M., Aubertin, J., and Piel, M. (2012). Fine control of nuclear confinement identifies a threshold deformation leading to lamina rupture and induction of specific genes. Integr. Biol. *4*, 1406–1414.

Le Berre, M., Liu, Y.J., Hu, J., Maiuri, P., Bénichou, O., Voituriez, R., Chen, Y., and Piel, M. (2013). Geometric Friction Directs Cell Migration. Phys. Rev. Lett. 111, 1–5.

Bhabha, G., Johnson, G.T., Schroeder, C.M., and Vale, R.D. (2016). How dynein moves along microtubules. Trends Biochem Sci 41, 94–105.

Bissell, M.J. (2017). Goodbye flat biology - time for the 3rd and the 4th dimensions. J. Cell Sci. 130, 3–5.

Boraas, L.C., Pineda, E.T., and Ahsan, T. (2018). Actin and myosin II modulate differentiation of pluripotent stem cells. PLoS One 13, 1–14.

Bos, J., Rehmann, H., and Wittinghofer, A. (2007). GEFs and GAPs: Critical Elements in the Control of Small G Proteins. Cell *129*, 865–877.

Boyden (1962). The Chemotactic Effect of Mixtures of Antibody and Antigen on Polymorphonucleaer Leucocytes. J. Exp. Med. 115, 453–466.

Brevier, J., Vallade, M., and Riveline, D. (2007). Force-extension relationship of cell-cell contacts. Phys. Rev. Lett. 98, 98–101.

Broedersz, C.P. (2016). Modeling semiflexible polymer networks. 5, 1–46.

Bronner, M.E., and LeDouarin, N.M. (2012). Development and evolution of the neural crest: An overview. Dev. Biol. *366*, 2–9.

Brugués, A., Anon, E., Conte, V., Veldhuis, J.H., Gupta, M., Colombelli, J., Muñoz, J.J., Brodland, G.W., Ladoux, B., and Trepat, X. (2014). Forces driving epithelial wound healing. Nat. Phys. *10*, 683–690.

Caballero, D., Voituriez, R., and Riveline, D. (2014). Protrusion fluctuations direct cell motion. Biophys. J. 107, 34–42.

Caballero, D., Voituriez, R., and Riveline, D. (2015a). The cell ratchet: Interplay between efficient protrusions and adhesion determines cell motion. Cell Adh. Migr. 9, 327–334.

Caballero, D., Comelles, J., Piel, M., Voituriez, R., and Riveline, D. (2015b). Ratchetaxis: Long-Range Directed Cell Migration by Local Cues. Trends Cell Biol. *25*, 815–827.

Caballero, D., Voituriez, R., and Riveline, D. (2015c). The cell ratchet: Interplay between efficient protrusions and adhesion determines cell motion. Cell Adhes. Migr. 9, 327–334.

Caggiati, A., Phillips, M., Lametschwandtner, A., and Allegra, C. (2006). Valves in Small Veins and Venules. Eur. J. Vasc. Endovasc. Surg. *32*, 447–452.

Callan-Jones, A.C., and Voituriez, R. (2016). Actin flows in cell migration: From locomotion and polarity to trajectories. Curr. Opin. Cell Biol. 38, 12–17.

Cao, J., and Schnittler, H. (2019). Putting VE-cadherin into JAIL for junction remodeling. J. Cell Sci. *132*, 1-15.

Cetera, M., Ramirez-San Juan, G.R., Oakes, P.W., Lewellyn, L., Fairchild, M.J., Tanentzapf, G., Gardel, M.L., and Horne-Badovinac, S. (2014). Epithelial rotation promotes the global alignment of contractile actin bundles during Drosophila egg chamber elongation. Nat. Commun. 5, 5511-5523.

Chambers, A.F., Groom, A.C., and MacDonald, I.C. (2002). Dissemination and growth of cancer cells in metastatic sites. Nat. Rev. Cancer 2, 563–572.

Chauwin, J.-F., Ajdari, A., and Prost, J. (1995). Current Reversal in Asymmetric Pumping. Europhys. Lett. *32*, 373–378.

Chen, C., and Chen, H. (2009). Functional suppression of E-cadherin by protein kinase C δ . J. Cell Sci. 122, 513–523.

Chen, S., Hourwitz, M., Campanello, L., Fourkas, J.T., Losert, W., and Parent, C.A. (2019). Actin Cytoskeleton and Focal Adhesions Regulate the Biased Migration of Breast Cancer Cells on Nanoscale Asymmetric Sawteeth. ACS Nano *13*, 1454–1468.

Cheney, R.E., Riley, M.A., and Mooseker, M.S. (1993). Phylogenetic Analysis of the Myosin Superfamily. Cell Motil. Cytoskeleton *24*, 215–223.

Chin, A.S., Worley, K.E., Ray, P., Kaur, G., Fan, J., and Wan, L.Q. (2018). Epithelial cell chirality revealed by three-dimensional spontaneous rotation. Proc. Natl. Acad. Sci. U. S. A. 115, 12188–12193.

Choi, S.M., Kim, W.H., Côté, D., Park, C.-W., and Lee, H. (2011). Blood cell assisted in vivo Particle Image Velocimetry using the confocal laser scanning microscope. Opt. Express 19, 4357-4365.

Comelles, J., Caballero, D., Voituriez, R., Hortiguela, V., Wollrab, V., Godeau, A.L., Samitier, J., Martinez, E., and Riveline, D. (2014). Cells as active particles in asymmetric potentials: Motility under external gradients. Biophys. J. 107, 1513–1522.

Comelles, J., Ss, S., Anvitha, S., Salbreux, G., Jülicher, F., Inamdar, M., and Riveline, D. (2019). Elongations of epithelial colony in vitro: symmetry breaking through collective effects. bioRxiv 755181.

Cooke, R. (1989). Structure of the Myosin Head. Cell Motil. Cytoskeleton 14, 183–186.

Copos, C., and Mogilner, A. (2020). A hybrid stochastic-deterministic mechanochemical model of cell polarization. Mol. Biol. Cell. 31, 1551-1649.

Courtemanche, N. (2018). Mechanisms of formin-mediated actin assembly and dynamics. Biophys. Rev. 10, 1553–1569.

Curtis, A.S.G. (1964). A Study by Interference Reflection Microscopy. J. Cell Biol. 20, 199–215.

Dalby, B., Cates, S., Harris, A., Ohki, E.C., Tilkins, M.L., Price, P.J., and Ciccarone, V.C. (2004). Advanced transfection with Lipofectamine 2000 reagent: primary neurons, siRNA, and high-throughput applications. Methods *33*, 95–103.

Deforet, M., Hakim, V., Yevick, H.G., Duclos, G., and Silberzan, P. (2014). Emergence of collective modes and tri-dimensional structures from epithelial confinement. Nat. Commun. 5, 1–9.

Delanoë-Ayari, H., Lenz, P., Brevier, J., Weidenhaupt, M., Vallade, M., Gulino, D., Joanny, J.F., and Riveline, D. (2004). Periodic adhesive fingers between contacting cells. Phys. Rev. Lett. *93*, 1–4.

Delanoë-Ayari, H., Brevier, J., and Riveline, D. (2011). Scaling concepts in cell physics: Paradigms for cell adhesion. Soft Matter 7, 824–829.

Doxzen, K., Vedula, S.R.K., Leong, M.C., Hirata, H., Gov, N.S., Kabla, A.J., Ladoux, B., and Lim, C.T. (2013). Guidance of collective cell migration by substrate geometry. Integr. Biol. *5*, 1026–1035.

Drug, T.C., Piazzesi, G., Reconditi, M., Linari, M., Lucii, L., Sun, Y., Narayanan, T., and Boesecke, P. (2002). Mechanism of force generation by myosin heads in skeletal muscle. Nature *517*, 659–662.

Le Duc, Q., Shi, Q., Blonk, I., Sonnenberg, A., Wang, N., Leckband, D., and Rooij, J. De (2010). Vinculin potentiates E-cadherin mechanosensing and is recruited to actin-anchored sites within adherens junctions in a myosin II—dependent manner. *189*, 1107–1115.

Dyche Mullins, R. (2010). Cytoskeletal Mechanisms for Breaking Cellular Symmetry. Cold Spring Harb. Perspect. Biol. *94*, 1–16.

Elzinga, M., Collins, J.H., Kuehlt, W.M., and Adelsteint, R.S. (1973). Complete Amino-Acid Sequence of Actin of Rabbit Skeletal Muscle. Proc. Natl. Acad. Sci. U. S. A. 70, 2687–2691.

Etournay, R., Popović, M., Merkel, M., Nandi, A., Blasse, C., Aigouy, B., Brandl, H., Myers, G., Salbreux, G., Jülicher, F., et al. (2015). Interplay of cell dynamics and epithelial tension during morphogenesis of the Drosophila pupal wing. Elife 4, 1–51.

Etournay, R., Merkel, M., Popović, M., Brandl, H., Dye, N.A., Aigouy, B., Salbreux, G., Eaton, S., and Jülicher, F. (2016). TissueMiner: A multiscale analysis toolkit to quantify how cellular

processes create tissue dynamics. Elife 5, 1–28.

Evangelista, M., Zigmond, S., and Boone, C. (2003). Formins: signaling effectors for assembly and polarization of actin filaments. J. Cell Sci. 116, 2603–2611.

Fabbretti, F., Iannetti, I., Guglielmi, L., Perconti, S., Evangelistella, C., De Santis, L.P., Bongiorni, S., and Prantera, G. (2016). Confocal analysis of nuclear lamina behavior during male meiosis and spermatogenesis in Drosophila melanogaster. PLoS One 11, 1–13.

Feynman, R.P., Leighton, R.B., and Sands, M. (1963). Ratchet and pawl. Feynman Lect. Phys. *1*, 46–51.

Friedl, P., and Gilmour, D. (2009). Collective cell migration in morphogenesis, regeneration and cancer. Nat. Rev. Mol. Cell Biol. *10*, 445–457.

Fürth, R. (1920). Die Brownsche Bewegung bei Berücksichtigung einer Persistenz der Bewegungsrichtung. Mit Anwendungen auf die Bewegung lebender Infusorien. Zeitschrift Für Phys. 2, 244–256.

Gañán-Calvo, A.M., and Gordillo, J.M. (2001). Perfectly monodisperse microbubbling by capillary flow focusing. Phys. Rev. Lett. 87, 2745011–2745014.

Garcia, S., Hannezo, E., Elgeti, J., Joanny, J.F., Silberzan, P., and Gov, N.S. (2015). Physics of active jamming during collective cellular motion in a monolayer. Proc. Natl. Acad. Sci. U. S. A. 112, 15314–15319.

Gardel, M.L., Schneider, I.C., Aratyn-Schaus, Y., and Waterman, C.M. (2010). Mechanical Integration of Actin and Adhesion Dynamics in Cell Migration. Annu. Rev. Cell. Dev. Biol. 26, 315–333.

Gardner, M.K., Zanic, M., and Jonathon, H. (2013). Microtubule Catastrophe and Rescue. Curr. Opin. Cell Biol. *25*, 14–22.

Giannone, G., Dubin-thaler, B.J., Döbereiner, H.-G., Kieffer, N., Bresnick, A.R., and Sheetz, M.P. (2004). Periodic Lamellipodial Contractions Correlate with Rearward Actin Waves. Cell *116*, 431–443.

Girkin, J.M., and Carvalho, M.T. (2018). The light-sheet microscopy revolution. J. Opt. 20, 1-15.

Godeau, A., Leoni, M., Comelles, J., Delanoe-Ayari, H., Ott, A., Harlepp, S., Sens, P., and Riveline, D. (2020). Temporal correlation between oscillating force dipoles drives single cell migration in 3D. bioRxiv 081984.

Goffin, J.M., Pittet, P., Csucs, G., Lussi, J.W., Meister, J., and Hinz, B. (2006). Focal adhesion size controls tension-dependent recruitment of α -smooth muscle actin to stress fibers. J. Cell Biol. *172*, 259–268.

Guevorkian, K., Colbert, M.-J., Durth, M., Dufour, S., and Brochard-Wyart, F. (2010). Aspiration of Biological Viscoelastic Drops. Phys. Rev. Lett. *218101*, 1–4.

Guthardt Torres, P., Bischofs, I.B., and Schwarz, U.S. (2012). Contractile network models for adherent cells. Phys. Rev. E *85*, 1–13.

Van Haastert, P.J.M., and Devreotes, P.N. (2004). Chemotaxis: Signalling the way forward. Nat. Rev. Mol. Cell Biol. *5*, 626–634.

Haigo, S.L., and Bilder, D. (2011). Global tissue revolutions in a morphogenetic movement controlling elongation. Science. *331*, 1071–1074.

Halfmann, C.T., Sears, R.M., Katiyar, A., Busselman, B.W., Aman, L.K., Zhang, Q., O'Bryan, C.S., Angelini, T.E., Lele, T.P., and Roux, K.J. (2019). Repair of nuclear ruptures requires barrier-to-autointegration factor. J. Cell Biol. *218*, 2136–2149.

Hawkins, R.J., Piel, M., Faure-Andre, G., Lennon-Dumenil, A.M., Joanny, J.F., Prost, J., and Voituriez, R. (2009). Pushing off the walls: A mechanism of cell motility in confinement. Phys. Rev. Lett. *102*, 1–4.

He, Y., Ren, Y., Wu, B., Decourt, B., Lee, A.C., Taylor, A., and Suter, D.M. (2015). Src and cortactin promote lamellipodia protrusion and filopodia formation and stability in growth cones. Mol. Biol. Cell *26*, 3229–3244.

Helfman, D.M., Levy, E.T., Berthier, C., Shtutman, M., Riveline, D., Grosheva, I., Lachish-Zalait, A., Elbaum, M., and Bershadsky, A.D. (1999). Caldesmon inhibits nonmuscle cell contractility and interferes with the formation of focal adhesions. Mol. Biol. Cell *10*, 3097–3112.

Herrmann, H., Bär, H., Kreplak, L., Strelkov, S. V, and Aebi, U. (2007). Intermediate filaments: from cell architecture to nanomechanics. Nat. Rev. Mol. Cell Biol. 8, 562–573.

Hodge, R.G., and Ridley, A.J. (2016). Regulating Rho GTPases and their regulators. Nat. Rev. Mol. Cell Biol. *17*, 496–510.

Hodgson, L., Shen, F., and Hahn, K. (2010). Biosensors for characterizing the dynamics of Rho family GTPases in living cells. Curr. Protoc. Cell Biol. *100*, 14111–141126.

Houben, F., Ramaekers, F.C.S., Snoeckx, L.H.E.H., and Broers, J.L.V. (2007). Role of nuclear lamina-cytoskeleton interactions in the maintenance of cellular strength. Biochim. Biophys. Acta - Mol. Cell Res. *1773*, 675–686.

Huveneers, S., and Rooij, J. De (2013). Mechanosensitive systems at the cadherin – F-actin interface. 120, 403-413.

Iglesias, P.A., and Devreotes, P.N. (2008a). Navigating through models of chemotaxis. Curr. Opin. Cell Biol. 60, 35–40.

Jaeger, P.A., McElfresh, C., Wong, L.R., and Ideker, T. (2015). Beyond agar: Gel substrates with improved optical clarity and drug efficiency and reduced autofluorescence for microbial growth experiments. Appl. Environ. Microbiol. *81*, 5639–5649.

Jain, S., Cachoux, V.M.L., Narayana, G.H.N.S., Beco, S. De, Alessandro, J.D., Cellerin, V., Chen, T., Heuzé, M.L., Marcq, P., Mège, R., et al. (2020). The role of single-cell mechanical behaviour and polarity in driving collective cell migration. Nat. Phys. *16*, 802–809.

Jiang, X., Bruzewicz, D.A., Wong, A.P., Piel, M., and Whitesides, G.M. (2005). Directing cell migration with asymmetric micropatterns. Proc. Natl. Acad. Sci. U. S. A. *102*, 975–978.

Joanny, J.F., and Prost, J. (2009). Active gels as a description of the actin-myosin cytoskeleton. HFSP J. 3, 94–104.

Juan, G.R.R., Oakes, P.W., and Gardel, M.L. (2017). Contact guidance requires spatial control of leading-edge protrusion. Mol. Biol. Cell 28, 1043–1053.

Jülicher, F., Ajdari, A., Prost, J., and Julicher, F. (1997). Modeling molecular motors. Rev. Mod. Phys. 69, 1269–1282.

Kaverina, I., and Straube, A. (2011). Regulation of cell migration by dynamics microtubules. Semin Cell Dev Biol *22*, 968–974.

Kicheva, A., Pantazis, P., Bollenbach, T., Kalaidzidis, Y., Bittig, T., Jülicher, F., and González-Gaitán, M. (2007). Kinetics of morphogen gradient formation. Science. *315*, 521–525.

Kicheva, A., Cohen, M., and Briscoe, J. (2012). Developmental pattern formation: Insights from physics and biology. Science. *338*, 210–212.

Kim, C., Lee, K.S., Kim, Y.E., Lee, K.J., Lee, S.H., Kim, T.S., and Kang, J.Y. (2009). Rapid exchange of oil-phase in microencapsulation chip to enhance cell viability. Lab Chip *9*, 1294–1297.

Kim, C., Chung, S., Kim, Y.E., Lee, K.S., Lee, S.H., Oh, K.W., and Kang, J.Y. (2011). Generation of core-shell microcapsules with three-dimensional focusing device for efficient formation of cell spheroid. Lab Chip *11*, 246–252.

Kimura, K., Ito, M., Amano, M., Chihara, K., Fukata, Y., Nakafuku, M., Yamamori, B., Feng, J., Nakano, T., Okawa, K., et al. (1996). Regulation of Myosin Phosphatase by Rho and Rho-associated kinase (Rho-kinase). Science. *273*, 245–248.

Kirfel, J., Magin, T.M., and Reichelt, J. (2003). Keratins: A structural scaffold with emerging functions. Cell. Mol. Life Sci. 60, 56–71.

Kondo, S., and Miura, T. (2010). Reaction-diffusion model as a framework for understanding biological pattern formation. Science. *329*, 1616–1620.

Koo, P.K., Weitzman, M., Sabanaygam, C.R., van Golen, K.L., and Mochrie, S.G.J. (2015). Extracting Diffusive States of Rho GTPase in Live Cells: Towards In Vivo Biochemistry. PLoS Comput. Biol. 11, 1–26.

Korobova, F., and Svitkina, T. (2008). Arp2/3 Complex Is Important for Filopodia Formation, Growth Cone Motility, and Neuritogenesis in Neuronal Cells. Mol. Biol. Cell 19, 1561–1574.

Kreten, F.H., Hoffmann, C., Riveline, D., and Kruse, K. (2018). Active bundles of polar and bipolar filaments. Phys. Rev. E *98*, 1–13.

Kruse, K., Joanny, J.F., Jülicher, F., Prost, J., and Sekimoto, K. (2004). Asters, Vortices, and Rotating Spirals in Active Gels of Polar Filaments. Phys. Rev. Lett. 92, 1–4.

Kruse, K., Joanny, J.F., Jülicher, F., Prost, J., and Sekimoto, K. (2005). Generic theory of active polar gels: A paradigm for cytoskeletal dynamics. Eur. Phys. J. E *16*, 5–16.

Ku, B., Kats, G., Roodink, I., Verrijp, K., Wesseling, P., Ruiter, D., de Waal, R., and Leenders, W. (2007). Micronodular transformation as a novel mechanism of VEGF-A-induced metastasis. Oncogene *26*, 5808–5815.

Kuhn, J.R., and Pollard, T.D. (2005). Real-Time Measurements of Actin Filament Polymerization by Total Internal Reflection Fluorescence Microscopy. Biophys. J. 88, 1387–1402.

Kühn, S., and Geyer, M. (2014). Formins as effector proteins of rho GTPases. Small GTPases 5, 1–16.

Kutejova, E., Briscoe, J., and Kicheva, A. (2009). Temporal dynamics of patterning by morphogen gradients. Curr. Opin. Genet. Dev. 19, 315–322.

Labelle, M., and Hynes, R.O. (2012). The initial hours of metastasis: The importance of cooperative host-tumor cell interactions during hematogenous dissemination. Cancer Discov. 2, 1091–1099.

Ladoux, B., and Mège, R.M. (2017). Mechanobiology of collective cell behaviours. Nat. Rev. Mol. Cell Biol. *18*, 743–757.

Langley, R.R., and Fidler, I.J. (2011). The seed and soil hypothesis revisited-The role of tumor-stroma interactions in metastasis to different organs. Int. J. Cancer 128, 2527–2535.

Langley, R.R., and Fidler, I.J. (2012). Interactions in Metastasis To Different Organs. Int. J. Cancer 128, 2527–2535.

Lellouch, A.C., Garcia, A., Bayonas, D., and Lecuit, T. (2018). Strengthen Your Junctions to Resist the Force. 47, 406–407.

Li, Y., Vieceli, F., Gonzalez, W., Li, A., Tang, W., Lois, C., and Bronner, M. (2019). In Vivo Quantitative Imaging Provides Insights into Trunk Neural Crest Migration. Cell Rep. 26, 1489–1500.

Liu, Y.J., Le Berre, M., Lautenschlaeger, F., Maiuri, P., Callan-Jones, A., Heuzé, M., Takaki, T., Voituriez, R., and Piel, M. (2015). Confinement and low adhesion induce fast amoeboid migration of slow mesenchymal cells. Cell *160*, 659–672.

Lowery, J., Kuczmarski, E.R., Herrmann, H., and Goldma, R.D. (2015). Intermediate filaments play a pivotal role in regulating cell architecture and function. J. Biol. Chem. *290*, 17145–17153.

Lvarez, P. (2018). Light-sheet microscopy: a tutorial. Adv. Opt. Phtonics 10, 111–179.

MacHacek, M., Hodgson, L., Welch, C., Elliott, H., Pertz, O., Nalbant, P., Abell, A., Johnson, G.L., Hahn, K.M., and Danuser, G. (2009). Coordination of Rho GTPase activities during cell protrusion. Nature *461*, 99–103.

Machesky, L.M. (2008). Lamellipodia and filopodia in metastasis and invasion. FEBS Lett. 582, 2102–2111.

Magnasco, M.O., and Stolovitzky, G. (1998). Feynman's Ratchet and Pawl. J. Stat. Phys. 93, 615–632.

Mahmud, G., Campbell, C.J., Bishop, K.J.M., Komarova, Y. a., Chaga, O., Soh, S., Huda, S., Kandere-Grzybowska, K., and Grzybowski, B. a. (2009). Directing cell motions on micropatterned ratchets. Nat. Phys. *5*, 606–612.

Maiuri, P., Terriac, E., Paul-Gilloteaux, P., Vignaud, T., McNally, K., Onuffer, J., Thorn, K., Nguyen, P.A., Georgoulia, N., Soong, D., et al. (2012). The first World Cell Race. Curr. Biol. 22, 673–675.

Maiuri, P., Rupprecht, J.-F., Wieser, S., Ruprecht, V., Bénichou, O., Carpi, N., Coppey, M., De Beco, S., Gov, N., Heisenberg, C.-P., et al. (2015). Actin Flows Mediate a Universal Coupling between Cell Speed and Cell Persistence. Cell *161*, 374–386.

Malik-Garbi, M., Ierushalmi, N., Jansen, S., Abu-Shah, E., Goode, B.L., Mogilner, A., and Keren, K. (2019). Scaling behaviour in steady-state contracting actomyosin networks. Nat. Phys. 15, 509–516.

Le Maout, E., Lo Vecchio, S., Bhat, A., and Riveline, D. (2018). Directing cell migration on flat substrates and in confinement with microfabrication and microfluidics. Methods Cell Biol. *147*, 109–132.

Martin, K., Reimann, A., Fritz, R.D., Ryu, H., Jeon, N.L., and Pertz, O. (2016). Spatio-temporal co-ordination of RhoA, Rac1 and Cdc42 activation during prototypical edge protrusion and retraction dynamics. Sci. Rep. *6*, 1–14.

Mattila, P.K., and Lappalainen, P. (2008). Filopodia: Molecular architecture and cellular functions. Nat. Rev. Mol. Cell Biol. 9, 446–454.

Mayer, M., Depken, M., Bois, J.S., Jülicher, F., and Grill, S.W. (2010). Anisotropies in cortical tension reveal the physical basis of polarizing cortical flows. Nature *467*, 617–621.

Mayor, R., and Theveneau, E. (2012). The neural crest. Development 140, 2247–2251.

Meunier, S., and Vernos, I. (2012). Microtubule assembly during mitosis – from distinct origins to distinct functions. J. Cell Sci. *125*, 2805–2814.

Mishra, A.K., Campanale, J.P., Mondo, J.A., and Montell, D.J. (2019). Cell interactions in collective cell migration. Dev. *146*, 1–7.

Munjal, A., Philippe, J., Munro, E., and Lecuit, T. (2015). A self-organized biomechanical network drives shape changes during tissue morphogenesis.

Nestor-Bergmann, A., Liang, X., Jensen, O.E., Bryant, Z., Yap, A.S., Acharya, B.R., Nestorbergmann, A., Liang, X., Gupta, S., Duszyc, K., et al. (2018). A Mechanosensitive RhoA Pathway that Protects Epithelia against Acute Tensile Stress Article A Mechanosensitive RhoA Pathway that Protects Epithelia against Acute Tensile Stress. Dev. Cell 47, 439–451.

Nier, V., Deforet, M., Duclos, G., Yevick, H.G., Cochet-Escartin, O., Marcq, P., and Silberzan, P. (2015). Tissue fusion over nonadhering surfaces. Proc. Natl. Acad. Sci. U. S. A. *112*, 9546–9551.

Niessen, C.M. (2007). Tight junctions/adherens junctions: Basic structure and function. J. Invest. Dermatol. 127, 2525–2532.

Nishikawa, M., Naganathan, S.R., Jülicher, F., and Grill, S.W. (2017). Controlling contractile instabilities in the actomyosin cortex. Elife *6*, 1–21.

Nooranidoost, M., Izbassarov, D., and Muradoglu, M. (2016). Droplet formation in a flow focusing configuration: Effects of viscoelasticity. Phys. Fluids 28, 23102-123112.

Nürnberg, A., Kitzing, T., and Grosse, R. (2011). Nucleating actin for invasion. Nat. Rev. Cancer 11, 117–187.

Nurse, P., Thuriaux, P., and Nasmyth, K. (1976). Genetic control of the cell division cycle in the fission yeast Schizosaccharomyces pombe. MGG Mol. Gen. Genet. *146*, 167–178.

Paget, S. (1889). The distribution of secondary growths in cancer of the breast. Lancet 133, 571–573.

Palecek, S.P., Loftus, J.C., Ginsberg, M.H., Lauffenburger, D.A., and Horwitz., A.F. (1997). Integrin-ligand binding properties govern cell migration speed through cell-substratum adhesiveness. Nat. Publ. Gr. 385, 537–540.

Pannekoek, W., Rooij, J. De, and Gloerich, M. (2019). Force transduction by cadherin adhesions in morphogenesis. F1000 Res. 8, 1–14.

Pellegrin, S., and Mellor, H. (2007). Actin stress fibers. J. Cell Sci. *120*, 3491–3499. Pertz, O. (2010). Spatio-temporal Rho GTPase signaling - Where are we now? J. Cell Sci. *123*, 1841–1850.

Pertz, O., Hodgson, L., Klemke, R.L., and Hahn, K.M. (2006). Spatiotemporal dynamics of RhoA activity in migrating cells. Nature 440, 1069–1072.

Petit, V., and Thiery, J. (2000). Focal adhesions: structure and dynamics. Biol. Cell 92, 477–494.

Petitjean, L., Reffay, M., Grasland-Mongrain, E., Poujade, M., Ladoux, B., Buguin, A., and Silberzan, P. (2010). Velocity fields in a collectively migrating epithelium. Biophys. J. 98,

1790–1800.

Pollard, T.D., and Korn, E.D. (1973). Isolation from acanthamoeba castellanii of an enzyme similar to muscle myosin. J. Biol. Chem. 248, 4682–4690.

Pollard, T.D., and Mooseker, M.S. (1981). Direct Measurement of Actin Polymerization Rate Constants by Electron Microscopy of Actin Filaments Nucleated by Isolated Microvillus Cores. J. Cell Biol. 88, 1–5.

Prost, J., Chauwin, J.F., Peliti, L., and Ajdari, A. (1994). Asymmetric pumping of particles. Phys. Rev. Lett. 72, 2652–2655.

Prost, J., Jülicher, F., and Joanny, J.F. (2015). Active gel physics. Nat. Phys. 11, 111–117.

Puliafito, A., Hufnagel, L., Neveu, P., Streichan, S., Sigal, A., Fygenson, D.K., and Shraiman, B.I. (2012). Collective and single cell behavior in epithelial contact inhibition. Proc. Natl. Acad. Sci. U. S. A. 109, 739–744.

Purcell, E.M. (1977). Life at low Reynolds number. Am. J. Phys. 45, 3–11.

Rahman, A., Carey, S.P., Kraning-rush, C.M., Goldblatt, Z.E., Bordeleau, F., Lampi, M.C., Lin, D.Y., García, A.J., and Reinhart-king, C.A. (2016). Vinculin regulates directionality and cell polarity in two- and three-dimensional matrix and three-dimensional microtrack migration. Mol. Biol. Cell *27*, 1431–1441.

Rappel, W.-J., and Loomis, W.F. (2009). Eukaryotic Chemotaxis. Wiley Interdiscip. Rev. Syst. Biol. Med. *1*, 141–149.

Ray, A., Lee, O., Win, Z., Edwards, R.M., Alford, P.W., Kim, D.H., and Provenzano, P.P. (2017). Anisotropic forces from spatially constrained focal adhesions mediate contact guidance directed cell migration. Nat. Commun. *8*, 1–17.

Raz-Ben Aroush, D., Ofer, N., Abu-Shah, E., Allard, J., Krichevsky, O., Mogilner, A., and Keren, K. (2017). Actin Turnover in Lamellipodial Fragments. Curr. Biol. *27*, 2963–2973.

Reffay, M., Parrini, M.C., Ladoux, B., Buguin, A., Coscoy, S., Amblard, F., Camonis, J., and Silberzan, P. (2014). Interplay of RhoA and mechanical forces in collective cell migration driven by leader cells. Nat. Cell Biol. *16*, 217–223.

Rejniak, K.A. (2016). Circulating Tumor Cells: When a Solid Tumor Meets a Fluid. Adv Exp Med Biol. *936*, 93–106.

Reymann, A.C., Suarez, C., Guérin, C., Martiel, J.L., Staiger, C.J., Blanchoin, L., and Boujemaa-Paterski, R. (2011). Turnover of branched actin filament networks by stochastic fragmentation with ADF/cofilin. Mol. Biol. Cell *22*, 2541–2550.

Ridley, A.J. (2015). Rho GTPase signalling in cell migration. Curr. Opin. Cell Biol. 36, 103–112.

Ridley, A.J., and Hall, A. (1992). The small GTP-binding protein rho regulates the assembly

of focal adhesions and actin stress fibers in response to growth factors. Cell 70, 389–399.

Ridley, A.J., Paterson, H.F., Johnston, C.L., Diekmann, D., and Hall, A. (1992). The small GTP-binding protein rac regulates growth factor-induced membrane ruffling. Cell *70*, 401–410.

Riveline, D., Zamir, E., Balaban, N.Q., Schwarz, U.S., Ishizaki, T., Narumiya, S., Kam, Z., Geiger, B., and Bershadsky, A.D. (2001). Focal Contacts as Mechanosensors: Externally Applied Local Mechanical Force Induces Growth of Focal Contacts by an mDia1-dependent and. J. Cell Biol. *153*, 1175–1185.

Robert, A., Hookway, C., and Gelfand, V.I. (2016). Intermediate filament dynamics: What we can see now and why it matters. BioEssays *38*, 232–243.

Roure, O., Saez, A., Buguin, A., Austin, R.H., Chavrier, P., Siberzan, P., and Ladoux, B. (2005). Force mapping in epithelial cell migration. Proc. Natl. Acad. Sci. U. S. A. 102, 2390–2395.

Rousselet, J., Salome, L., Ajdari, A., and Prostt, J. (1994). Directional motion of brownian particles induced by a periodic asymmetric potential. Nature *370*, 446–448.

Roussos, E.T., Codeelis, J.S., and Patsialou, A. (2014). Chemotaxis in cancer. Nat. Rev. Cancer 11, 573–587.

Schaus, T.E., Taylor, E.W., and Borisy, G.G. (2007). Self-organization of actin filament orientation in the dendritic- nucleation/array-treadmilling model. Proc. Natl. Acad. Sci. U. S. A. 104, 7086–7091.

Schulze, K.D., Zehnder, S.M., Urueña, J.M., Bhattacharjee, T., Sawyer, W.G., and Angelini, T.E. (2017). Elastic modulus and hydraulic permeability of MDCK monolayers. J. Biomech. *12*, 2–5.

Schuppler, M., Keber, F.C., Kroger, M., and Bausch, A.R. (2016). Boundaries steer the contraction of active gels. Nat. Commun. 7, 1–10.

Schwartz, M. (2004). Rho signalling at a glance. J. Cell Sci. 117, 5457–5458.

Schwarz, U.S., and Safran, S.A. (2013). Physics of adherent cells. Rev. Mod. Phys. 85, 1327–1381.

Selmeczi, D., Li, L., Pedersen, L.I.I., Nrrelykke, S.F., Hagedorn, P.H., Mosler, S., Larsen, N.B., Cox, E.C., and Flyvbjerg, H. (2008). Cell motility as random motion: A review. Eur. Phys. J. Spec. Top. *157*, 1–15.

Shaebani, M.R., Wysocki, A., Winkler, R.G., Gompper, G., and Rieger, H. (2020). Computational models for active matter. Nat. Rev. Phys. 2, 181–199.

Siedlik, M.J., Manivannan, S., Kevrekidis, I.G., and Nelson, C.M. (2017). Cell Division Induces and Switches Coherent Angular Motion within Bounded Cellular Collectives. Biophys. J. 112, 2419–2427.

Silva, S.S., Mano, J.F., and Reis, R.L. (2010). Potential applications of natural origin polymer-based systems in soft tissue regeneration. Crit. Rev. Biotechnol. *30*, 200–221.

Sit, S.T., and Manser, E. (2011). Rho GTPases and their role in organizing the actin cytoskeleton. J. Cell Sci. 124, 679–683.

Soumya, S.S., Gupta, A., Cugno, A., Deseri, L., Dayal, K., Das, D., Sen, S., and Inamdar, M.M. (2015). Coherent Motion of Monolayer Sheets under Confinement and Its Pathological Implications. PLoS Comput. Biol. *11*, 1–30.

Stuelten, C.H., Parent, C.A., and Montell, D.J. (2018). Cell motility in cancer invasion and metastasis: insights from simple model organisms. Nature. 18, 296–312.

Sun, X., Driscoll, M.K., Guven, C., Das, S., Parent, C.A., Fourkas, J.T., and Losert, W. (2015). Asymmetric nanotopography biases cytoskeletal dynamics and promotes unidirectional cell guidance. Proc. Natl. Acad. Sci. U. S. A. *112*, 12557–12562.

Svitkina, T. (2018). The actin cytoskeleton and actin-based motility. Cold Spring Harb. Perspect. Biol. 10, 1–21.

Svitkina, T.M., and Borisy, G.G. (1999). Arp2/3 Complex and Actin Depolymerizing Factor/Cofilin in Dendritic Organization and Treadmilling of Actin Filament Array in Lamellipodia. J. Cell Biol. *145*, 1009–1026.

Szewczyk, D., Yamamoto, T., and Riveline, D. (2013). Non-monotonic relationships between cell adhesion and protrusions. New J. Phys. *15*, 1-21.

Talmadge, J.E., and Fidler, I.J. (2010). AACR centennial series: The biology of cancer metastasis: Historical perspective. Cancer Res. 70, 5649–5669.

Tanimoto, H., and Sano, M. (2014). A Simple Force-Motion Relation for Migrating Cells Revealed by Multipole Analysis of Traction Stress. Biophys. J. 106, 16–25.

Tanner, K., Mori, H., Mroue, R., Bruni-Cardoso, A., and Bissell, M.J. (2012). Coherent angular motion in the establishment of multicellular architecture of glandular tissues. Proc. Natl. Acad. Sci. U. S. A. *109*, 1973–1978.

Théry, M., and Piel, M. (2019). Adhesive Micropatterns for Cells: A Microcontact Printing Protocol. Cold Spring Harb Protoc 4, 1–12.

Trushko, A., Meglio, I. Di, Merzouki, A., Blanch-Mercader, C., Abuhattum, S., Guck, J., Alessandri, K., Nassoy, P., Kruse, K., Chopard, B., et al. (2019). Buckling of epithelium growing under spherical confinement. bioRxiv 513119.

Tsai, F.J., Lai, M.T., Cheng, J., Chao, S.C.C., Korla, P.K., Chen, H.J., Lin, C.M., Tsai, M.H., Hua, C.H., Jan, C.I., et al. (2019). Novel K6-K14 keratin fusion enhances cancer stemness and aggressiveness in oral squamous cell carcinoma. Oncogene *38*, 5113–5126.

Turing, A.M. (1952). The chemical basis of morphogenesis. Philos. Trans. R. Soc. London 237, 37–72.

Valiron, O., Caudron, N., and Job, D. (2001). Microtubule dynamics. Cell. Mol. Life Sci. 58, 2069–2084.

Vedula, S.R.K., Leong, M.C., Lai, T.L., Hersen, P., Kabla, A.J., Lim, C.T., and Ladoux, B. (2012). Emerging modes of collective cell migration induced by geometrical constraints. Proc. Natl. Acad. Sci. U. S. A. *109*, 12974–12979.

Vicsek, T., Czirk, A., Ben-Jacob, E., Cohen, I., and Shochet, O. (1995). Novel type of phase transition in a system of self-driven particles. Phys. Rev. Lett. 75, 1226–1229.

Vilela, M., Halidi, N., Besson, S., Elliot, H., Hahn, K., Tytell, J., and Danuser, G. (2014). Fluctuation analysis of activity biosensor images for the study of information flow in signaling pathways. Methods Enzym. *519*, 253–276.

Wang, F. (2009). The signaling mechanisms underlying cell polarity and chemotaxis. Cold Spring Harb. Perspect. Biol. *1*, 002980.

Wang, H., Lacoche, S., Huang, L., Xue, B., and Muthuswamy, S.K. (2013). Rotational motion during three-dimensional morphogenesis of mammary epithelial acini relates to laminin matrix assembly. Proc. Natl. Acad. Sci. U. S. A. *110*, 163–168.

Wang, Y., Chen, C., and Iijima, M. (2011). Signaling mechanisms for chemotaxis. Dev. Growth Differ *59*, 495–502.

Watanabe, T., Hosoya, H., Yonemura, S. (2007). Regulation of Myosin II Dynamics by Phosphorylation and Dephosphorylation of Its Light Chain in Epithelial Cells. Mol. Biol. Cell. 18, 605-616.

Wehrle-haller, B. (2012). Structure and function of focal adhesions. Curr. Opin. Cell Biol. 24, 116–124.

Wijnholds, J. (2019). "Basal Cell Migration" in Regeneration of the Corneal Wound-Bed. Stem Cell Reports 12, 3–5.

Winder, S.J., and Ayscough, K.R. (2005). Actin-binding proteins Actin-binding Proteins. J. Cell Sci. 118, 651–654.

Wottawah, F., Schinkinger, S., Lincoln, B., Ananthakrishnan, R., Romeyke, M., Guck, J., and Käs, J. (2005). Optical rheology of biological cells. Phys. Rev. Lett. *94*, 1–4.

Xu, X., Wen, X., Veltman, D.M., Keizer-Gunnink, I., Pots, H., Kortholt, A., and Jin, T. (2017). GPCR-controlled membrane recruitment of negative regulator C2GAP1 locally inhibits Ras signaling for adaptation and long-range chemotaxis. Proc. Natl. Acad. Sci. U. S. A. 114, 10092–10101.

Yam, P.T., Wilson, C.A., Ji, L., Hebert, B., Barnhart, E.L., Dye, N.A., Wiseman, P.W., Danuser, G., and Theriot, J.A. (2007). Actin-myosin network reorganization breaks symmetry at the cell rear to spontaneously initiate polarized cell motility. J. Cell Biol. 178, 1207–1221.

Yamauchi, K., Yang, M., Jiang, P., Yamamoto, N., Xu, M., Amoh, Y., Tsuji, K., Bouvet, M., Tsuchiya, H., Tomita, K., et al. (2005). Real-time in vivo dual-color imaging of intracapillarycancer cell and nucleus deformation and migration. Cancer Res. 65, 4246–4252.

Yang, C., Czech, L., Gerboth, S., Kojima, S.I., Scita, G., and Svitkina, T. (2007). Novel roles of formin mDia2 in lamellipodia and filopodia formation in motile cells. PLoS Biol. *5*, 2624–2645.

Yoshinaga, N., and Marcq, P. (2012). Contraction of cross-linked actomyosin bundles. Phys. Biol. *9*, 46004-46016.

Zigmond, S. (1977). Ability of polymorphonuclear leukocytes to orient in gradients of chemotactic factors. J. Cell Biol. 75, 606–616.

Zustiak, S.P., Wei, Y., and Leach, J.B. (2013). Protein-hydrogel interactions in tissue engineering: Mechanisms and applications. Tissue Eng. - Part B Rev. 19, 160–171.

10. APPENDIX

This appendix details additional experiments related to Chapter 6 made with drugs or different geometries (such as ellipses) along with other side projects made during the PhD work (printing of protein patterns with an ink-jet printer).

10.1 Drug experiments for multicellular rings

We used many drugs throughout this work in order to change cell mechanics and to analyse the short and long-term answers to the generated perturbation. We tested standard incubation protocols, but we also tried pipette delivering in order to locally stimulate cells. Drugs act at many cellular levels and targets are often multiple. Therefore, disentangling and extracting specific actors can be challenging.

10.1.1 Inhibition of RhoA activity (80µm)

Because we reported in 6.5 a clear relationship between RhoA activity and cell velocity together with an effect on coherence, we sought to decrease RhoA levels using C3-transferase, a specific RhoA inhibitor.

After incubation, we reported a decrease in the overall FRET intensity, confirming the efficacy of the drug. Cells phenotype shifted to highly motile with a higher lamellipodia growth (Figure 10.1a, Movies 37-38). This led to a decrease in coherence, as reported in Figure 10.1b.

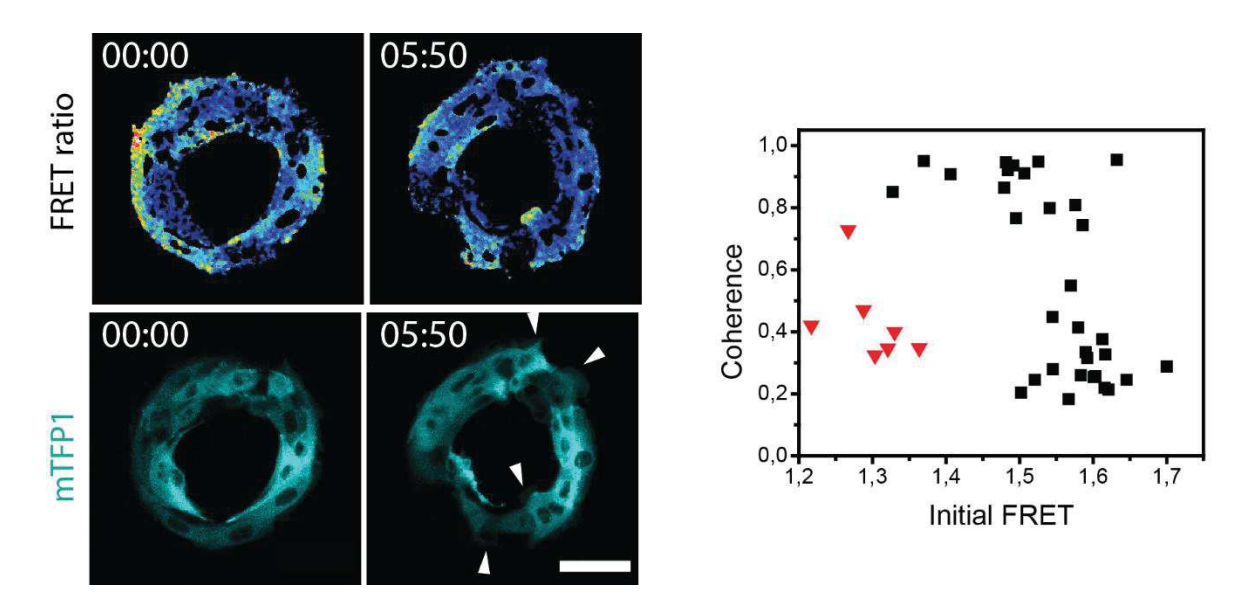


Figure 10.1. Inhibition of RhoA activity decreases coherence and induces lamellipodia formation. (a) Multicellular ring ($80\mu m$) with C3-transferase treatment. Cells were incubated 2H while they seed and spread on the patterns. Arrows indicate lamellipodia. Levels of RhoA activity are lower than the one seen in 6.5.3. They are reported in (b) (red triangles). Scale bar = $50\mu m$. Time in hh:mm.

10.1.2 Increase in RhoA activity (80μm)

We next used a specific RhoA activator (see 10.4) to see whether or not increase in RhoA activity would promote different behaviours. This was tested in MDCK E-cadherin-DsRED cell line, without visualisation of FRET intensity. However, controls with the drug made in section 6.5.1 suggest a proper action.

As shown in the sequence from Figure 10.2 and Movie S39, we reported spontaneous breakages in 46% of the cases. Coherent motion was still possible as we saw some rings rotating and other initiating rotation before breakage.

The cell pointed by a white arrow in Figure 10.2 remains still, strongly adherent without significant motion, suggesting that gradients in velocity could lead to spontaneous breakages.

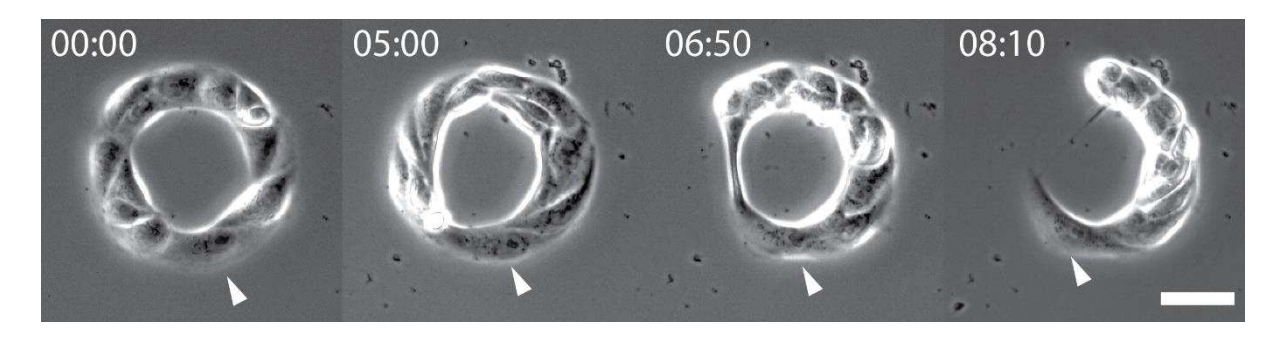


Figure 10.2. Stimulation of RhoA activity leads to the ring breakage. Sequence of a ring (80 μ m) incubated with RhoA activator II (see 10.4). Spontaneous breakage happens where a strongly adherent cell, marked with a white arrow, doesn't follow the rest of the cohort. Scale bar = 50 μ m. Time in hh:mm.

10.1.3 Calcium switch (80μm)

We incubated cells with EDTA in order to chelate calcium and tune cells mechanics (Jain et al., 2020). We observed cell spreading and an absence of coherence in all the cases (see Figure 10.3a, Movie S40). This could be the consequence of two parallel phenomena: (i) cadherin junctions, as reported in 2.4.1.1 are calcium-dependent. Therefore, chelation of calcium fraction will partially disrupt adherens junctions. This could lead to a decrease in coherence, as reported in (Jain et al., 2020) for a 1D configuration under confinement. (ii) Myosin activity is also calcium-dependent. In this context, calcium chelation could impair the acto-myosin cables, acting as an internally driven-constraint (reported in 6.4), leading to a loss of coherence due to radial spreading and escape.

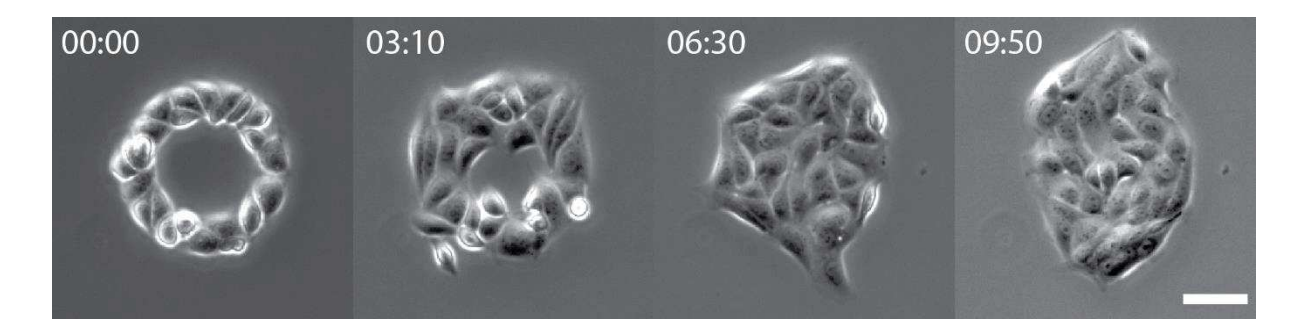


Figure 10.3. Calcium switch impairs coherence. Multicellular ring (80 μ m) incubated with 2mM EDTA, chelating calcium ions. Scale bar = 50 μ m. Time in hh:mm.

10.1.4 Calyculin A (300μm)

Calyculin A is a phosphatase inhibitor. More specifically, it inhibits phosphatase PP1 associated to the protein kinase A. Consequently, this leads to an increase in the fraction of phosphorylated myosin, promoting contraction.

Upon incubation, we saw a fast response (the full process takes 5-10min), leading to breakage of adherens junctions and rounding of cells with no subsequent motion (see Figure 10.4, Movie S41).

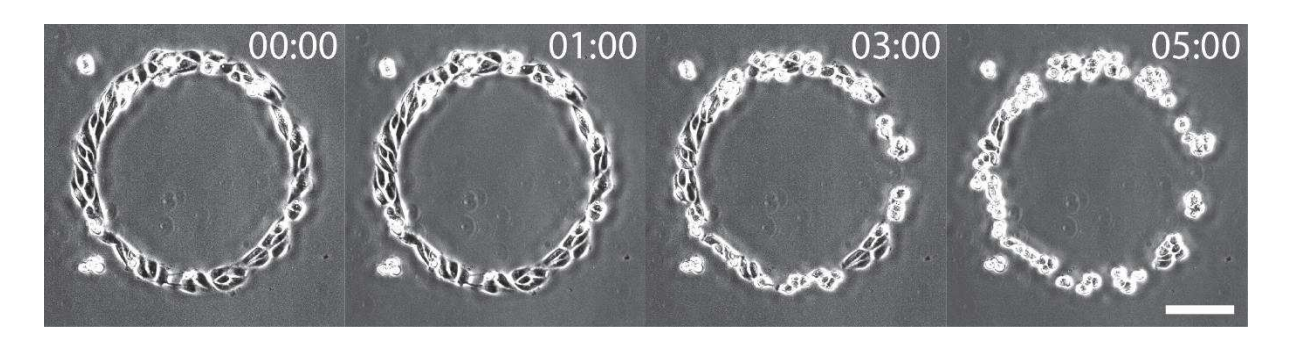


Figure 10.4. Increase in myosin activity leads to cell clustering. $300\mu m$ ring incubated with Calyculin A, increasing myosin activity. Scale bar = $100\mu m$. Time in mm:ss

10.1.5 ML-7 (300μm)

Myosin activity can also be decreased with the usage of specific drugs. In this context, ML-7 is a myosin light chain kinase inhibitor (Watanabe et al, 2007). We incubated rings with this drug and we reported an increase in outwards extensions: while WT cells mainly "close" inwards before extending out, cells treated with ML-7 exhibited similar extension in both radial directions (Figure 10.5, Movie S42) with no closure of the ring. This could be linked to the perturbation of the acto-myosin cables, releasing the constraint applied on cells. However, myosin inhibition also modify cell mechanics and disruption of the acto-myosin cables cannot be considered as the only cause for the observed phenotype.

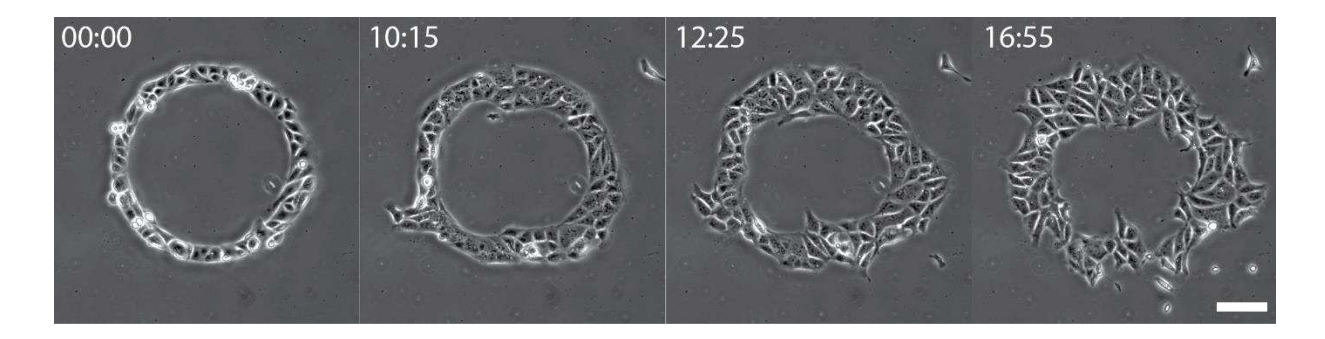


Figure 10.5. Inhibition of myosin induces spreading in and out. $300\mu m$ ring with ML-7, an inibitor of the MRLC kinase. Scale bar = $100\mu m$. Time in hh:mm.

10.1.6 CK666 (300µm)

CK666 is an Arp2/3 inhibitor. We reported a behaviour somehow similar with the non-treated cells (inward closure) but with an apparent decrease of closure speed: after 24 hours, the ring did not close whereas most of the WT rings are already closed by that time (Figure 10.6, Movie S43).

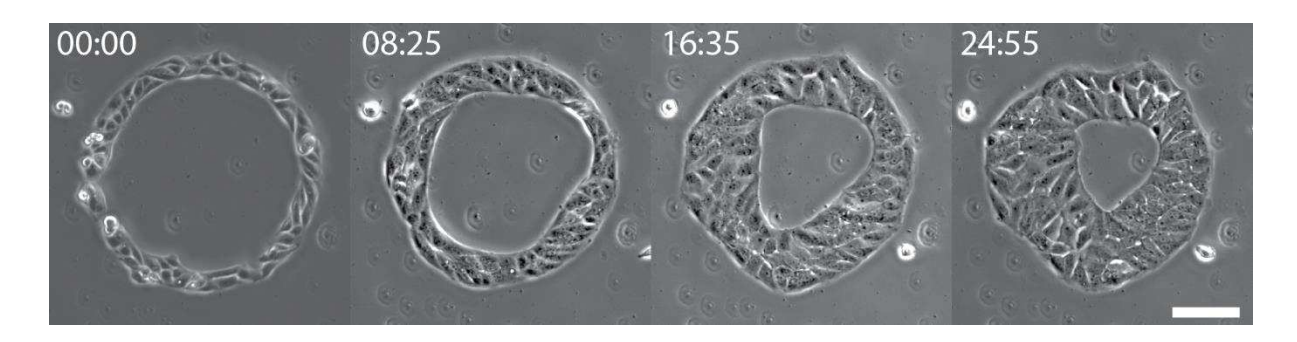


Figure 10.6. Inhibition of Arp2/3 complex increases closure time and impairs tangential motion. 300 μ m ring incubated with CK666, inhibiting Arp2/3 and lamellipodia growth. Scale bar = 100 μ m. Time in hh:mm.

10.1.7 Trypsin-EDTA (300μm – pipette)

We used micro-pipette in order to stimulate locally cells with specific drugs. In this context, we tried to deliver Trypsin-EDTA to cells within the ring. Upon delivery, we saw a fast response (minute timescale) leading to spontaneous breakage of the ring and retraction of the opening (Figure 10.7, Movie S44).

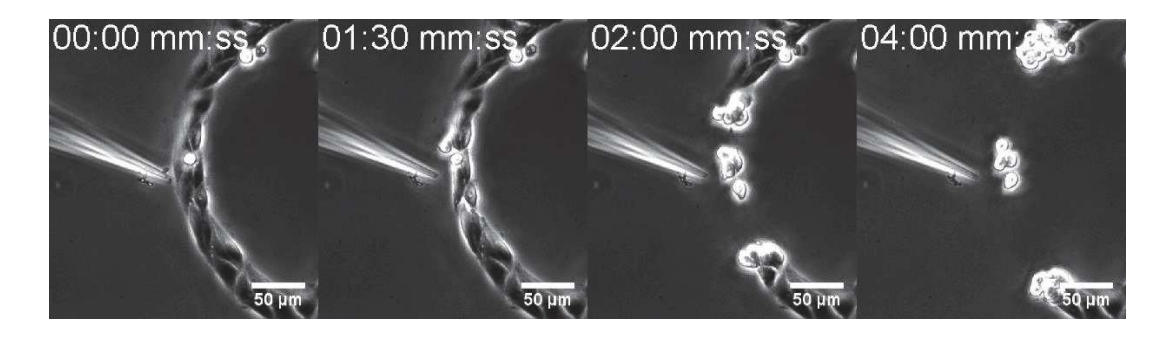


Figure 10.7. Local incubation with Trypsin-EDTA leads to local breakage. Trypsin-EDTA locally delivered by a micropipette. Upon incubation and disruption of adherens junctions, a local breakage appears and the ring retracts with a high velocity (minute timescale).

10.2 Multicellular ellipses

In the course of the project, we designed ellipsoid shapes to probe curvature effects on cells. We observed closure of the ellipse as shown by Figure 10.8 resembling to *Drosophila* dorsal closure (Movie S45).



Figure 10.8. Multicellular ellipse. $300\mu m$ diameter ellipse, with MDCK cells. Flow lines in yellow indicates the radial closure during the 6 hours. Scale bar = $100\mu m$. Time in hh:mm.

10.3 Micro-printing with ink jet

NB: This side project was done with a 2 months internship student, Paras Agrawal from Dehli.

We tried to design a cheap and straightforward way to generate micro-patterns on glass substrates. To do this, we modified an ink jet printer to print protein motifs. Briefly, we modified and filled with a fibronectin solution an ink tank. With a standard image software (in this case illustrator) we designed and printed micro-patterns on plasma activated coverslip. Cells were then seeded on the patterns and results are shown in Figure 10.9.

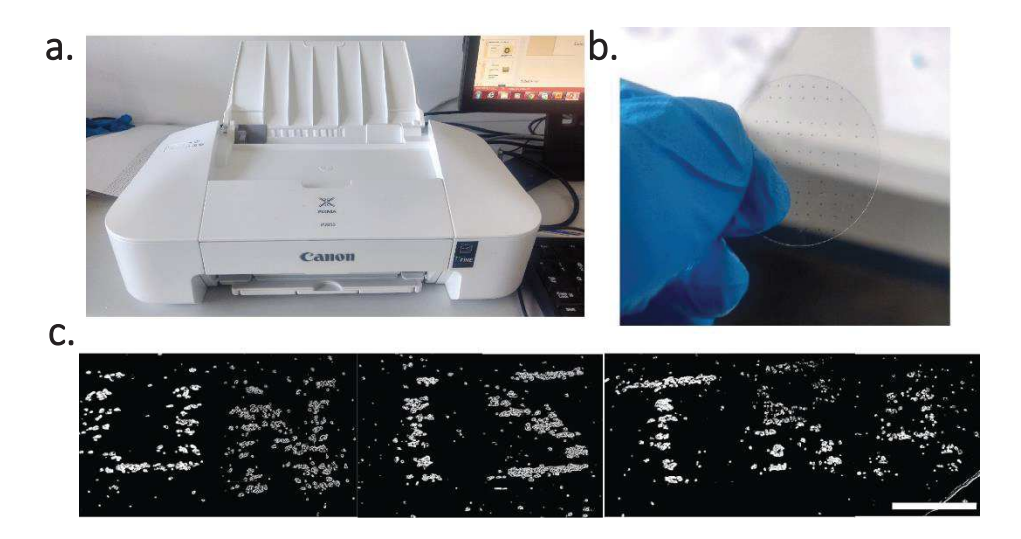


Figure 10.9. Micro-printing with an ink jet printer. (a) Standard printer (38 euros) with a resolution of 4800*600 dpi ($\sim 5.3 \mu m*42.3 \mu m$). (b) Micro-patterns on a glass slide with standard ink. (c) The word "UNISTRA" printed with fibronectin and cultured with MDCK cells. The non-printed area was passivated with 0.1 mg/ml PLL-g-PEG. Scale bar = $1000 \mu m$.

However, the size of the patterns was limited by the nozzle aperture and by the wetting of the drop on the substrate. Therefore, we only managed to produce micro-motifs of about 1mm.

10.4 Parameters for numerical simulations

Parameters used for simulations done in chapter 6 with the Vicsek-based model are listed in the table below.

Parameter	Symbol	Value	Units
Particle radius	r	7.5	μm
Velocity	С	26.92	μm.h ⁻¹
Angular diffusion coefficient	D	0.96	rad ² .h ⁻¹
Stretching modulus	k_{st}	5.10^3	pN.μm ⁻¹
Bending modulus	k_b	10^{3}	pN.μm
Relaxation rate on $\overline{P_k}$	μ	6	rad.h ⁻¹
Relaxation rate on $\frac{V_k}{\ V_k\ }$	ν	6	rad.h ⁻¹
Active force	f	10	nN

10.5 Table of drug concentrations

Drug	Target	Action	Concentration
C3-transferase	RhoA	Decreases RhoA activity	1μg/mL
Calyculin A	PP2 and PP1 Phosphatases	Increases myosin activity	25nM
CK666	Arp 2/3	Inhibits lamellipodia formation	100μΜ
EDTA	Calcium	Disrupts cadherin junctions and decrease myosin activity	2mM
Mitomycin	Proliferation	Decreases cell division	10μΜ
ML-7	MRLC-Kinase	Inhibits myosin activity	40μΜ
RhoA Activator II	RhoA	Decreases RhoA activity	1μg/mL
0.25% Trypsin-EDTA (1X)	Cell adhesion	Disrupts cell-cell adhesions	Stock

10.6 List of constructs

Construct	Type of transfection
Vinculin-GFP	Liposome
VASP-GFP	Lentivirus
RhoA biosensor	Piggy-Bac
RhoA control biosensor	Piggy-Bac
Actin-GFP	Liposome
Zyxin-GFP	Liposome

10.7 List of products

REAGENT or RESOURCE	SOURCE	IDENTIFIER
Antibodies/staining molecules		<u>'</u>
Mouse anti-Paxillin	BD Biosciences	Cat#610051
Goat anti-mouse IgG Cy3	Jackson Immunology	Cat#115-165-146
Goat anti-mouse IgG Alexa Fluor 488	Invitrogen	Cat#A11029
DAPI	Invitrogen	Cat#D1306
Phalloidin Alexa Fluor 488	Invitrogen	Cat#O7466
Phalloidin Alexa Fluor 546	Invitrogen	Cat#A22283
Phalloidin Alexa Fluor 647	Invitrogen	Cat#A22287
Mouse anti-Phosphomyosin	Cell signaling Technology	Cat#3675
Chemicals, Peptides, and Recombinant Proteins		
Rhodamin-labelled fibronectin	Cytoskeleton	Cat#FNR01-A
Polylysine-grafted-PEG	SuSoS	PLL(20)-g[3.5]- PEG(2)
3-(mercapto)propyltrimethoxysilane C6H16O3SSi	FluoroChem	CAS4420-74-0
Sulfuric acid	Sigma-Aldrich	CAS7664-93-9 Cat#258105-M
Hydrogen peroxide	Sigma-Aldrich	CAS7722-84-1 Cat#216763
HEPES	Gibco	Cat#15630-056
Polydimethylsiloxane	Sylgard	Cat#DC184-1.1
Triton	Sigma-Aldrich	Cat#93443-100ML
D C 111 1	Electron Microscopy	CAS30525-89-4
Paraformaldehyde	Sciences	Cat#15710
Alginate	Sigma-Aldrich	CAS9005-38-3 Cat#A1112
Phytagel	Sigma-Aldrich	CAS71010-52-1 Cat#P8169
Agarose	Sigma-Aldrich	CAS9012-36-6 Cat#A9539
Agarose LMP	Invitrogen	CAS9012-36-6 Cat# 16520050
BSA	Sigma-Aldrich	CAS 9048-46-8 Cat#A2153
Oleic Acid	Sigma-Aldrich	CAS112-80-1 Cat#sc-200797A
2-methyl-1-propanol	Sigma-Aldrich	78-83-1 Cat#294829
TRITC Dextran		Cat#
Polylysine	Sigma-Aldrich	CAS25988-63-0 Cat#P1274
ML-7	Sigma-Aldrich	CAS110448833-1 Cat#12764
Calyculin A	Sigma-Aldrich	CAS101932-71-2 Cat#C5552

CK666	Sigma-Aldrich	CAS442633-00-3 Cat# SML0006
Rho Activator II	Cytoskeleton Inc.	Cat#CN03-A
C3-transferase	Cytoskeleton Inc.	Cat#CT03-A
Experimental Models: Cell Lines		
NIH 3T3	ATCC	Ref. CRL-1658
MDCK II	Nelson's lab	N.A.
CAL27	Bioresource Collection and Research Center	CRL-2095
Software and Algorithms		-
Origin Pro 8.6	OriginLab	N/A
Anaconda 2.4	Anaconda	https://anaconda.co m
Focal adhesion detection and force measurement	This paper	N/A
ImageJ	Schneider et al., 2012	https://imagej.nih.g ov/ij/

10.8 FAs mapping – python code

```
import numpy as np
import imageio
import matplotlib.pyplot as plt
np.set printoptions(linewidth=50000,precision=2)
def getData():
  img = imageio.imread("filename.png")
  print("img.shape:",img.shape)
  oneChannel = img[:, :]
  return np.array(oneChannel)
def analyseImg():
  img=getData()
  plt.hist(img.reshape([-1]))
  plt.show()
def add neighbours in stack(image:np.ndarray, threshold:int, stack:list, i:int, j:int,
inComponent:np.ndarray)->None:
  .....
We consider the pixel (i,j) and its 4 neighbours. Neighbouring pixels with intensity above a threshold
will be added to the treated pixel stack.
  :param image: image to treat
  :param threshold: threshold
  :param stack: pixels to treat
  :param i: i-coordinate from the treated pixel
  :param j: j-coordinate from the treated pixel
  :param inComponent: boolean mask. inComponent[a,b]=True means that pixel (a,b) has been
saved
  inComponent[i, j] = True
  neighbours = [(i+1,j),(i-1,j),(i,j-1),(i,j+1)]
  for (k,l) in neighbours:
    if 0<=k<image.shape[0] and 0<=l<image.shape[1]:</pre>
      if image[k,l]<threshold and not inComponent[k, l]:</pre>
        inComponent[k, I] = True
        stack.append((k,l))
"""Find barycenter and number of pixels of a FA"""
def connected_component_baryCenter(image:np.ndarray, seuil:int, i0:int, j0:int,
inComponent:np.ndarray)->tuple:
  stack = [(i0,j0)]
  component=[]
```

```
while len(stack)>0:
    (i,i) = stack.pop()
    component.append(np.array([i,j]))
    add_neighbours_in_stack(image, seuil, stack, i, j, inComponent)
  return np.array(component)
def all_connected_components(image:np.ndarray, seuil:int)->list:
  inComponent = np.empty(image.shape, dtype=np.bool)
  inComponent[:, :] = False
  components=[]
  for i in range(image.shape[0]):
    for j in range(image.shape[1]):
      if image[i,j]<seuil and not inComponent[i,j]:</pre>
        comp = connected_component_baryCenter(image, seuil, i, j, inComponent)
        components.append(comp)
  return components
def detectExtremPoints(component,bary):
  component=np.array(component)
  p=component[0]
  imax=np.argmax(np.linalg.norm(p-component,axis=1))
  pp=component[imax]
  jmax=np.argmax(np.linalg.norm(pp-component,axis=1))
  point1=np.array(pp)
  point2=np.array(component[jmax])
  dist1=np.linalg.norm(point1-bary)
  dist2=np.linalg.norm(point2-bary)
  if (dist1>dist2):
    couple=(point2,point1)
  else:
    couple=(point1,point2)
  return np.array(couple)
def img_to_physics(components, shape, pixelsize):
  components_phys = []
  for comp in components:
    comp_phys = np.array(comp, dtype=float)
```

```
comp_phys[:,0] = shape[0] - comp_phys[:,0]
    for i in range(comp.shape[0]):
      comp_phys[i,0],comp_phys[i,1] = comp_phys[i,1],comp_phys[i,0]
    comp_phys *= pixelsize
    components_phys.append(comp_phys)
  return components phys
def main():
  img=getData()
  pixelsize = 0.183
  pixel_to_nN = 5.5 * (pixelsize ** 2)
  plt.imshow(img, cmap="gray", extent=[0, pixelsize * img.shape[1], 0, pixelsize * img.shape[0]])
  components = all_connected_components(img, 200)
  components_phys = img_to_physics(components, img.shape, pixelsize)
  #-- compute barycenter --#
  bary=np.zeros([2])
  for comp in components phys:
    bary+=np.sum(comp,axis=0)/len(comp)
  bary/=len(components)
  print("barycenter:",bary)
  #-- compute arrows and sum of arrows --#
  sumVec=np.zeros((2))
  for comp in components_phys:
    couple=detectExtremPoints(comp,bary)
    vec = couple[0,:]-couple[1,:]
    nbpixel = len(comp)
    vec = pixel_to_nN * nbpixel * vec / np.linalg.norm(vec)
    sumVec += vec
    plt.arrow( couple[0,0], couple[0,1], vec[0], vec[1], head_width=1, head_length=2,color="g",
linewidth=1.5,length_includes_head=True)
  print('total force =', sumVec)
  print("Total force norm =", np.linalg.norm(sumVec))
  rescale = 10
```

plt.arrow(bary[0],bary[1],sumVec[0]/5,sumVec[1]/5,head_width=1,head_length=2,color="r",length_includes_head=True, linewidth=6)

```
plt.plot(0,0,"k",marker="+",linewidth=0.8)

plt.title("Force Distribution",size=40)

plt.xlabel("Force (nN)",size=40)

plt.ylabel("Force (nN)",size=40)

plt.tick_params(axis='both',labelsize=40, grid_linewidth=3)

plt.show()

main()
```

10.9 Published and submitted articles

Published:

- 1. Lo Vecchio S., Thiagarajan R., Caballero D., Vigon V., Navoret L., Voituriez R. Riveline D. Collective Dynamics of Focal Adhesions Regulate Direction of Cell Motion. *Cell Systems*. 2020; 10:535-542.
- 2. Le Maout E.*, **Lo Vecchio S.***, Kumar Korla P., Jinn-Chyuan Sheu J., Riveline D. Ratchetaxis in Channels: Entry Point and Local Asymmetry Set Cell Directions in Confinement. *Biophys J.* 119:1301-1308.
- 3. Riveline D. and **Lo Vecchio S.** "Stochastic Resonance" for Individual Cells. *Biophys J.* 2020. 118:533-534.
- 4. Le Maout E, **Lo Vecchio S.**, Bhat A, Riveline D. Directing cell migration on flat substrates and in confinement with microfabrication and microfluidics. *Methods Cell Biol.* 2018; 147:109–32.
- 5. Bhat A., Lu L., Wang CH., **Lo Vecchio S.**, Maraspini R., Honigmann A., Riveline D. How to Orient Cells in Microcavities for High Resolution Imaging of Cytokinesis and Lumen Formation. *Methods Cell Biol.* 2020; 158:25-41.

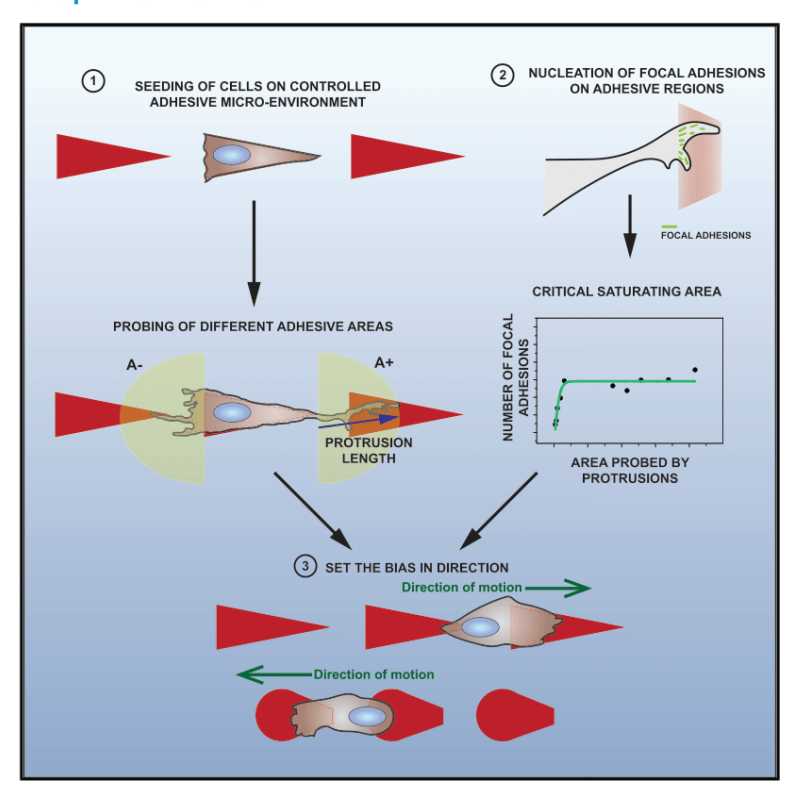
In preparation:

6. **Lo Vecchio S.**, Sopoz M., Navoret L., Pertz O., Riveline D. Turing rings: spontaneous rotations as an interplay between polarity and RhoA activity. *In preparation*.

Cell Systems

Collective Dynamics of Focal Adhesions Regulate Direction of Cell Motion

Graphical Abstract



Highlights

- Net bias in motion is a non-linear function of gap distance between adhesive regions
- Force inference on focal adhesions distributions correlates with cell direction
- Distributions of focal adhesions exhibit a collective saturating behavior
- Geometrical arguments on cell and its environment allow to predict directionality

Authors

Simon Lo Vecchio, Raghavan Thiagarajan, David Caballero, Vincent Vigon, Laurent Navoret, Raphaël Voituriez, Daniel Riveline

Correspondence

riveline@unistra.fr

In Brief

In this work, Lo Vecchio et al. investigate the interplay between micro-environment geometry, focal adhesion distributions, and net bias in cell migration. Cells are plated on ratchet adhesive motifs separated by tunable gap interdistance. They identify a saturating behavior of focal contact distributions that leads to a non-linear relationship between bias in cell motion and motif interdistance. Simple geometrical arguments on cell and its environment with collective effects of focal adhesions enable to predict quantitatively the net bias in cell motion for new geometries.



Cell Systems



Report

Collective Dynamics of Focal Adhesions Regulate Direction of Cell Motion

Simon Lo Vecchio, 1,2,3,4,5 Raghavan Thiagarajan, 1,2,3,4,5,9 David Caballero, 1,2,3,4,5,10 Vincent Vigon, 6 Laurent Navoret, 6 Raphaël Voituriez, 7,8 and Daniel Riveline 1,2,3,4,5,11,*

¹Laboratory of Cell Physics ISIS/IGBMC, CNRS and University of Strasbourg, Strasbourg, France

*Correspondence: riveline@unistra.fr https://doi.org/10.1016/j.cels.2020.05.005

SUMMARY

Directed cell motion is essential in physiological and pathological processes such as morphogenesis, wound healing, and cancer spreading. Chemotaxis has often been proposed as the driving mechanism, even though evidence of long-range gradients is often lacking *in vivo*. By patterning adhesive regions in space, we control cell shape and the potential to move along one direction in another migration mode coined ratchetaxis. We report that focal contact distributions collectively dictate cell directionality, and bias is non-linearly increased by gap distance between adhesive regions. Focal contact dynamics on micro-patterns allow to integrate these phenomena in a model where each focal contact is translated into a force with known amplitude and direction, leading to quantitative predictions for cell motion in new conditions with their successful experimental tests. Altogether, our study shows how local and minute timescale dynamics of focal adhesions and their distribution lead to long-term cellular motion with simple geometric rules.

A record of this paper's Transparent Peer Review process is included in the Supplemental Information.

INTRODUCTION

Cell motion plays key roles in biology in a variety of phenomena ranging from development to immune responses and metastasis (Carmona-Fontaine et al., 2008; Machesky, 2008; Stuelten et al., 2018; Wijnholds, 2019). Its proper mode of operating requires the relevant orchestration of the cytoskeletal networks (microtubular and actin networks) and the adhesion environment over length and timescales of hundreds of micrometers and hours. As such, cell motion calls for characterizations with new approaches at the mesoscopic levels, allowing to go beyond the molecular details of proteins involved in the phenomenon.

In this context, focal adhesions (FAs) play a central role from many perspectives. They constitute micrometer scale *adhesion interfacial* zone at the cell membrane between the extracellular matrix and cytoplasm with direct connection to acto-myosin stress fibers. FAs were also shown to act as *mechanosensors*, i.e. at the FA site, stress fibers apply local forces toward the cell

center, and as a result, "dot-like" FAs elongate along the direction of the force "centripetally" while keeping constant their density of matter (Balaban et al., 2001; Goffin et al., 2006; Riveline et al., 2001). Focal contact symmetry is thus broken with this local force application directed from the outside of the cell inward. In addition, the local force-area relation-similar to a spring constantwas established to be 5.5 nN.μm⁻² (Balaban et al., 2001; Goffin et al., 2006). This relation opens the possibility to infer total forces for a single cell from focal contact length distributions at the surface. Moreover, it has been shown that FAs and specific patterns of contacts are involved in biased migration and that downregulation of their proteins leads to a significant decrease in directionality (Chen et al., 2019; Ramirez-San Juan et al., 2017; Rahman et al., 2016; Ray et al., 2017). It seems therefore important to connect quantitatively single focal contact and their spatio-temporal distribution at the whole cell level and cell motion. If successful, this approach could lead to predictions for cell motions with simple arguments based on geometry and FAs.

²Institut de Génétique et de Biologie Moléculaire et Cellulaire, Illkirch, France

³Centre National de la Recherche Scientifique, UMR7104, Illkirch, France

⁴Institut National de la Santé et de la Recherche Médicale, U964, Illkirch, France

⁵Université de Strasbourg, Illkirch, France

⁶Institut de Recherche Mathématique Avancée, UMR 7501, Université de Strasbourg et CNRS

⁷Laboratoire de Physique Théorique de la Matière Condensée, UMR 7600 CNRS/Sorbonne Université, 4 Place Jussieu, 75255 Paris Cedex, France

⁸Laboratoire Jean Perrin, UMR 8237 CNRS/Sorbonne Université, 4 Place Jussieu, 75255 Paris Cedex, France

⁹Present address: Center for Stem Cell Research and Developmental Biology (DanStem), University of Copenhagen, Copenhagen, Denmark ¹⁰Present address: 3B's Research Group, I3Bs - Research Institute on Biomaterials, Biodegradables and Biomimetics of University of Minho, 4805-017 Barco, Guimarães, Portugal

¹¹Lead Contact



Cell Systems

In this context, it is interesting to understand how a cell can go from random to directed motion. Biases in cell migration have been widely studied in vitro, and it has been shown that soluble gradients of specific chemicals could trigger directionality by regulating signaling pathways and reorganizing the acto-myosin cytoskeleton (Affolter and Weijer, 2005; Wang et al., 2011). This phenomenon, known as chemotaxis, remains the widespread way to explain cell directionality in vivo (Iglesias and Devreotes, 2008; Roussos et al., 2011). However, these gradients are rarely demonstrated or quantified in vivo. In addition, if they are reported, they are not necessarily shown to be causal for cell motion in these specific directions. How cells can sustain sense of migration in vivo remains therefore unclear.

Previous works showed in vitro, as a proof of a principle, that local asymmetries in cellular environment can bias cell directionality in another mode of migration named ratchetaxis (Caballero et al., 2014, 2015a, 2015b; Comelles et al., 2014; Jiang et al., 2005; Mahmud et al., 2009; Sun et al., 2015). This phenomenon is distinct from chemotaxis: individual cells are plated on a substrate with no chemical gradient over long distances, and still, cells migrate toward a preferential direction. Various realizations were performed in terms of designs for the local asymmetry at the cellular scale and for cell types but with a similar simple outcome for setting cell direction (Caballero et al., 2014, 2015a, 2015b; Comelles et al., 2014; Jiang et al., 2005; Mahmud et al., 2009; Sun et al., 2015). This established ratchetaxis as a migration mode that can lead to long-term directionality without external gradient. This phenomenon shows the importance of stochastic probing associated to cell protrusions, as well as the role of environment topology.

So far, the report for the existence of such phenomenon has been the central focus of these studies (Caballero et al., 2014, 2015a, 2015b; Comelles et al., 2014; Jiang et al., 2005; Mahmud et al., 2009; Sun et al., 2015) but no explicit connection with focal contacts was shown. Such a link is required to capture the basic mechanism of cellular force transmission on the surface allowing the cell to undergo actual motion. For example, Caballero et al. (Caballero et al., 2014, 2015a, 2015b) had shown rectification on adhesive fibronectin (FN) triangles with constant gap distances. However, prediction for the efficiency in rectificationi.e., the presence of a net bias—with simple variation of external parameters was not systematically tested, and the key role of "efficient protrusions" was outlined but not visualized, even though focal contacts were expected to encode this parameter.

In this work, we addressed these questions and tested the interplay between geometry, FA dynamics, and directionality. We matched the dimension of adhesive motifs to cell size, and we varied systematically the distance between motifs to test how gap could modify the long-term motion. Using ratchet-like patterns which break the cell symmetry, we controlled the potential of the cell to move along one preferential direction. We report that cell directionality is primarily determined by the collective behavior of its adhesion sites-the FAs-and can be tuned and predicted using simple geometric rules describing the surrounding environment. We also define a critical saturation area responsible of the observed bias: below this area, FAs nucleate linearly with the accessible adhesive region, and above this area, nucleation saturates. The competition of these two regimes sets the bias. This framework is supported by a simple theoretical model integrating accessible parameters and involving a single fitting parameter. We finally test predictions of this model with new geometric motifs. Experiments together with their measurements validate our framework.

RESULTS

Bias in Directionality Increases Non-linearly with Gap

Cells locally elongate protrusions, which eventually lead to adhesion and its subsequent force generation and motion as a whole. To test this interplay between cell protrusion dynamics and cell motion, we designed an assay where an array of triangular adhesive motifs over a range of gap distances were fabricated using standard microfabrication techniques (see STAR Methods). Triangular rhodamine-labeled FN motifs were patterned to guide adhesion and morphodynamics of NIH3T3 cells (see Figure 1A). Non-printed areas were passivated with poly(L-lysine) grafted poly(ethylene glycol) (PLL-g-PEG), so that cells mainly adhere on FN motifs and have their shapes imposed during the spreading phase. We studied the long-term migration of NIH3T3 fibroblasts along the micro-patterns for 48 h. Cells were able to move from one motif to the neighboring motifs and eventually exhibited persistent motion toward one particular direction (see Figures 1B-1E; Videos S1, S2, S3, and S4). Cells migrated faster on separated motifs than on connected ones (see Figure 1F) consistent with the fact that friction is increased with larger adhesive areas (Palecek et al., 1997).

For each cell moving along a lattice unit (defined as the distance between the centers of adjacent triangles), we defined a final bias, which is determined by the position of the cell at the end of its trajectory relative to its original location after 2 days of migration: the final bias for an individual cell was set as "+" if it migrated toward the tip of the motif and "-" if it migrated toward the base of the motif (see Figure 1G). While no clear bias was visible for triangles separated by 13, 16, and 19 μm gap distances, we found that the average bias increased and reached close to complete rectification on triangles separated by gaps of 22 µm: almost 80% of the cells moved, on average, toward the "+" direction in this condition (Figure 1G). We tested large gap distances (d = $45 \mu m$), and as expected, no migration was observed (see Video S5) because the distance exceeded the maximum length of protrusions; cells were unable to extend protrusions and find a "docking site". These results show the sharp increase of rectification as a function of gap distance.

We next sought to quantify the complete trajectory of cells for each experimental condition where cells can move back and forth during 2 days. We computed the bias p per lattice unit for a given trajectory defined as:

$$\rho = \frac{N_+ - N_-}{N_+ + N_-}$$
 (Equation 1)

where N_i corresponds to the number of steps performed in the idirection. This readout reports how cells behave for each gap distance independently of the total duration of a trajectory. We averaged over trajectories, and the resulting confirms the behavior observed for the total bias (see Figure 1H). For $22 \mu m$, the total bias is maximal, and the mean bias per step is

Cell SystemsReport



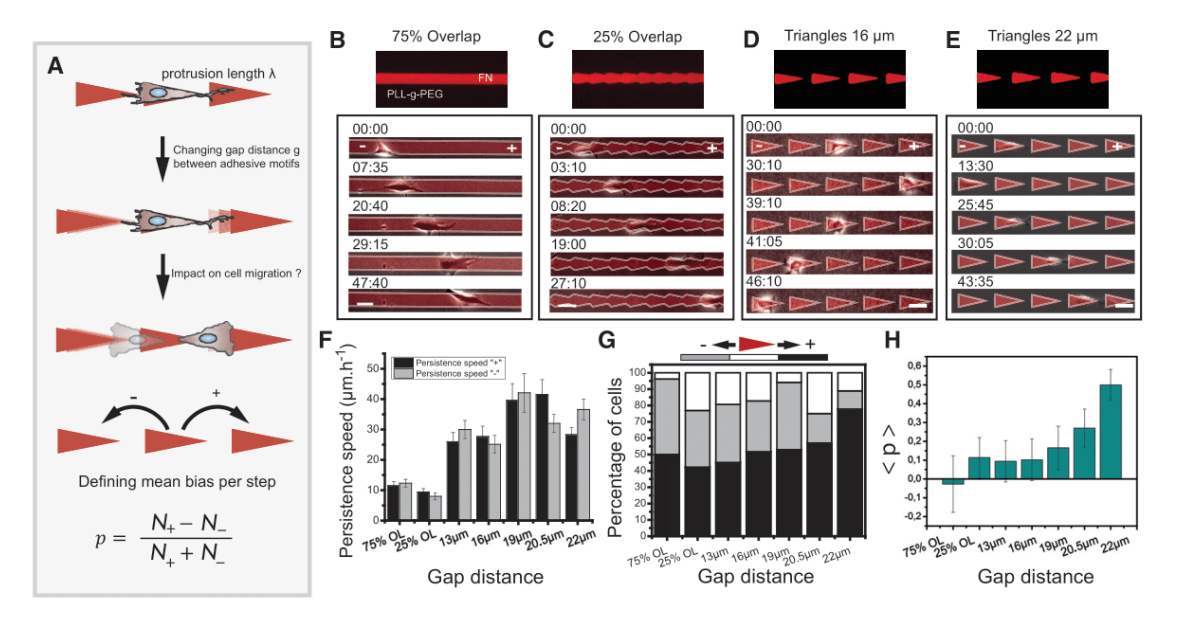


Figure 1. Cell Motion Depends on Gap Distance

(A) Scheme showing the experimental setup where a cell is seeded on a microcontact printed array of asymmetric FN triangles. The gap distance is systematically increased, which determines the final direction of migration. Quantitatively, p describes the bias in directionality taking into account all steps made during the motion.

(B–E) Cells are able to move from one motif to another on separated triangles and crawl on connected ones. Cells migrate on 75% overlapped triangles (B), on 25% overlapped triangles (C), and on patterns separated by 16 μ m gaps (D) and 22 μ m gaps (E). Time in hh:mm, scale bars represent 50 μ m. (F) Persistence speed in μ m.hr⁻¹.

(G) Final bias in percentage as a function of gap distance.

(H) Average p given by Equation 1 for each condition. Data set: $25 < N_{cells} < 30$ and $N_{biological} > 5$ for 75% OL, 25% OL, 13, 16, 19, and 22 μ m. $N_{cells} = 16$ for 20.5 μ m. Data are shown as mean \pm SEM. For the condition 20.5 μ m in (F) and (G), datasets are taken from Caballero et al., 2014.

also sharply increased and reaches 0.48 (\pm 0.08). Distributions of p are also informative: the distribution obtained for the line of FN (75% overlap [OL]) corresponds to a stochastic bimodal behavior with two peaks around p=1 and p=-1 (see Figure S1) and no preferred direction; this is consistent with a symmetric persistent motion. This feature progressively vanishes, and bimodality is transformed into a unimodal distribution with one single peak located around p=1 for 22 μ m, which is consistent with a strongly biased motion. Altogether, these results suggest that cell micro-environment architecture and simple geometrical features are sufficient to tune bimodality into an almost deterministic cell directionality and in the absence of chemical gradients.

Asymmetry in FA Distribution Correlates Quantitatively with Direction of Cell Motion

Considering the unimodal condition ($22~\mu m$) being the most simple and efficient configuration, we next asked whether FA dynamics and distribution could be sufficient to explain rectification. Using NIH3T3 fibroblasts stably expressing GFP vasodilator-stimulated phosphoprotein (VASP, see STAR Methods; Figure S2), we recorded the dynamics of adhesion sites during motion on the micro-patterned FN motifs (see Video S6). We observed that all protrusions, as soon as they touch FN regions, generate FAs (see Figure 2; Video S6). When the first row of FAs nucleates on the neighboring adhesive pattern, new contacts appear next in subsequent rows along the motif in a "wave"-like manner (see Figure S3; Video S7). This phenomenon resembles waves of lamellipodial

growth reported in previous works (Giannone et al., 2004). Such dynamics indicate a *collective* behavior. FA growth on adhesive motifs is distinct from the protrusions on PLL-g-PEG. In this latter case, protrusion growth stops and retracts after nucleation of FAs (see Figure S3). Altogether our observations suggest that FA dynamics could be a relevant readout for cell motion.

As reported in the Introduction, it was shown that FAs act as mechanosensors and can apply a force per unit area of 5.5 nN.μm⁻² (Balaban et al., 2001; Goffin et al., 2006; Riveline et al., 2001), which is conserved across cell types and substrates (Balaban et al., 2001; Goffin et al., 2006). Also, stress fibers apply "centripetal" forces through these focal contacts: the direction of the force goes from the location of the focal contact toward the center of the cell. We used this relationship to test whether the force inferred from focal contacts could be predictive for motion. While the global balance of forces applied on the cell is verified at all times (Tanimoto and Sano, 2014), the spatial distribution of forces is informative of local dynamics and global cell motion. We mapped force vectors at three different relevant time points (see Figures 2A and 2B). Each focal adhesion mediates a local force f_i exerted by the cell on the substrate along the long axis of the focal contacts, and its orientation points toward the interior of the cell. Its magnitude is deduced from the measured area of the FA by assuming a constant stress of 5.5 $nN.\mu m^{-2}$ (Figure 2B). From these vectors, we extracted the local instantaneous force associated with each focal contact, its amplitude, and its direction along x and y axis for different cells (Figures 2C and 2D). We found that cells apply a large total force



Cell Systems Report

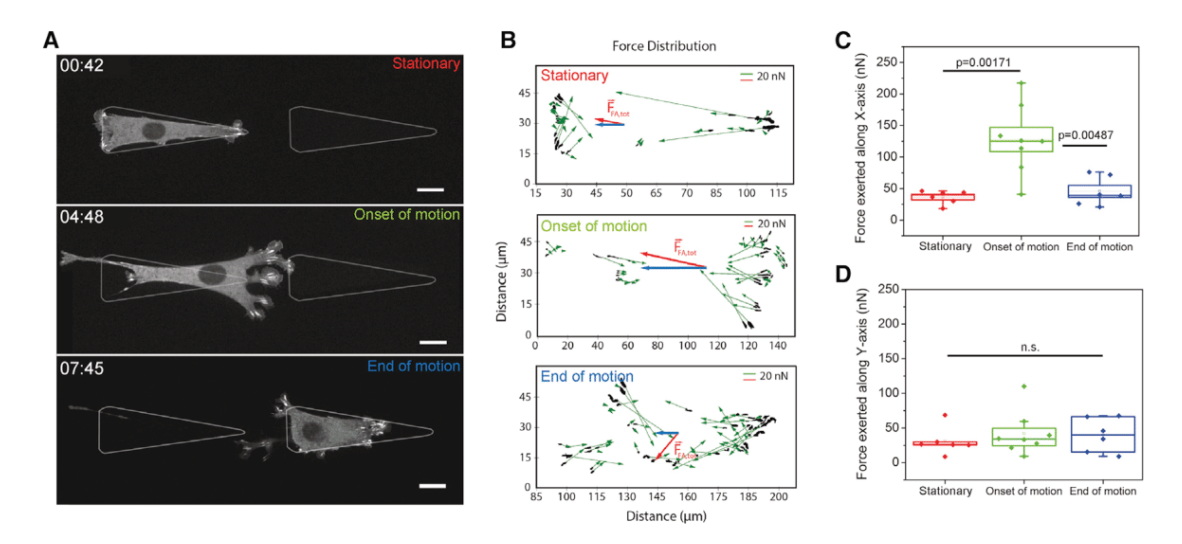


Figure 2. Force Inference Based on FA Distributions Correlates with Motion

(A) Time-lapse images of an NIH3T3 cell stably expressing VASP-GFP. Three time points are extracted for analysis: (1) during the stationary phase, (2) at the onset of motion, and (3) at the end of motion. Time in hh:mm, scale bar represents 15 μm.

(B) Force vectors map. Each FA is linked to a force vector oriented in the direction of adhesion zone (in green). Its amplitude is set according to the relationship 1 µm² corresponds to 5.5 nN. The total force vector is displayed in red, its x component in blue.

(C and D) The total force amplitudes exerted (C) along x axis and (D) along y axis during the three time points. Statistical tests comparing distributions are done with a one-way ANOVA. N_{biological_repeat} = 4, N_{cells} = 8.

 $\vec{F} = \sum \vec{f}_i$ of about 130 nN along the x axis in the direction of motion during motion phases, 3-fold larger than prior and after motion. To satisfy global force balance on the cell, a resistive friction force has to be considered. Assuming viscous friction, the corresponding friction coefficient can be estimated as ~25 N.s.m⁻¹, also consistent with reported values of friction of ~30 N.s.m⁻¹ (Palecek et al, 1997). This further confirms our conversion of focal contacts sizes to local forces.

Since every protrusion generates FAs as soon as it touches the patterns (see Figure 3A), distributions of contacts, and therefore cell direction, are expected to be critically governed by adhesive area accessible to protrusions.

Collective Effect of FAs

The core hypothesis is that the direction of a step is dictated by the direction of the resulting force transduced by all FAs. Decomposing this resulting force into + pointing and - pointing forces, and projecting along the ratchet axis x, one has:

$$F_x = \sum_{i=1,n+} f_{xi} + \sum_{j=1,n-} f_{xj}$$
 (Equation 2)

Note that F_x is a random variable that depends on the fluctuating quantities, n_i , which denote the number of FAs that transduce forces pointing in the i direction. The probability p+ of a step in the + direction (which directly yields the bias per step p = 2p ±1) is given in the model by the probability that $F_x>0$. Experimentally one expects a minimal threshold force that we neglect here for the sake of simplicity. While p+, as defined, in principle can depend on the full distribution of n_i and f_{xi} , it is controlled to linear order (small bias limit) only by the mean value of the resulting force, which is obtained from Equation 3:

$$\langle F_x \rangle = \langle n_+ \rangle \langle f \rangle - \langle n_- \rangle \langle f \rangle$$
 (Equation 3)

where f is the mean intensity of the force mediated by a single FA. Finally, the bias per step can be written as: $p \propto (\langle n_+ \rangle - \langle n_- \rangle)/(\langle n_+ \rangle + \langle n_- \rangle)$. A first approach would be to consider a linear relationship between the mean number of FAs and the available area $n_i = \alpha A_i$. This yields to:

$$p \propto \frac{(A_{+} - A_{-})}{(A_{+} + A_{-})}$$
, (Equation 4)

which relates explicitly the bias to the local geometry. To test linearity, we fixed samples for the different conditions (Figure 3B), and we plotted the mean number of FAs as a function of the available area (Figure 3C). We reported two different regimes: a linear behavior for small A (which corresponds to the – direction, see also insert) and a plateau for larger A (corresponding to the + direction). This typical saturating behavior can be fitted with a hyperbolic tangent function $y = C * tanh\left(\frac{A}{A_0}\right)$, where A_0 translates the idea of a saturation area into a measurable readout.

To go beyond the linear description of Equation 4, we incorporated in the model A_0 , the saturation area, a phenomenological parameter representing the typical area over which nucleation of FAs saturates, as observed in immunostainings:

$$\rho = \frac{\tanh\left(\frac{A_{+}}{A_{0}}\right) - \tanh\left(\frac{A_{-}}{A_{0}}\right)}{\sum_{i=+,-} \tanh\left(\frac{A_{i}}{A_{0}}\right)}$$
(Equation 5)

The resulting prediction of p yielded an excellent agreement with experimental values (see Figure 3D—red line), where notably the single fitting parameter A_0 was involved. A linear description gave a poor fit (blue dashed line). Notably, the fit

Cell Systems

Report



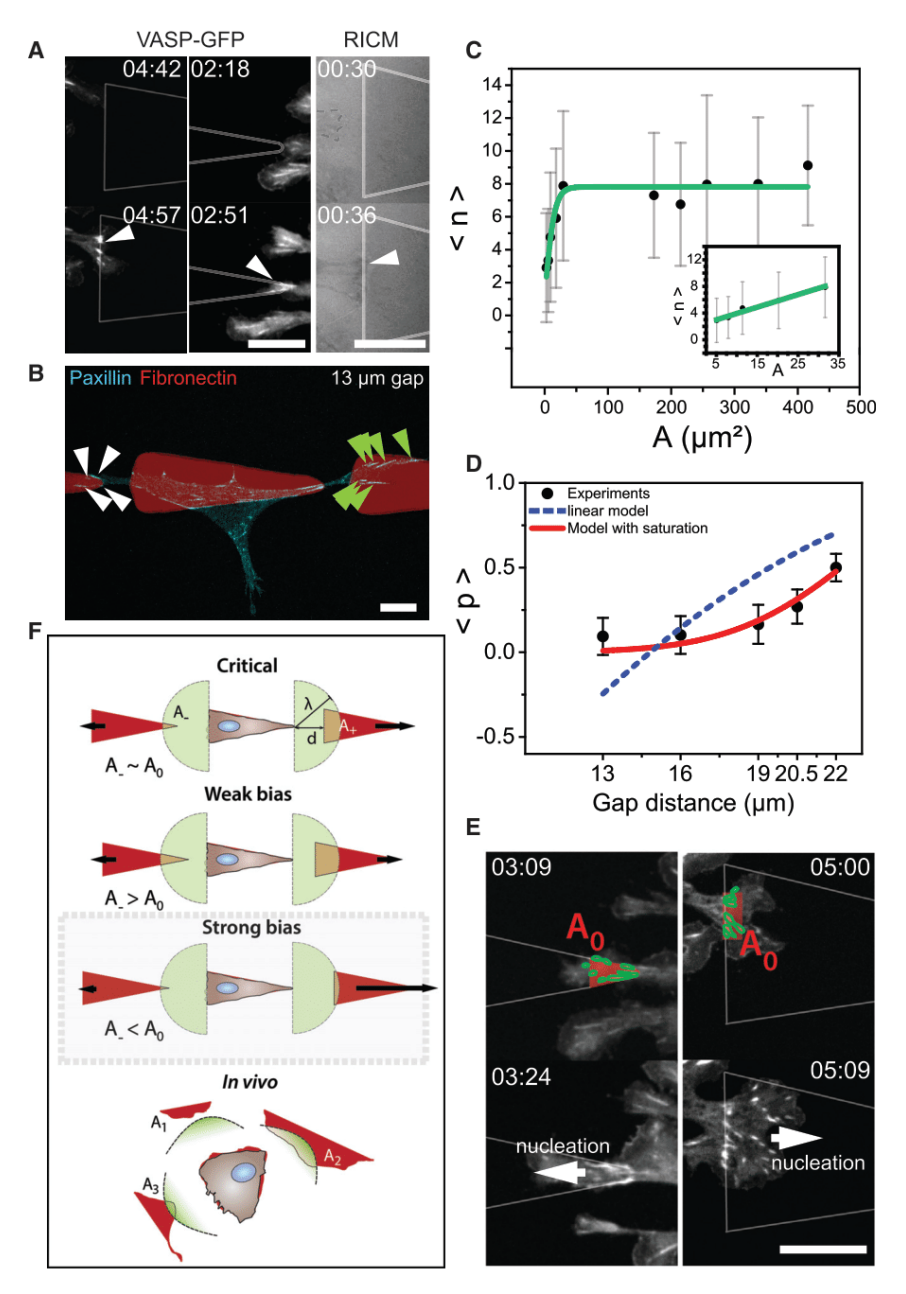


Figure 3. The Source of the Bias

(A) Protrusions touching an adhesive motif imaged with fluorescence microscopy and reflection interference contrast microscopy (RICM). FAs are nucleated right after contact with FN motifs. Arrows indicate FAs on patterns.

(B) NIH3T3 fixed and stained with paxillin. FAs on the + side and the – side are indicated by arrows. (C) Average number of FAs < n > as a function of the available theoretical area A. Data are fitted with a hyperbolic tangent; insert, linear part of the plot. (D) Comparisons between model and experiments. The blue fit assumes mechanisms with areas probed by cells only, whereas the red fit includes the saturating area A_0 . Fit corresponds to A_0 = 13.5 μ m² and λ = 28 μ m (measured, see Figure S4).

(E) Experimental description of A₀. From this region, subsequent rows of FAs are nucleated. Arrows indicate direction of nucleation. Two examples are shown.

(F) Graphical description of A_0 and its influence on bias. Beyond A_0 , the bias is weak. If one side gets close or below A_0 , the bias in the opposite direction becomes strong.

Time in hh:mm, scale bars represent 15 μ m. Data are shown as mean \pm SEM

Experimental Test of the Model

To further test our models, we designed new motifs with "teardrop" shapes separated with varying gaps and equilateral triangles separated with our optimal gap distance in the triangular configuration (see Figure 4). These conditions allowed the scan of sharp onset of rectification as a function of gap distance and the effect of the motif geometry. We computed the predictions for p with Equation 5, with the value of A₀ fitted previously and independently from a different set of geometries. The new conditions are reported in Figure 4 and examples of trajectories are shown in Video S8. The teardrops case confirms the sharp increase in rectification in the direction of the initial polarization for the gap distance 27 μm .

Indeed, this geometry increases the area ratio $\frac{A_-}{A_+}$ with $A_+ < A_0$. In contrast, in the equilateral case with optimal gap distance, the areas are above A_0 on both sides of the cell, and then no rectification occurs. Finally, comparisons between theoretical and experimental are plotted in Figure 4E showing successful predictions. Altogether, these controls with new conditions and their predictions with a posteriori experimental tests and no adjustable parameters validate our approach and its predictive power in new future configurations.

DISCUSSION

Overall, our study shows that cell migration can be tuned and captured by simple geometric rules associated with cellular

with the inclusion of saturation area A_0 yields 13.5 μm^2 (Figure 3D), a value which is in excellent agreement with the value found in the <n>-A plot (Figure 3C) of $A_0=16.43\pm2.22~\mu m^2.$ This further confirms the relevance of our hypothesis and the strength of our model.

We turned back to experiments of focal contact dynamics: the saturating area A_0 indeed matched the nucleation area on motifs (see Figure 3E). This suggests that: (1) a collection of focal contacts is required to perform firm cellular anchors on neighboring motifs, and (2) distribution of FAs encodes polarity. The model involves only a single fitting parameter that can be directly measured, and no *ad hoc* adjustable parameter was involved to recapitulate the trend observed in experiments. This supports the relevance of our hypothesis.

CellPress

Cell Systems Report

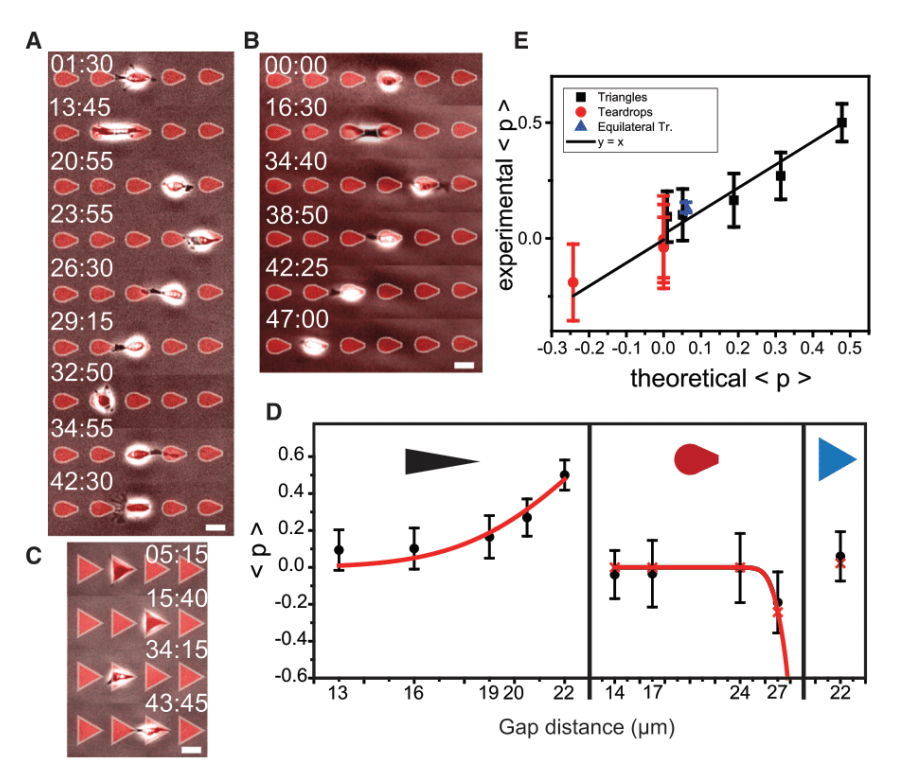


Figure 4. Experimental Test of the Model (A and B) Cell moving on teardrops separated (A) by 24 μm gaps and (B) by 27 μm gaps.

(C) NIH3T3 on equilateral triangles separated by 22 µm gaps. Time in hh:mm, scale bars represent 50

(D) Experimental data (black dots) together with the model (in red) with fixed A_0 . The sharp change in the mean bias per step is critically governed by geometry and accessible areas as shown by the two different trends for the triangles and the teardrops. Changing aspect ratio while keeping a gap of $22~\mu m$ also strongly affects the bias due to a change of areas probed in both sides.

(E) Plot of the experimental mean bias per step versus the theoretical predicted mean bias. Experimental points are compared with y = x line, showing an excellent agreement between model and experiments. Data are shown as mean ± SEM

features. By inferring forces from the FA distributions, we could propose that asymmetry in FAs is correlated to cell direction. The translation from local forces to whole cell integration was incorporated into a model. The assumed linearity of FA number with the available area appeared to be wrong. When we plotted the number of FAs as a function of the available area, we found a saturation area A₀ over which number of FAs did not increase anymore. We included this parameter in the model, and it allowed us to successfully fit the plot of the mean bias as a function of the gap distance. Altogether, this ratchetaxis phenomenon can be summarized with the following scheme. If the area available on both sides is greater than A₀, the cell will be able to create stable saturated anchoring zones on both sides, leading to $F_x = 0$. Therefore, the bias will be poor even if $A_+ >>$ A_{-} (13 to 19 μm conditions, see Figure 3F). On the other hand, if one side goes close or below A₀, the bias becomes stronger in the opposite direction.

So far, focal contacts have been studied mainly individually, and their integrated action was often overlooked. Force inference allows us to properly deduce the cell direction as we reported. However, the long-term motion requires the sum of the individual contributions of FAs together with the emergence of a readout, the saturating area, composed of a finite number of many FAs. Our results illustrate how collective behavior of FAs can mediate cell motion and establish rules for cell direction from the coupled dynamics of focal contacts and the cellular environment.

Cell motion requires orchestration of actin, microtubules, nucleus and centrosome positioning, as well as focal contacts dynamics (Bone and Starr, 2016; Euteneuer and Schliwa, 1984; Maiuri et al., 2015; Mogilner and Oster, 1996). These organelles undergo self-organization at the cellular scale. However, to pro-

ceed for actual motion on a coverslip, cells transfer their local forces onto the surface through focal contacts. As such, 2D distribution of focal contacts per cell encodes the essential readouts for predicting cell polarity and directions. In other words, our results show that focal contacts complete distributions in a sin-

gle cell translated into local forces and actually allowed to predict motility.

This type of coupling between geometry and cellular features could be relevant *in vivo* where distributions of adhesive regions are not homogeneous (Figure 3F; Bajanca et al., 2019) and could be probed in the future, along lines recently suggested (Bajanca et al., 2019). To test this framework, anisotropy in adhesion sites need to be tracked. In addition, protrusions and cell contacts dynamics have to be acquired and correlated over time quantitatively together with long-term cell motion. These readouts are now accessible *in vivo* for a variety of model systems, but their simultaneous observations and correlations are not performed yet. New experiments will need to be conducted to establish this potential source of rectification for cell migration *in vivo*.

This study provides a systematic integration of efficiency in rectification with a complete parameter that tracks motion of cells over time together with a model and tests of geometric configurations with actual visualizations of the relevant cellular readouts-the focal contacts-connected to the prediction. Our assay allowed the cell to engage FAs anywhere on the surface, letting the cell spontaneously break its symmetry while probing its environment. This is in contrast to other studies where gaps apparently prevented the potential passage (Mahmud et al., 2009). Systematic comparison of adhesions distributions in each former set-up (Caballero et al., 2014, 2015a, 2015b; Comelles et al., 2014; Jiang et al., 2005; Mahmud et al., 2009; Sun et al., 2015) together with the measurement of will allow us to propose explanations for the differences in behavior reported in ratchetaxis studies with many cell types. This also places this study in a complementary way with other types of works that characterize cell motion through either deterministic or stochastic models (Brückner et al., 2019; Metzner et al., 2015; Selmeczi

Cell Systems

Report



et al., 2005). In our context, the systematic variation of geometries is the leading control parameter with the perspective of capturing motility through integration of *local cellular readouts* and their collective effects. It would be interesting to generate connections between these different ways of treating cell motility. This could bring new effects with connections between assays and theoretical approaches.

In addition to its way of operating for cell migration, *ratchetaxis* encodes cellular mechanisms allowing the capture of cell motion with quantitative readouts extracted from experiments. Distribution of focal contacts yields a field of active forces on the surface. When asymmetric, a measure of its asymmetry could give actual values and extensions to *polarity* together with setting cell direction. In addition, quantitative links between these measures and the mean bias open the road to complete characterization of cell trajectories based on the quantitative integration of focal contacts extractions and their fluctuations. Altogether, with this simple scheme, *ratchetaxis* could be important in extracting generic parameters and principles often used in the physics of active matter

Key Changes Prompted by Reviewer Comments

The reviewers suggested to test the model predictions with new geometrical configurations by changing aspect ratio and/or pattern shape. We designed new motifs, computed the bias, and then performed new experiments. Measurements successfully matched the model predictions. Along their comments, we also showed explicitly the non-linear relation between the mean number of FAs and the probed area.

For context, the complete Transparent Peer Review Record is included within the Supplemental Information.

STAR*METHODS

Detailed methods are provided in the online version of this paper and include the following:

- KEY RESOURCES TABLE
- RESOURCE AVAILABILITY
 - Lead Contact
 - Material Availability
 - Data and Code Availability
- EXPERIMENTAL MODEL AND SUBJECT DETAILS
 - O NIH3T3
- METHOD DETAILS
 - Micro-Contact Printing
 - Cell Culture
 - Time-Lapse Microscopy
 - Immuno-Staining
- QUANTIFICATION AND STATISTICAL ANALYSIS
 - Exclusion Criteria
 - Statistical Tests and Significance
 - Image Analysis
 - Theory

SUPPLEMENTAL INFORMATION

Supplemental Information can be found online at https://doi.org/10.1016/j.cels.2020.05.005.

ACKNOWLEDGMENTS

We thank O. Pertz, P. Rossolilo, T. Charitat and A. Dupont; the Imaging Platform of IGBMC; and the Riveline Lab for constructs and discussions. This study with the reference ANR-10-LABX-0030-INRT has been also supported by a French state fund through the Agence Nationale de la Recherche under the frame program Investissements d'avenir labeled ANR-10-IDEX-0002-02. S.L.V. is supported by the University of Strasbourg and by la Fondation pour la Recherche Médicale. R.T. was an IGBMC International PhD Programme fellow supported by Labex INRT funds. D.R. acknowledges support from ciFRC Strasbourg, the University of Strasbourg, CNRS, and Foundation Cino del Duca.

AUTHOR CONTRIBUTIONS

D.R. conceived and supervised the project; S.L.V. performed experiments and analysis with the help of R.T. and D.C.; R.V. proposed the model; L.N. and V.V. helped with the force inference; S.L.V., R.V., and D.R. wrote the article with feedback from all co-authors.

DECLARATION OF INTERESTS

The authors declare no competing interests.

Received: July 25, 2019 Revised: February 20, 2020 Accepted: May 19, 2020 Published: June 17, 2020

REFERENCES

Affolter, M., and Weijer, C.J. (2005). Signaling to cytoskeletal dynamics during chemotaxis. Dev. Cell 9, 19–34.

Bajanca, F., Gouignard, N., Colle, C., Parsons, M., Mayor, R., and Theveneau, E. (2019). In vivo topology converts competition for cell-matrix adhesion into directional migration. Nat. Commun. *10*, 1518.

Balaban, N.Q., Schwarz, U.S., Riveline, D., Goichberg, P., Tzur, G., Sabanay, I., Mahalu, D., Safran, S., Bershadsky, A., Addadi, L., and Geiger, B. (2001). Force and focal adhesion assembly: a close relationship studied using elastic micropatterned substrates. Nat. Cell Biol. *3*, 466–472.

Bone, C.R., and Starr, D.A. (2016). Nuclear migration events throughout development. J. Cell Sci. *129*, 1951–1961.

Brückner, D.B., Fink, A., Schreiber, C., Röttgermann, P.J.F., Rädler, J.O., and Broedersz, C.P. (2019). Stochastic nonlinear dynamics of confined cell migration in two-state systems. Nat. Phys. *15*, 595–601.

Caballero, D., Comelles, J., Piel, M., Voituriez, R., and Riveline, D. (2015a). Ratchetaxis: long-range directed cell migration by local cues. Trends Cell Biol. *25*. 815–827.

Caballero, D., Voituriez, R., and Riveline, D. (2014). Protrusion fluctuations direct cell motion. Biophys. J. *107*, 34–42.

Caballero, D., Voituriez, R., and Riveline, D. (2015b). The cell ratchet: interplay between efficient protrusions and adhesion determines cell motion. Cell Adhes. Migr. 9, 327–334.

Carmona-Fontaine, C., Matthews, H., and Mayor, R. (2008). Directional cell migration in vivo: wnt at the crest. Cell Adhes. Migr. 2, 240–242.

Chen, S., Hourwitz, M.J., Campanello, L., Fourkas, J.T., Losert, W., and Parent, C.A. (2019). Actin cytoskeleton and focal adhesions regulate the biased migration of breast cancer cells on nanoscale asymmetric sawteeth. ACS Nano *13*, 1454–1468.

Comelles, J., Caballero, D., Voituriez, R., Hortigüela, V., Wollrab, V., Godeau, A.L., Samitier, J., Martínez, E., and Riveline, D. (2014). Cells as active particles in asymmetric potentials: motility under external gradients. Biophys. J. *107*, 1513–1522.

Curtis, A.S.G. (1964). The mechanism of adhesion of cells to glass. A study by interference reflection microscopy. J. Cell Biol. 20, 199–215.



Cell Systems

Euteneuer, U., and Schliwa, M. (1984). Persistent, directional motility of cells and cytoplasmic fragments in the absence of microtubules. Nature 310, 58-61.

Giannone, G., Dubin-Thaler, B.J., Döbereiner, H.G., Kieffer, N., Bresnick, A.R., and Sheetz, M.P. (2004). Periodic lamellipodial contractions correlate with rearward actin waves. Cell 116, 431-443.

Goffin, J.M., Pittet, P., Csucs, G., Lussi, J.W., Meister, J.J., and Hinz, B. (2006). Focal adhesion size controls tension-dependent recruitment of α -smooth muscle actin to stress fibers. J. Cell Biol. 172, 259-268.

Iglesias, P.A., and Devreotes, P.N. (2008). Navigating through models of chemotaxis. Curr. Opin. Cell Biol. 20, 35-40.

Jiang, X., Bruzewicz, D.A., Wong, A.P., Piel, M., and Whitesides, G.M. (2005). Directing cell migration with asymmetric micropatterns. Proc. Natl. Acad. Sci. USA 102, 975-978

Le Maout, E., Lo Vecchio, S., Bhat, A., and Riveline, D. (2018). Directing cell migration on flat substrates and in confinement with microfabrication and microfluidics. Methods Cell Biol 147, 109-132.

Machesky, L.M. (2008), Lamellipodia and filopodia in metastasis and invasion. FEBS Lett 582, 2102-2111.

Mahmud, G., Campbell, C.J., Bishop, K.J.M., Komarova, Y.A., Chaga, O., Soh, S., Huda, S., Kandere-Grzybowska, K., and Grzybowski, B.A. (2009). Directing cell motions on micropatterned ratchets. Nat. Phys. 5, 606-612.

Maiuri, P., Rupprecht, J.F., Wieser, S., Ruprecht, V., Bénichou, O., Carpi, N., Coppey, M., De Beco, S., Gov, N., Heisenberg, C.P., et al. (2015). Actin flows mediate a universal coupling between cell speed and cell persistence. Cell 161, 374-386

Martin, K., Vilela, M., Jeon, N.L., Danuser, G., and Pertz, O. (2014). A growth factor-induced, spatially organizing cytoskeletal module enables rapid and persistent fibroblast migration. Dev. Cell 30, 701–716.

Metzner, C., Mark, C., Steinwachs, J., Lautscham, L., Stadler, F., and Fabry, B. (2015). Superstatistical analysis and modelling of heterogeneous random walks. Nat. Commun. 6, 7516.

Mogilner, A., and Oster, G. (1996). Cell motility driven by actin polymerization. Biophys. J. 71, 3030-3045.

Palecek, S.P., Loftus, J.C., Ginsberg, M.H., Lauffenburger, D.A., and Horwitz, A.F. (1997). Integrin-ligand binding properties govern cell migration speed through cell-substratum adhesiveness. Nature 385, 537-540.

Rahman, A., Carey, S.P., Kraning-Rush, C.M., Goldblatt, Z.E., Bordeleau, F., Lampi, M.C., Lin, D.Y., García, A.J., and Reinhart-king, C.A. (2016). Vinculin regulates directionality and cell polarity in two- and three-dimensional matrix and three-dimensional microtrack migration. MBoC 27, 1431-1441.

Ramirez-San Juan, G.R.R., Oakes, P.W., and Gardel, M.L. (2017). Contact guidance requires spatial control of leading-edge protrusion. Mol. Biol. Cell 28, 1043-1053.

Ray, A., Lee, O., Win, Z., Edwards, R.M., Alford, P.W., Kim, D.H., and Provenzano, P.P. (2017). Anisotropic forces from spatially constrained focal adhesions mediate contact guidance directed cell migration, Nat. Commun. 8, 14923.

Riveline, D., Zamir, E., Balaban, N.Q., Schwarz, U.S., Ishizaki, T., Narumiya, S., Kam, Z., Geiger, B., and Bershadsky, A.D. (2001). Focal contacts as mechanosensors: externally applied local mechanical force induces growth of focal contacts by an mDia1-dependent and ROCK-independent mechanism. J. Cell Biol. 153, 1175-1186.

Roussos, E.T., Condeelis, J.S., and Patsialou, A. (2011). Chemotaxis in cancer. Nat. Rev. Cancer 11, 573-587.

Schneider, C.A., Rasband, W.S., and Eliceiri, K.W. (2012). NIH Image to ImageJ: 25 years of image analysis. Nat. Methods 9, 671-675.

Selmeczi, D., Mosler, S., Hagedorn, P.H., Larsen, N.B., and Flyvbjerg, H. (2005). Cell motility as persistent random motion: theories from experiments. Biophys. J. 89, 912-931.

Stuelten, C.H., Parent, C.A., and Montell, D.J. (2018). Cell motility in cancer invasion and metastasis: insights from simple model organisms. Nat. Rev. Cancer 18, 296-312.

Sun, X., Driscoll, M.K., Guven, C., Das, S., Parent, C.A., Fourkas, J.T., and Losert, W. (2015). Asymmetric nanotopography biases cytoskeletal dynamics and promotes unidirectional cell guidance. Proc. Natl. Acad. Sci. USA 112,

Tanimoto, H., and Sano, M. (2014). A simple force-motion relation for migrating cells revealed by multipole analysis of traction stress. Biophys. J. 106, 16-25.

Théry, M., and Piel, M. (2019). Adhesive micropatterns for cells: a microcontact printing protocol. Cold Spring Harb. Protoc. 2009, pdb.prot5255.

Wang, Y., Chen, C.L., and lijima, M. (2011). Signaling mechanisms for chemotaxis. Dev. Growth Differ. 53, 495-502.

Wijnholds, J. (2019). "Basal cell migration" in regeneration of the corneal wound-bed. Stem Cell Rep. 12, 3-5.

Cell Systems Report



STAR*METHODS

KEY RESOURCES TABLE

REAGENT or RESOURCE	SOURCE	IDENTIFIER
Deposited Data		
Dataset	This work	https://git.unistra.fr/s.lovecchio/cell-motion- as-a-stochastic-process-controlled-by- focal-contacts-dynamics-dataset
Antibodies		
Mouse anti-Paxillin	BD Biosciences	Cat#610051; AB_397463
Goat anti-mouse IgG Cy3	Jackson ImmunoResearch	Cat#115-165-146; AB_2338690
Goat anti-mouse IgG Alexa Fluor 488	Invitrogen	Cat#A11029; AB_2534088
Chemicals, Peptides, and Recombinant Prote	eins	
Rhodamine-labelled fibronectin	Cytoskeleton	Cat#FNR01-A
Polylysine-grafted-PEG	SuSoS	PLL(20)-g[3.5]- PEG(2)
3-(mercapto)propyltrimethoxysilane C6H16O3SSi	FluoroChem	CAS4420-74-0
Sulfuric acid	Sigma-Aldrich	CAS7664-93-9 Cat#258105-M
Hydrogen peroxide	Sigma-Aldrich	CAS7722-84-1 Cat#216763
HEPES	Gibco	Cat#15630-056
Polydimethylsiloxane	Dow Corning (Sylgard 184 kit)	Cat#DC184-1.1
Triton X-100	Sigma-Aldrich	Cat#93443-100ML
Paraformaldehyde	Electron Microscopy Sciences	CAS30525-89-4 Cat#15710
Experimental Models: Cell Lines		
NIH3T3	ATCC	Ref. CRL-1658
Software and Algorithms		
Origin Pro 8.6	OriginLab	N/A
Anaconda 2.4	Anaconda	https://anaconda.com
Focal adhesion detection and force inference	This paper	N/A
ImageJ	Schneider et al., 2012	https://imagej.nih.gov/ij/
Recombinant DNA		
VASP-GFP	Martin et al., 2014	N/A

RESOURCE AVAILABILITY

Lead Contact

Further information and requests for resources and reagents should be directed to and will be fulfilled by the Lead Contact, Daniel Riveline (riveline@unistra.fr).

Material Availability

This study did not generate new unique reagents.

Data and Code Availability

Dataset and codes are available on the public repository https://git.unistra.fr/s.lovecchio/cell-motion-as-a-stochastic-processcontrolled-by-focal-contacts-dynamics-dataset.git





EXPERIMENTAL MODEL AND SUBJECT DETAILS

NIH3T3 mouse fibroblasts (ATCC) were cultured in high glucose Dulbecco's Modified Eagle's Medium (DMEM) (Fisher Scientific, cat. 11574486) supplemented with 10% Bovine Calf Serum (BCS, Sigma, cat. 12133C) and 1% Penicillin-Streptomycin. Cells have also been controlled negative for mycoplasma.

METHOD DETAILS

Micro-Contact Printing

Fibronectin asymmetric motifs were patterned using standard microcontact printing protocol (Le Maout et al., 2018; Théry and Piel, 2019). Polydimethylsiloxane (PDMS, 1:10 w/w cross-linker:pre-polymer) (Sylgard 184 kit, Dow Corning, cat. DC184-1.1) stamps were replicated from SU-8 molds fabricated by standard UV-photolithography. After cleaning in ethanol 70%, stamps were rendered hydrophilic by oxygen plasma activation (Diener Electronic, cat. ZeptoB) for 30 s. Then, stamps were incubated for 1 h with a 10 µg/ mL rhodamine-labelled fibronectin solution (Cytoskeleton, cat. FNR01-A) and dried at room temperature for about 5 min. Next, stamps were placed in contact on top of a glass coverslip functionalized by vapour phase for 1 h with 3-(mercapto)propyltrimethoxysilane (FluroChem). A 50 g weight was placed on the top of the stamp during 30 min to ensure a constant and isotropic pressure during stamping. After release, the coverslip was cleaned in PBS 1x. The non-patterned areas were passivated with a 0.1 mg/mL solution of PLL-g-PEG (in 1 mM HEPES pH 7.4, SuSoS AG, cat. SZ33-15) for 20 min at room temperature. Finally, the patterned glass coverslips were again rinsed in PBS 1x prior cell deposition.

Cell Culture

NIH3T3 mouse fibroblasts (ATCC) were cultured in high glucose Dulbecco's Modified Eagle's Medium (DMEM) (Fisher Scientific, cat. 11574486) supplemented with 10% Bovine Calf Serum (BCS, Sigma, cat. 12133C) and 1% Penicillin-Streptomycin. Cells were detached from the Petri dish with Trypsin-0.25% EDTA (Fisher Scientific, cat. 11570626), centrifuged, and re-suspended in DMEM 10% BCS. About 2000 cells were seeded on micro-patterns and the non-adhering cells were washed out after 30 min of incubation at 37°C and 5% CO2. Medium was replaced by L-15 (Leibovitz Medium, Fisher Scientific, cat. 11540556) supplemented with 1% of BCS in order to reduce cell division during experiments.

FAs were monitored by fluorescence microscopy. NIH3T3 mouse fibroblasts stably expressing a VASP-GFP vector were kindly provided by Olivier Pertz (Institute of Cell Biology, Bern University, Switzerland) (Martin et al., 2014). The construct is expressed in lentivirus derived from pLenti CMV MVS. The viruses were added to a culture of wild-type NIH3T3 and cells were selected after 24 h with 2 μg/mL of puromycin.

Time-Lapse Microscopy

Long-term phase-contrast images (48 h) were acquired using a low magnification objective (4x, N.A. 0.25) with an image acquisition frequency of 1 image each 5 min. Micro-patterns were visualized by means of a standard epifluorescence lamp (FluoArc Hg Lamp) coupled with a rhodamine fluorescence filter. A thin layer of mineral oil (Sigma, M5904) was deposited on top of the cell culture media in order to prevent medium evaporation. In Figure 1, cells were imaged using a 10x objective (N.A. 0.4). Focal contacts dynamics were monitored every 3 min with a Nikon Spinning-Disk confocal microscope with a 60x oil objective (N.A. 1.4) using the Perfect Focus System. These settings provided highly resolved images with a low phototoxicity for long-term experiments (15 h). To test whether VASP-GFP protein revealed focal contacts localizations, we used Reflection Interference Contrast Microscopy (RICM) as described in Curtis et al. (Curtis, 1964). We used a homogeneous white light source (FluoArc Hg Lamp) through a 50% dichroic and we imaged interferences between the cell-surface interface (see Figure S2B).

Immuno-Staining

We checked that GFP-VASP was a direct and reliable readout of FAs. This was confirmed by immuno-staining cells expressing GFP-VASP with paxillin. Cells were fixed with 4% paraformaldehyde for 8 min. Then they were treated with Triton 0.5X during 3 min. After washout, an anti-paxillin mouse primary antibody (BD transduction, cat. 610051) was used together with an anti-mouse secondary antibody grafted with Cy3 (Jackson Immuno Research, cat. 115-165-146). We observed co-localisation providing us good evidence that GFP-VASP signal reveals focal contacts (see Figure S2).

This protocol was also applied to count the number of FAs in Figure 2. Cells were fixed 4 h after their seeding on the patterns so they have time to spread and probe the neighboring regions. The same anti-paxillin antibody was used but an Alexa-488 secondary antibody was added instead (Invitrogen Cat. A11029).

QUANTIFICATION AND STATISTICAL ANALYSIS

Exclusion Criteria

Cells taken in analysis follow strict criteria defined as follows:

Cell Systems

CellPress

Report

- Cells should not undergo division during the 48 h of migration
- Cells dying before 48 h are ruled out
- 'Colliding' cells are not taken in the analysis
- Cells should be separated at least by 500 μm
- Cells should move more than one step
- Patterns should be well defined and the fibronectin coating homogeneous

Statistical Tests and Significance

Plots derived from data as well as statistical tests were done using OriginLab Pro (OriginLab). Significance (p < 0.05) of differences between distributions in Figure 2 was tested with a one-way Anova. P values are shown in the plot itself.

For each plot, error bars represent the standard error of mean (s.e.m) $SEM = \frac{\sigma}{\sqrt{N}}$ where N represents the number of biological repeats.

Number of analyzed cells as well as the number of replicates are the following:

- $In \ Figure \ 1: \ n_{cells-13\mu m} = 31, \ n_{cells-16\mu m} = 29, \ n_{cells-19\mu m} = 35, \ n_{cells-20.5\mu m} = 17, \ n_{cells-22\mu m} = 27. \ N_{repeats-13\mu m} = 7, \ N_{repeats-16\mu m} = 8, \ N_{repeats-19\mu m} = 8, \ N_{repeats-20.5\mu m} = 3, \ N_{repeats-22\mu m} = 9.$
- In Figures 2A-2C: n_{cells} = 8, N_{repeats} = 4
- In Figures 2E and 2G: $n_{cells-13\mu m} = 33$, $n_{cells-16\mu m} = 46$, $n_{cells-19\mu m} = 26$, $n_{cells-20.5\mu m} = 29$ $n_{cells-22\mu m} = 44$. $N_{repeats-13\mu m} = 3$, $N_{repeats-16\mu m} = 4$, $N_{repeats-19\mu m} = 2$, $N_{repeats-20.5\mu m} = 3$ $N_{repeats-20.5\mu m} = 3$.
- In Figure 4: $n_{cells-TD14\mu m}=26$, $n_{cells-TD17\mu m}=23$, $n_{cells-TD24\mu m}=23$, $n_{cells-TD27\mu m}=28$, $n_{cells-TD27\mu m}=28$, $n_{cells-TD22\mu m}=28$, $n_{cells-TD22$
- In Figure S2: N_{repeats} = 2

Image Analysis

Tracking of the cells (nucleus) was performed with ImageJ (Schneider et al., 2012) using Multiple Tracking plug-in. The generated coordinates were used to compute cell trajectories. Force analysis made on focal contacts was performed with a custom Python code computing areas of adhesion zones, their orientations and barycenters, force vectors for each of them and total force vectors taking the rule 1 μ m² corresponds to 5.5 nN (Balaban et al., 2001; Goffin et al., 2006). Fits with experimental data were done with OriginLab Pro.

Theory

The theoretical estimates of A_+ and A_- are extracted using the following expressions, based on the scheme from Figure S4:

For triangles:

$$A_{-} = \frac{1}{2} (\lambda - g)^{2} \cdot \theta$$
 (Equation 6)

$$A_{+} = \left(B - (\lambda - g)\sqrt{\frac{1 - \sin \alpha^{2}}{\sin \alpha^{2}}}\right)(\lambda - g)$$
 (Equation 7)

where g, λ , θ and α correspond, respectively, to the gap distance, the protrusion length, the angle of the triangle tip, and the angle at the base of the triangle.

- For teardrops:

$$A_{-} = \left(\frac{1}{\tan \phi} \cdot (\lambda - g) + b\right) (\lambda - g)$$
 (Equation 8)



Cell Systems Report

$$A_{+} = \lambda^{2}.\arccos\left(\frac{d'}{\lambda}\right) + R^{2}.\arccos\left(\frac{d'}{R}\right) - \left(d + d'\right)\sqrt{\lambda^{2} - d^{2}}$$
 (Equation 9)

where R corresponds to the radius of the circular part of the teardrop (20 μ m) and Φ the angle of the trapezoid part. d and d' have the following expressions:

$$d = \frac{\lambda^2 - R^2 + (R+g)^2}{2.(R+g)}$$
 and $d' = R+g-d$

Directing cell migration on flat substrates and in confinement with microfabrication and microfluidics

Emilie Le Maout*,†,‡,§,¶, Simon Lo Vecchio*,†,‡,§,¶, Alka Bhat*,†,‡,§,¶

Daniel Riveline*,+,+,\$,¶,1

*Laboratory of Cell Physics ISIS/IGBMC, CNRS and University of Strasbourg, Strasbourg, France

† Institut de Génétique et de Biologie Moléculaire et Cellulaire, Illkirch, France

‡ Centre National de la Recherche Scientifique, UMR7104, Illkirch, France

§ Institut National de la Sante et de la Recherche Médicale, U964, Illkirch, France

¶ Université de Strasbourg, Illkirch, France

1 Corresponding author: e-mail address: riveline@unistra.fr

CHAPTER OUTLINE

	1 Introduction	2
	1.1 Petri Dishes and Boyden Chambers: Their Limits	3
	1.2 The Microfabrication Revolution and Its Impacts	4
	1.3 Designing the Motifs: Scaling Arguments	5
	2 Microfabrication of Motifs	6
	2.1 Designing the Motifs	6
	2.2 Microfabrication	7
	2.2.1 Protocol	7
	3 Rectifying Cell Motion with Asymmetrical Patterns: Micro-Contact	ct Printing
	of Adhesive Motifs	
	3.1 The Design of Pattern	10
	3.2 Micro-Contact Printing	10
	3.2.1 Protocol	
	3.2.2 2D Cell Migration Experiment	
4	Control of Cell Migration in Confined 3D Environment	
	4.1 The Design of Pattern	
	4.2 Confined Open Microchannel Configuration	
	4.2.1 Protocol	13
	4.2.2 Cell Migration Experiment	15
	4.3 Confined Closed Microchannel Configuration	16
	4.3.1 Protocol	16
	4.3.2 Cell Migration Experiment	17
5	Control of Cell Migration in 3D with Chemotaxis	18
	5.1 Protocol	18
	5.1.1 Materials	18
	5.1.2 Equipment	19
	5.1.3 Methods	19
	5.2 Cell Migration Experiment	20
	5.2.1 Materials	20
	5.2.2 Equipment	20
	5.2.3 Method	20
	6 Troubleshooting	
	6.1 Microfabrication	22

6.2 Micro-Contact Printing	22
6.3 Microfluidics	23
Conclusion	23
References	24

Abstract

Cell motility has been mainly characterized *in vitro* through the motion of cells on 2D flat Petri dishes, and in Boyden chambers with the passage of cells through sub-cellular sized cavities. These experimental conditions have contributed to understand important features, but these artificial designs can prevent elucidation of mechanisms involved in guiding cell migration *in vivo*. In this context, microfabrication and microfluidics have provided unprecedented tools to design new assays with local controls in two and three dimensions. Single cells are surrounded by specific environments at a scale where cellular organelles like the nucleus, the cortex, and protrusions can be probed locally in time and in space. Here, we report methods to direct cell motion with emphasis on micro-contact printing for 2D cell migration, and ratchetaxis/chemotaxis in 3D confinements. While sharing similarities, both environments generate distinct experimental issues and questions with potential relevance for *in vivo* situations.

1 INTRODUCTION

Cell motility plays a key role during development (Helvert, Storm, & Friedl, 2018). When its normal mode of operation is altered, defects appear in tissues, and they can be involved in diseases such as cancer progression. Many genes and pathways have been shown to be important for regulating cell motions *in vivo*, and their roles were further characterized *in vitro*.

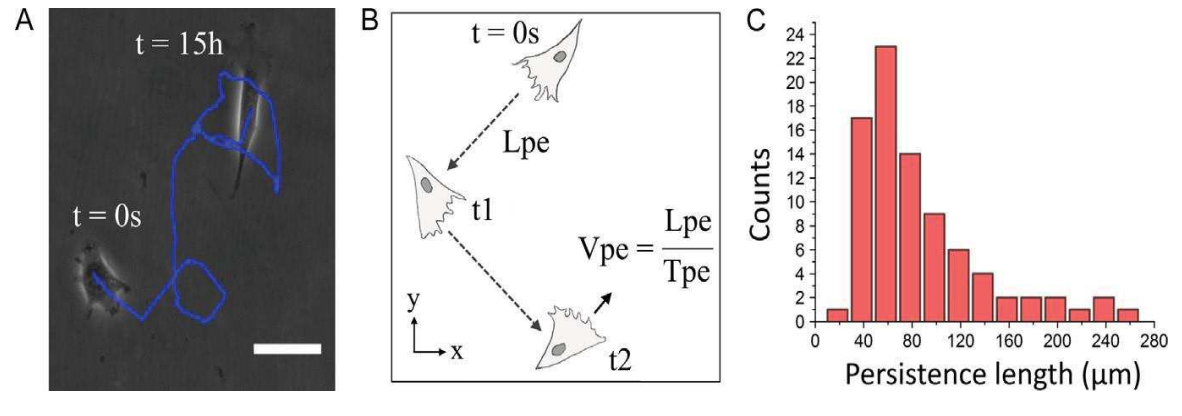


FIG. 1

Characterization of NIH3T3 fibroblast migration on a 2D flat substrate. (A) Typical trajectory of a cell moving randomly on a flat coverslip, the blue trace shows the trajectory. Scale bar $100\mu m$. (B) Schematics showing the migration of a cell, Lpe represents the persistence length, Tpe the persistence time and Vpe the persistence speed; pausing time and number of turns per unit time can also be measured. (C) Distribution of a parameter, here the persistence length, for NIH3T3 fibroblasts migrating on flat surface (n=84 trajectories).

Indeed cell motion can be recapitulated on 2D flat coverslips or on Petri dishes: a polarized cell migrates in one direction, pauses, potentially changes polarity and migrates in another direction. Their typical motions over days are represented in Fig. 1. Five parameters can encode cell motility. Persistence length is the length traveled "straight" by the cell during a certain time with no pause. This time is called persistence time. Persistence speed is deduced from the ratio of these two values (see Fig. 1B). Next, cell pauses and this phase can be characterized by its duration time; the number of turn per unit time captures the changes in directions. Measurements of these five parameters can lead to interesting results to characterize cell motion in a generic way (see Fig. 1C; Caballero, Voituriez, & Riveline, 2014).

1.1 PETRI DISHES AND BOYDEN CHAMBERS: THEIR LIMITS

Experiments have been mainly performed so far in conditions which can be viewed as "artificial" compared to in vivo conditions. For example, cells are cultured and observed in flat Petri dishes (see Figs. 1A and 2A), and this method was kept probably for historical reasons (Petri, 1887). In this setup, cells have random shapes and this can alter their migration; also, they evolve on 2D flat substrates which constitutes an important difference with 3D physiological environments. At the stage of plating, cells can appear as single cells or as groups of cells with an ill-controlled number of cells per group. These varying initial conditions can lead to bias in the study of motility. Other assays using Boyden chambers, for example, can also generate artificial conditions (see Fig. 2C; Boyden, 1962): cells are placed in an upper chamber and are exposed to a membrane with cavities of controlled dimensions, typically 10μ m in diameter and 10μ m in depth. In the presence of chemical gradients between the top and bottom compartments, cells eventually migrate. However, the motion itself is restricted to a small fraction of the cell size.

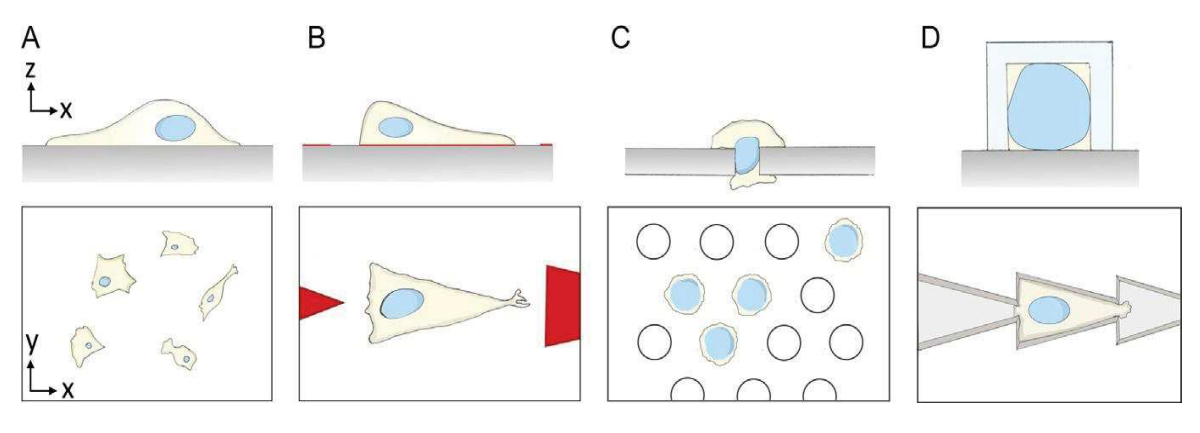


FIG. 2

Cell motility on different configurations. (A) Cell on Petri dish/flat 2D substrate. (B) Cell on 2D ratchet. (C) Cell on a "membrane" in a Boyden chamber experiment. (D) Cell in 3D confined ratchet. The nucleus is depicted in blue. In all panels, we represent x–z plane (top) and x–y plane (bottom).

This $10\mu m$ cavity limits considerably the potential extrapolation to in vivo situations. As a result, with Petri dishes and Boyden chambers, the study of cell migration lacks control and the assays can be far from reproducing physiological conditions.

1.2 THE MICROFABRICATION REVOLUTION AND ITS IMPACTS

The usage of techniques developed through microfabrication and microfluidics (Whitesides, 2006) have opened a new era for the study of cell migration (Caballero et al., 2014; Cramer, 2010; Hawkins et al., 2009; Jiang, Bruzewicz, Wong, Piel, & Whitesides, 2005; Prentice-Mott et al., 2013). When studying 2D cell migration, the shape of cells can be imposed on surfaces through adhesive microcontact printed proteins surrounded by cell repellent (see Fig. 2B; Thery & Piel, 2009). Cell symmetry and its effect on migration can be analyzed quantitatively and encoded in physical models (Fig. 5; Caballero et al., 2014; Hawkins et al., 2009). In addition, cells can be confined in 3D through the appropriate preparation of micro channels (see Fig. 2D); this can reproduce conditions where single cells are trapped in blood vessels with diameters smaller than cell dimensions. This configuration can also lead to controlled cell symmetries (see Figs. 7 and 8). In both cases, on flat 2D printed substrates and in 3D confined geometries, motions can be acquired in the presence of chemical gradients (Comelles et al., 2014; Prentice-Mott et al., 2013).

These developments have been possible because polydimethylsiloxane(PDMS)— the main material to prepare these assays—is biocompatible and easy to manipulate. The material is still liquid right after addition of the cross-linker and can be deposited on molds and cured in a 65°C oven. The PDMS solid mold can be replicated with negative/positive combinations with up to nanometer resolutions in the reproduction of motifs (Qin, Xia, & Whitesides, 2010). Altogether, cell shapes and dimensions are now

controlled with microfabrication, and these methods have shown to be essential for obtaining new standardized tests.

We report below experimental procedures to prepare these assays for the same cell type, i.e. NIH 3T3 fibroblasts. Any cell can be used, but the fact of probing the same cell line allows to identify changes in behaviors between experimental conditions set by the assay, such as speeds and directions.

1.3 DESIGNING THE MOTIFS: SCALING ARGUMENTS

In order to match the motility assays to each cell type, cell dimensions need to be determined first. The mean area of resting cells on flat coverslips allows to evaluate the optimal surface area needed to micro-contact print adhesive motifs on 2D flat surfaces. Cells will spread on these motifs with their spontaneous resting shape (Fig. 2B). In addition, measure of the mean cell diameter after trypsinization and before cells start spreading, helps to evaluate the cell volume and this can guide the design of motifs for 3D confinements (Fig. 2D). As reported above, the cell symmetry can also be modified: cells can adopt disk shapes (2D; Caballero et al., 2014) or move along straight channels (3D; Prentice-Mott et al., 2013), and their symmetry can be broken while keeping the projected area/volume constant in 2D/3D assays respectively. In fact, several studies have reported that the presence of asymmetric patterns in the environment can direct cell motion. This kind of motion has been named ratchetaxis (Caballero, Comelles, Piel, Voituriez, & Riveline, 2015). In 2D configuration, lines of periodic triangles can be generated to simplify the *ratchetaxis* motion along a single direction. For the 3D case, lines of periodic connected triangles can be generated to study the motion in confined environments with a local broken symmetry. In addition, the junction/gap between subsequent motifs can be controlled. In 2D, a cell on a motif will have different dynamics depending on the gap between neighboring motifs. In 3D confined situations, the opening width of connecting triangles will test different regimes in cell motility.

Altogether, cell area in 2D and cell volume in 3D will set rules for the design of the microfabricated unit. Gaps/junctions between motifs will test cell probing and confinement respectively. The sum of microfabricated unit length and junction's length can be integrated in a lattice unit or in cell dimension to compare between conditions and between cell types (L is about $100\mu m$ for NIH 3T3 cells, see Fig. 1A). Cells trajectory can be then calculated as lattice unit/cell length dimensions. Symmetry/asymmetry will be generated by keeping constant area/volume in 2D/3D respectively. Finally, the cell velocity should be taken into account for the design of experiments. Specifically, trajectories should be sufficiently long to acquire reliable statistics; this can be evaluated with cell velocity. For example, let us say that cells move at $10\mu m/h$ speed with a typical cell dimension of $100\mu m$. If we want to follow the cell migration for 10 times the length of a cell (around $1000\mu m$), taking into account the frequent pauses on 2D flat surfaces (see Fig. 1A), this would require an acquisition of at least 24h. In turn, the number of periodic lattice units should be prepared accordingly to allow cells to potentially move along this $1000\mu m$ long trajectory.

With these simple orders of magnitude in mind, the masks containing the motifs can be designed for microfabrication.

2 MICROFABRICATION OF MOTIFS

2.1 DESIGNING THE MOTIFS

Design of the mask can be done using different softwares, e.g. Clewin (Freeware) or Autocad[®]. A light sensitive material called photoresist is used during microfabrication: it is spin-coated on a wafer before exposure of the wafer to UV light when substrate and mask are in close contact (Fig. 3).

Motifs are designed according to the type of photoresist, positive or negative. Here in our study, epoxy based photoresist SU-8 (MicroChem) was used. SU-8 being a "negative" photoresist becomes insoluble to the SU-8 developer when exposed to UV light. The unexposed regions will be stripped off during the development process leaving behind the micro-structures. Masks have to be prepared accordingly, in order to fabricate either holes or pillars on the wafer.

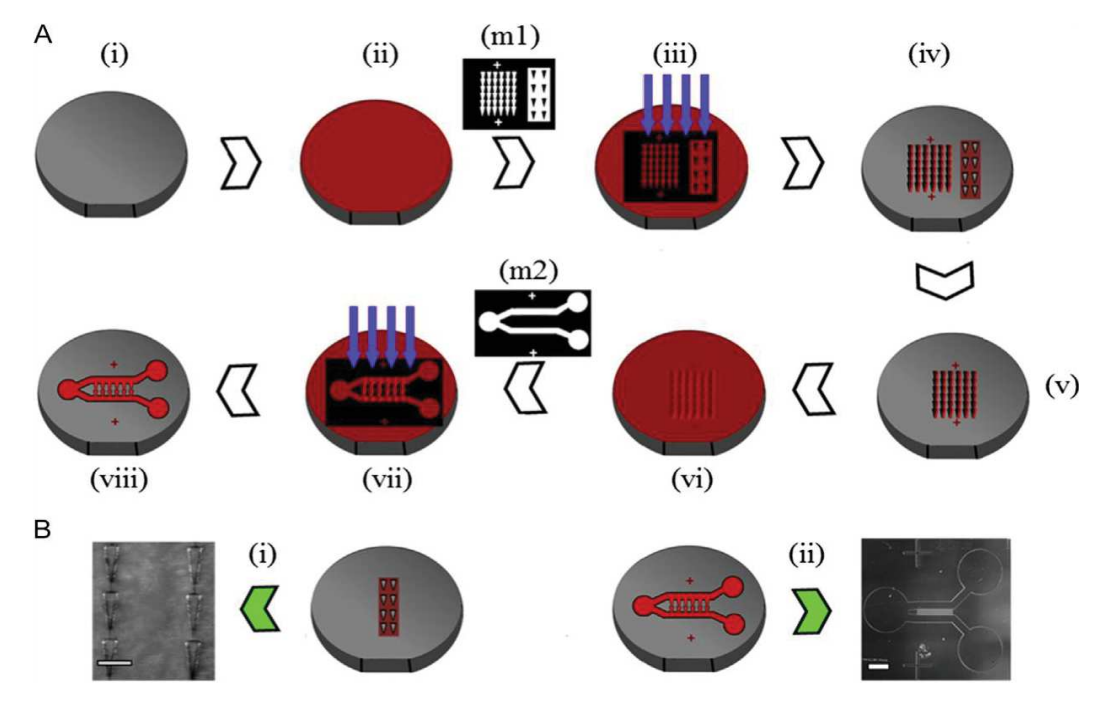


FIG. 3

Microfabrication for the study of 2D and 3D ratchetaxis. (A) Steps followed to obtain motifs. (i) Silicon wafer (ii) spin-coated with SU-8 (2005, 2025) according to the required height/ depth. (iii) UV exposure of the spin-coated wafer through the desired mask (m1) for the first layer. (iv) Developed motifs of the first layer with 5 μ m high connected triangles; left side of the wafer and 25 μ m deep first layer of separated triangles; right side of the wafer. (v) Wafer with 5 μ m high connected triangles (vi) spin-coated with photoresist; SU-8 2025 for 50 μ m thickness. (vii) UV exposure of the spin-coated wafer through the desired mask (m2) for the second layer. (viii) Developed motifs of the second layer; connected triangles with the reservoir. (B) Developed resin motifs on a Si wafer of (i) 25 μ m thick first layer of separated triangles (right side: holes on wafer; left side: image of the wafer, scale bar 100 μ m); and (ii) 5 μ m thick connected triangles with 50 μ m thick reservoir (left side: pillars on wafer: right side, image of the wafer, scale bar 1mm).

It is important to have dark motifs ("+" polarity) on the mask, so that the UV light cannot pass through, in turn fabricating holes on the wafer. Similarly, for fabricating pillars, transparent motifs ("2" polarity) have to be designed, which would allow the UV light to pass through the motifs, cross-linking the exposed photoresist. Structures fabricated in such a way have excellent thermal and mechanical stability.

After the masks with the desired dimensions are printed, motifs are prepared through microfabrication (see Section 2.2.1.3).

2.2 MICROFABRICATION

2.2.1 Protocol

2.2.1.1 Materials

- Silicon wafers (Si-Mat, cat. PRIME/76.5mm/381mm)
- Wafer tweezers
- Chromium/plastic photomask (Selba) with printed motifs to micro-fabricate
- SU-8 photoresist (MicroChem cat. SU8/2025/0.5)
- SU-8 developer (Chimie Tech Services, cat. DevSU8/4)
- Acetone
- 2-Propanol
- Ethanol 70%

2.2.1.2 Equipment

- Mask aligner (SUSS MicroTec, cat. MJB3)
- Spin-coater (Laurell Technologies, cat. WS-400B-6NPP)
- Hot plates (65°C and 95°C)
- Disposable graduated dropper (to remove air bubbles)

2.2.1.3 Method

Two sets of motifs are required for the processes reported in Sections 3–5. Section 3: micro-contact printing requires one layer of the photoresist ($25\mu m$). The depth is tuned to have an optimal aspect ratio: if the pillars are too high and the motif area is too small, pillars will bend during stamping and the quality of the printed patterns will not be optimum. Section 4: open microchannel configuration requires one layer of the photoresist ($25\mu m$): height of the photoresist pillars is tuned to have an optimal aspect ratio, and PDMS should be high enough to trap cells (see Fig. 7A). Sections 4 and 5: closed microchannel configuration requires two layers; a first layer of $5\mu m$ thickness and a second layer of $50\mu m$ thickness. The first layer is the microchannel which confines the cells from the top, whereas the second layer constitutes the reservoir for cells and should be high enough to allow cell movement and positioning. The following steps are performed in a clean room, if available (see Fig. 3):

1. Clean the silicon wafers with first acetone and then ethanol. Dry the wafer using a nitrogen stream after each solvent cleaning. Solvent cleaning insures complete removal of oils and organic residues from the surface of silicon wafers; while they do remove contaminants, solvents themselves actually leave residues on the surface of wafers as well. For this reason, a two-solvents method is implemented to ensure that the wafer is contaminant-free. After this step, heat the wafers at 200°C for 15–30min for a complete removal of humidity from the wafer surface.

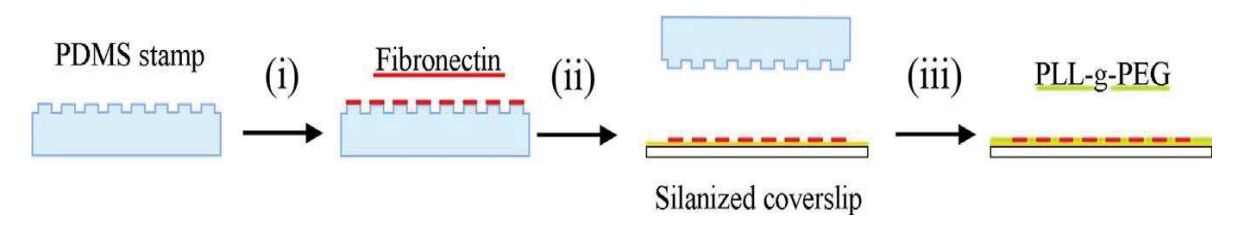


FIG. 4

Micro-contact printing procedure: (i) Incubation of the PDMS stamp with fibronectin. (ii) Stamping. (iii) Passivation with PLL-g-PEG.

- Spin-coat the first photoresist layer according to the target thickness. To obtain separated triangular patterns for micro-contact printing (see Fig. 4) and open micro-channels (see Fig. 7), pour the photoresist (SU-8 2025) on the wafer and remove air bubbles with the aid of a plastic dropper. Set a two-step spinning process on the spin-coater. Spin at 500rpm for 10s with an acceleration of 100rpm/s during the first step to homogenize the layer over the wafer.
- 3. Next, spin the wafer containing the resin at 3000rpm for 30s with acceleration of 300rpm/s for the second step. This should result in a photoresist layer of $25\mu m$ thickness (see Fig. 3A (ii)).
- 4. To obtain the first layer for the closed connected triangular microchannel (see Fig. 8), a $5\mu m$ thick layer is required. After repeating step (2) using the desired photoresist (SU-8 2005), spin at 3000rpm for 30s with acceleration of 300rpm/s for the second spin step. This should result in a photoresist thickness of $5\mu m$ (see Fig. 3A (ii)).

- 5. After obtaining the evenly spread photoresist, pre-bake has to be done to ensure a firm attachment of the photoresist to the wafer. For a $25\mu m$ thick layer, this step has to be done during 5min at 95° C and for a $5\mu m$ thick layer during 2min at 95° C.
- 6. After pre-bake, make a firm contact between the wafer and the mask containing the respective motifs. A defective contact will lead to ill-defined motifs (see Troubleshooting: Tr.1; Fig. 10A). The masks should have negative polarity for 25μm thick layer (Separated Triangles) to give holes and positive polarity for 5μm thick layer (Connected Triangles) to obtain pillars on photoresist (SU-8) layer. After tight contact with the mask (see Fig. 3A (m1)) cross-link the photoresist by exposing the wafer to UV irradiation with a dose of 150mJ/cm² for 25μm thick Separated Triangles and 105mJ/cm² for 5μm thick Connected Triangles (see Fig. 3A (iii)). The time of exposure will depend on the power/wavelength of the device (e.g., mask aligner) for the UV light exposure.
- 7. As soon as the exposure is over, for Separated Triangles: follow a post-bake of 1min at 65°C and then 5min at 95°C; and for Connected Triangle: 3min at 95°C. An image of the mask should be visible on the (SU-8) photoresist coating.
- 8. After post-bake, develop the structures by immersing them in the SU-8 developer solution, while gently agitating the container; 4min for 25μm thick Separated Triangles and 1min for 5μm thick Connected Triangles layer. This would strip off the non-cross-linked resin, leaving behind the required motifs (see Fig. 3A (iv)). Finally, rinse the surface with 2-propanol to remove the leftover photoresist.
- 9. Dry the wafer containing motifs, using a nitrogen stream after rinsing with 2-propanol.
- 10. After preparing a 5μm thick layer of Connected Triangles (see Fig. 3A (v)), a second layer has to be prepared in order to obtain a microchannel of connected triangles with a reservoir for cells on either side of the Connected Triangles, in order to introduce cells in micro channels (see Fig. 8B).
- 11. The second layer (for reservoir) is recommended to be 50μm thick to facilitate the entry of cells with the cell culture media. For this purpose, follow step (2) and spin the wafer containing the resin (SU-8 2025) at 1700rpm for 30s with an acceleration of 300rpm/s for the second spin step (see Fig. 3A (vi)).
- 12. Then follow a pre-bake of 6min at 95°C.
- 13. Before the next step of UV exposure for cross-linking, check on the silicon wafer that the mask for the second layer containing motif for reservoir (see Fig. 3A (m2)) is perfectly aligned with the developed first layer of Connected Triangles. For alignment purpose, it is recommended to design masks with two crosses each, on both mask 1 (containing microchannel motif) and mask 2 (containing the reservoir motif) exactly at the same position. During microfabrication and alignment process, both crosses should superimpose between the first photoresist (SU-8) layer and the second mask to ensure optimal alignment of the first and second layers (see Troubleshooting: Tr. 2)
- 14. Once the alignment is performed, secure the tight contact between the wafer and the mask (for reservoir). Cross-link the photoresist by exposing the wafer to UV irradiation with a dose of 150–155mJ/cm² for a 50μm layer of reservoir (see Fig. 3A (vii)).
- 15. As soon as exposure is over, follow a post-bake of 1min at 65°C and then 6min at 95°C. After post-bake at 95°C, an image of the mask should be visible on the photoresist coating.
- 16. Next, develop the structures by immersing the sample in the SU-8 developer solution while gently agitating the container for 5min. This would strip off the non-cross-linked resin, leaving behind motifs (see Fig. 3A (viii)). Finally, rinse the surface with 2-propanol to remove the leftovers of photoresist. 16. After the silicon wafers are ready with motifs (with one or two layers), do a "hard bake" step at 150°C for a couple of minutes. This is useful for annealing any surface cracks that may have appeared after development; this step is relevant to all layer thicknesses.

- 17. After obtaining the motifs for Separated Triangles ($25\mu m$ thick layer) and Connected Triangles (first layer: $5\mu m$, second layer: $50\mu m$), cover the wafers with PDMS (cross-linker:prepolymer [1:10]).
- 18. Remove all air bubbles through desiccation, and finally cure overnight at 65°C on a leveled surface.
- 19. Once cured, peel off the PDMS, the chip is ready.

3 RECTIFYING CELL MOTION WITH ASYMMETRICAL PATTERNS: MICRO-CONTACT PRINTING OF ADHESIVE MOTIFS

3.1 THE DESIGN OF PATTERN

The scaling arguments are presented in Caballero et al. (2014) for this assay.

3.2 MICRO-CONTACT PRINTING

3.2.1 Protocol

In this section, we detail the protocol for printing adhesive motifs on a glass coverslip. We use fluorescent fibronectin to visualize motifs with microscopy (other proteins could also be used). Poly-L-lysine-g-polyethylene glycol (PLL-g-PEG) is used for surface passivation (see Fig. 4).

3.2.1.1 Materials

- "Piranha" solution (sulfuric acid: hydrogen peroxide [7:3])
- Glass coverslips, N°1–25mm diameter
- 3-(Mercapto)propyltrimethoxysilane
- Phosphate-buffered saline 1 (PBS)
- 10µg/mL Rhodamine labeled Fibronectin (FN) (Cytoskeleton, cat. FNR01-A) in PBS
- 0.1mg/mL PLL-g-PEG diluted in HEPES 10mM (SuSoS AG, cat. SZ33-15)
- PDMS (Dow Corning, cat. DC184-1.1)
- Milli-Q Water
- Ethanol 70%
- Parafilm

3.2.1.2 Equipment

- Plasma Cleaner (Diener Electronic, cat. ZeptoB)
- Oven
- Sonicator
- Vacuum pump
- Desiccator

3.2.1.3 Methods

1. Clean the coverslips inside "Piranha" solution during 10min (this step should be performed cautiously under a hood). Bubbles will form, check that coverslips stay immersed throughout the process. Carefully rinse the glass coverslips with Milli-Q water. Then, sonicate one by one each coverslip in beakers during 5min and dry them with a nitrogen stream. Finally, put them in an oven at 65°C for 10min.

- 2. Place the "Piranha" cleaned coverslips inside the desiccator with a small Petri dish filled with $100\mu L$ of 3-(mercapto)propyltrimethoxysilane. Generate a vacuum, then close the pump and let the silane deposit on substrates for 1h.
- 3. Place the silanized coverslips for at least 90min at 65°C (up to 4h); note that non bound silane is very sensitive to temperature and humidity.
- 4. Meanwhile, cut the PDMS to have 1cm1cm stamps; sonicate them for 5min in ethanol and dry them with a nitrogen stream.
- 5. Activate the surface of each stamp with oxygen plasma (air can also be used). This step will make sure that the surface is hydrophilic and suitable for protein incubation and binding. Be sure that patterns face up during activation.
- 6. Incubate activated stamps with a $100\mu L$ drop of $10\mu g/mL$ solution of Rhodamine labeled FN for 1h.
- 7. After incubation, remove the drop with a pipette and quickly dry the stamp with a nitrogen stream. It should take only few seconds. You can also let the stamp dry at room temperature for about 5min. This step is critical and differences in drying will impact the overall quality of patterns (see Troubleshooting: Tr.3 and Tr.4).
- 8. Put the stamp (face with the patterns down) on the silanized coverslip with a 50g weight on top of it. Wait for 30min and gently remove weight and stamp from the coverslip. Store the patterned glass coverslips in PBS at 4°C. At this point, patterns can be stored up to one week, even if immediate usage is recommended.
- 9. Deposit a 100μ L drop of PLL-g-PEG on a piece of parafilm and put the patterned face of the coverslip onto the drop. Incubate for 20min. This step will passivate the surface and will decrease adhesion of cells outside the patterns.

3.2.2 2D Cell migration experiment

The cells should be carefully placed on the micro-contact printed motifs. Proper washing allows to generate samples with cells exclusively on motifs. Cells should be plated at low density. This will help prevent them to migrate along the same path and in turn potentially "collide." Such phenomenon would interfere with cells trajectories. Finally, low serum condition allows to keep standard cell motility while preventing cell division during migration.

3.2.2.1 Materials

- NIH3T3 cells (or other migratory fibroblasts)
- Dulbecco's Modified Eagle Medium (DMEM) 4.5g/L glucose 1% Penicillin

 streptomycin
- Bovine Calf Serum (BCS)
- Leibovitz's (L-15) medium
- Trypsin-EDTA
- Cell counter
- Pipettes
- 5mL Petri dishes (60mm in diameter)

3.2.2.2 Equipment

- Epifluorescence microscope with phase contrast and temperature control
- Sterile hood
- Incubator with CO₂
- Centrifuge

3.2.2.3 Methods

At this stage, all steps should be performed under a sterile hood with a laminar flow.

- 1. Trypsinize a 5mL Petri dish with adherent cells 3min, and add 3mL of DMEM 10% BCS.
- 2. Centrifuge cells at 500rpm during 3min and re-suspend the pellet in 5mL of DMEM 10% BCS.
- 3. Count cells and place 2000 cells on the micro-patterned coverslip.
- 4. Incubate cells for 30min at 37°C with 5% CO₂. Wash out the sample to remove non-adherent cells, and replace medium by L-15 with 1% BCS. This low serum condition will ensure standard cell motility while reducing cell division during the 48h experiments.
- 5. Go to the microscope and image patterns and cells (see Troubleshooting: Tr.5) (Fig. 5).

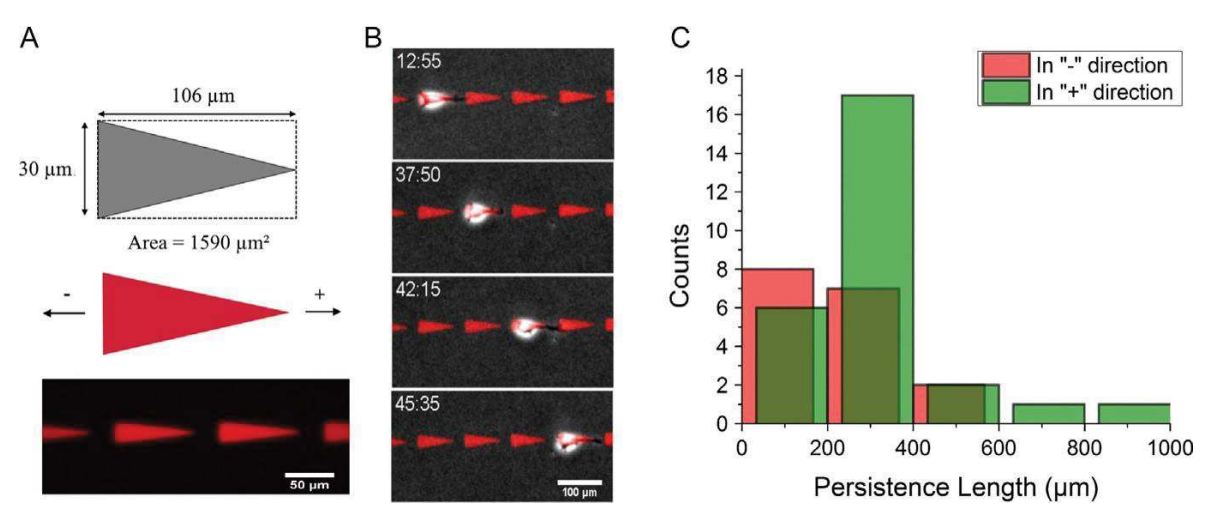


FIG. 5

(A) Pattern characteristics and dimensions (up) and motifs printed on a surface with micro-contact printing (bottom). Patterns are stamped with rhodamine labeled fibronectin. For clarity, tip direction is set as "+" and triangle base direction as "-" (middle). (B) Sequence of a NIH3T3 cell moving on triangles separated by $22\mu m$ gaps. T_0 corresponds to the beginning of acquisition (shortly after plating). Migration is directed toward the "+" direction in this sequence; Scale bar $50\mu m$. Time in hh:mm. (C) Persistence length distribution of NIH3T3 cells migrating in "+" direction and in "-" direction. Motion is directed, or rectified, to the + direction on average.

4 CONTROL OF CELL MIGRATION IN CONFINED 3D ENVIRONMENT 4.1 THE DESIGN OF PATTERN

Along the scaling arguments (see Section 1), we measured cell volumes after trypsinization. We obtained a mean diameter for individual rounded cells of D_{cell} =14.4±1.6µm (n=388 cells, s.d.), which corresponds to a mean volume of V_{cell} = 1560±520µm3. Nuclei were stained on spread cells using Hoechst, and their volume and height were measured. The mean volume was $V_{nucleus}$ =740±180µm³ (n=199 nuclei, s.d.) and the mean height $H_{nucleus}$ =8.5±1.4µm (n=199 nuclei, s.d.). Altogether, we used V_{cell} , $V_{nucleus}$, $V_{nucleus}$ to design the 3D triangle channel motif: each triangular motif has the volume of a NIH3T3 fibroblast (1500µm³). Taking into account these values, we selected the height of the microchannel of 5µm to allow confinement of cell and nucleus. We calculated the xy area for each triangle to be 300µm2. After selecting an angle of 16° similar to the angle used in triangles on 2D ratchetaxis and to further confine the nucleus, we selected an opening width of 4µm between connected ratchets. Using the following parameters (area: 300µm2, angle: 16° and opening width: 4µm), base and length of a ratchet were calculated. They are equal respectively to 14µm and 34µm (see Figs. 7 and 8). In ratchetaxis experiments, we used this motif in a closed microchannel configuration, where cells were confined from the top and sides (see Fig. 8); and in open microchannel configuration, cells were confined only from the sides (see Fig. 7).

In order to have a large number of trajectories per experiment, we designed a mask with 50 rows of connected triangles. For the closed configuration, two layers of SU-8 are required. The first layer contains connected ratchets of 5μ m height. The second layer allows to fabricate the cells reservoir of 50μ m height. In order to generate chemical gradients, the second layer has a Y-shaped channel of 50μ m height (see Figs. 3 and 9B). For the open microchannel configuration, a layer of 25μ m height SU-8 is required in order to trap cells (see Fig. 7A).

4.2 CONFINED OPEN MICROCHANNEL CONFIGURATION

4.2.1 Protocol

4.2.1.1 Materials

- Masks/silicon wafer
- PDMS
- Glass coverslips (N°1–25mm diameter)
- Chlorotrimethylsilane (Sigma, cat. 92360)
- 2mL Petri dish (35mm in diameter)

4.2.1.2 Equipment

- Plasma cleaner
- Tweezer
- Blade
- Oven
- Spin-coater
- Vacuum pump
- Desiccator

4.2.1.3 Methods

- 1. Pour PDMS (cross-linker:prepolymer [1:10]) on a silicon wafer. Remove air bubbles by placing the wafer into desiccator for 1h. Cure at 65°C for at least 4h.
- 2. Cut PDMS with a blade and remove the PDMS 1 stamp from the wafer (see Fig. 6A (i)).
- 3. Activate the surface of PDMS stamp 1 with oxygen plasma. Put it inside the desiccator with a small Petri dish filled with $100\mu L$ of chlorotrimethylsilane. Generate a vacuum, then close the pump and let the silane deposit on the substrate for 30min.
- 4. Pour PDMS (cross-linker:prepolymer (1:10)) on PDMS 1 placed on Petri dish. Check that patterns are "face up." Remove air bubbles by placing the wafer into the desiccator for 1h. Cure at 65°C for at least 4h (see Fig. 6A (ii)).
- 5. Cut PDMS with a blade and remove the PDMS stamp 2 from the Petri dish containing PDMS stamp 1.
- 6. Activate with oxygen plasma the surface of PDMS stamp 2. Put it inside the desiccator with a small Petri dish filled with $100\mu L$ of chlorotrimethylsilane. Generate a vacuum, then close the pump and let the silane deposit on the substrate for 30min.
- 7. Spin liquid PDMS on PDMS stamp 2. Set a two-step spinning process on the spin-coater. Spin at 500rpm for 10s during the first step to homogenize the PDMS layer over the PDMS stamp 2. The speed used in the second step will define the height of PDMS stamp 3. Spin-coating at a speed of 2000rpm allows the spreading of PDMS at a height of approximately $40\mu m$. Cure at 65° C for at least 4h (see Fig. 6A (iii)).

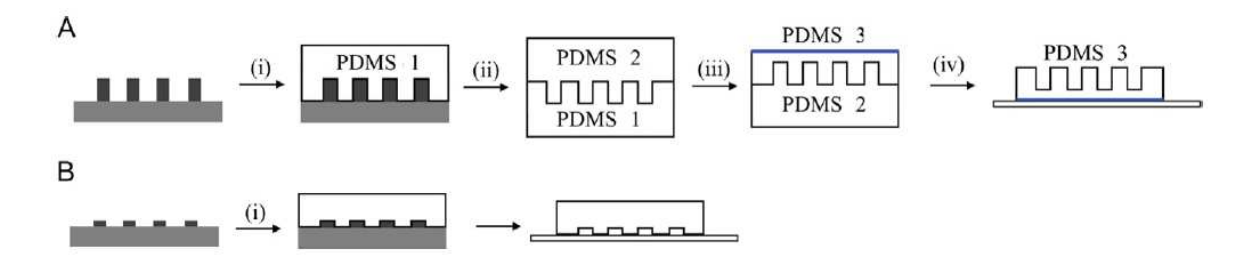


FIG. 7

Schematics of the method to obtain closed (A) and open (B) microchannel configuration. (i) PDMS is poured on SU-8 wafers and cured 4h at 65° C. In closed configuration, microchannels are 5μ m height. (ii) After activation of PDMS and coverslip with oxygen plasma, they are both bonded together. In open configuration, microchannels are 25μ m height. (ii) PDMS 1 is cut, activate with oxygen, treated with chlorotrimethylsilane and PDMS is poured on it and cured 4h at 65° C. (iii) PDMS 2 is cut, activated with oxygen, treated with chlorotrimethylsilane and PDMS is spin-coated on top of PDMS 2 at 2000rpm to obtain 40μ m PDMS layer. (iv) After curing at 65° C for 4h and activation with oxygen plasma, PDMS 3 is bonded to a coverslip and incubated overnight at 65° C to consolidate the bonding. PDMS 2 is then peeled off.

- 8. Activate both coverslip and PDMS stamp 3 (see Fig. 6A (iv); blue side) with oxygen plasma. Bind the blue surface side of PDMS stamp 3 to the coverslip. Incubate them at 65°C overnight to secure the binding between the PDMS stamp 3 and the glass coverslip.
- 9. With a tweezer, gently peel off the PDMS stamp 2 from the PDMS stamp 3 (which is attach to the coverslip).

4.2.2 Cell migration experiment

4.2.2.1 Materials

- NIH3T3 cells (or other migratory fibroblasts)
- DMEM 4.5g/L glucose 1% Penicillin–streptomycin
- BCS
- L-15 medium
- Trypsin-EDTA
- Cell counter
- Pipettes
- 5mL Petri dishes (60mm in diameter

4.2.2.2 Equipment

- Epifluorescence microscope with phase contrast and temperature control
- Sterile hood
- Incubator with CO2
- Centrifuge

4.2.2.3 Methods

At this stage, all steps should be performed under a sterile hood with a laminar flow. We report now how to place cells in the sample.

Before the experiment, activate the surface of the stamp with oxygen plasma. This step will make the surface hydrophilic and will facilitate media distribution within the sample. Place the open microchannel sample under UV for 10min sterilization.

Trypsinize a 5mL Petri dish with adherent cells 3min and add 4mL of DMEM 10% BCS. Count cells.

Centrifuge cells at 500rpm during 3min and re-suspend cells in DMEM 10% BCS at a density of 100,000 cells/mL.

Place $100\mu L$ of the cell suspension on the open microchannel configuration.

Incubate 30min at 37°C with 5% CO2. Wash out the sample to remove non-adherent cells and replace the medium with L-15 containing 1% BCS.

Go to the microscope and acquire cell migration with a 10min interval.

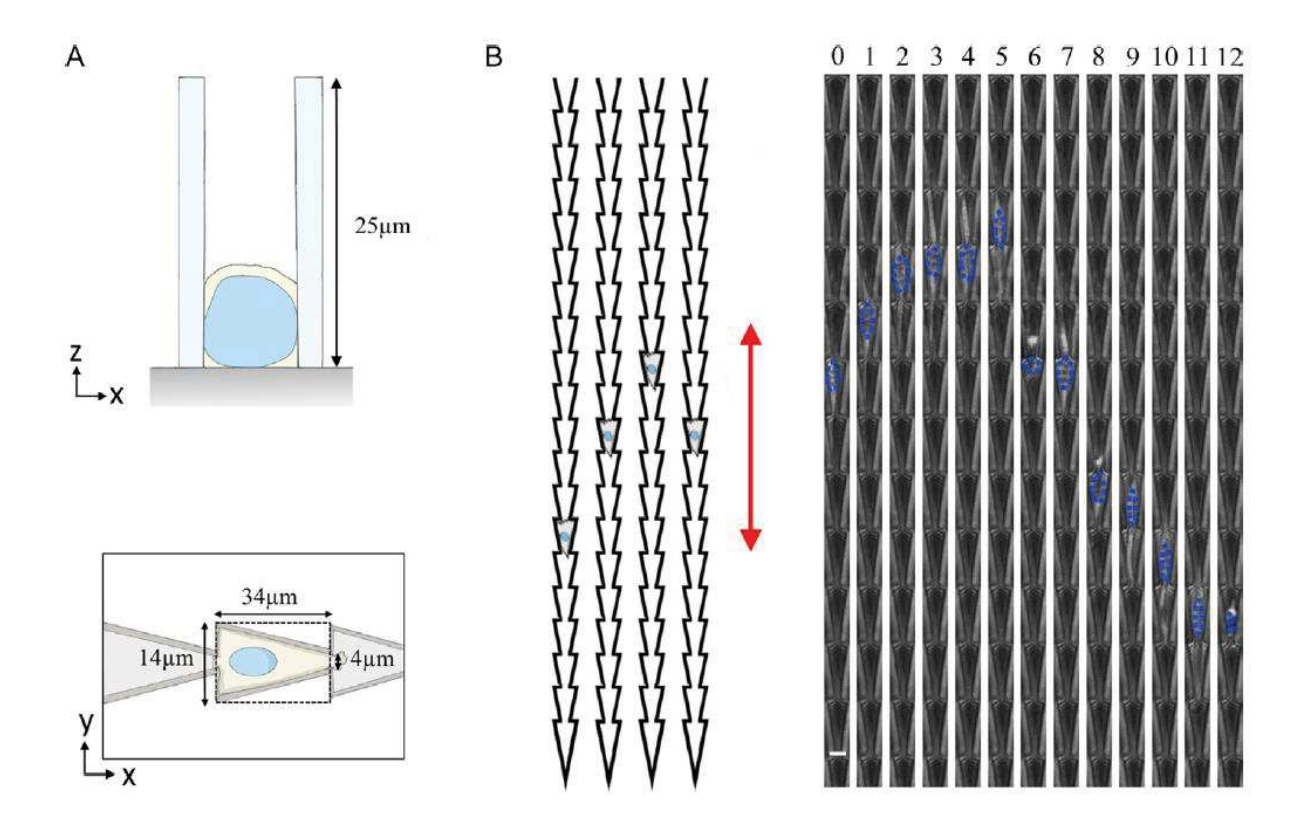


FIG. 8

(A) Dimension of the triangular 3D open configuration, xz plane (top) and xy plane (bottom). (B) Left: Schematic of the experimental setup. Cells are seeded in the middle of open ratchet microchannel. Right: Time-lapse images of a NIH3T3 fibroblast migrating in an open ratchet microchannel configuration. Blue dots outline the nucleus over time. Scale bar $10\mu m$, time in hour.

In open ratchet microchannel configuration, cells seeded in channels migrate longer and preferentially in the "+" direction after probing in both directions (see a typical example Fig. 7B.

4.3 CONFINED CLOSED MICROCHANNEL CONFIGURATION

4.3.1 Protocol

4.3.1.1 Materials

- Masks/silicon wafer
- PDMS
- Glass coverslips (N°1–25mm diameter)
- Holes puncher

4.3.1.2 Equipment

- Plasma cleaner
- Tweezer

- Blade
- Oven

4.3.1.3 Methods

- 1. Pour PDMS (cross-linker:prepolymer (1:10)) on a silicon wafer. Remove air bubbles by placing the wafer in the desiccator for 1h.
- 2. Cure at 65°C for at least 4h.
- 3. Cut PDMS with a blade and remove the PDMS stamp from the wafer (see Fig. 6B (i)).
- 4. Punch holes in the reservoirs with a 0.75mm diameter puncher.
- 5. Use adhesive tape to remove dusts and PDMS residues deposited on the motifs.
- 6. Activate the coverslip and PDMS stamp with oxygen plasma. Bind PDMS to the coverslip (see Fig. 6A (ii0)).
- 7. Incubate the chip at 65°C overnight to secure the binding between the PDMS stamp and the glass coverslip.

4.3.2 Cell migration experiment

At this stage, all steps should be performed under a sterile hood with a laminar flow. To place cells in the sample, we follow this protocol.

4.3.2.1 Materials

- NIH3T3 fibroblasts (or other migratory fibroblasts)
- Trypsin-EDTA
- DMEM 4.5g/L glucose 1% Penicillin–streptomycin
- Leibovitz's L-15 medium
- BCS
- Pipettes
- Petri dishes
- Eppendorf micro-loader (Eppendorf, cat. 5242956003)

4.3.2.2 Equipment

- Laminar flow hood
- Incubator
- Centrifuge
- Epifluorescence microscope with phase contrast and temperature control
- Metallic holder

4.3.2.3 Method

- 1. Activate the chip with oxygen plasma to make it hydrophilic. Fill in the PDMS chip with L-15 with 10% BCS.
- 2. Trypsinize a 5mL Petri dish with adherent cells for 3min, and add 4mL of DMEM 10% BCS. Count cells.
- 3. Centrifuge for 3min at 500rpm. Cells will form a pellet. Remove the supernatant and resuspend cells in L-15 10% BCS at a density of 30 million cells/mL.

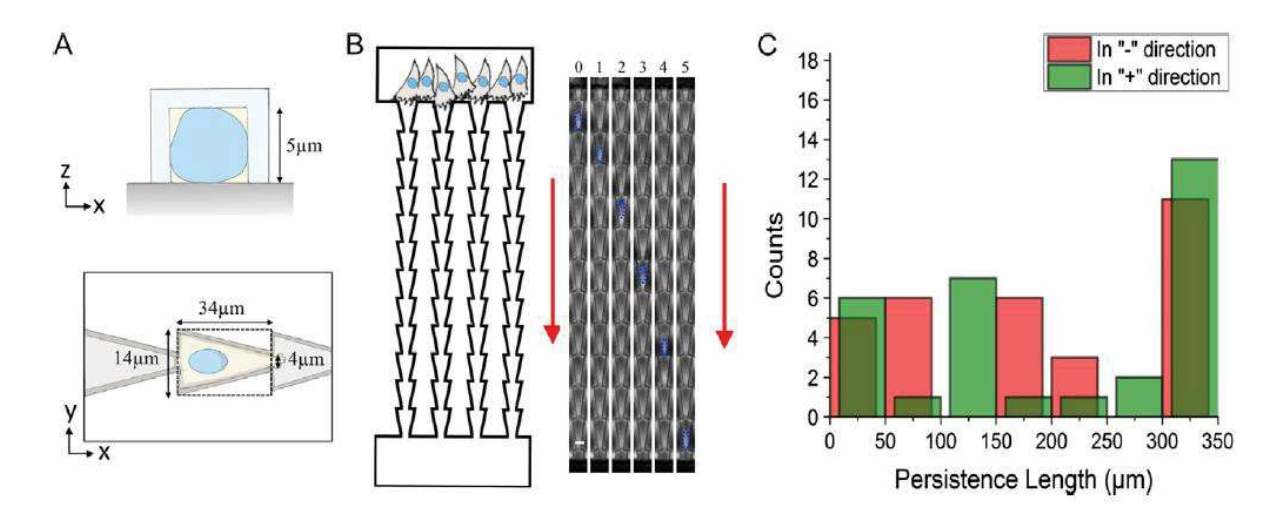


FIG. 8

Dimension of the triangle 3D confined motifs. (A) Schematic of a ratchet unit with its dimensions, xz axis (top) and xy axis (bottom). (B) Left: Schematics of the experimental setup. Cells are seeded in one side of the channel allowing the entry and migration of the cells in the "+" direction (red arrow). Right: Time-lapse images of a NIH3T3 fibroblast migrating in a ratchet microchannel in the "+" direction (red arrow). Blue dots outline the nucleus over time. Scale bar $10\mu m$, time in hours. (C) Persistence length distributions of cells migrating in "+" direction and in "-" direction. Experiments in (B) were repeated with cells plated on the other side of the channel. Altogether, the confined configuration forces cells to follow the polarity set at the entry of channels (in preparation).

- 4. With an Eppendorf micro-loader, inject 20μL of cells suspension into one inlet (see Fig. 8B). Slowly aspirate L-15 medium from the second inlet to allow accumulation of cells at the entry of channel.
- 5. Immerse the PDMS chip in L-15 containing 10% BCS.
- 6. Incubate for 2h at 37°C to let cells adhere and spread.
- 7. Transfer the chip into sterile holder and start the time-lapse acquisition with a 10 objective and 10min interval. Note that due to the presence of a thin layer of PDMS in the optical path, phase contrast images might not be optimal. To improve the phase contrast, use an objective with a numerical aperture of a minimum 0.40.

5 CONTROL OF CELL MIGRATION IN 3D WITH CHEMOTAXIS

With this setup, the motion of cells can be challenged by a chemical gradient when the sample is closed (see Fig. 9B). We report now the protocol.

5.1 PROTOCOL

5.1.1 Materials

- Masks/silicon wafer
- PDMS
- Glass coverslips (N°1–25mm diameter)
- Holes puncher

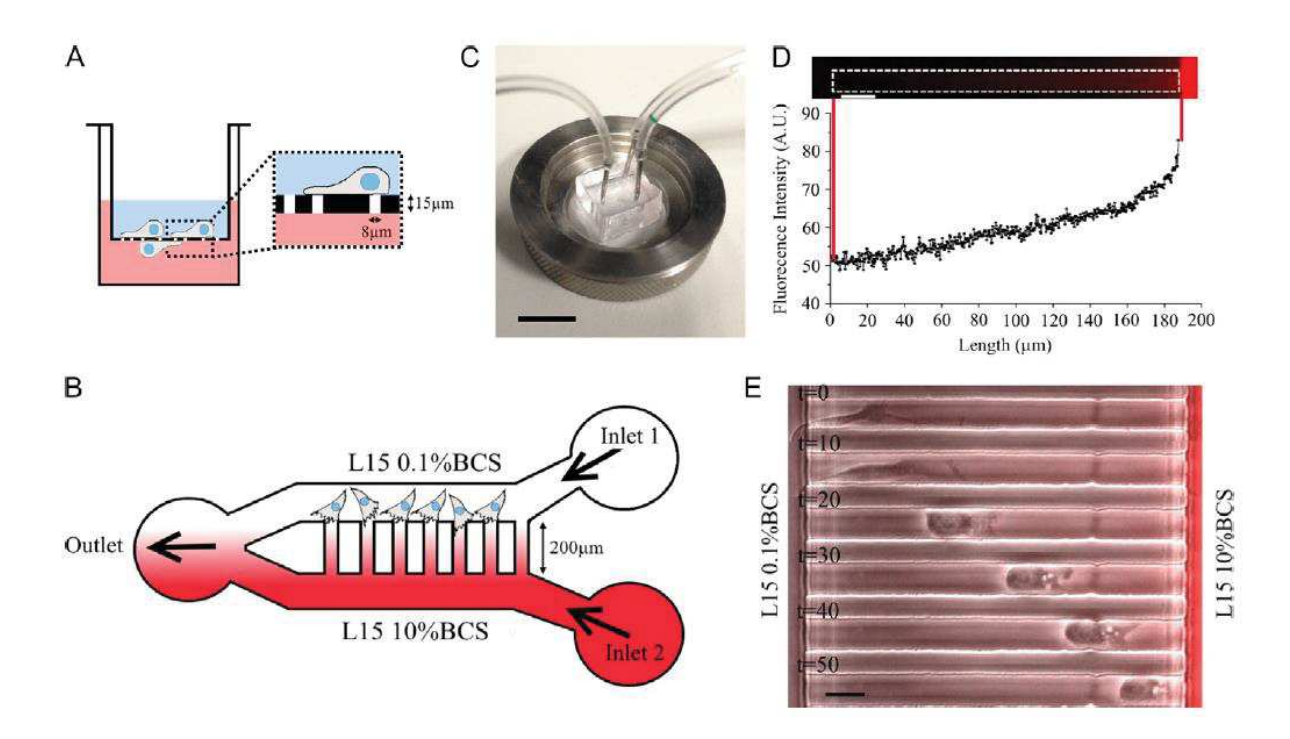


FIG. 9

Boyden and microfluidics experiments to study chemotaxis. (A) Schematic of a Boyden chamber. Typically, a Boyden chamber is composed of two chambers separated by a 15μ m thickness membrane with 8μ m pores (Boyden, 1962). Cells are seeded in the upper chamber in medium without chemo-attractant. The lower chamber is filled with medium containing the chemo-attractant. After incubation for 12h, migration is stopped and migrating cells which crossed the membrane are counted. (B) Schematic of the microfluidic chip used to follow cell migration in response to a chemical gradient. Cells are seeded in the microfluidics chamber. Gradient is formed in the micro-channels by connecting two syringes, one with the chemo-attractant and fluorescent dye and the other one without. A syringe pump is necessary to form stable gradient up to 24h. (C) Image of the device. Scale bar 1cm. (D) Top: Fluorescent image of the microchannel and the chemical gradient visualized with fluorescent dye. Bottom: Corresponding fluorescent intensity profile along the microchannel. Scale bar 20μ m. (E) Timelapse images of a NIH3T3 fibroblast migrating in a microchannel in a gradient of 10% serum. Scale bar 20μ m, time in minutes.

5.1.2 Equipment

- Plasma cleaner
- Tweezer
- Blade
- Oven

5.1.3 Methods

- 1. Pour PDMS (cross-linker:prepolymer (1:10)) on a silicon wafer. Remove air bubbles by placing the wafer in the desiccator for 1h.
- 2. Cure at 65°C for at least 4h.
- 3. Cut PDMS with a blade and remove the PDMS stamp from the wafer (see Fig. 6A (i)).
- 4. Punch holes in the inlets—outlet with a 0.75mm diameter puncher.

- 5. Use adhesive tape on the motifs to remove any residual dusts and/or PDMS residues.
- 6. Activate the coverslip and PDMS stamp with oxygen plasma. Bind PDMS to the coverslip (see Fig. 6A (ii)).
- 7. Incubate the chip at 65°C overnight to secure the binding between the PDMS stamp and the glass coverslip.

5.2 CELL MIGRATION EXPERIMENT

At this stage, all steps should be performed under a sterile hood with a laminar flow. To place cells in the sample, we follow this protocol.

5.2.1 Materials

- NIH3T3 fibroblasts (or other migratory fibroblasts)
- Trypsin-EDTA
- DMEM 4.5g/L glucose 1% Penicillin–streptomycin
- Leibovitz's L-15 medium
- BCS
- Petri dishes
- Eppendorf micro-loader
- Tetramethylrhodamine isothiocyanate—Dextran, molecular weight 20kDa (Sigma, cat. 73766)
- 1mL syringe (Henke-Sass Wolf Soft-Ject, cat. 5010-A00V0)
- 20Gx100 needle (Terumo 0.925mm Luer)
- 23Gx100 needle (Terumo 0.625mm Luer)
- Tygon tubing (Saint Gobain, cat. AAD04103)

5.2.2 Equipment

- Laminar flow hood
- Incubator
- Centrifuge
- Epifluorescence microscope with phase contrast and temperature control
- Metallic holder
- Syringe pump

5.2.3 Method

- 1. Activate the chip with oxygen plasma to make it hydrophilic. Fill in the PDMS chip with L-15 with no BCS (0% BCS).
- 2. Trypsinize a 5mL Petri dish with adherent cells 3min, and add 4mL of DMEM containing 10% BCS. Count cells.
- 3. Centrifuge for 3min at 500rpm. Cells will form a pellet. Remove the supernatant and resuspend cells in L-15 0% BCS at a density of 30 million cells/mL. Cells are re-suspended in L-15 0% BCS in order to starve cells prior stimulation to the serum gradient.
- 4. With an elongated tip, inject 20μL of cell suspension into the outlet. Slowly aspirate L-15 medium from inlet 1 to allow accumulation of cells at the channels entry (see Fig. 9B).
- 5. Immerse the PDMS chip in L-15 0% BCS.
- 6. Incubate for 2h at 37°C to let cells adhere and spread.
- 7. Transfer the chip into the sample holder.
- 8. To form the serum gradient, two 1mL syringes are prepared with L-15 0.1% BCS or L-15 containing 10% BCS and fluorescent dextran, enabling visualization of the chemical gradient.
- 9. Connect syringes to syringe needles (23Gx100) and Tygon tubing which have previously been rinsed with L-15.

10. Make sure that there are no bubbles into the tubing during experiment. This can prevent a good flow and detach cells if bubbles enter the microfluidic device (see Troubleshooting: Tr.6; Fig. 10F).

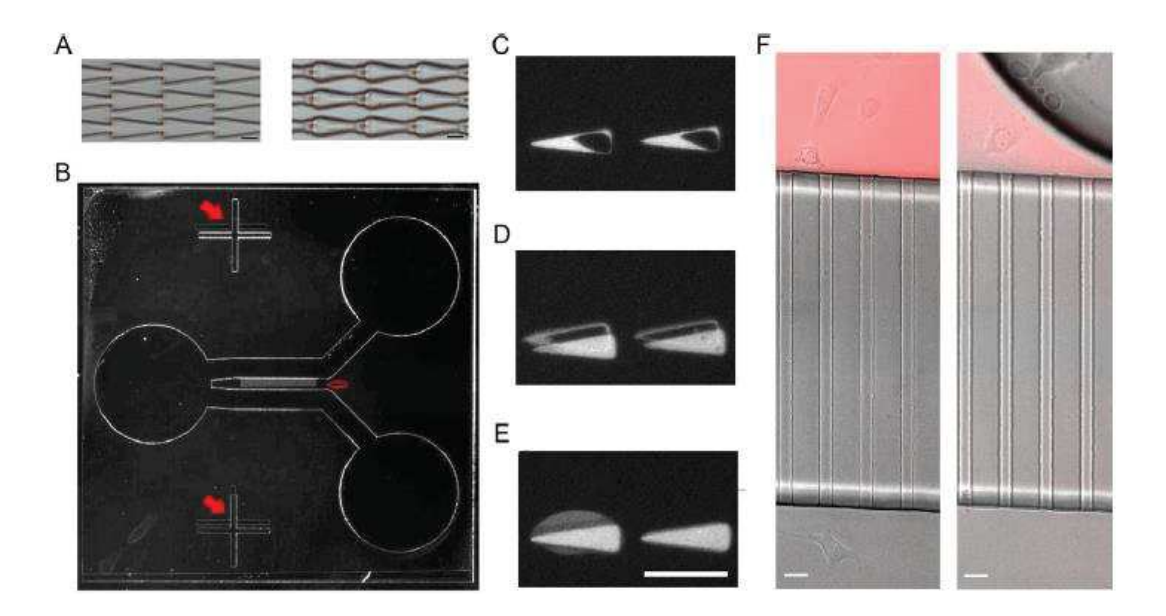


FIG.10

Issues during microfabrication (A and B), micro-contact printing process (C, D, and E) and microfluidics experiments (F). (A) Images of two wafers. Left: Image of connected ratchet microchannel properly defined. Right: Image of ill-defined connected ratchet microchannel due to poor contact between SU-8 on wafer and mask. Scale bar $20\mu m$. (B) Image of a wafer where first and second layers are misaligned. Filled red arrows show non-aligned crosses, empty red arrow shows that micro-channels are not connected to the main channel at the bottom side. Scale bar $100\mu m$. (C) Patterns with overdried stamp. (D) Double stamping. (E) Wet patterns. (F) Appearance of bubbles during chemical gradient experiment in microchannel. Chemical gradient is removed in the presence of bubble. Scale bar $20\mu m$.

- 11. Connect tubing to the two inlets of the chip by using cut syringe needles (20Gx100). The outer diameter of the needles (0.9mm) is slightly larger than the diameter of the punched holes (0.75mm). This allows to make sure that upon insertion the connection is sealed securely (see Fig. 9C).
- 12. Place syringes on the pump. Flow the two solutions at a rate of 10μ L/h. After few minutes, a stable gradient forms into microchannels which can be visualized with fluorescent dextran as seen in Fig. 9D and E.

Conclusion: With this method, chemical gradients can be generated in closed configurations—but not in open configurations. They can be imposed in competition or in cooperation with other external cues such as confinement and ratchetaxis. The net results can be reported through the analysis of trajectories like in the other examples presented above.

6 TROUBLESHOOTING

Many issues can appear in the preparation of samples, during the microfabrication, micro-patterning, or even during acquisition under the microscope. We follow the order of their appearance below.

6.1 MICROFABRICATION

Tr.1: During microfabrication process, a critical step is to obtain well defined structures, for example, triangles should have sharp edges. Ill-defined structures will appear, if there is not a firm contact maintained between SU-8 and mask (see step in Figs. 3 (iii) and 10A). To prevent this, make sure that the contact is tight enough. This can also happen during the development step when motifs are under or overdeveloped. To avoid this, immerse back the wafer in SU-8 developing solution for 30s, rinse with isopropanol and check the motifs.

Tr.2: If two layers are required, they need to be perfectly aligned. A misalignment is observed when crosses on the wafer of layer 1 do not overlap with crosses on the mask for the layer 2 (see Fig. 10B filled arrows). This results in disconnected structures from the first and second SU-8 layers (see Fig. 10B empty arrow). To prevent this, be patient and pay attention during alignment step that both crosses are aligned. During the design of the mask, it is possible to insert more asymmetric motifs in both masks (for the layers 1 and 2) along the motifs to make sure that there is optimal alignment, before UV exposure.

6.2 MICRO-CONTACT PRINTING

Tr.3: Drying time critically depends on humidity, the ambient temperature in the room and on patterns characteristics (area, aspect ratio and spacing between motifs). It can vary from 2min to 6min depending on the design. Drying the stamps with a nitrogen stream can prevent these problems, but this method is more difficult to control. Drying too much the stamp will impede fibronectin transfer to the glass surface (Fig. 10C). On the other hand, a stamp too wet gives ill-defined patterns (Fig. 10E). This is the most critical step.

Tr.4: Double stamping (Fig. 10D) usually happens when the stamp moves while applying pressure or when it touches again the coverslip while removing it. Using two tweezers to remove the stamp (one on the coverslip, the other one holding the stamp) is a good solution to carefully release the PDMS stamp from the coverslip.

Tr.5: Cell death during acquisition might happen for the following reasons:

Coverslips are not well rinsed after "piranha" treatment.

Stability of PLL-g-PEG: it is recommended not to use the diluted solution after 2–3 weeks.

Cells are too confluent on the plate, prior deposition on patterns: contact inhibition might affect cell motility and prevent motion leading to death on the motifs (especially for large gap distances).

6.3 MICROFLUIDICS

Tr.6: While imaging, air bubbles can affect the stability of chemical gradients (see Fig. 10F), and can lead to detachment of cells from the coverslip. Typically, this type of experiments cannot be analyzed. To prevent this, make sure that there are no bubbles in the tubing while preparing them and before starting experiment.

Tr.7: Even after the sealing of PDMS stamps to the coverslip, sometimes detachment can occur. A proper binding is particularly important for generating the chemical gradient. In this situation, check that plasma binding is properly achieved. Also, check if PDMS and coverslips are clean and without dusts, which if present could prevent proper sealing.

Optimal z-focus: In order to image cells during typical timescales relevant for reliable measures, i.e., days, cells need to remain within the same focal plane. When acquiring for longer time periods at 37° C, microscopes might exhibit some drift due to thermal gradients, in particular along the z-direction. A good solution involves placing the entire experimental set-up in an environment with temperature control ahead of time, prior the experiment to secure a good mechanical stability. Alternatively, feedback loops to control the objective-sample distance can be used to keep focus throughout acquisition. Also, μ m size beads can be deposited on the sample, and images can be realigned after experiments using these fiducial markers.

7 CONCLUSION

The methods reported in this article show how cell migration can be controlled specifically for a quantitative study. Their implementations do not require large and expensive equipment and these assays can be used in any laboratories. Designs of 2D and 3D cellular controls have allowed to reveal new modes of migrations (Bergert et al., 2015; Caballero et al., 2015; Liu et al., 2015). With such setups, more migration modes could appear and the associated signaling networks could be studied. Finally, these microfabrication techniques could also open potential new methods for diagnosis at cellular scales in diseases where migration is impaired, in cancer for example (Mitchell, Jain, & Langer, 2017).

REFERENCES

Bergert, M., Erzberger, A., Desai, R. A., Aspalter, I. M., Oates, A. C., Charras, G., et al. (2015). Force transmission during adhesion-independent migration. Nature Cell Biology, 17(4), 524–529. Boyden, S. (1962). The chemotactic effect of mixtures of antibody and antigen on polymorphonuclear leucocytes. Journal of Experimental Medicine, 115(3), 453–466. Caballero, D., Comelles, J., Piel, M., Voituriez, R., & Riveline, D. (2015). Ratchetaxis: Longrange directed cell migration by local cues. Trends in Cell Biology, 25(12), 815–827.

Caballero, D., Voituriez, R., & Riveline, D. (2014). Protrusion fluctuations direct cell motion. Biophysical Journal, 107(1), 34–42.

Comelles, J., Caballero, D., Voituriez, R., Hortig€uela, V., Wollrab, V., Godeau, A. L., et al. (2014). Cells as active particles in asymmetric potentials: Motility under external gradients. Biophysical Journal, 107(7), 1513–1522.

Cramer, L. P. (2010). Forming the cell rear first: Breaking cell symmetry to trigger directed cell migration. Nature Cell Biology, 12(7), 628–632.

Hawkins, R. J., Piel, M., Faure-Andre, G., Lennon-Dumenil, A. M., Joanny, J. F., Prost, J., et al. (2009). Pushing off the walls: A mechanism of cell motility in confinement. Physical Review Letters, 102, 058103-1–058103-4.

Helvert, S. V., Storm, C., & Friedl, P. (2018). Mechanoreciprocity in cell migration. Nature Cell Biology, 20(1), 8–20.

Jiang, X., Bruzewicz, D. A., Wong, A. P., Piel, M., & Whitesides, G. M. (2005). Directing cell migration with asymmetric micropatterns. Proceedings of the National Academy of Sciences of the United States of America, 102(4), 975–978.

Liu, Y. J., Le Berre, M., Lautenschlaeger, F., Maiuri, P., Callan-Jones, A., Heuze, M., et al. (2015). Confinement and low adhesion induce fast amoeboid migration of slow mesenchymal cells. Cell, 160, 659–672.

Mitchell, M. J., Jain, R. K., & Langer, R. (2017). Engineering and physical sciences in oncology: Challenges and opportunities. Nature Reviews. Cancer, 17, 659–675.

Petri, J. R. (1887). Eine kleine Modification des Koch'schen Plattenverfahrens. Centralblatt fu€r Bakteriologie und Parasitenkunde, 1, 279–280.

Prentice-Mott, H. V., Chang, C.-H., Mahadevan, L., Mitchison, T. J., Irimia, D., & Shah, J. V. (2013). Biased migration of confined neutrophil-like cells in asymmetric hydraulic environments. Proceedings of the National Academy of Sciences of the United States of America, 110(52), 21006–21011.

Qin, D., Xia, Y., & Whitesides, G. M. (2010). Soft lithography for micro- and nanoscale patterning. Nature Protocols, 5(3), 491–502.

Thery, M., & Piel, M. (2009). Adhesive micropatterns for cells: A microcontact printing protocol. Cold Spring Harbor Protocols, 4(7), 1–12.

Whitesides, G. M. (2006). The origins and the future of microfluidics. Nature, 442, 368-3





Simon LO VECCHIO

Brisures de symétrie et directionnalité dans les systèmes vivants

Résumé

La manière dont les cellules suivent un mouvement dirigé sur de longues distances constitue une question fondamentale en Biologie. Ces migrations, individuelles ou collectives, émergent spontanément. Dans ce travail de thèse aux Interfaces entre la Physique et la Biologie, nous avons étudié les brisures de symétrie pour des cellules individuelles et pour un ensemble cellulaire. Nous montrons que des cellules migrant au sein d'environnements dont la symétrie a été brisée localement adoptent un mouvement directionnel. Ce type de phénomène, appelé *ratchetaxis*, est dicté par la dynamique des adhésions focales sur les aires accessibles à la cellule. En 3D, la compression du noyau cellulaire et l'organisation du cytosquelette sont les principaux déterminants. Nous avons enfin étudié le comportement d'un ensemble de cellules sur des anneaux. Dans ce contexte, la symétrie de l'environnement n'est pas brisée, mais les cellules adoptent spontanément un mouvement directionnel, cohérent, impliquant l'ensemble de la cohorte. Nous montrons que cette cohérence est le résultat d'interactions entre polarités voisines, effets de bord imposés par les câbles d'acto-myosine, activité Rho.

Mots clés : physique cellulaire, biologie quantitative, GTPase Rho, cytosquelette, adhésions focales, migration dirigée, ratchetaxis, brisure de symétrie, mouvements collectifs, cohérence, polarité cellulaire, micro-fabrication, simulation numérique.

Résumé en anglais

Directed cell migration is fundamental in Biology. These motions – at the single cell level or at the multicellular scale – can emerge spontaneously. In this work at the Interface between Physics and Biology, we studied directed motion at these two different scales. We show that single cells migrate directionally when placed into micro-environments with local broken symmetries. This motion, coined *ratchetaxis*, is driven by the dynamics of focal adhesions. In 3D, nucleus compression and cytoskeleton organization are involved in setting cell direction. We next studied the behaviour of a collection of cells on rings patterns. In this context, the micro-environment is isotropic. However, cells spontaneously undergo a directed coherent motion which involves the cellular cohort. We show that the onset of coherence is driven by simple interaction rules between single cell polarities, acto-myosin cables at boundaries and RhoA activity.

Keywords: cell physics, quantitative biology, Rho GTPase, cytoskeleton, focal adhesions, directed migration, ratchetaxis, broken symmetry, collective motion, coherence, cell polarity, microfabrication, numerical simulation.